CERN Yellow Reports: Monographs CERN-2025-003

Status and challenges of Nb$_3$Sn accelerator magnets at CERN: Lessons learned from ITER to HL-LHC

A. Devred[1], C. Abad Cabrera[2], I. Aviles Santillana[1], J. Axensalva[1], H. Bajas[3], M. Bednarek[1], A. Bertarelli[1], N. Bourcey[1], M. Crouvizier[1], D. Duarte Ramos[1], J. Ferradas Troitino[1], L. Fiscarelli[1], J. Fleiter[1], C. Garion[1], E. Gautheron[1], S.C. Hopkins[1], J.-M. Jimenez[1], D. Larbalestier[4], P. Lee[4], N. Lusa[1], F. Mangiarotti[1], A. Moros[1], M. Morrone[1], D. Perini[1], R. Piccin[1], H. Prin[1], R. Principe[1], F. Rodriguez Mateos[1], P. Rogacki[1], J.-L. Rudeiros Fernandez[5], S. Russenschuck[1], F. Savary[1], C. Scheuerlein[1], S. Sgobba[1], G. Spigo[6], E. Takala[7], G. Vernassa[1], and G. Willering[1]

[1] CERN, Geneva, Switzerland
[2] Formerly CERN, now IMI plc, Geneva, Switzerland
[3] Formerly CERN, now GSI Helmholtz Centre for Heavy Ion Research, Darmstadt, Germany
[4] National High Magnetic Field Laboratory, Tallahassee (FL), USA
[5] Formerly CERN, now Lawrence Berkeley National Laboratory, Berkeley (CA), USA
[5] Formerly CERN
[7] Formerly CERN, now IQM, Espoo, Finland

CERN Yellow Reports: Monographs
Published by CERN, CH-1211 Geneva 23, Switzerland

ISBN 978-92-9083-679-7 (paperback)
ISBN 978-92-9083-680-3 (PDF)
ISSN 2519-8068 (Print)
ISSN 2519-8076 (Online)
DOI https://doi.org/10.23731/CYRM-2025-003

This volume should be cited as:
Status and challenges of Nb_3Sn accelerator magnets at CERN: Lessons learned from ITER to HL-LHC, A. Devred *et al.*, CERN Yellow Reports: Monographs, CERN-2025-003 (CERN, Geneva, 2025), doi.org/10.23731/CYRM-2025-003

Accepted January, 2025, by the CERN Reports Editorial Board
(contact Carlos.Lourenco@cern.ch).
Published by the CERN Scientific Information Service (contact Jens.Vigen@cern.ch).
Indexed in the CERN Document Server and in INSPIRE.
Published Open Access to permit its wide dissemination, as knowledge transfer is an integral part of the mission of CERN.

Status and challenges of Nb_3Sn accelerator magnets at CERN: lessons learned from ITER to HL-LHC

A. Devred[1], C. Abad Cabrera[2], I. Aviles Santillana[1], J. Axensalva[1], H. Bajas[3], M. Bednarek[1], A. Bertarelli[1], N. Bourcey[1], M. Crouvizier[1], D. Duarte Ramos[1], J. Ferradas-Troitino[1], L. Fiscarelli[1], J. Fleiter[1], C. Garion[1], E. Gautheron[1], S.C. Hopkins[1], J.-M. Jimenez[1], D. Larbalestier[4], P. Lee[4], N. Lusa[1], F. Mangiarotti[1], A. Moros[1], M. Morrone[1], D. Perini[1], R. Piccin[1], H. Prin[1], R. Principe[1], F. Rodriguez Mateos[1], P. Rogacki[1], J.-L. Rudeiros Fernandez[5], S. Russenschuck[1], F. Savary[1], C. Scheuerlein[1], S. Sgobba[1], G. Spigo[6], E. Takala[7], G. Vernassa[1], and G. Willering[1]
[1] CERN, Geneva, Switzerland
[2] Formerly CERN, now IMI plc, Geneva, Switzerland
[3] Formerly CERN, now GSI Helmholtz Centre for Heavy Ion Research, Darmstadt, Germany
[4] National High Magnetic Field Laboratory, Tallahassee (FL), USA
[5] Formerly CERN, now Lawrence Berkeley National Laboratory, Berkeley (CA), USA
[6] Formerly CERN
[7] Formerly CERN, now IQM, Espoo, Finland

Abstract

The High-Luminosity Large Hadron Collider (HL-LHC) project at CERN has offered the opportunity to promote and develop various types of enabling accelerator technologies, such as MgB_2 superconducting links for cold powering and Nb_3Sn accelerator magnets for the interaction regions where the two high-luminosity experimental areas of the machine are located. A prototype superconducting link system has been successfully tested in the second quarter of 2024 and series production is now ongoing. The Nb_3Sn magnet development has encountered some difficulties characterized by performance limitation or degradation, which have now been overcome. We report on the status and challenges of HL-LHC Nb_3Sn accelerator magnets at CERN, with a primary focus on the root-cause analyses and recovery actions implemented for the 11 T dipole magnet program and for the final-focusing quadrupole magnet program. The symptoms have similarities with those encountered over a decade ago on the Nb_3Sn Cable-in-Conduit conductors for the magnets of the International Thermonuclear Experimental Reactor (ITER) and the methodology to address them was inspired from that developed to resolve the ITER crisis. Thanks to the successful efforts of ITER and HL-LHC, Nb_3Sn has been demonstrated to be a viable technology for fusion and accelerator magnet applications and is now reaching maturity.

Keywords

Low temperature superconductors, Nb_3Sn, accelerator magnets, fusion magnets, ITER, LHC, HL-LHC, electrical design criterion at cryogenic temperature, post-mortem analysis, metallography, finite element simulation.

Table of Contents

Acronyms

ASIPP: Institute of Plasma Physics, Chinese Academy of Sciences

ALICE: A Large Ion Collider Experiment, a detector dedicated to heavy-ion physics at the LHC

ASC: Applied Superconductivity Center associated with NHMFH and FSU

ATLAS: A Toroidal LHC ApparatuS, a detector dedicated to heavy-ion physics at the LHC

AUP: HL-LHC Accelerator Upgrade Project, funded by US DOE

BNL: Brookhaven National Laboratory

BSE: Back Scattered Electron images

CEA: Alternative Energies and Atomic Energy Commission

CAD: Computer Aided Design

CARE: Coordinated Accelerator Research in Europe Integrated Activity, funded as part of EU Framework Program 5

CC: Correction Coil (*e.g.*, of ITER)

CCT: Canted Cosine Theta magnet design

CERN: Conseil Européen pour la Recherche Nucléaire (European Council for Nuclear Research)

CFETR: Chinese Fusion Engineering Testing Reactor

CICC: Cable-In-Conduit Conductor

CLIQ: Coupling Loss Induced Quench

CMAC: CERN Machine Advisory Committee

CMM: Coordinate Measuring Machine

CMS: Compact Muon Solenoid, one of two general-purpose detectors at LHC

COVID-19: COronaVIrus Disease 2019

CRAFT: Comprehensive Research Facility for Fusion Technology project at ASIPP

CS: Central Solenoid (*e.g.*, of ITER or of CFETR)

CS: Connection Side of a magnet coil

CSMC: Central Solenoid Model Coil (*e.g.*, of ITER or of CFETR)

CTE: Coefficient of Thermal Expansion

DESY: Deutsches Elektronen-Synchrotron (German Electron Synchrotron)

DOE: US Department Of Energy

EDA: Engineering Design Activities (of ITER)

ELQA: ELectrical Quality Assurance

EM: ElectroMagnetic

EOB: End Of plasma Burn

EU: European Union

EuCARD: European Coordination for Accelerator Research and Development, funded as part of EU Framework Program 7

FCC: Future Circular Collider Design Study at CERN

FCC-hh: FCC option with hadron-hadron collisions

FE: Finite Element model or analysis

FESEM: Field Emission Scanning Electron Microscope

FIB: Focused Ion Beam technique

FNAL: Fermi National Accelerator Laboratory

FRESCA: Facility for REception of Superconducting CAbles at CERN

FSU: Florida State University

GHe: Gaseous Helium

GN$_2$: Nitrogen Gas

HERA: Hadron-Elektron RingAnlage (Hadron-Electron Ring Accelerator) at DESY

IFS: Instrumentation Feedthrough

INFN: Istituto Nazionale di Fisica Nucleare (National Institute for Nuclear Physics)

IR: Interaction Region(s) of the LHC

ITER: International Thermo-nuclear Experimental Reactor

JAEA: Japan Atomic Energy Agency

HL-LHC: High Luminosity LHC project at CERN

HTS: High Temperature Superconductor

IL: Inner Layer of a two-layer coil

LARP: LHC Accelerator Research Program, funded by US DOE

LBNL: Lawrence Berkeley National Laboratory

LHC: Large Hadron Collider at CERN

LHCb: Large Hadron Collider Beauty, a detector dedicated to beauty quark physics

LHe: Liquid Helium

LINAC: LiNear ACcelerator

LS1, 2 or 3: Long Shutdown of CERN accelerator complex

LSCM: Laser Scanning Confocal Microscope

MIP: Manufacturing and Inspection Plan

NCS: Non-Connection Side of a magnet coil

NED: Next European Dipole Joint Research Activity, funded as part of CARE

NHMFL: National High Magnetic Field Laboratory

NOC: Normal Operating Conditions

OL: Outer Layer of a two-layer coil

PCB: Printed Circuit Board

PIT: Powder-In-Tube process for Nb_3Sn wire production

PF: Poloidal Field coil (*e.g.*, of ITER)

QA: Quality Assurance

QC: Quality Control

QH: Quench Heater

QST: National Institute for Quantum Science and Technology

RADES: Relic Axion Detector Exploratory Setup

RAL: Rutherford Appleton Laboratory

RHIC: Relativistic Heavy Ion Collider at BNL

RHT: Reaction Heat Treatment

ROXIE: Routine for the Optimization of magnet X-sections, Inverse field calculation and coil End design

RRP®: Rod Retack Process for Nb_3Sn wire production

RRR: Residual Resistivity Ratio (*e.g.*, of copper)

SEM: Scanning Electron Microscope

SOD: Start Of plasma Discharge

SS: Stainless Steel

SSC: Superconducting Super Collider project at SSCL

SSCL: Superconducting Super Collider Laboratory

SLAC: Standford Linear Accelerator Center

SULTAN: SUpraLeiter Test ANlage (superconducting test facility)

TF: Toroidal Field coil (*e.g.*, of ITER)

US: United States

VARTM: Vacuum Assisted Resin Transfer Mold

VOI: Volume Of Interest

VPI: Vacuum Pressure Impregnation

WUCD: Warm-Up CoolDown cycle

XCT: X-ray Computed Tomography

Notation

A, B: parameters related to first Townsend coefficient, α ($\mathrm{Pa^{-1}m^{-1}}$ and $\mathrm{VPa^{-1}m^{-1}}$)

A_0, B_0: A and B values at T_0 ($\mathrm{Pa^{-1}m^{-1}}$ and $\mathrm{VPa^{-1}m^{-1}}$)

e: Euler number (~2.71828)

E: Young's modulus (Pa)

E_a, E_l, E_r, E_t: Young's modulus in the axial, longitudinal, radial and transverse directions (Pa)

F_x, F_y, F_z: x-, y-, z-component of the Lorentz force (N)

$F_{\theta,\mathrm{inner}}$, $F_{\theta,\mathrm{outer}}$: azimuthal components of the Lorentz force for the coil inner and outer layers (N)

d: distance (m)

f: function

G: Shear modulus (Pa)

$G_{a\theta}$, G_{ra}, G_{tl}, $G_{\theta r}$: components of the shear modulus tensor (Pa)

I_C: critical current ($\mathrm{A/mm^2}$)

J_C: critical current density ($\mathrm{A/mm^2}$)

ln: natural logarithm function

P: gas pressure (Pa)

P_{sim}: computed temperature at time when V_{sim} occurs (Pa)

$(Pd)_{\mathrm{min}}$: pressure times distance corresponding to $V_{\mathrm{B,min}}$ (Pam)

$(Pd)_{\mathrm{min,0}}$: $(Pd)_{\mathrm{min}}$ value corresponding to $V_{\mathrm{B,min,0}}$ at T_0 (Pam)

T: temperature (K)

T_0: a given value of T (K)

T_{sim}: computed temperature at time when V_{sim} occurs (K)

T_{CS}: current sharing temperature (K)

V_B: breakdown voltage (V)

$V_{\mathrm{B,min}}$: minimum breakdown voltage (V)

$V_{\mathrm{B,min,0}}$: minimum breakdown voltage value at T_0 (V)

V_{sim}: peak voltage derived from numerical simulation for worst-case failure scenario (V)

$V_{\mathrm{sim,MQXFB}}$: peak voltage derived from numerical simulation for worst-case failure scenario of full-length MQXFB quadrupole magnet (V)

$V_{\mathrm{sim,QH\text{-}to\text{-}coil}}$: peak voltage for worst-case failure scenario of quench heater to magnet coil (V)

$V_{\mathrm{sim,11\ T}}$: peak voltage derived from numerical simulation for worst-case failure scenario of full-length 11 T dipole magnet (V)

$V_{\mathrm{test,i}}$: voltage withstand requirement for test condition (i), where i = 1, 2, 3, 4, ou 5 (V)

V_0: voltage offset (V)

α: first Townsend coefficient characterizing the ionization rate of a gas ($\mathrm{m^{-1}}$)

α_a, α_θ, α_r: integrated thermal contraction coefficient between room and cryogenic temperatures, in the axial, azimuthal and radial directions (m/m)

γ: second Townsend coefficient characterizing the secondary electron emission rate of a surface (dimensionless)

γ_0: second Townsend coefficient value at T_0 (dimensionless)

ν: Poisson's ratio (dimensionless)

$\nu_{a\theta}$, ν_{ra}, ν_{tl}, ν_{tt}, $\nu_{\theta r}$: components of Poisson's ratio tensor (dimensionless)

σ: stress (Pa)

$\sigma_{r,nose}$: radial stress in collar nose (Pa)

$\sigma_{\theta,pole}$: azimuthal stress at coil pole (Pa)

1 Introduction

1.1 Low-Temperature Superconductors for High-Field Magnet Applications

1.1.1 From Nb–Ti to Nb_3Sn

The quest for ever higher magnetic fields in the operation of large physics instruments, such as experimental tokamak reactors for nuclear fusion or particle accelerators for high-energy physics, has driven the development of applied superconductivity. For applications in the 2–10 T range, the preferred, low-temperature, superconducting material is Nb–Ti, a ductile alloy that is easy to co-process with copper [1]. However, to generate fields beyond 10 T, the only other low-temperature superconducting material readily available at an industrial scale is the intermetallic compound Nb_3Sn.

The superconductivity of Nb_3Sn was discovered in 1954 [2], but it was not until the mid/late-1990s that it was considered for large-scale applications, thanks to two parallel efforts:

- the Engineering Design Activities (EDA) carried out in the framework of the International Thermonuclear Experimental Reactor (ITER) program [3][4]*;*
- a vigorous program initiated in fiscal year 2001 by the US Department Of Energy (DOE) to promote the development of high-performance Nb_3Sn wires for High Energy Physics (HEP) applications [5][6].

A European Joint Research Activity, referred to as the Next European Dipole (NED), seconded the DOE efforts and also included an ambitious Nb_3Sn conductor development program [7][8]. NED was initiated in 2004 as part of the EU-funded Coordinated Accelerator Research in Europe (CARE) Integrated Activity [9]. It followed, among others, a successful collaboration between CERN and Twente University, in the Netherlands, which, in the mid-1990s, built and tested a 1-m-long, 50-mm-aperture Nb_3Sn dipole magnet model, referred to as MSUT, which achieved ~11.25 T at 4.5 K [10][11][12][13]. The magnet model was retested in 2021 and repeated its good performance after nearly 24 years (see Section 1.6.2 and [14]).

1.1.2 First Large-Scale Production of Nb_3Sn Wires for ITER

The ITER EDA led to the set-up of the ITER Organization in Saint-Paul-lez-Durance, France, in October 2007. ITER Organization launched the largest ever in-kind procurement arrangements for the supply of ~700 tons of Nb_3Sn wires, with non-copper critical current densities in the 700–1200 A/mm^2 range at 4.2 K and 12 T [15]. The procurement involved 9 producers in 6 countries, 3 of the producers being new and having been set up by their government to contribute their share of ITER conductors.

Among the available process routes for Nb_3Sn strands [1], five suppliers selected the so-called *bronze route*, while the other four selected the so-called *internal tin route* [15]. Figure 1 shows cross-sectional views of the 8 different wire types for the Toroidal Field coil conductors. The bronze-route wires had non-copper critical current densities, J_C, in the 700–1000 A/mm^2 range at 4.2 K and 12 T, while the internal-tin route wires had non-copper critical current densities in the 900–1200 A/mm^2 range at 4.2 K and 12 T [16]. For the ITER Central Solenoid, Japanese suppliers developed high-tin content bronze route wires that could achieve non-copper critical current densities around 1100 A/mm^2 at 4.2 K and 12 T [17].

The ITER production called for a ramp-up by one order of magnitude of the world production of Nb_3Sn wires. It offered unprecedented challenges in terms of follow-up and quality control [15][16]. However, it enabled several suppliers to master mass production of Nb_3Sn wires and to develop their infrastructure for other needs.

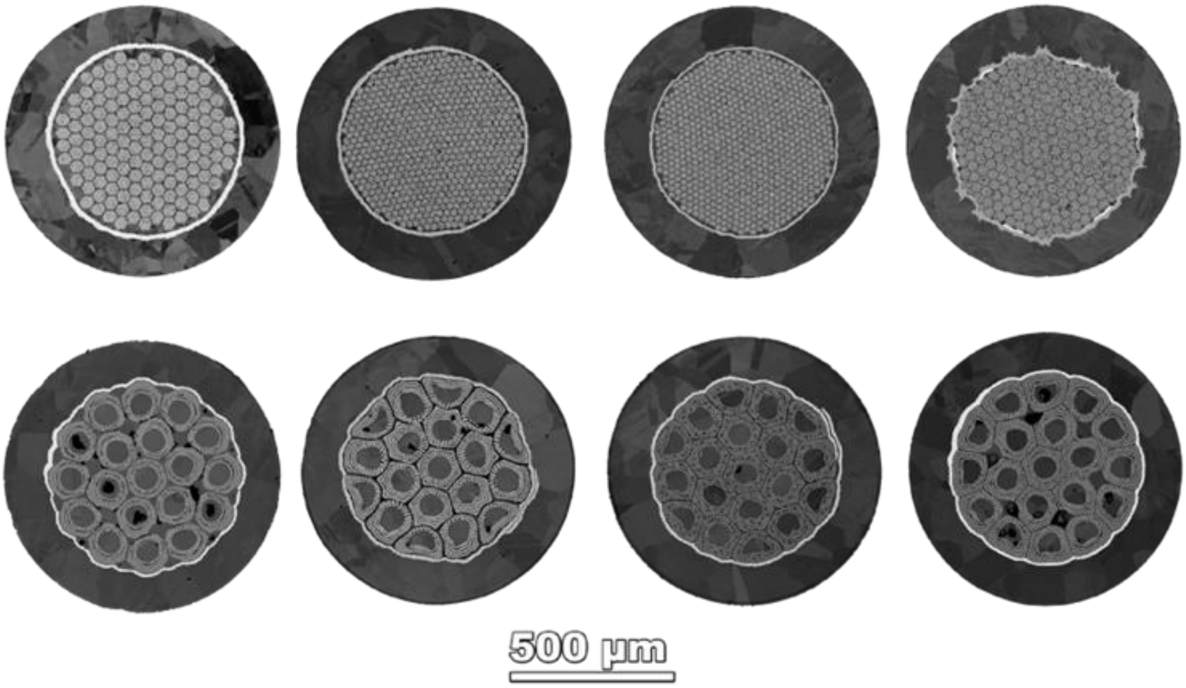

Figure 1: Cross-sectional views of eight types of 0.82-mm Nb_3Sn wires produced worldwide for ITER Toroidal Field cable-in-conduit-conductors (after heat treatment). Top: bronze route wires. Bottom: internal-tin route wires (Courtesy of P. Lee, Applied Superconductivity Center, National High Magnetic Field Laboratory).

1.1.3 Development of High-Performance Nb_3Sn Wires for HL-LHC

The US-DOE program was equally fruitful and enabled the development of Nb_3Sn wires approaching non-copper critical current densities of 3000 A/mm^2 at 4.2 K and 12 T [18][19]. Such spectacular progress was achieved on a variation of the internal tin route, patented under the name of Rod Restack Process (RRP$^®$). This progress paved the way for the consideration of Nb_3Sn dipole/quadrupole magnets for the High Luminosity (HL) upgrade of the Large Hadron Collider (LHC) at CERN, which was officially launched circa 2010 [20][21].

For HL-LHC, the J_C requirement was set to the more conservative value of ~2450 A/mm^2 at 4.2 K and 12 T (corresponding to ~1000 A/mm^2 at 4.2 and 16 T) [22]. Figure 2 presents a cross-sectional view of a 0.85-mm wire for HL-LHC MQXF quadrupole magnets, which relies on the so-called *RRP$^®$ 108/127 layout*. This design is based on an array of 127 hexagonal rod restacks, among which 108 are composite sub-elements and 19 are pure copper. The sub-elements are made up of a copper matrix, with a tin core at its centre, surrounded by niobium filaments homogeneously distributed around the tin core. A thin barrier of niobium is placed at the periphery of the filament array of each sub-element to prevent tin diffusion into the surrounding copper. At the end of heat treatment, the reacted filaments of each sub-element are aggregated, forming a tubular Nb_3Sn phase (see right side of Figure 2). The outer diameter of the tube corresponds more or less to the so-called *effective filament diameter* [1]. For MQXF RRP$^®$ 108/127 wires, the geometrical sub-element size is ~54 μm, while the effective filament diameter derived from magnetization measurements is ~60 μm.

Industrial production of about 30 tons of MQXF RRP$^®$ 108/127 wires is still ongoing at a single supplier, Bruker OST, LLC, located in Carteret, NJ, USA [23][24]. Although more modest in quantity than ITER, the HL-LHC production represents a significant achievement in terms of industrial production of high-performance Nb_3Sn wires. As a comparison, internal tin wires produced by the same supplier for ITER counted only 19 sub-elements.

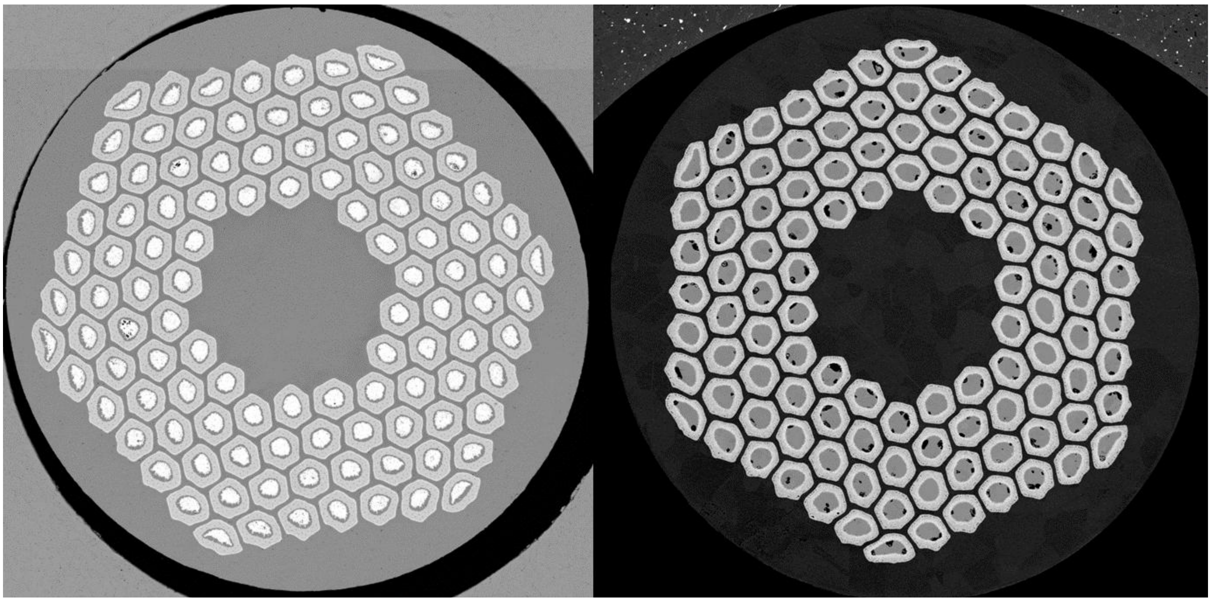

Figure 2: Back-scattered electron micrographs of 0.85-mm Nb_3Sn wire produced for HL-LHC MQXF quadrupole magnets, based on RRP® 108/127 layout. Left: before heat treatment. Right: after heat treatment (Courtesy of M. Malabaila and S.C. Hopkins, CERN).

At the beginning of HL-LHC, CERN considered another type of Nb_3Sn wire, produced by the so-called *Powder-In-Tube (PIT) route* [1]. In order to improve the balance of critical current (I_C) and Residual Resistivity Ratio (RRR), the strand layout was modified to introduce an external common diffusion barrier, the so-called *bundle barrier* [25]. This was successful in increasing RRR, but the degradation of I_C on cabling was found to be variable and often higher than the 5% specified. The PIT wire was eventually set aside in 2019, and the production focused on RRP®. However, a number of model and prototype coils for both 11 T and MQXF magnets were manufactured with PIT wire cables and will be alluded to in the report.

1.1.4 Exploring the Limits of Nb_3Sn Wires

R&D programs beyond HL-LHC are already underway at CERN within the framework of the Future Circular Collider (FCC) Design Study [26]. For the hadron collider version of FCC, referred to as FCC-hh, an ambitious J_C target of 1500 A/mm^2 at 4.2 K and 16 T has been set [27].

The target critical current density has been achieved at a small laboratory scale [28] and a worldwide effort has been initiated to boost the production of high-performance Nb_3Sn wires at an industrial scale [29].

1.2 Challenges of Nb_3Sn Technology

Nb_3Sn offers very good transport-current properties under a high magnetic field. Still, it has one major drawback: once reacted, it becomes brittle and its superconducting properties are strain sensitive (see Refs. [30][31] for historical references, [32] for a practical scaling law and [33] for a detailed assessment of RRP® wires). The strain sensitivity and brittleness of Nb_3Sn have been a severe restrain in its development as it requires delicate and well-controlled manufacturing procedures from wire production to cabling, conductor integration, winding, magnet and cold mass assembly. Operational limits may also be required to reduce risks of performance degradation over the full life cycle of the instrument.

Table 1: Salient parameters of Nb_3Sn strands for ITER and CERN magnets.

Parameter	**ITER (TF)**	**ITER (CS)**	**CERN HL-LHC (11 T)**	**CERN HL-LHC (MQXF)**	**CERN FCC-hh**
Outer diameter (mm)	0.820 ± 0.005	0.830 ± 0.005	0.700 ± 0.002	0.850 ± 0.003	~1
Plating type	Cr	Cr	n/a	n/a	n/a
Plating thickness (µm)	2 (+0/-1)	2 (+0/-1)	n/a	n/a	n/a
Twist pitch (mm)	15 ± 2	15 ± 2	14 ± 2	19 ± 3	
Cu/non-Cu ratio	1 ± 0.1	1 ± 0.1	1.15 ± 0.1	1.2 ± 0.1	~1
Residual Resistivity Ratio[a]	≥ 100[b]	≥ 100[b]	≥ 150[c]	≥ 150[c]	≥ 150
Critical current @12 T, 4.22 K (A)	≥ 190[d]	≥ 220[d]	≥ 438	≥ 632	
Critical current @15 T, 4.22 K (A)				≥ 331	
Critical current density @16 T, 4.22 K (A/mm^2)				≥ 1000	≥ 1500
Resistive transition index	≥ 20	≥ 20	≥ 30	≥ 30	
Reference field cycle, temperature	± 3 T, 4.22 K	± 3 T, 4.22 K	n/a	n/a	
Hysteresis loss for reference field cycle and temperature (mJ/cm^3)	< 500	< 500	n/a	n/a	
Sub-element diameter (µm)	n/a	n/a	≤ 50	≤ 60	
Effective filament diameter (µm)					≤ 20
Magnetization width @3 T, 1.9 K (mT)	n/a	n/a	≤ 330	≤ 330	
Magnetization width @1 T, 4.22 K (mT)					≤ 150
Piece length (m)	≥ 1000	≥ 1000	≥ 720	≥ 840[e]	≥ 5000
Produced quantity (metric tons)	~510	~175	~5	~30[f]	< 1

[a] After heat treatment.
[b] On plated strands.
[c] HL-LHC also requires a minimum of 100 after 15% rolling.
[d] To be revised for each conductor supplier after Conductor Performance Qualification Sample test [15].
[e] For MQXFB at CERN (> 500 m for MQXFA in the USA).
[f] For both CERN and AUP.

To overcome the issues of working with a brittle material, the so-called *wind-and-react* process was introduced very early on and is now the preferred option for fusion and HEP magnets. In this approach, the wire is processed to final diameter using only ductile precursor materials as shown in the left of Figure 2 [1]. If required, the wire is cabled, and the conductor is wound into a coil of the desired shape. Once the conductor has undergone the most potentially deleterious mechanical deformations, the whole coil is heat treated at temperatures of up to 650–700 °C for several days to enable formation of the brittle superconducting Nb_3Sn phase with the desired microstructure (*e.g.*, grains in the 100–200 nm range [1]). Subsequently, additional conductor deformations or displacements must be tightly controlled, and the reacted coil must be handled with care.

Upon coil winding and heat treatment completion, a resin impregnation step is usually carried out to rigidify the coil body, facilitate subsequent handling, and to complement/ reinforce electrical insulation [34]. The resin also acts as a filler to improve magnet stability and reduce risks of mechanical deformation and/or motion of reacted conductors under the effect of Lorentz forces [35]. The technical requirements on conductor insulation are particularly stringent for accelerator magnet coils, where the conductors are wrapped or braided with glass fibers or glass fiber tapes prior to winding and the glass fiber insulation must be able to sustain the reaction heat treatment [36].

1.3 ITER and HL-LHC Crises

Since the pioneering work of W.B. Sampson at BNL, who built the first 76-mm-aperture, 85-T/m quadrupole magnet model, wound from Nb_3Sn ribbons and cold-tested in January 1966 [37], Nb_3Sn technology has reached a level of development making it suitable for several components of the ITER magnet system [38] and for HL-LHC magnets [20][21].

However, with almost a 10-year interval, both ITER and HL-LHC projects underwent challenging episodes that could have put the viability of Nb_3Sn technology into question (see Sections 1.4.2, 1.5.5 and 1.5.6). In both cases, engineering solutions were found, which addressed the performance issues and enabled the projects to move forward.

1.4 Nb_3Sn Cable-In-Conduit Conductors for Fusion Magnets

1.4.1 ITER Magnet System Overview

The main goal of the ITER project is to demonstrate the scientific and technological feasibility of fusion power [39]. It relies on the tokamak concept and calls for a sophisticated magnet system for plasma confinement, shaping and stability. The tokamak cryostat is 28 m tall and 29 m in diameter. The ITER magnet system is fully superconducting. and has a stored magnetic energy of 51 GJ, making it the largest superconducting magnet system ever designed. It includes four types of coils [38]:

- 18 toroidal field (TF) coils, located around the plasma chamber, manufactured in EU [40] and Japan [41];.
- a central solenoid (CS), made up of a stack of six modules and positioned at the machine center, manufactured in the USA [42][43];
- 6 poloidal field (PF) coils, surrounding the TF coils, manufactured in Russia (for PF1) [44], EU (for PF2 to 5) [40] and China (for PF6, under contract with EU) [40][45];
- 9 pairs of correction coils (CC), attached to the PF coils and manufactured in China [46].

As illustrated in Figure 3, the ITER magnet coils are wound from cable-in-conduit conductors (CICC), a concept originally developed at Francis Bitter National Magnet Laboratory, in Cambridge, MA, in the mid-1970s [47]. The ITER CICC consists of a multi-stage, rope-type cable, inserted into a stainless-steel conduit fabricated from butt-welded jacket sections [15]. Upon completion of cable insertion, the conductor is compacted to its final shape and dimensions. The conduit delimits the volume where a forced flow of supercritical helium is circulated.

The ITER PF and CC conductors rely on Nb–Ti strands, but the field requirements for TF and CS coils require the use of Nb_3Sn strands, with non-copper critical current densities in the 700–1000 A/mm^2 range at 4.2 K and 12 T. The TF magnet system will be operated in a steady state mode, while the CS will be operated in a pulsed mode and must be able to sustain up to 60,000 power cycles.

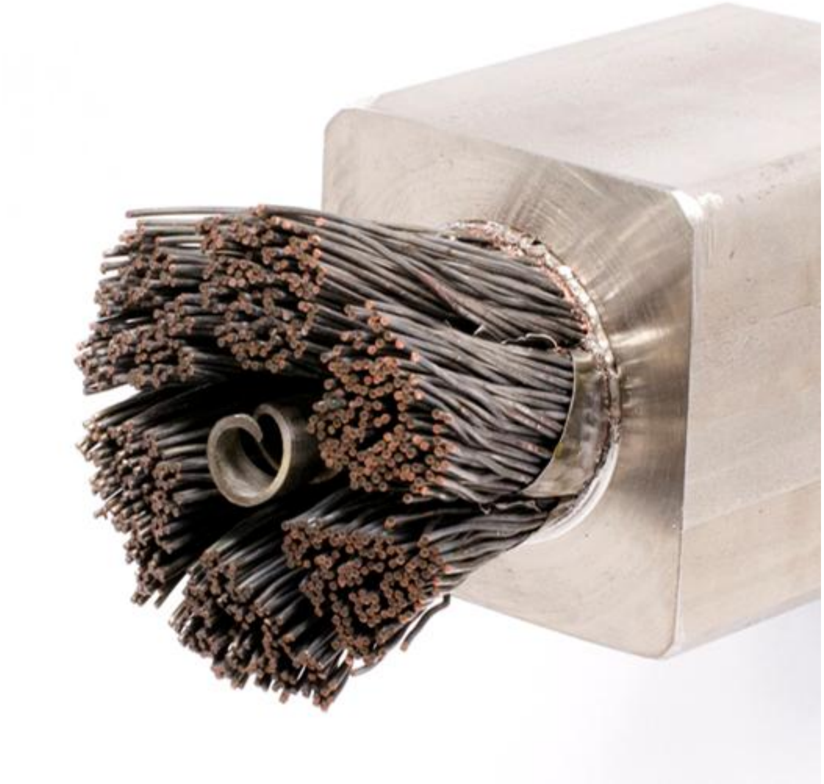

Figure 3: Photograph of a reacted ITER CS Cable-in-Conduit Conductor after partial removal of the austenitic steel, circle-in-square jacket and of the stainless-steel wraps around the 6 petals of the rope-type cable. The cable is manufactured in 5 stages and is made up of 576 Cr-plated Nb_3Sn strands, mixed with 276 pure Cu strands, arranged around a central, austenitic steel, cooling spiral (courtesy of C. Sanabria, formerly ASC, 2013).

1.4.2 Issue with ITER CS Conductors

Around 2010, the first two CICC performance qualification samples for the ITER CS that were tested at the SULTAN facility, located in Villigen, Switzerland, exhibited severe performance degradation as a function of electromagnetic (EM) and thermal cycles and did not meet technical requirements (see Figure 4) [49][50]. This undesirable behavior generated a large turmoil in the scientific community, raising alarms about the feasibility of ITER [51].

The issue of performance degradation of Nb_3Sn CICC as a function of cycling had been identified for some time, following the testing of the ITER TF and CS Model Coils manufactured as part of ITER EDA [48]. Starting in 2007, a significant effort was launched among ITER partners around the world to determine the root cause(s) of the performance degradation and to identify possible corrective actions to be implemented. As described thereafter, these efforts were articulated around four main axes. A detailed account of the work and findings along the four axes, with all relevant references, can be found in Ref. [15]. In the present report, we only present a brief summary, highlighting key elements of the methodology and take-away points that may be of use for other projects.

The four main axes were:

(1) modeling of electro-mechanical behavior of CICCs during all phases of manufacturing, cooldown and energization –the development of a numerical model describing the mechanical behavior of a CICC for the various loading steps was very useful to identify critical parameters and guiding design choices; the model was developed based on physical parameters and laws (no fudge factor), which were determined from or benchmarked by *ad hoc* experiments;

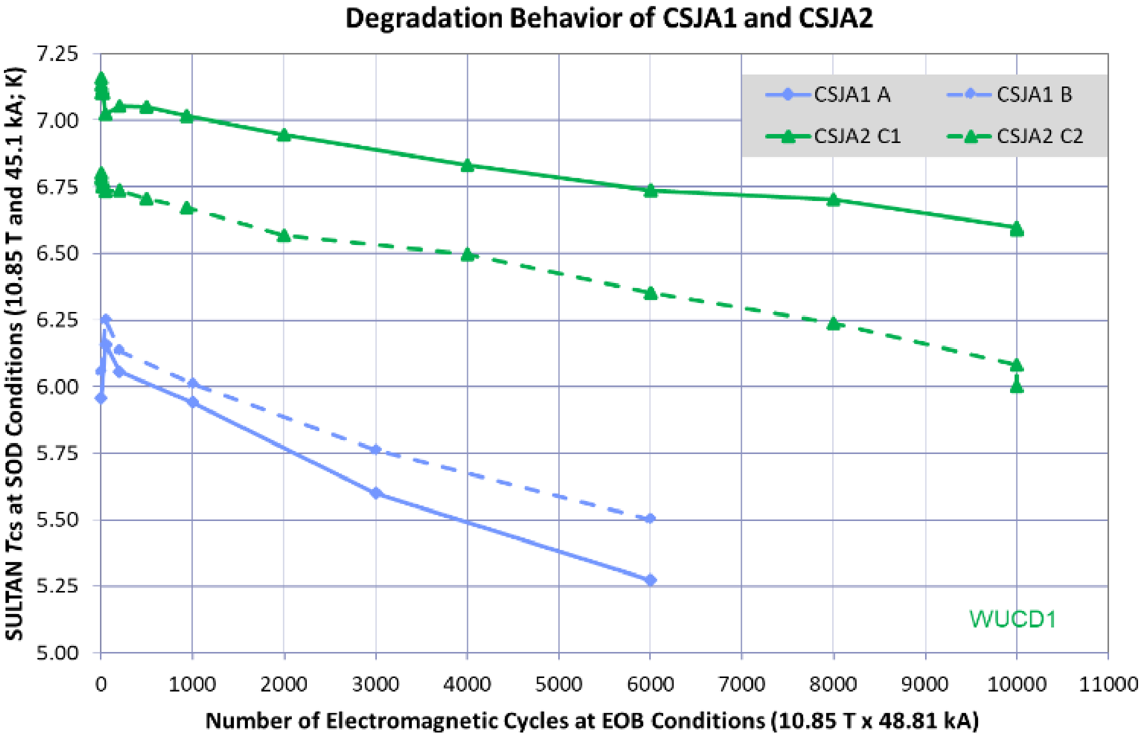

Figure 4: Results of first two ITER CS conductor performance qualification samples (CSJA1 & CSJA2) tested at the SULTAN facility and exhibiting severe performance degradation as a function of electromagnetic and thermal cycling. Each sample includes two legs spliced at the bottom. The current sharing temperature, T_{CS}, is measured at conditions corresponding to Start of Discharge (SOD): 10.85 T and 45.1 K, while the electromagnetic cycling is carried out to conditions corresponding to End Of plasma Burn (EOB): 10.85 T and 48.81 kA [49] [50].

(2) improving assembly, instrumentation and analyses of SULTAN samples –the significant effort to improve sample preparation (*e.g.*, fully-soldered conductor splicing to ensure more uniform current distribution among cable stands), instrumentation (*e.g.*, implementation of crown arrays of voltage taps to measure average electric field on conductor jacket rather than local values), and data processing (*e.g.*, offset removal based on physical arguments rather than fitting convenience) were instrumental in improving repeatability and reproducibility, and, *in fine*, reliability of the measurements; each of these tasks usually called for the development of dedicated numerical models as in (1);

(3) post-mortem examinations –being able to visualize the presence (or not) of cracks within the Nb_3Sn phase of the cable strands, and to study the cracks' morphology and distribution, has been of great help, in association with (1), to identify the root cause of the problems (see Section 3.1);

(4) design of experiments to assess potential solutions in a rigorous and systematic manner –having a proper plan, which utilizes the findings of (1) and (3) to select which parameters to change and which benefits from (2) to test the impact of the changes in a sequential and controlled manner was key to determine the proper recovery actions.

Let us stress that the teams working on the different axes had regular exchanges, which enabled cross-fertilization and out-of-the-box thinking.

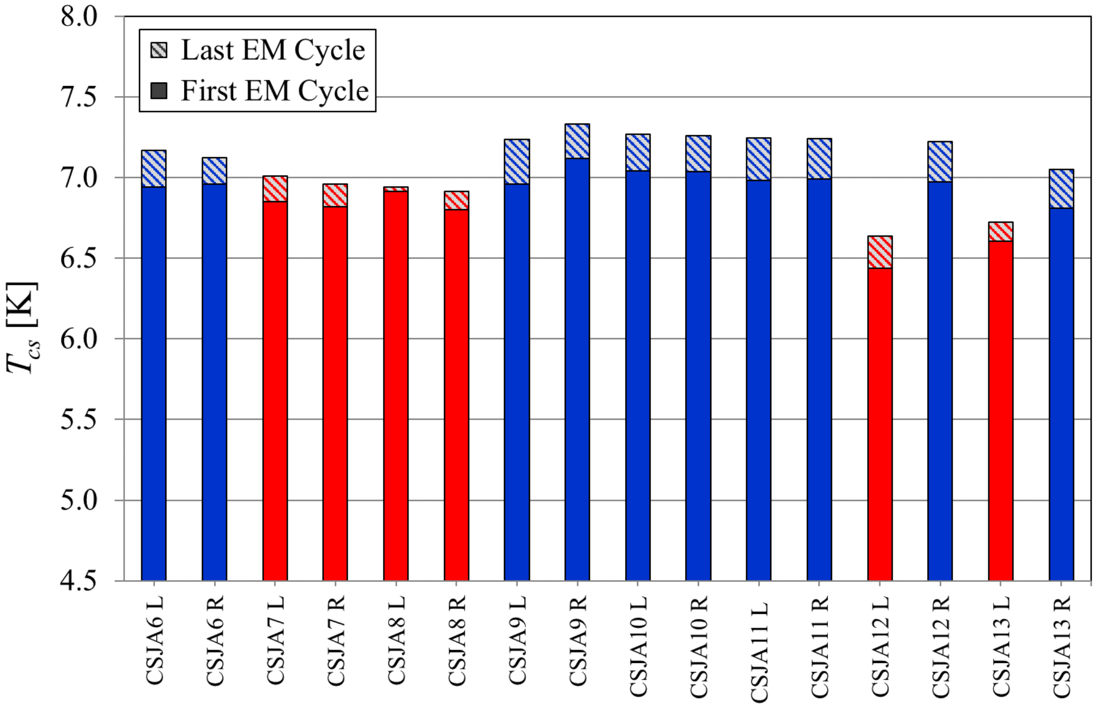

Figure 5: Results from ITER CS conductor production samples tested at the SULTAN facility, showing a systematic performance increase between the first and last electromagnetic cycles after the first cooldown. The different colors refer to different strand technologies (blue: bronze, red: internal tin); the number of electromagnetic cycles varies between samples in a range between 5000 and 10000 [53].

A solution was eventually found for the ITER CS conductors by optimizing the twist pitch sequence of the rope-type cable [51]. In particular, the twist pitch of the first cabling stage, made from two superconducting and one copper strand, was reduced from ~45 to ~20 mm. Such twist pitch tightening provides better local support to the Nb_3Sn strands and prevents undesirable bending [49][51]. It also prevents Nb_3Sn filament cracking (see Section 3.1).

After this change, all ITER CS SULTAN samples with short twist pitch conductors exhibited good performance upon EM and thermal cycling, for both bronze and internal-tin strand technologies. As an illustration, Figure 5 presents a summary plot of current-sharing temperature, T_{CS}, measured at working conditions of 10.85 T and 45.1 kA, on quality control SULTAN samples tested during series production of CS conductors [53]. They all meet the acceptance criterion of 5.8 K. They also exhibit a slight performance increase upon the first EM cycles, likely due to internal stress release. Furthermore, the good in-coil performance of short twist pitch conductors was confirmed by the manufacture, in Japan, under contract with the USA, of a CS insert coil that was tested in 2015 in the ITER CS Model Coil (CSMC) facility in Naka, Japan [54]. Since then, several ITER CS modules have been cold tested at the supplier's premises in the USA and perform according to expectations [43][55].

The implementation of the short twist pitch sequence was a real breakthrough and put an end to over a decade of arguments in the community on how to optimize ITER CICC parameters. Unfortunately, it was too late to retrofit the short-twist pitch design parameters to the conductors for ITER TF coils, which were already in an advanced stage of production worldwide at the time of CS conductor crisis resolution [56][57]. However, as mentioned before, electromagnetic cycling is much less severe for TF magnets, which are to be operated in a steady-state mode, and a strategy has been devised on how to limit the potential performance degradation of the various types of TF conductors over the expected ITER machine life cycle [58].

1.4.3 CICC with High-Performance Nb_3Sn Strands

Since 2014, the Institute of Plasma Physics, Chinese Academy of Sciences (ASIPP), located in Hefei, China, has been working on a plan for the Chinese Fusion Engineering Testing Reactor (CFETR) [59]. This plan includes the design, manufacture, and test of a Central Solenoid Model Coil (CSMC), based on ITER technologies [60]. The model coil is designed to operate with a nominal current of 47.65 kA and a conductor peak field of 12 T. It relies on a CICC design similar to that of the ITER CS, with ITER-grade strands (non-copper critical density of ~1000 A/mm^2) and a short twist pitch sequence. CSMC conductor samples have been produced and successfully tested at SULTAN, showing performances similar those of ITER CS conductor samples [61]. The model coil was successfully powered up to 48 kA in December 2024 further confirming the in-coil performance of the conductor [62].

More recently, ASIPP has initiated the Comprehensive Research Facility for Fusion Technology (CRAFT) project, which includes the manufacture and test of a full-size, Toroidal Field coil prototype for CFETR. CFETR TF coils are designed to operate with a current of 95.6 kA and a conductor peak field of 14.5 T [63]. Given the field requirements, ASIPP has launched an R&D program to investigate whether high-performance, Nb_3Sn strands, like those developed for HL-LHC (with non-copper critical current densities in the 2000–2500 A/mm^2 range at 4.2 K and 12 T), could be used in a cable-in-conduit conductor configuration with short twist pitches, like those for ITER CS and CFETR CSMC.

Before going to the final CFETR TF conductor size, ASIPP included an intermediate qualification step and produced conductor samples with the same layout and parameters as for the CSMC, but relying on high-performance Nb_3Sn strands, thereby enabling a direct comparison between CICCs with ITER-like strands and non-copper critical current densities of ~1000 A/mm^2 at 4.2 K and 12 T with HL-LHC-like strands and non-copper critical current densities exceeding 2200 A/mm^2 at 4.2 K and 12 T [64]. The SULTAN test results show that the CICC with high-performance strands exhibits stable performances as a function of electromagnetic and thermal cycling under nominal loading conditions, but with a significantly higher current sharing temperature than the CSMC samples (the T_{CS} gain is larger than 0.5 K) [64]. Degradation is only observed for EM overloads in excess of 30%. The good results under nominal loading conditions confirm the robustness of the short twist pitch cable design also for high-performance Nb_3Sn strands.

In addition, CRAFT includes a task to design, manufacture, and commission a conductor test facility, called Super-X. Super-X is based on pairs of split solenoid coils and is expected to produce 15 T in a test well of 100 x 160 x 550 mm; the so-called *high field coils* have an operating current of 8 kA and a conductor peak field of 15.75 T [65]. All coils rely on rectangular CICCs with much smaller cross-sections than for ITER CS and CFETR CSMC. Samples of Super-X conductors have been produced and tested in SULTAN, including cables made from high-performance Nb_3Sn strands. They also exhibit good and stable performances versus electromagnetic and thermal cycling [66].

The above results are a good example of a virtuous circle between fusion and HEP conductor and magnet development: ITER enabled the scale-up and industrial production of Nb_3Sn strands, which benefited the HL-LHC program, and, in turn, the development of high-performance Nb_3Sn strands for HL-LHC is now benefiting fusion applications.

1.5 Nb_3Sn Magnets for the HL-LHC

1.5.1 LHC Overview

The 27-km Large Hadron Collider (LHC), installed in an underground tunnel at a depth of 50 to 175 m at the French–Swiss border near Geneva, Switzerland, is the crown jewel of the CERN accelerator complex [67]. In LHC, protons (or lead ions) circulate in two beams traveling in opposite directions in two separated beam pipes. The two beams are designed to collide at four interaction points, surrounded by large physics experiments.

Figure 6: Cross-sectional view of an un-reacted MQXFB Rutherford-type, cable made up of 40 Nb_3Sn RRP® strands and a 25-μm-thick, 12-mm-wide stainless-steel core between the strand layers. The cable has a slight keystone angle of 0.42° (the thin edge is on the right side of the picture). The grey zones between strands correspond to the resin used for potting the cable sample for metallographic purposes (Courtesy of A. Bonasia, CERN).

ATLAS and CMS are two general physics detectors, which enabled the discovery of the Higgs boson in 2012 [68], while ALICE and LHCb look after more specific physics phenomena (quark-gluon plasma and matter/antimatter symmetries). ATLAS includes a large superconducting magnet system with a barrel toroid, two end-cap toroids and a central solenoid [69][70], while CMS includes a large superconducting solenoid [70]. ATLAS and CMS magnets rely on Nb–Ti technology, while ALICE and LHCb rely on normal conducting magnets.

The LHC machine is made up of eight arcs and eight insertion regions. The arcs contain a regular magnet lattice of 23 cells, which are 106.9 m long and include 6 x 15-m-long, 56-mm-two-in-one-aperture dipole magnets, 2 x 3.5-m-long, 56-mm-two-in-one aperture quadrupole magnets and several high-order multipole magnets. The insertion regions consist of a long straight section plus transition regions at both ends, which are referred to as *dispersion suppressors*. The straight section layout depends on its specific use: as mentioned above, four of them, referred to as interaction regions, are for physics experiments, while the remaining four are: one for acceleration with radio frequency (RF) cavities, two for beam cleaning (so-called *betatron* and *momentum* cleaning) and one for beam dumping. Insertion regions also include dipole, quadrupole and high-order multipole magnets.

Most LHC arc and insertion magnets rely on Nb−Ti technology and are cooled down by superfluid Helium at 1.9 K [72][73]. The coils are usually wound from Rutherford-type cables, made up of a few tens of strands, twisted together, and shaped into a flat, two-layer cable as shown in Figure 6. This type of cables was developed in the early 1970s at Rutherford Appleton Laboratory (RAL), in Chilton, England (hence the name) [74]. They are given a slight keystone shape to facilitate stacking into an arch and forming a so-called $cos\theta$ or $cos2\theta$ coil geometry in the 2-dimensional cross-section [1][75][76]. The keystone angle must be kept small to limit cabling degradation and therefore is usually not enough for arch stacking [77], thereby calling for the use of angular wedges to achieve the desired coil shape and field quality.

The LHC now operates reliably at a record energy of 6.8 TeV per beam, corresponding to a bore/peak field of 8.06/8.45 T in the arc dipole magnets. However, it does require a large number of training quenches after each warm-up/cooldown cycle to restore the desired operation level [78][79]. As is also foreseen for the ITER magnets, the number of warm-up/cooldown cycles applied to LHC superconducting magnets, both in the arcs and insertion regions, are strictly controlled and limited.

1.5.2 The Next Step: HL-LHC

The next step for CERN is the High-Luminosity upgrade of the LHC (HL-LHC), aimed at generating 5 times more collisions at the interaction points of ATLAS and CMS, with respect to the presently achieved (levelled) instantaneous luminosity [20][21]. This will result in a 10-fold increase of the integrated luminosity over the HL-LHC era (nominal of 3000 fb^{-1}) compared to the design value of 300 fb^{-1} for LHC. The luminosity increase will provide a statistical boost to the data analysis, thereby giving access to higher precision and rare phenomena, and offering greater discovery potentials. In the present schedule, HL-LHC is expected to start operation in 2030 and to run until the end of 2041.

HL-LHC initially envisioned relying on two types of Nb_3Sn magnets [20][21]:

- two pairs of 5.3-m-long, 60-mm-two-in-one-aperture, 11 T dipole magnets for replacing one 15-m-long, 56-mm-two-in-one-aperture, 8 T LHC dipole magnet in each of the two dispersion suppressor areas of the machine, providing the same integrated bending field strength but making room (~3 m) for installation of additional collimators that were thought to be needed for HL-LHC operation;
- four sets of large, 150-mm-single-aperture quadrupole magnets (referred to as MQXF) for replacing the present 70-mm-single-aperture quadrupole magnets in the interaction regions of ATLAS and CMS, providing a similar integrated focusing field gradient, but enabling better optimization of the optics layout with more squeezed beams at the collision points while opening space for radiation shielding.

The shorter lengths and larger apertures are the parameters driving the need for a switch from Nb–Ti to Nb_3Sn technology to permit operation at higher conductor peak fields. The idea of relying on large-aperture, Nb_3Sn quadrupole magnets for the interaction regions of LHC was first developed in the mid-1990s at INFN/Milan, Italy [80].

As for ITER, a fraction of HL-LHC components is provided in-kind by external collaborations, although at a far more modest level: the in-kind ratio is ~10% for HL-LHC and 90% for ITER. In the case of the 11 T dipole magnets, the 4 (plus 2 spares) units were supposed to be produced at CERN. For the interaction region magnets, several of them are provided by external collaborations [81]. In particular, the production of MQXF quadrupole magnets is shared between CERN and a consortium of US laboratories, now regrouped within the so-called *HL-LHC Accelerator Upgrade Project (AUP)*, which involves Fermi National Accelerator Laboratory (FNAL) in Batavia, IL, Lawrence Berkeley National Laboratory (LBNL), in Berkeley, CA, Brookhaven National Laboratory (BNL), in Upton, NY, and Stanford Linear Accelerator Center (SLAC), in Stanford, CA. In this sharing, the USA are responsible for the production of 16 (plus 4 spares) 4.2-m-long MQXFA quadrupole magnets, while CERN is responsible for the production of 8 (plus 2 spares) 7.2-m-long MQXFB quadrupole magnet. Save for their lengths, MQXFA and MQXFB magnets rely on similar designs and manufacturing processes (but with some differences due to available infrastructure and large tooling).

1.5.3 Nominal and Ultimate Requirements for HL-HC Magnets

Early on, the HL-LHC project defined two levels of performance requirements for its magnets:

(1) a nominal level, corresponding to a 7.0 TeV operation of the LHC;

(2) an ultimate level, corresponding to a 7.5 TeV operation of the LHC.

As the LHC is presently operating at 6.8 TeV and there is no plan to push its limit beyond 7.0 TeV, it was decided, in the course of the HL-LHC Nb_3Sn magnet development program, to drop the ultimate requirement on full-length Nb_3Sn magnets (however, it is maintained for all HL-LHC Nb–Ti magnets).

1.5.4 Choice of HL-LHC Quadrupole Magnet Lengths

The choice of US colleagues to go for more and shorter MQXFA magnets was based on the experience accumulated during a decade of R&D on N_3Sn magnet technology, carried out mainly within the framework of the LHC Accelerator Research Program (LARP), set up by US DOE in 2004 [82][83][84]. LARP followed suit to previous Nb_3Sn accelerator magnet R&D programs in the USA, including that of the short, 5-cm-single-aperture D20 dipole magnet model at LBNL, which, in 1997, achieved a field in excess of 13 T at 1.9 K [85][86][87]. The LARP R&D efforts enabled the validation of key design parameters and manufacturing processes on several 3.7-m-long, 90-mm-aperture quadrupole magnet prototypes [88][89]. A length of 4.2 m and an aperture of 150 mm were perceived as conservative extrapolations for MQXFA.

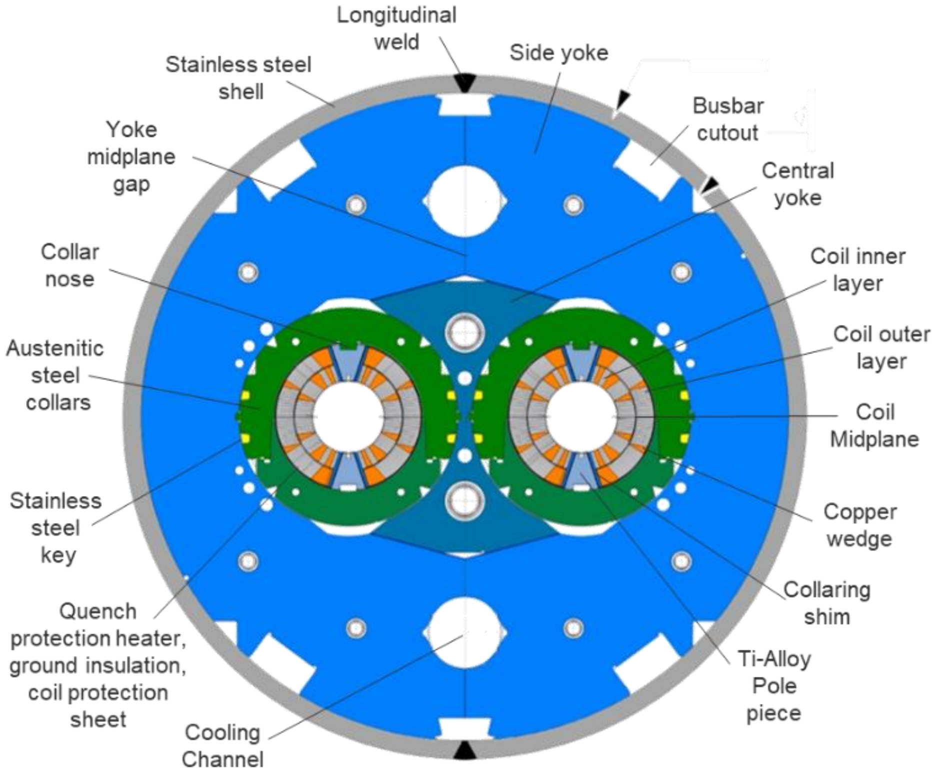

Figure 7: Cross-sectional view of 60-mm, two-in-one-aperture, HL-LHC 11 T dipole magnet, showing the double-layer, $\cos\theta$ coils (grey) with angular Cu wedges (orange) and a removable pole (light blue), surrounded by austenitic steel collars (green), a low-carbon steel iron yoke (darker shades of blue) and a welded outer stainless steel shell (grey).

The ambitious choice of CERN to go for fewer and longer MQXFB magnets was made to reduce the number of magnet interconnects and to push N_3Sn technology further, as may be required for future collider projects; let us recall that the LHC dipole magnet length is ~15 m [90]. However, as detailed thereafter, the length scaling beyond 4.2 m did not prove to be so straightforward.

1.5.5 Issues with 5.3-m-Long 11 T Dipole Magnets

1.5.5.1 Design and Assembly Overview

The use of 11 T dipole magnets for opening a 3-m gap in the two dispersion suppressors areas of LHC point 7 for additional collimation was first proposed in July 2010, along with main technical requirements [91]. The magnet design was initially developed by a collaboration between CERN and FNAL [92][95]. FNAL built a few short magnet models [92][93][94], before the task was taken over by CERN [95][96][97]. The nominal current is 11.85 kA and corresponds to a central/peak field of 11.23 T/11.77 T; the ultimate current is 12.84 kA and corresponds to a central/peak field of 12.14 T/12.74 T. As for all LHC arc magnets, the operating temperature is 1.9 K. Table 2 summarizes salient magnet design parameters.

Figure 7 shows a cross-sectional view of the 60-mm-two-in-one-aperture 11 T dipole magnet, featuring for each aperture and from inside out: an assembly of two double-layer, $\cos\theta$ coils, surrounded by laminated, austenitic steel collars, a vertically split, low-carbon steel iron yoke and a welded outer stainless-steel shell. The coils are wound from slightly keystoned, Rutherford-type cables (similar to the MQXF cable shown in Figure 6), which have been optimized to limit cabling degradation [98].

Table 2: Salient design parameters of Nb_3Sn dipole and quadrupole magnets for HL-LHC at CERN.

Parameter	**Units**	**11 T**	**MQXF**
Cable			
Number of strands		40	40
Transposition pitch	mm	100 ± 3	109 ± 3
Bare width	mm	14.70 ± 0.05	18.15 ± 0.05
Bare mid-thickness	mm	1.250 ± 0.01	1.525 ± 0.01
Keystone angle	°	0.79 ± 0.1	0.4 ± 0.1
Stainless steel core width	mm	12 ± 1	12 ± 1
Stainless steel core thickness	µm	25 ± 1.5	25 ± 1.5
Unit length	M	655	760[a]/465[b]
Extracted strand I_c degradation @12 T and 4.22 K	%	≤ 5	≤ 5
Cold mass			
Type		Two-in-One	Single Aperture
Aperture @room temperature	mm	60	150
Distance between apertures @1.9 K	mm	194	n/a
Number of coil layers		2	2
Number of turns per layer (inner/outer)		22/34	22/28
Nominal current @7 TeV	kA	11.85	16.23
Central field @nominal current	T	11.23	n/a
Gradient field @nominal current	T/m	n/a	132.2
Conductor peak field @nominal current	T	11.77	11.3
Effective fraction of short sample @1.9 K and nominal current[c]	%	78	74
Effective temperature margin @1.9 K and nominal current[c]	K	4.6	5.3
Magnetic length @1.9 K	M	5.3	7.2[a]/4.2[b]
Stored energy @nominal current	MJ/m	0.9	1.15
F_x/F_y @nominal current (per half coil)	MN/m	+3.64/-1.86	+2.41/-3.38
$F_{\theta,\text{inner}}/F_{\theta,\text{outer}}$ @nominal current (per half coil)	MN/m	-1.26/-1.69	-1.58/-2.14
F_z @nominal current (per aperture)	MN	0.44	1.15
Outer shell thickness	mm	15	8
Cold mass outer diameter	mm	570	630

[a] For MQXFB @CERN.

[b] For MQXFA @AUP

[c] Based on averaged QC strand data and assuming a 5% cabling degradation.

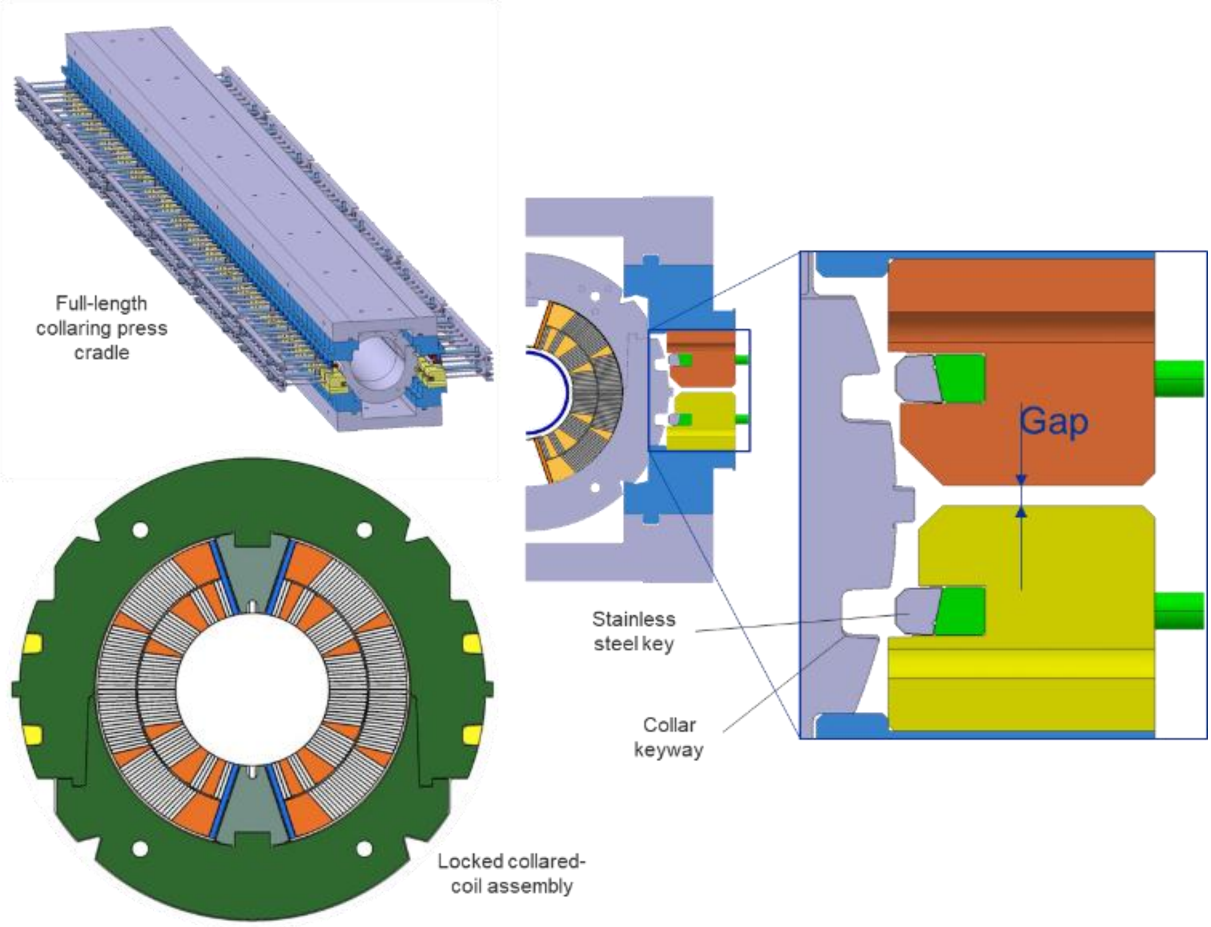

Figure 8: Illustration of collaring process of 5.3-m-long, 60-mm two-in-one-aperture, HL-LHC 11 T dipole magnet at CERN. Top left: schematic of full-length collaring cradle. Center: detail of contact areas tooling to transfer the press vertical force to the collared-coil assembly. Right: Detail of mechanical stops integrating the tooling necessary to push the stainless-steel keys laterally into their keyways. Bottom left: final collared coil assembly (Courtesy of J.-L. Rudeiros Ferńandez, formerly CERN, now LBNL, and F. Savary, CERN).

The poles used for coil winding and heat treatment are removable and made from segmented, annealed 316LN pieces. They are replaced by annealed Ti6Al4V pieces at the time of coil assembly, and, thereby, are not resin-impregnated with the coils. The Ti-alloy pole pieces feature a groove on their outer radius to house the so-called *collar nose* and a shim allowing fine adjustment of the coil stress if needed (see Section 4.5.6.1 and Figure 88).

A key consideration in the design and assembly of $\cos\theta$ and $\cos2\theta$ magnets is the need to apply an azimuthal and a longitudinal pre-compression to the coils to compensate for the effects of the Lorentz forces, which, during energization, tend to squeeze the coils towards their midplane and to stretch them outwardly (see Section 4.5.5.5) [75].

For the 11 T magnets, the azimuthal pre-compression is provided by mean of a collaring press, which applies a vertical force onto the coils and collars assembly. The force is gradually increased until the keyways at the midplane of the top and bottom collars are sufficiently open to enable insertion of lateral stainless-steel keys (see Figure 8). Upon release of the press force, the collared-coil assembly relaxes but the collars remain locked by the keys around the pre-compressed coils. The level of coil pre-compression can be adjusted thanks to shims of variable thickness at the coil pole and at the bottom of the collar nose housing. The collar noses can be equipped with strain gauges to measure the pressure exerted on the Ti-alloy pieces and transferred to the coils.

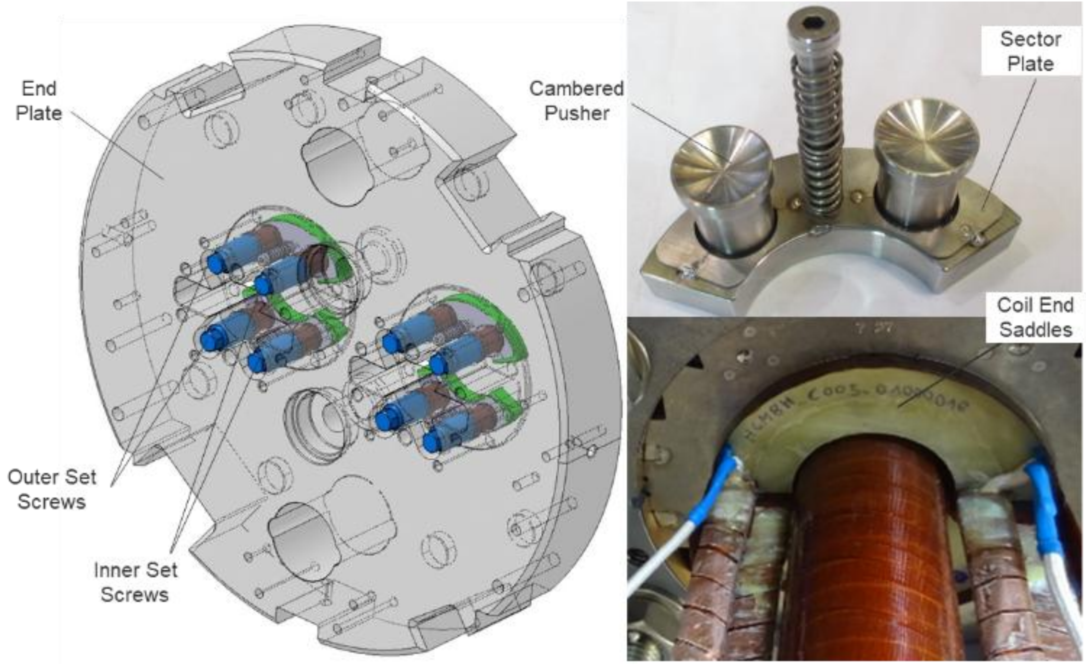

Figure 9: Details of longitudinal support and loading of 5.3-m-long, 60-mm two-in-one-aperture, HL-LHC 11 T dipole magnet at CERN. Left: stainless-steel end plates featuring 2 x 4 stainless-steel set screws. Top right: view of stainless-steel pushers and sector plate. Bottom right: view of a coil end featuring the extremities of the inner- and outer-layer G11 saddles (Courtesy of H. Prin and F. Savary, CERN).

The longitudinal pre-compression is provided by a system that comprises a set of screws, pushers, and circular sector plates, all made from stainless steel (see Figure 9). The M24 screws are bolted through 75-mm-thick, stainless-steel end plates, which are orbitally welded to the outer shell and provide a rigid support. The screws press onto the pushers, which, in turn, press onto the sector plates, which are in contact with so-called *coil end saddles* made up of G11. The pushers' extremities are cambered and coated with silver to reduce friction. They are housed in small cavities machined on the sector plates. The pusher cambers can accommodate some misalignment of the coil end saddles.

There are four bullet screws at both ends of each aperture. They are mounted before end plate assembly and torqued to a nominal value of ~30 N.m after longitudinal and orbital welding completion. The sector plates enable the load to be spread over the G11 end saddles. The pushers can be equipped with strain gauges, referred as *bullet gauges,* to monitor the forces exerted onto the coils.

1.5.5.2 Issues with Short Magnet Models and First Task Force

The CERN program started with the manufacture and test of short, single- and two-in-one-aperture magnet models and the first two-in-one dipole magnet model, referred to as MBHDP101, made from reused and previously tested coils, achieved a current level in excess of ultimate [99]. However, issues were encountered circa 2018 with subsequent magnet models (see Figure 10). A first Task Force was set up in November 2017, and a crash program was initiated to identify root causes and validate recovery actions. The Task Force concluded that the poor performances likely originated from over-squeezing the conductors at the coil midplane, in particular, at the time of collaring under the press [100][101].

The Task Force recommended implementing recovery measures to limit coil peak stress during collaring below ~150 MPa. The recommendations were implemented in the next short magnet model that was assembled and tested, referred to as MBHSP107. The magnet model exhibited good quench performance up to the ultimate current (see top of Figure 11) as well as good endurance when subjected to numerous electromagnetic and thermal cycles (see bottom of Figure 11).

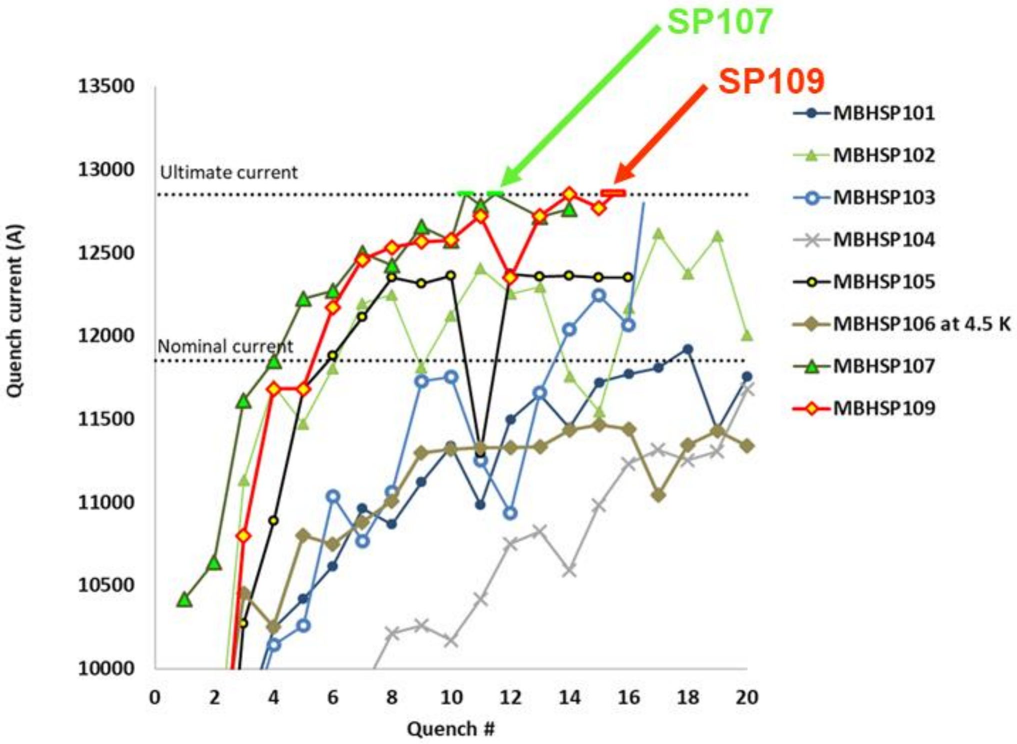

Figure 10: initial quench performance of short, 60-mm-single-aperture HL-LHC 11 T MBHSP dipole magnet models at CERN (Courtesy of G. Willering, CERN).

MBHSP107 was even used to provide a background field to test superconducting radio frequency cavities coated with Nb_3Sn and high temperature superconductors (HTS), as part of a technological development for the Relic Axion Detector Exploratory Setup (RADES) at CERN [102]. Another test for RADES was carried out in November 2024, which is a good valorization of the Task Force efforts and of the good behavior of MBHSP107.

1.5.5.3 Issues with Full-Length Magnets and Descoping

In the meantime, a 5.3-m-long 11 T magnet protype, referred to as MBHBP, had been assembled and tested in the Summer of 2018. This prototype, which relied on a previous cable layout and whose apertures were collared before the establishment of the first Task Force, exhibited a poor quench performance: it appeared limited to ~10 kA, with most of the limiting quenches located in the ends of one coil (coil CR07).

Looking back at the fabrication records, it was found that a major non-conformity had been raised after opening of the heat treatment retort of coil CR07 because severe delamination/displacements had been observed in the coil heads (see Section 5.5.5.4 and Figure 132). The delamination/ displacements were fixed by manually putting the conductors and end spacers back in place. It is likely that the poor performance results from conductor damage that arose during heat treatment (due to thermal expansion differentials), or when opening the retort, or even at the time of repair.

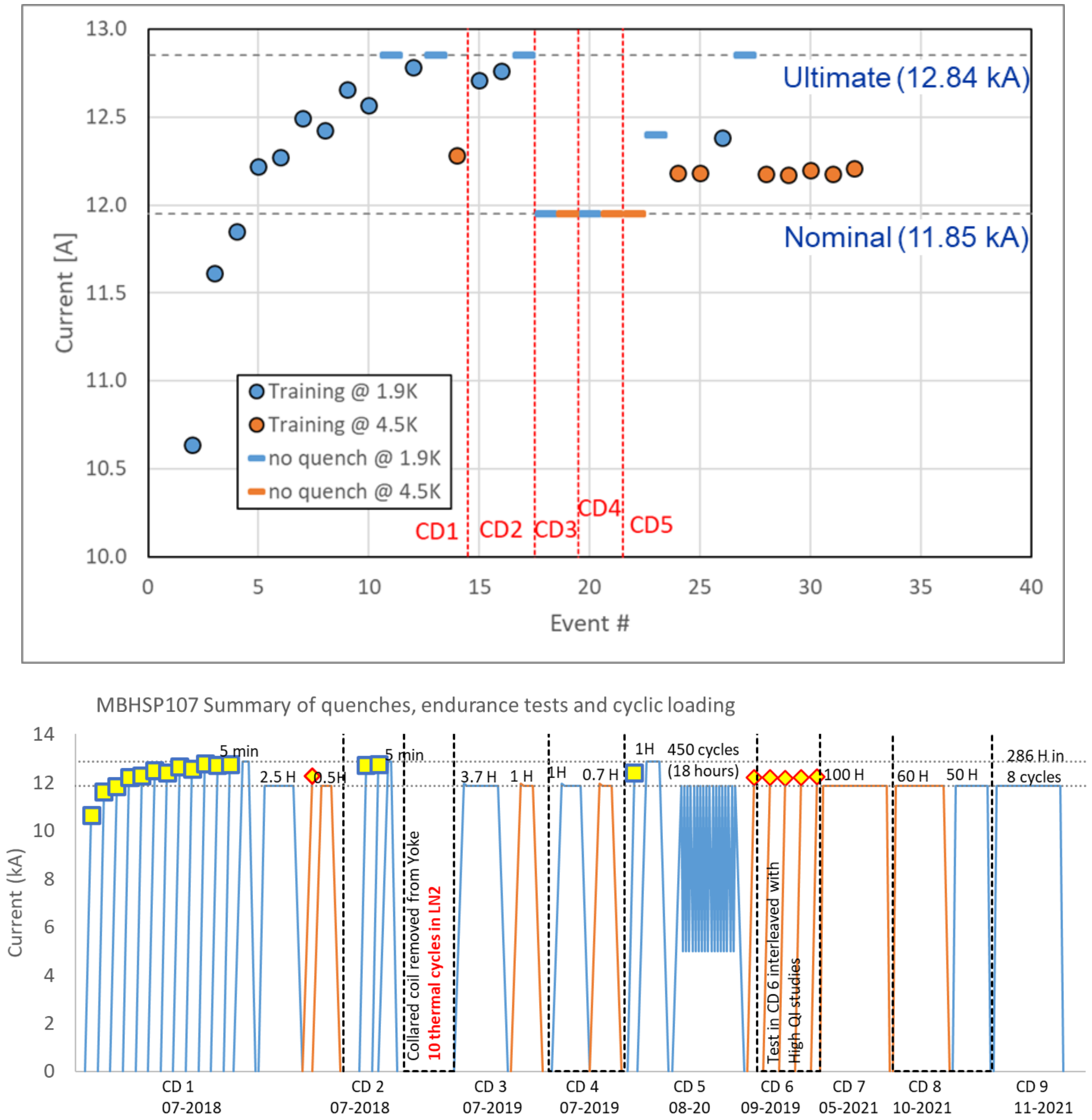

Figure 11: Test results of short, 60-mm-single-aperture HL-LHC 11 T dipole magnet model MBHSP107, which underwent numerous electromagnetic and cooldown cycles without showing signs of degradation. Top: performances after the first 5 cooldowns. Bottom: powering cycles over 9 cooldowns (Courtesy of G. Willering, CERN).

Nevertheless, the good results of MBHSP107 were encouraging enough to proceed with the series production of full-length magnets, which were due for installation during the Long Shutdown 2 (LS2) of the LHC starting in December 2018. At first, it was decided to manufacture and test a so-called *hybrid* magnet prototype. This prototype reused the structure of the 5.3-m-long, two-in-one-aperture MBHBP, but the collared-coil assembly with coil CR07 was taken out and replaced by a new collared-coil assembly, CC01, made from two virgin, series production coils (GE02 and GE03) that were collared following the procedure optimized by the Task Force. The qualifier “hybrid” refers to the fact that the electrical circuit of the magnet enables powering of each collared-coil assembly independently.

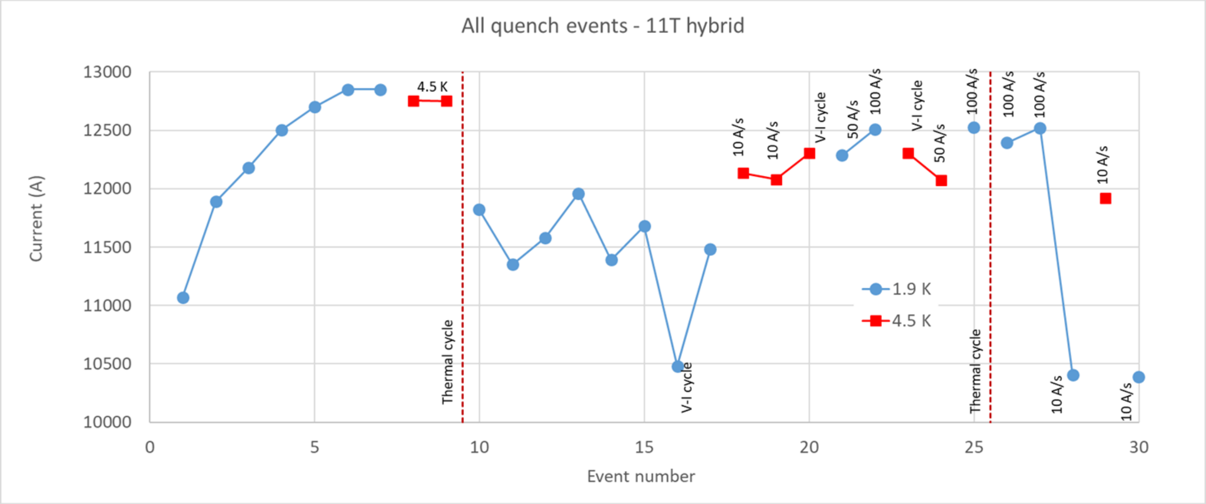

Figure 12: quench performance of Aperture 1 of 5.3-m-long, 60-mm-aperture HL-LHC 11 T "hybrid" dipole magnet prototype (courtesy of G. Willering, CERN).

In the end, only the new collared-coil assembly, corresponding to Aperture 1, was powered during the cold test. As illustrated in Figure 12, upon the first cooldown, Aperture 1 achieved nominal current after two quenches and ultimate current after 5 quenches, in line with the performance of MBHSP107. However, it exhibited severe detraining after warm-up/cooldown cycle, with erratic behavior and all detraining quenches (but one) located in the connection-side end of coil GE02. Upon analysis of the warm-up/cooldown procedure it was found that the magnet had been subjected to uncontrolled temperature gradients (in excess of 200 K over the magnet length), with the thermal front first hitting the connection-side end of the magnet where the detraining quenches originated.

In LHC operation, warm-up/cooldown of magnet strings are tightly controlled, with temperature gradients limited to 50 K between magnets and cooldown rates limited to 10 K/hour. It was concluded that the observed performance degradation could have been due to the too brutal cooldown rate. From then on, it was decided to impose a limitation of 50 K on the temperature gradient across the length of both short and long Nb_3Sn magnets tested vertically or horizontally at CERN.

The new cooldown procedure was successfully applied and validated during the test of the first, full-length, two-in-one-aperture 11 T series dipole magnet (referred to as S1), which reached nominal current with two training quenches and did not exhibit any retraining after warm-up/cooldown (see Figure 13). Note that S1 was the first magnet tested at CERN for which the requirement of achieving ultimate current had been removed as explained in Section 1.5.3. However, the test results of all three subsequent 11 T series dipole magnets (referred to as S2, S3 and S4) were not satisfactory: they all exhibited performance degradation after a sequence of electromagnetic and warm-up/cooldown cycles (see Figure 18).

The poor results of full-length 11 T dipole magnets led to the decision, at the end of 2020, to forsake the installation of these magnets during LS2. Since then, additional beam optic analyses and data from the ongoing LHC Run 3 have shown that HL-LHC could be operated without the additional collimation that was thought to be needed, and which triggered the 11 T magnet development. As a result, the 11 T dipole magnets have been descoped from the HL-LHC project. Although the unsuccessful 11 T dipole magnet development did not endanger the HL-LHC project, it did raise questions about Nb_3Sn accelerator magnet technology.

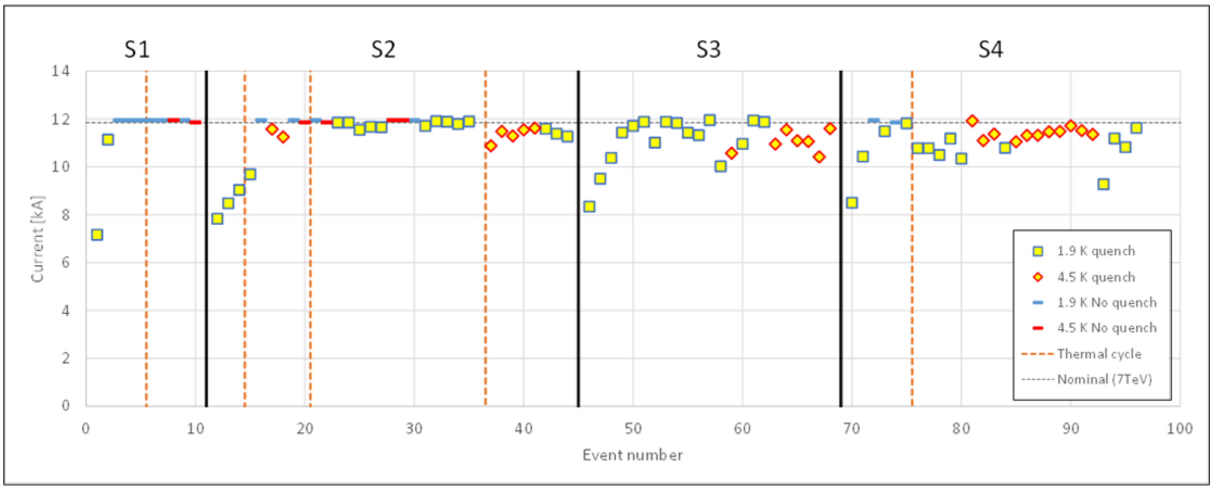

Figure 13: Quench performance of 5.3-m-long, 60-mm-two-in-one-aperture HL-LHC 11 T series dipole magnets at CERN (courtesy of G. Willering, CERN).

1.5.5.4 Second Task Force and Recovery Plan

Following the decision of not installing the 11 T magnets during LS2, it was nevertheless decided to set up a second Task Force, aimed at relaunching comprehensive root-cause analyses and at developing a recovery plan. Although it is unlikely that, even if successful, 11 T magnets would be considered for tunnel installation, it was assessed that what could be learned and corrected as part of this effort would be valuable for other or future Nb_3Sn accelerator magnet projects.

The details of the analyses and of the recovery plan are presented in Section 4. The methodology followed for these analyses and the techniques that were developed for magnet autopsy and post-mortem investigations of coils were inspired by the ITER experience described in Section 1.4.2. As expected, the analyses on the 11 T proved very useful and served as test beds for the investigations on MQXF quadrupole magnets. The 11 T recovery plan, which includes the assembly/re-assembly of one short and one long, two-in-one-aperture, dipole magnet model and prototype is still ongoing (albeit at a slow pace). The main goal is to assess mitigation measures to resolve several non-conformities that were identified in the assembly and mechanical support of the coil ends of the full-length series magnets (see Section 4).

1.5.6 Issues with 7.2-m-Long MQXFB Quadrupole Magnets

1.5.6.1 Design and Assembly Overview

The design requirements for the so-called *low-β* or *interaction region* quadrupole magnets for HL-LHC went through several iterations before being finalized in 2012 to the present parameters [90][103]. The nominal current is 16.23 kA corresponding to a field gradient and a conductor peak field of 132.2 T/m and 11.3 T, respectively; the ultimate current is 17.5 kA, corresponding to a field gradient and a conductor peak field of 142.1 T/m and 12.2 T, respectively. The magnets are to be operated at 1.9 K but are expected to achieve nominal current at 4.5 K to demonstrate that they have enough operating margin. Table 2 summarizes salient magnet design parameters. The MQXF magnets were developed in collaboration between CERN and LARP but rely extensively on the LARP experience for many technological aspects and for the choice of tooling and manufacturing processes.

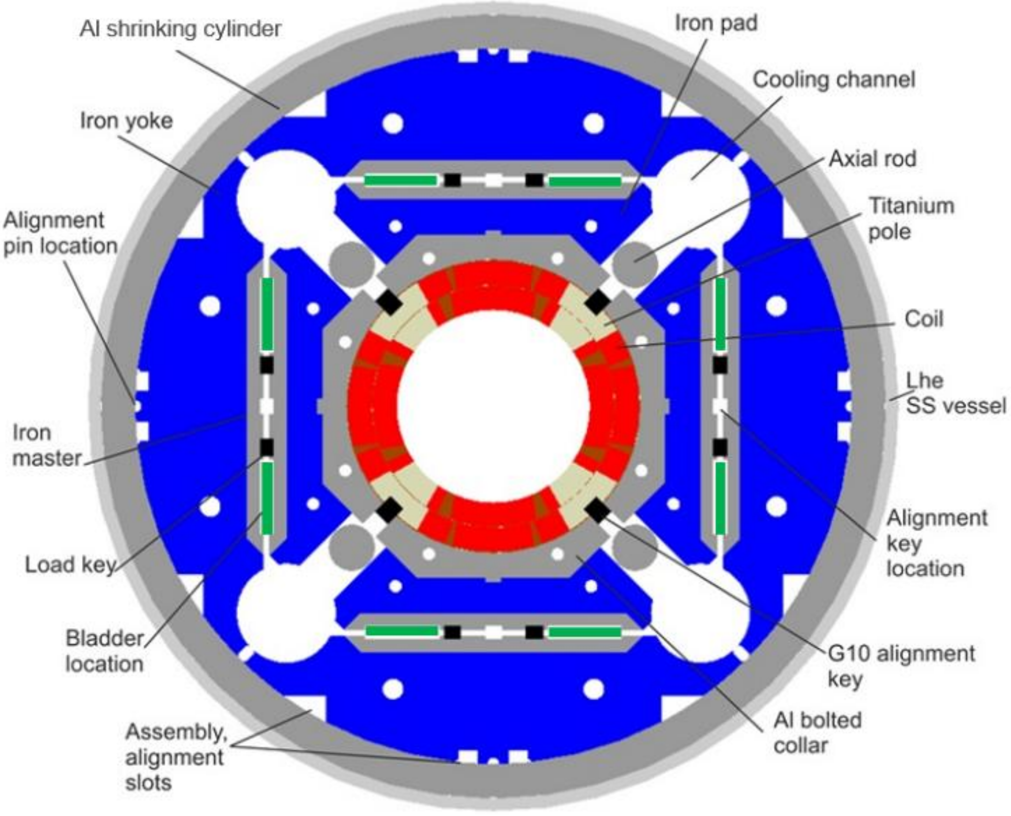

Figure 14: Cross-sectional view of 150-mm-aperture HL-LHC MQXF quadrupole magnet showing the double-layer, cos2θ coils (red) with separate poles (beige), surrounded by aluminum collar packs (grey), low-carbon steel pads and yoke (dark blue), aluminum shrinking cylinders (dark gray) and welded stainless steel outer shell (light grey). The original positions of the bladders are shown in green; they are replaced by keys shown in black.

Figure 14 shows a cross-sectional view of the 150-mm-single-aperture MQXF quadrupole magnet, featuring from inside out: an assembly of 4 double-layer, cos2θ coils with separate poles, surrounded by aluminum collar packs, low-carbon steel pads and yoke, precisely machined, aluminum 7075 T6, shrinking cylinders and a welded stainless-steel outer shell. The coils are wound from slightly keystoned, Rutherford-type cables (see Figure 6) [98][104]. The poles are made from segmented, annealed Ti6Al4V pieces, which are integrated into the coils and resin impregnated with them.

The azimuthal pre-compression is provided to the coils by means of bladders, which are inserted into the structure between the iron pads and yoke (see Section 5.4). The bladders are inflated in a stepwise manner until a large enough clearance is opened between pads and yoke to enable the insertion of stainless-steel keys of increasing sizes. Once the final-size keys are in place, the bladders are deflated, and the structure remains pre-loaded. To facilitate the process, bladders and keys are half the length of the magnet and are inserted from both sides.

As detailed in Ref. [81], each side of the two HL-LHC interaction regions calls for a total of four cryomagnets: 1 x Q1, integrating two MQXFA quadrupole magnets, 2 x Q2, each integrating one MQXFB quadrupole magnet and one MCBXFB nested dipole magnet corrector, and 1 x Q3, integrating two other MQXFA quadrupole magnets. All Q1, Q2, and Q3 cryomagnet assemblies will eventually be cold tested, but to enable shorter feedback times, AUP decided to cold test all MQXFA magnets in vertical configuration at BNL, prior to outer shell welding. At CERN, the longer magnet length does not permit vertical testing. It was decided, at least for the prototypes, to cold test MQXFB magnets in a test cold mass and cryostat configuration, with a welded outer shell but without MCBXFB correctors.

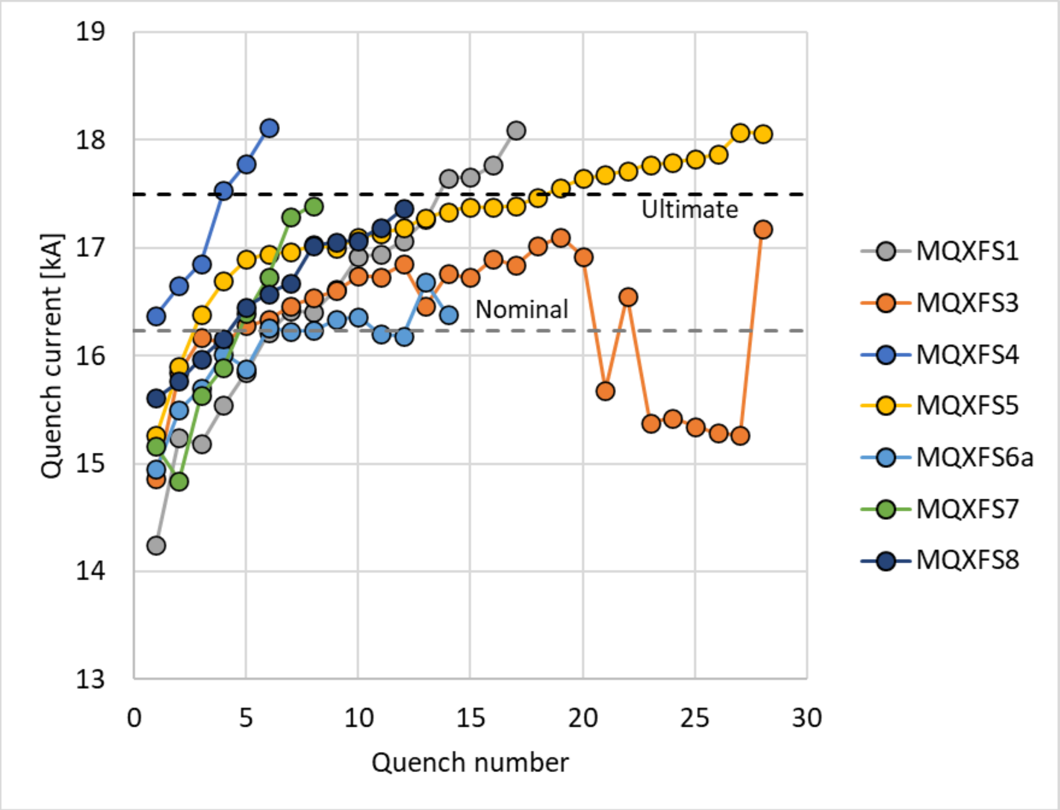

Figure 15: Initial quench performance of short HL-LHC MQXFS quadrupole magnet models at 1.9 K (Courtesy of F. Mangiarotti, CERN).

1.5.6.2 Short Quadrupole Magnet Models

As in the case of the 11 T dipole magnets, a comprehensive short magnet model program was carried out, which enabled optimization of critical design parameters and demonstrated the feasibility of achieving nominal current [105] [106] and, even well beyond ultimate current [107], with a limited number of training quenches at 1.9 K (see Figure 15).

1.5.6.3 LARP/AUP 4.2-m-Long MQXFA Quadrupole Magnets

US LARP was the first to manufacture and test long HL-LHC quadrupole magnets (4.2 m in their case) of the final design. The magnets were tested vertically at BNL prior to welding of the outer stainless-steel shell. The first two prototypes, referred to as MQXFAP1 and MQXFAP2, gave mixed results, but the origins of the problems were readily identified: electrical short from coil to ground in the case of MQXFAP1, failure of an aluminum-alloy shrinking cylinder due to sharp edge machining for MQXFAP2 [108].

Lessons learned from the prototypes were applied to the next two pre-series magnets, referred to as MQXFA03 and MQXFA04, which met HL-LHC project requirements [109][110]. Since then, the series production of MQXFA magnets has been proceeding, with a few setbacks, for which corrective actions were derived and implemented [111].

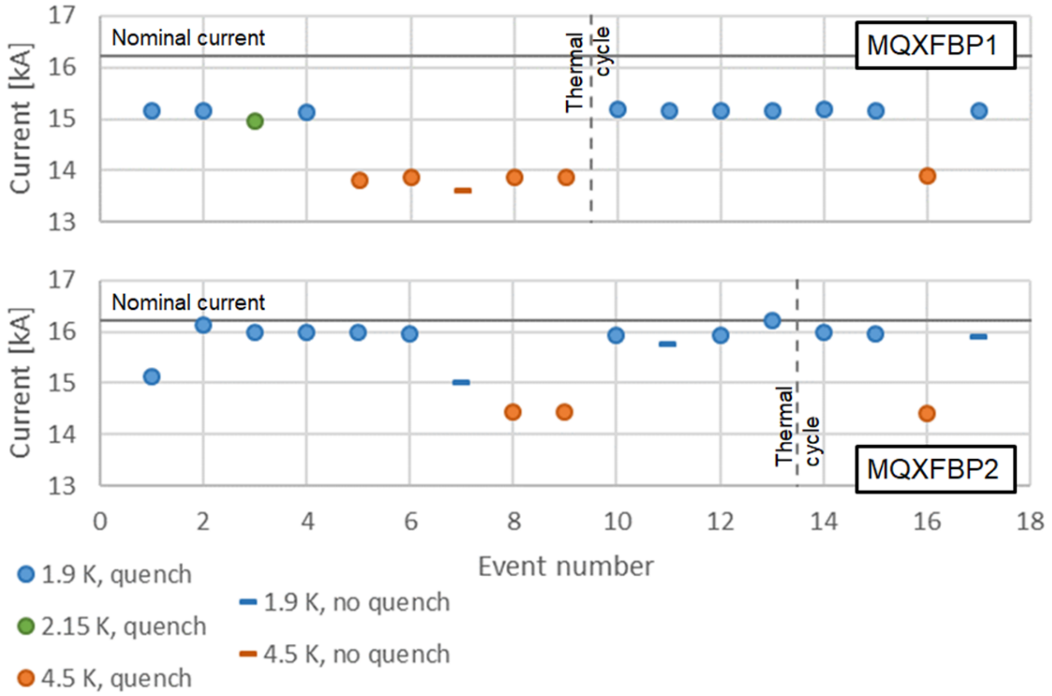

Figure 16: Quench performance of 7.2-m-long, 150-mm-single-aperture HL-LHC MQXFBP1 and MQXFBP2 quadrupole magnet prototypes at CERN in a test cold mass configuration and test cryostat (Courtesy of F. Mangiarotti, CERN).

In addition, AUP has completed in 2023 the first Q1/Q3 cryomagnet assembly, made up of the two pre-series magnets MQXFA3 and MQXFA4 magnets, with a welded outer stainless-steel shell and mounted inside a cryostat. The cryomagnet was cold tested horizontally at FNAL and demonstrated good performances at both 1.9 and 4.5 K, with only two high current level quenches, possibly due to issues with helium level control in the test facility [112]. The cyromagnet was shipped to CERN at the end of 2023 where it was retested in the Spring of 2024.

1.5.6.4 CERN 7.2-m-Long MQXFB Quadrupole Magnets

The first 7.2-m-long MQXFBP1 quadrupole magnet prototype manufactured at CERN was tested in 2021, and the second, MQXFBP2, in 2022. Both prototypes exhibited a performance limitation below the nominal current (see Figure 16), with a very similar phenomenology [113]: reproducible quenches at reproducible locations (towards the longitudinal center of one of the coils), and with a decrease of quench level between 1.9 K and 4.5 K in accordance with the expected scaling law of Nb_3Sn conductor critical current versus temperature. These disappointing results prompted a pause of MQXFB production at CERN and triggered a comprehensive root cause analysis aimed at identifying the origin(s) of the limitation and possible corrective actions.

Unlike in the case of the 11 T dipole magnet program, the performance limitation of the MQXFB prototypes was a serious issue for the HL-LHC project, as these magnets are at the core of the luminosity upgrade, which cannot be done without them. This generated a situation similar to the one encountered at ITER, nearly a decade before, with the SULTAN test results of the first two CS conductor samples (see Section 1.4.2). As in the case of ITER, the problem compounded technical, human, and management factors, and the ITER and 11 T experience were very useful in developing a suitable methodology to cope with it. The details of the efforts carried out to resolve this problem are presented in Section 5.

1.6 European Efforts on Nb_3Sn Accelerator Magnet Development and Retest of MSUT

1.6.1 Brief History

As mentioned, the setbacks in the 11 T and MQXFB programs raised some alarms regarding the viability of the Nb_3Sn technology for accelerator magnet applications. The design and assembly of HL-LHC Nb_3Sn magnets relied extensively on the experience and developments carried out in the USA. Although they were much more limited in scope, a few pioneer Nb_3Sn accelerator magnet programs were also carried out in Europe (surprisingly, the authors of [91] do not refer to any of these efforts).

The EU programs included:

- a short quadrupole magnet model, which was the first application of the wind-and-react process at CERN in the early 1980s [114];
- short dipole magnet models for LHC, designed, built and tested by a collaboration between CERN and Elin GmbH, Germany, in the late 1980s [115][116];
- a 1-m-long, 50-mm-single-aperture dipole magnet model, referred to as MSUT, was designed, built and tested by a collaboration between Twente University, the Netherlands and CERN in the mid-1990s [10][11][12][13];
- a short quadrupole magnet model relying on the same coil geometry as the LHC arc quadrupole magnets designed and built by the French Alternative Energies and Atomic Commission (CEA) at Paris-Saclay, France, in the 2000s [117][118][119];
- the Joint Research Activity for the Next European Dipole (NED) introduced in Section 1.1 and which was initiated in 2004 [7][120][121][122].

As part of the NED efforts, RAL, who was one of the collaborators, unearthed the concept of helical dipoles [123]. This design, initially proposed in 1970 at the University of Michigan, in Ann Arbor [124], has, since then, steered a lot of interest. It is now better known under the more fashionable name of *Canted Cosine Theta (CCT)* magnet design [125].

The CARE Integrated Activity was eventually followed by the European Coordination for Accelerator Research and Development (EuCARD) Integrated Activity and NED evolved into FRESCA2. FRESCA2 is a 1.5-m-long, 100-mm-aperture dipole magnet model designed and built by a collaboration between CERN and CEA/Paris-Saclay, to be used as a background field magnet for an upgrade of the CERN cable test facility.

The design of FRESCA2 started in 2009 [126]. It relies on a so-called *block-coil* layout, with each pole made of two, double-pancake, racetrack-type coils, with flared ends. The coils are wound from rectangular cables made of 40 strands, with a diameter of 1 mm and a Cu-to-non-Cu ratio of 1.25. Two types of strands are used: PIT and RRP® 132/169. Coil winding was carried out at CEA/Paris-Saclay [127][128], while all other activities were carried out at CERN. The magnet was assembled first in the fall of 2016 [129] and cold tested in February 2017. It was subsequently disassembled to replace one coil [130][131], and the second assembly, referred to as *FRESCA2b*, was tested in August 2017 [132]. It was disassembled and reassembled again, and the final assembly, referred to as *FRESCA2c*, achieved in the Summer of 2018 a record dipole field of 14.6 T at 1.9 K The magnet has now been installed in a dedicated cryostat and the cryogenic commissioning of the FRESCA2 cable test facility has started in the 4th quarter of 2024.

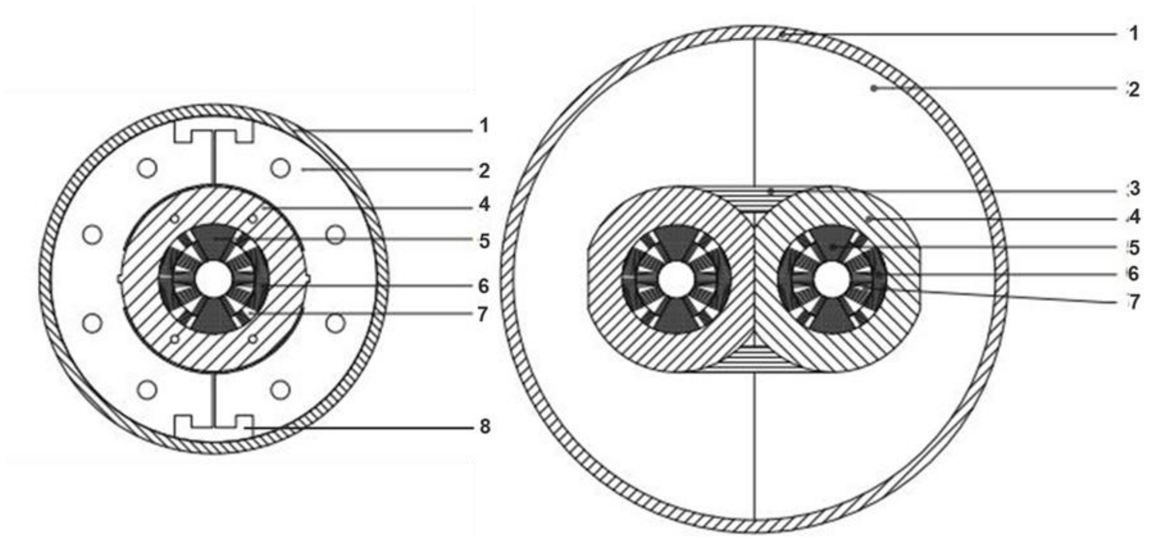

Figure 17: Cross-sectional views of 50-mm-aperture MSUT dipole magnet designs. Left: single-aperture design used for the short magnet model. Right: proposed two-in-one-aperture design. 1: stainless-steel outer cylinder; 2: low-carbon-steel yoke; 3: stainless steel yoke insert; 4: aluminum-alloy ring collars; 5: stainless steel pole insert; 6: conductor blocks; 7: copper wedges; 8: aluminum clamps (Courtesy of A. den Ouden, formerly CERN and H.J. ten Kate, formerly CERN [10][13]).

1.6.2 Retest of MSUT

The most relevant program for HL-LHC is the MSUT magnet model, which relies on a 2-layer, $\cos\theta$ design aimed at a central field of 11.5 T at 4.5 K, and incorporates a number of specific features suitable to accelerator magnets [10][11]. The left part of Figure 17 shows a cross-sectional view of the single-aperture model magnet, while the right part illustrates how it could be scaled up to a two-in-one-aperture design.

As mentioned in Section 1.1, the magnet was first tested in 1995 and retested in 1997, both times at 4.5 K (see Figure 18). After first cooldown in 1995, the magnet achieved 18.7 kA, corresponding to a central dipole field of 11.03 T, on its first ramp to quench [12]. After the second cooldown in 1997, the magnet achieved a maximum current of 19.1 kA, corresponding to a central dipole field of 11.27 T, in a few training steps [13]. After the tests, the magnet was left in storage at CERN without any particular precaution.

Given the parameters and good initial performances of MSUT, it was thought interesting, in 2021, at the time of the 11 T and MQXFB turmoil, to retest it and assess its endurance and repeatability after 24 years. It was also decided, after a retest at 4.5 K, to cool it down to 1.9 K. The retest results are shown in Figure 18 [14]. The magnet model restored its previous performance at 4.5 K on the first ramp without any retraining, achieving a quench current of 19.1 kA. When cooled down to 1.9 K, the magnet had one training quench, at a current of 19.57 kA, and then reached the 20-kA limit of the power converter, corresponding to a central dipole field of 11.76 T, without quenching.

These results are quite remarkable and provided reassurance that a Nb_3Sn magnet model designed and manufactured in Europe in the mid-1990s could achieve central dipole fields in the 11–11.5 T range and exhibit excellent durability over nearly two decades and half.

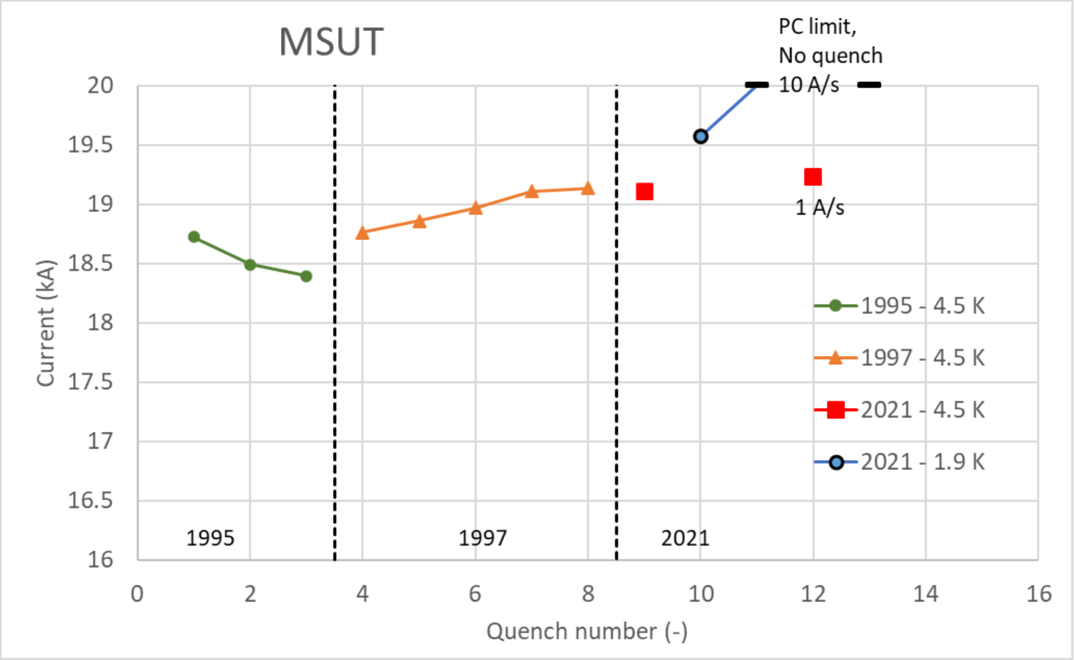

Figure 18: Quench Performance of 1-m-long, 50-mm-aperture, Nb_3Sn dipole magnet model MSUT (Courtesy of G. Willering, CERN, A. den Ouden, formerly Twente University and H.J. ten Kate, formerly CERN [14]).

1.7 Goal of this Report

The goal of this report is to relate the actions that were undertaken at CERN in the past few years to improve instrumentation and diagnostics of Nb_3Sn accelerator magnets, to refine post-mortem examinations of Nb_3Sn conductors and coils, to identify possible root causes for the performance limitation/degradation of HL-LHC Nb_3Sn magnets, and to systematically address each of the root causes through recovery actions.

At the end of the process, a full-size quadrupole magnet, MQXFB03, which was manufactured and tested in Summer/Fall 2023, and which integrated all agreed recovery actions, was successful and demonstrated that the main root cause of the performance limitation had been cured. These results confirmed, alongside the results of AUP, that Nb_3Sn accelerator magnet technology can be made to work, and production is now ongoing on both sides of the Atlantic for the small series of MQXFA and MQXFB magnets needed for HL-LHC.

2 Improved Diagnostics, Electrical Test Requirements and Ancillaries for Nb$_3$Sn Accelerator Magnets

2.1 Quench Performance Phenomenology

2.1.1 Performance Limitation (MQXFB)

The first two full-length MQXFB magnet prototypes exhibited what we refer to as performance limitation. Such behavior is characterized by the fact that, after the first cooldown, the magnet reaches a stable quench plateau that is below the target current (see Figure 16). Other features include:

- reproducible localization of plateau quenches at both 1.9 K and 4.5 K (in the inner-layer pole turn of one specific coil, towards its longitudinal center);
- proper scaling of the plateau current between 1.9 K and 4.5 K (see Figure 19);
- more or less monotonic decrease of quench current as a function of ramp rate (see Figure 20);
- reproducible quench behavior after warm-up/cooldown cycles.

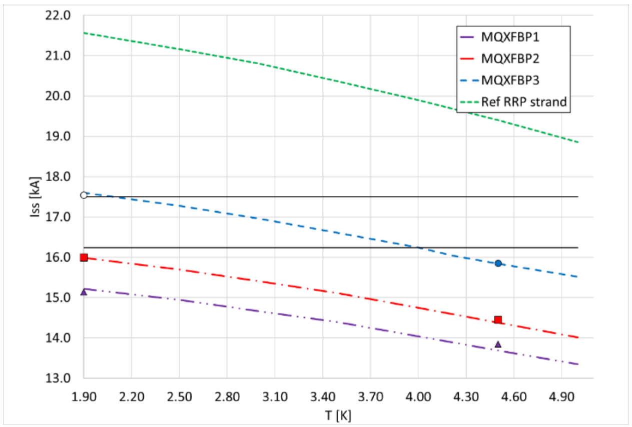

Figure 19: Quench plateau current versus temperature measured on 7.2-m-long HL-LHC quadrupole magnet prototypes; scaling is in-line with the expected critical current vs. temperature curve of Nb$_3$Sn conductor (Courtesy of F. Mangiarotti, CERN).

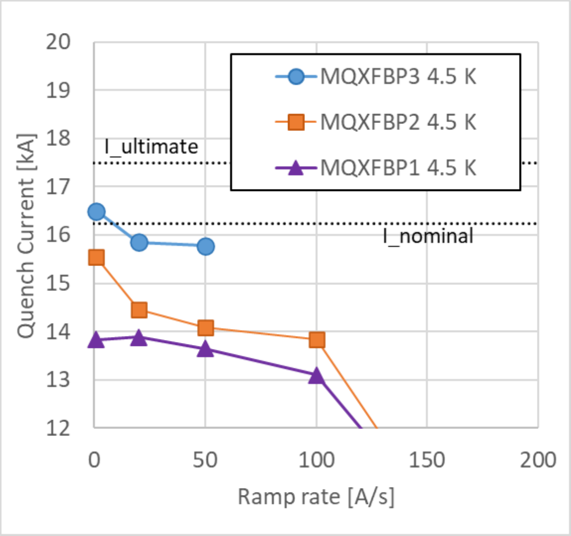

Figure 20: Ramp rate behavior of 7.2-m-long HL-LHC quadrupole magnet prototypes at 4.5 K exhibiting a more or less monotonic behavior (Courtesy of F. Mangiarotti, CERN).

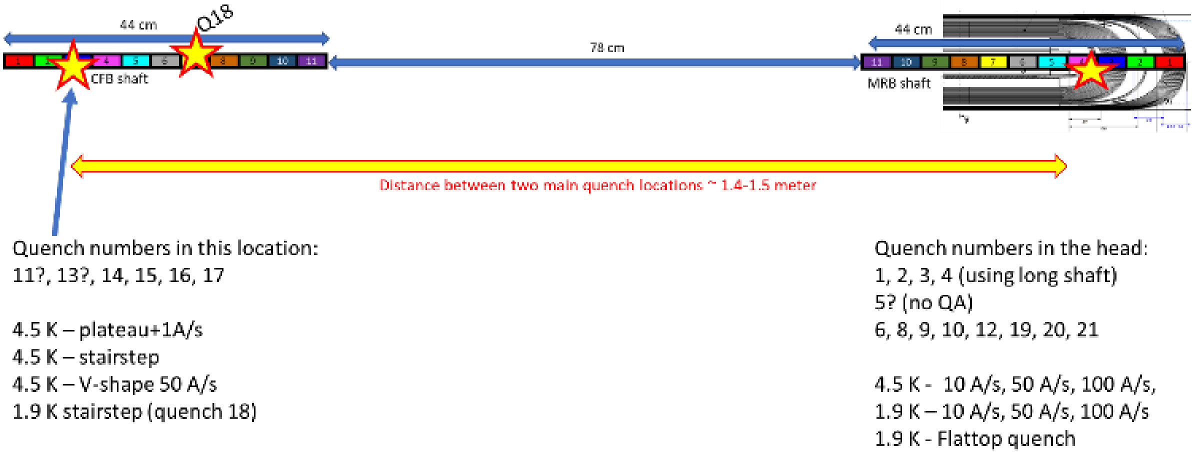

Figure 21: Quench-start localizations assessed on 5.3-m-long, series production, HL-LHC 11 T dipole magnet S4, showing the impact of the type of current ramps (Courtesy of G. Willering, CERN).

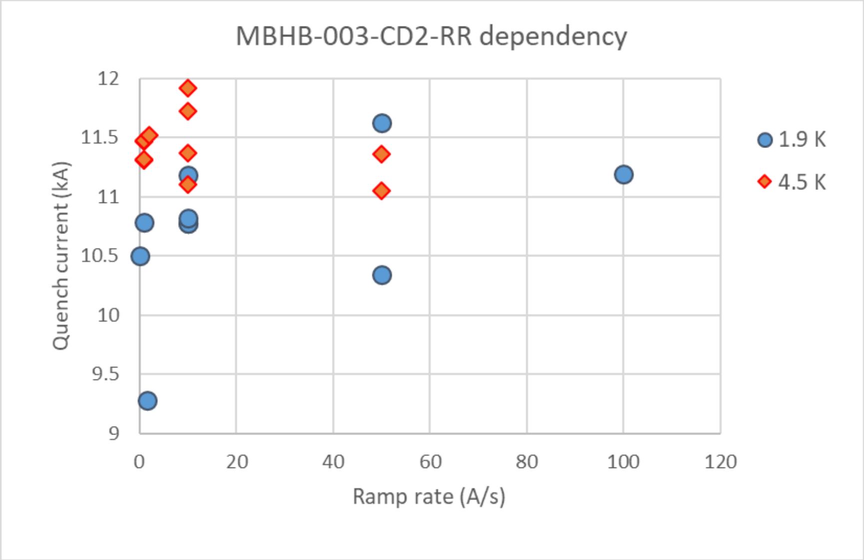

Figure 22: Ramp rate sensitivity of 5.3-m-long, series production, HL-LHC 11 T dipole magnet S4 showing a non-monotonic behavior (Courtesy of G. Willering, CERN).

2.1.2 Performance Degradation (11 T)

The full-length, series production, 11 T dipole magnets exhibited what we shall refer to as *performance degradation*. In this case, most magnets achieve target current after the first cooldown, but the quench performance subsequently degrades after a sequence of electromagnetic and warm-up/cooldown cycles and become somewhat erratic (see Figure 13). Other features include:

- quench localization mostly in coil heads and affected by the type of current ramps (see Figure 21);
- quench performance not scaling with temperature;
- quench performance exhibiting an erratic behavior as a function of ramp rate (see Figure 22**)**;
- quench performance strongly affected by warm up/cooldown cycles.

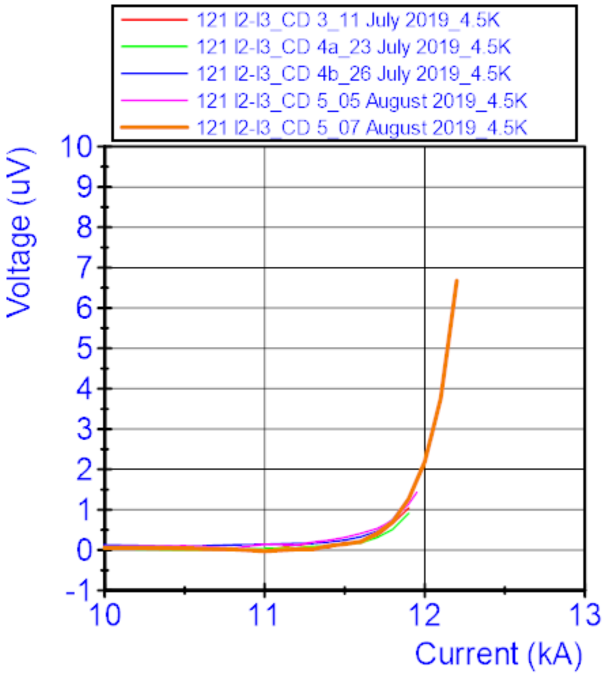

Figure 23: *V-I* measurements carried out across the midplane turn of coil SD121 at various stages of the testing of short, 60-mm-single-aperture HL-LHC 11 T dipole magnet model MBHSP107 starting from its third cooldown (all measurements at 4.5 K; courtesy of G. Willering, CERN).

2.2 Improved Diagnostics

2.2.1 V-I Measurements on Magnets

Voltage versus current measurements (or *V-I* measurements) are usually carried out on wire or conductor samples as a function of field, temperature and, eventually, strain to determine the critical current and resistive transition index (*n*-value) scaling laws [1]. The measurements become more complex for large-size CICCs and call for specific care in sample preparation and instrumentation (*e.g.*, implementation of crown arrays of voltage taps [15]). Voltage measurements across full or sections of magnet coils are usually too noisy or are not recorded with enough resolution to capture the initial voltage rise preceding a quench.

Starting from ~2018, during the later part of the 11 T short and series magnet programs, CERN has been able to carry out sensitive voltage measurements during magnet testing, permitting the detection of early resistive transitions, and the monitoring of their evolution as a function of electromagnetic and thermal cycling [99]. The technique was subsequently applied to short MQXFS [107] and long MQXFB [113] quadrupole magnets at CERN. Note that the measurements are more sensitive at 4.5 K than at 1.9 K.

Figure 23 shows *V-I* measurements carried out across the straight section of the midplane turn of coil SD121 used to manufacture the short, 60-mm-single-aperture HL-LHC 11 T dipole magnet model MBHSP107. The measurements were initiated after the third cooldown. The curves clearly show the start of a resistive transition, but it remains very stable throughout subsequent electromagnetic and thermal cycling, which is consistent with the reproducible performance of MBHSP107 featured in Figure 11.

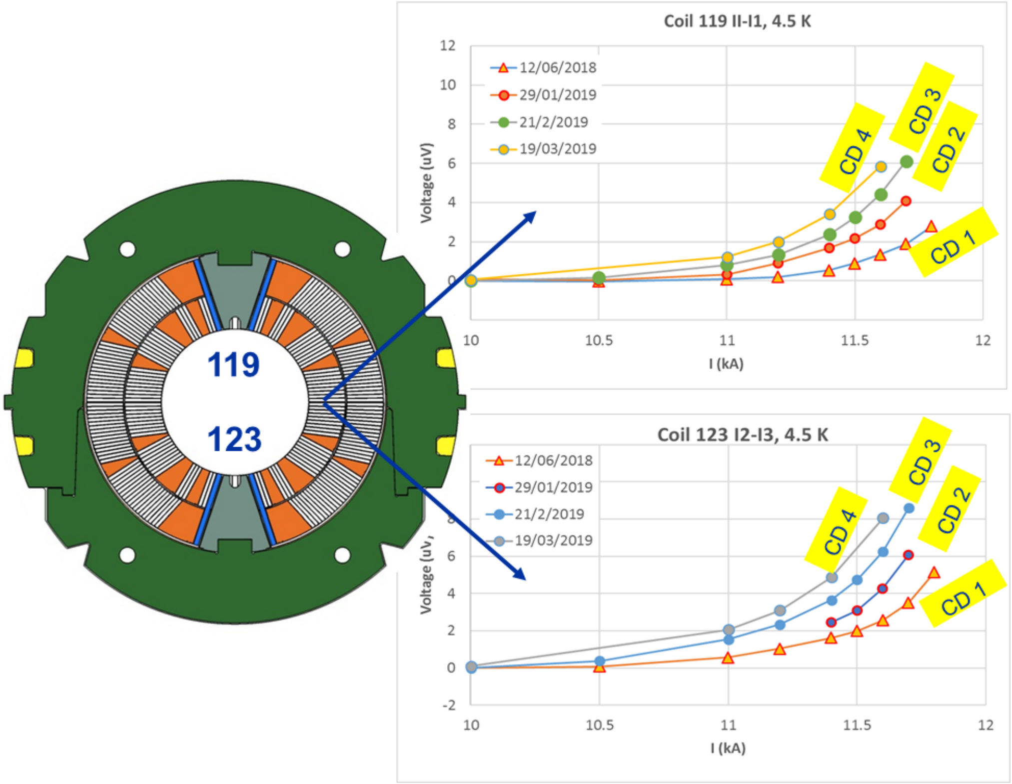

Figure 24: *V-I* measurements carried out across the midplane turns of coils SD119 and SD123 at various stages of the testing of short, 60-mm-single-aperture HL-LHC 11 T dipole magnet model MBHSP109, showing evidence of degradation as a function of warm-up/cooldown cycles (all measurements at 4.5 K; courtesy of G. Willering, CERN).

On the contrary, Figure 24 illustrates the case of the short 11 T dipole magnet model MBHSP109, where the voltages measured across the midplane turns of the inner layers of the top and bottom coils exhibit a progressive degradation as a function of warm-up/cooldown. This degradation is consistent with the observed quench performance degradation (see details in Section 4.2.6 and Figure 71). A further degradation was observed when carrying out midplane quenches with hot spot temperatures above 300 K.

The two examples presented above illustrate the benefit that can be derived from *V-I* measurements on coils (or coil sections if equipped with voltage taps, which, of course, provide a higher resolution), to better assess or confirm magnet performance. It is now a routine procedure on all magnets tested at CERN. These measurements are usually carried out during a dedicated staircase current ramp at 4.5 K.

While on the flats of the current stairs, the observed voltage can exhibit some decay with time (see Figure 25). This decay is attributed to current redistributions among Rutherford-type cable strands likely caused by the presence of local defects [133][134]. The complex electrodynamical effects of interstrand current redistribution have been known and studied for many years in Nb–Ti cables [135][136] and are influenced by a wide range of parameters [137]. They have been revisited in recent years to analyze the impact of local defects in Nb_3Sn cables [138][139] However, let us not forget that these phenomena are a consequence of the defects and not the root cause of the performance degradation. They need to be understood and properly taken into consideration to accurately determine the defects' localization, which may differ from the quench-start localization, assessed from the quench antenna, and from the actual quench origin, as the latter two can be affected by the type of current ramp and the ensuing current redistribution.

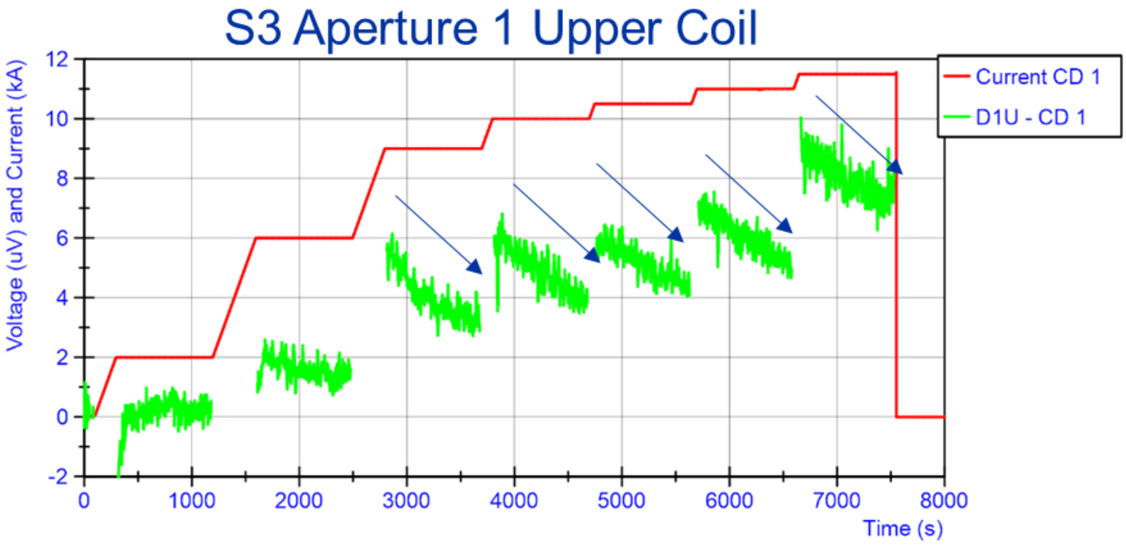

Figure 25: *V-I* measurements carried out during a staircase current ramp across the upper coil of Aperture 1 of 5.3-m-long, 60-mm-two-in-one-aperture HL-LHC 11 T series dipole magnet S3, showing evidence of voltage decay on current flattops (Courtesy of G. Willering, CERN).

2.2.2 Trim Powering

When testing an accelerator magnet made from several coils whose quench performance is limited below nominal current, it is often the case that all limiting quenches originate in one, and only one coil. Then, the question arises: what are the performances of other coils, and are they also limited?

The active quench protection scheme of MQXF magnets includes traditional quench protection heaters, mounted on the outer surface of the coils, like those used in LHC Nb–Ti magnets [140][141]. It also includes the so-called *Coupling-Loss Induced Quench (CLIQ)* system. CLIQ relies on a capacitive discharge to inject AC current into the middle of the series-connected coil circuit, thereby inducing a fast oscillation in transport current and field, resulting in high inter-filament coupling losses, which, in turn, generate heat directly inside the cables and accelerate quench development [142] (high interstrand coupling losses are also produced when the Rutherford-cable does not integrate a stainless-steel core). CLIQ was first demonstrated on a 120-mm-aperture, Nb–Ti quadrupole magnet that was developed in an initial phase as a potential candidate for the HL-LHC upgrade [143]; it was subsequently validated on short MQXFS magnet models [144] and on a long MQXFA magnet prototype [145]. It is now part of the baseline protection scheme for MQXFA and MQXFB magnets.

The implementation of CLIQ requires the installation of two dedicated leads per magnet (blue circuit in Figure 26). For model magnets and full-length test assemblies, the leads were made of a small, rectangular Nb–Ti cable, while for series production, they are made of copper and can carry a peak current of 3 kA. Following the test of MQXFBP1, it was proposed to use such leads to inject a negative, trim, DC current into the limiting coil(s) and probe the performances of other coil(s) at higher current (red circuit in Figure 26). In the present setup, the peak current in the trim leads is limited to 1.5 kA.

The trim powering scheme was first validated on a short quadrupole magnet model (MQXFS7) before being applied to full-length prototype MQXFBP2 [113]. The results of the MQXFBP2 tests are summarized in Figure 27. It appears that, in addition to coil P1, which was the limiting coil during normal operation, two out of the three remaining coils (P2 and P3) also exhibit performance limitation during trim powering, with similar quench localizations to that of the limiting quenches of P1 (inner-layer pole turn, straight section, towards coil mechanical center).

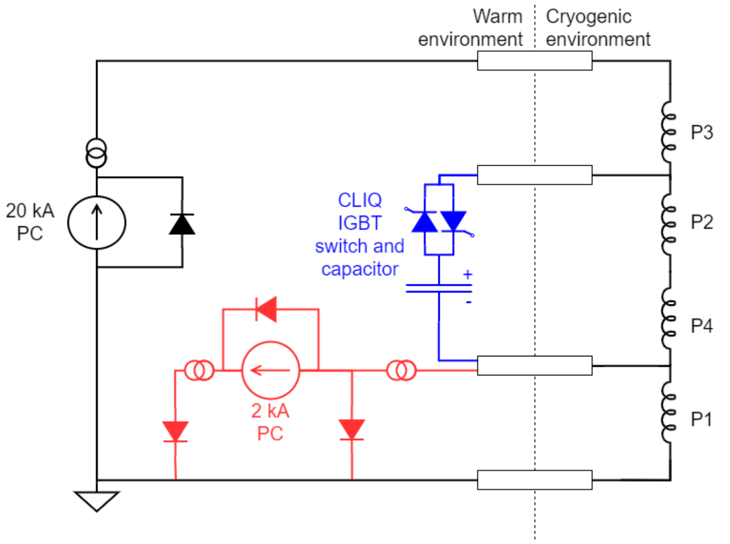

Figure 26: Electrical circuit for testing of 7.2-m-long HL-LHC MQXFBP2 quadrupole magnet prototype at CERN. P1 through P4 designates the four series-connected coils of the magnet assembly; PC indicates the DC power converter; black elements show the standard powering scheme; blue elements correspond to the CLIQ system; red elements show the additional circuit for trimmed powering of coil P1; the blue and red circuits were not connected simultaneously (Courtesy of F. Mangiarotti, CERN [113]).

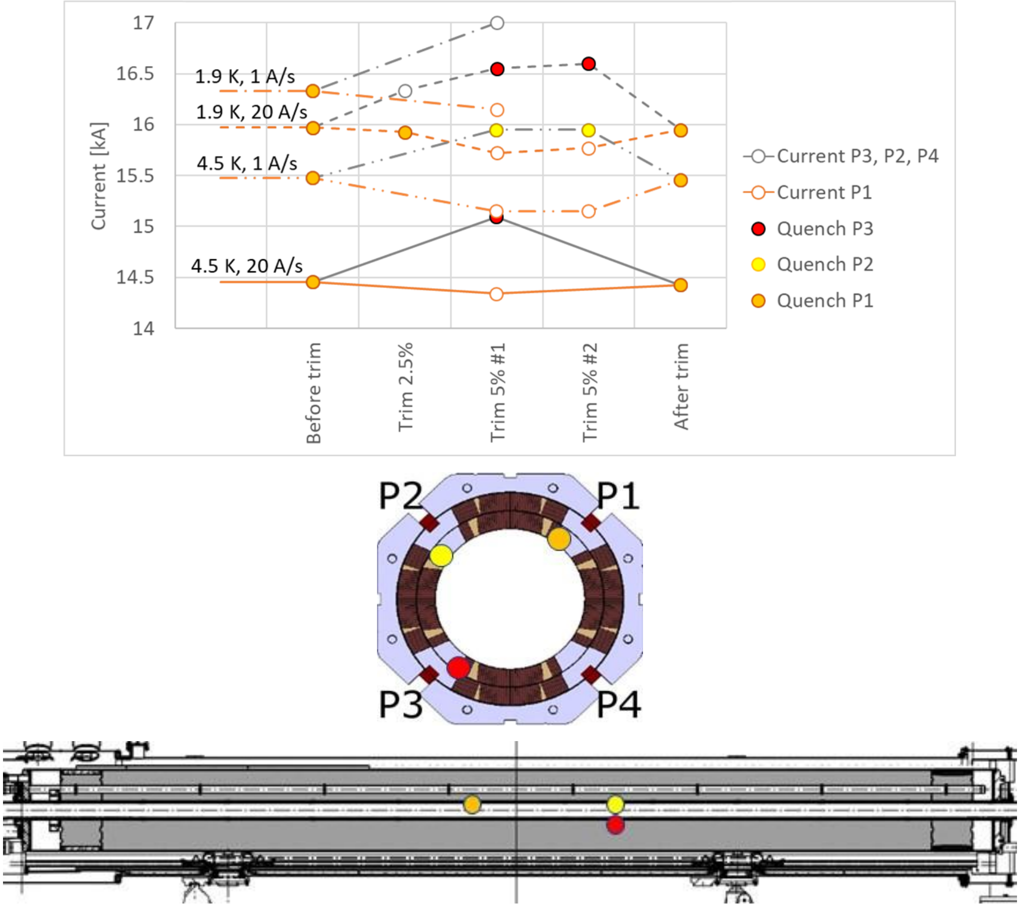

Figure 27: Summary of trim powering test results for 7.2-m-long HL-LHC MQXFBP2 quadrupole magnet prototype at CERN (in a temporary test cryostat). Top: quench current as a function of trim current for various ramp rates and test temperatures; middle: quench localization in 2D cross-section; bottom: quench localization along magnet length (Courtesy of F. Mangiarotti, CERN).

The above results provide an important information: the problem we are dealing with is not due to a singularity in one coil but has been observed on at least four coils (one in MQXFBP1 and three in MQXFBP2), with similar symptoms. Therefore, it seems systematic. As we will see in Section 5, the root cause of the limitation can be traced back to an issue related to coil manufacturing, which can be expected to happen in all coils produced with the same process.

2.2.3 3-D Quench Antenna

The idea of using an array of stationary pick-up coils to detect field perturbations caused by the occurrence of a quench and, thereby, to derive its spatial localization was first proposed and successfully demonstrated at CERN on a short LHC dipole magnet model in the early 1990s [146].

The quench antenna concept was readily adopted by the Superconducting Super Collider Laboratory (SSCL), located in Dallas, TX [147], which, instead of simple radial or tangential coils, proposed to rely on Morgan coils [148], which are sensitive to multipole components of the main field (*e.g.*, normal and skew quadrupole and sextupole components in the case of a dipole magnet). Indeed, to extract the signals relevant to quench initiation and localization, one needs to eliminate (in the jargon of magnetic measurements: to *buck out*) the field distortions caused by environmental noise or ripples of the magnet power supply. In a system with radial or tangential coils, this is done by subtracting the signals from two coils of the same geometry, which, in normal conditions, are expected to pick-up the same fluxes and flux changes (*e.g.*, two longitudinally adjacent coils in the magnet straight section). However, such coils are never identical, and the bucking cannot be perfect. When relying on Morgan coils and looking at multipole components of the main field, the noise effects are already strongly attenuated, giving direct access to quench-relevant information.

The aforementioned design was first validated on 50-mm-aperture, 15-m-long SSC dipole magnet prototypes [147] and was then adapted to quadrupole magnets for the Relativistic Heavy Ion Collider (RHIC) at BNL [149]. For a quadrupole magnet, the preferred geometry are coils sensitive to the sextupole and octupole field components. A similar design was later used for an LHC arc quadrupole magnet prototype built and tested at CEA/Saclay [150].

In the early 2010s, FNAL promoted the use of Printed Circuit Boards (PCBs) to replace the hand-wound coils that were used at the time for magnetic measurement probes, offering a significant simplification in manufacturing while still achieving the required tolerances for precise field measurements [151]. This technique was also applied for the quench antenna array that was developed by FNAL for MQXFA quadrupole magnets tested vertically at BNL [152]. PCBs offer a large freedom on how to design the coils and buck out the noise from the main components, but the coils still need to be segmented in the axial direction to achieve a good longitudinal quench localization.

In 2021, the need to derive accurate quench-start localization in MQXFB magnets offered CERN the opportunity to develop a quench antenna system based on a similar concept. The choice was made to rely on coils sensitive to normal and skew sextupole and octupole components. As illustrated in Figure 28, the CERN system comprises a chain of 600-mm-long elements that are inserted into an anticroystat mounted in the bore of the magnet on its horizontal test bench. Each element is made up of a four-layer flexible PCB, wrapped around a G10 shaft. Efforts were also made to improve the signal-to-noise ratio of the amplifier cards used for data acquisition, enabling a gain of a factor 10. The new antenna system was first tried on 7.2-m-long MQXFBP3 quadrupole magnet prototype and yielded good results on the azimuthal localization, confirming that the limiting quenches at 4.5 K were originating in the inner-layer pole turn of one coil.

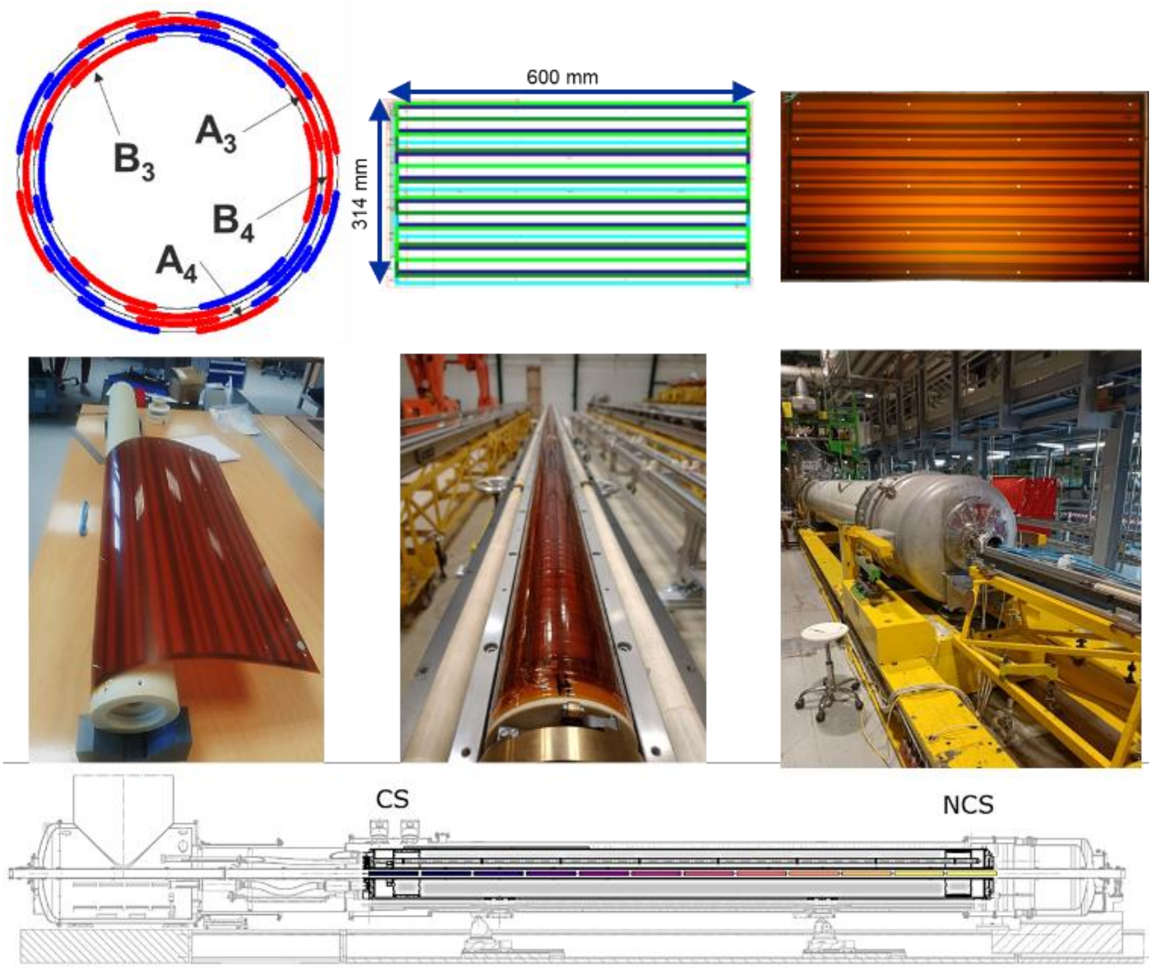

Figure 28: Quench antenna system developed for horizontal testing of 7.3-m-long HL-LHC MQXFB quadrupole magnets at CERN. Top Left and Center: layout of coils sensitive to normal and skew sextupole and octupole field components. Top Right: top view of PCB. Middle Left and Center: views of PCB coils before and after wrapping around shaft. Middle right: view of quench antenna inserted into the anticryostat mounted in magnet bore. Bottom: schematic the of quench-antenna array in longitudinal direction (Courtesy of L. Fiscarelli and P. Rogacki, CERN).

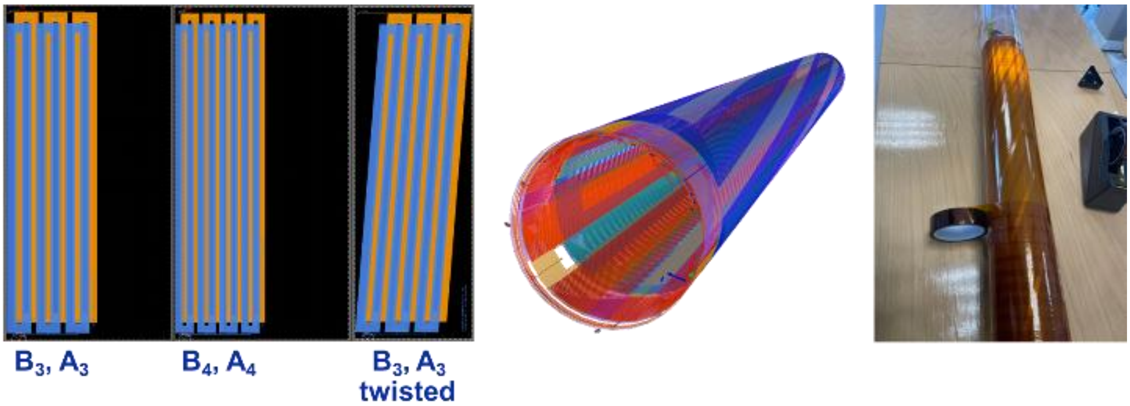

Figure 29: Conceptual design of quench antenna with a two-layer PCB with helically twisted coils wrapped on top of regular four-layer PCB with straight coils (Courtesy of L. Fiscarelli and P. Rogacki, CERN).

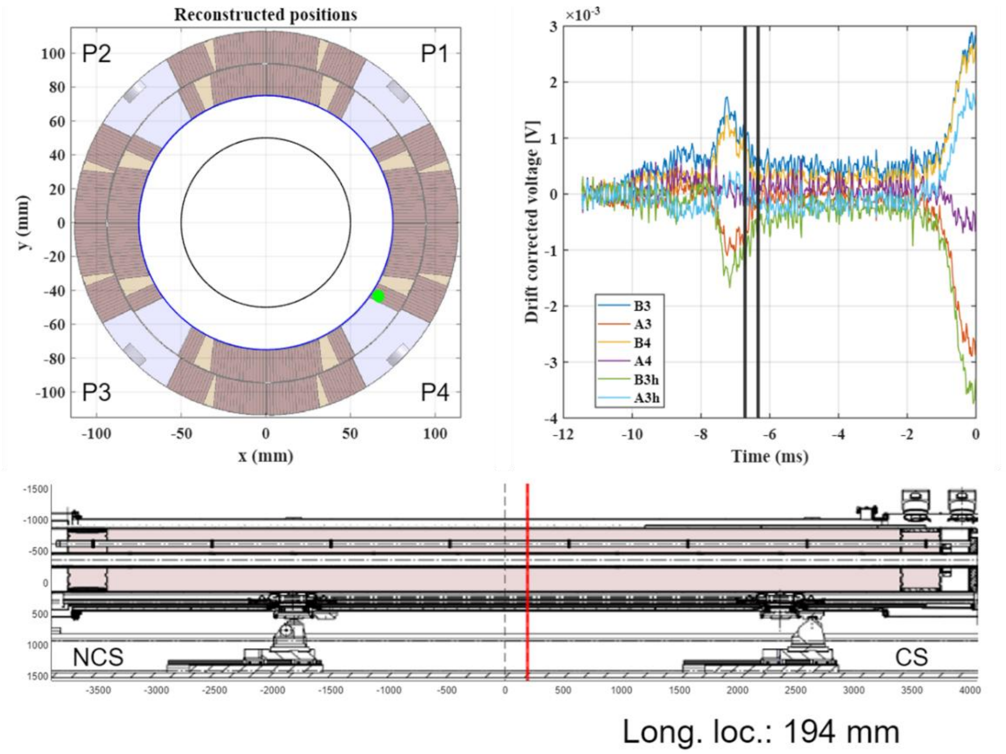

Figure 30: Results from quench antenna system with additional 2-layer PCB with helically twisted coils during the test of the 1st HL-LHC Q2 assembly at CERN, integrating the MQXFBP3 cold mass. Top left: azimuthal localization in 2D cross-section. Top right: signals from straight coils compared with signals from twisted coils. Bottom: longitudinal localization (Courtesy of L. Fiscarelli and P. Rogacki, CERN).

A subsequent innovation was introduced in 2023 to improve the longitudinal localization within the coil array of each quench antenna element. The idea was, on top of the regular 4-layer PCB with straight coils, to integrate another PCB with two helically twisted coils with a well-defined twist angle (see Figure 29). Then, by comparing the phase shift between the voltage signals recorded from the straight and twisted coils, it is possible to extract a more precise information on the longitudinal localization. This innovation was validated during the test of the first HL-LHC Q2 assembly at CERN, which included the MQXFBP3 cold mass that had been previously tested in a temporary configuration (see Figure 30). The data from the twisted coils confirmed the localization towards the longitudinal center of the magnet with an accuracy of ± 1 cm. The system can also be used to observe the development and propagation of flux jumps during current ramps [153].

Having an accurate estimate of the quench-start localization, both azimuthally and longitudinally, is instrumental for root-cause analyses, in particular, to determine the volumes of interest to be subjected to postmortem examinations (see Section 3.3). Also, in the model and prototype phases of a magnet development program, the magnet coils are usually instrumented with numerous voltage taps, but the number of taps is greatly reduced in series magnets. Then, quench antenna systems like the ones described above are the only available tools enabling non-intrusive quench start analysis.

So far, the quench antenna concept has mainly been used for $\cos\theta$ and $\cos2\theta$ magnets and for Canted-Cosine-Theta (CCT) dipole magnets [154]. It can also be applied to other types of magnet configurations, such as block-coil or common-coil magnets, and possibly, to iron-dominated (so called *superferric*) magnets as well. Of course, the type, shape and position of the pick-up coils need to be customized and may require integration into the magnet structure. However, the use of PCBs makes them cost effective and their implementation into a magnet's structure is not expected to be more difficult than that of quench protection heaters.

2.3 Electrical Tests and Ancillaries

2.3.1 Introduction

2.3.1.1 Electrical Design Considerations

Accelerator magnets are usually mounted in a string of magnets that are connected electrically in series [75]. In case of a quench in one of the magnets, significant voltages may develop in the circuit and thereby, each individual magnet should be designed, qualified and tested to ensure it can withstand such voltages with enough safety margin.

Good engineering practice calls for designing electrical components according to the voltages they are expected to withstand during operation [155]. Magnet insulation should be designed according to the worst conditions that can be encountered, with suitable margins, and electrical test requirements should be defined accordingly. Of course, electrical tests should be carried out at the various stages of the magnet life cycle, to detect, and possibly correct, issues during manufacturing and assembly, and to monitor the evolution of the magnet insulation during operation and, eventually, identify early signs of degradation. On the other hand, the test requirements should be based on realistic scenarios to avoid excessive and repeated overstress of the insulation. Defining pragmatic testing conditions is key to the process and requires the understanding of both the design of components and of their operational aspects.

Usually, insulation materials used in superconducting magnets operated at cryogenic conditions display high dielectric strength, *e.g.*, polyimides can sustain voltages in excess of 200 kV/mm at both room and liquid nitrogen temperatures [156]. Liquid helium has also a high voltage breakdown: 40-50 kV/mm at 4.2 K and 1 bar [157]. However, as any other liquid dielectric, the voltage withstand is highly affected by the formation of bubbles and the presence of gaseous phases. This requires a very cautious approach and the consideration of the so-called *Paschen law*.

2.3.1.2 Breakdown Voltage and Paschen Law

For an ideal gas at a pressure, P, and temperature, T, the breakdown voltage, V_B, between two surfaces separated by a distance, d, can be expressed as [158][159][160]

$$V_\mathrm{B} = \frac{BPd}{\ln[APd\,] - \ln\left[\ln\left(1+\frac{1}{\gamma}\right)\right]} \quad , \tag{1}$$

where A and B are two parameters related to the first Townsend coefficient, α, which characterizes the ionization rate of the gas, and γ is the second Townsend coefficient, which characterizes the secondary electron emission rate of the cathode. Equation (1) is referred to as *Paschen Law*, and is named after W. Paschen, who was first to study this phenomenon in the late 1800s [161].

Taking the derivative of the function $V_\mathrm{B} = f(Pd)$ in Eq. (1) shows that it goes through a minimum for $(Pd)_\mathrm{min}$ given by

$$(Pd)_\mathrm{min} = \frac{\mathrm{e}}{A} \ln\left(1 + \frac{1}{\gamma}\right) \quad . \tag{2}$$

The value of this minimum, $V_\mathrm{B,min}$, is

$$V_\mathrm{B,min} = \frac{B\,\mathrm{e}}{A} \ln\left(1 + \frac{1}{\gamma}\right) \quad . \tag{3}$$

Equation (3) shows that, for a given gas and cathode, $V_\mathrm{B,min}$ is constant. It is referred to as the *minimum Pashen breakdown voltage.*

Table 3: Minimum Paschen breakdown voltages and corresponding (pressure x electrode gap) parameters for selected gases at room temperature (293 K).

Gas	Minimum Paschen Breakdown Voltage $V_{B,min}$ (V)	Pressure x Electrode Gap @Minimum $(Pd)_{min}$ (mbar.mm)	Reference
Air	330	9	Fit of measured data in Fig. 31[a]
Argon	165	20	[155]
Helium	150	60	Fit of measured data in Fig. 31[a]
Neon	245	53	[158]
Nitrogen	275	10	Fit of measured data in Fig. 31[a]

[a] In agreement with values provided in Refs. [155] and [158].

Combining Eqs. (1), (2) and (3) yield

$$V_B = \frac{\frac{Pd}{(Pd)_{\min}}}{1+\ln\left[\frac{Pd}{(Pd)_{\min}}\right]} V_{B,\min} \quad , \tag{4}$$

which provides a simple formulation of the Pashen law as a function of the $(Pd)_{min}$ and $V_{B,min}$ parameters.

Table 3 presents typical values of $(Pd)_{min}$ and $V_{B,min}$ for selected gases at room temperate while Figure 31 presents plots of V_B versus (Pd) for air, helium and nitrogen gas, also at room temperature. The measured data for air come from [162], those for helium, from [163] and those for nitrogen from [164]. The fits are computed using Eq. (4) and the parameter values from Table 3.

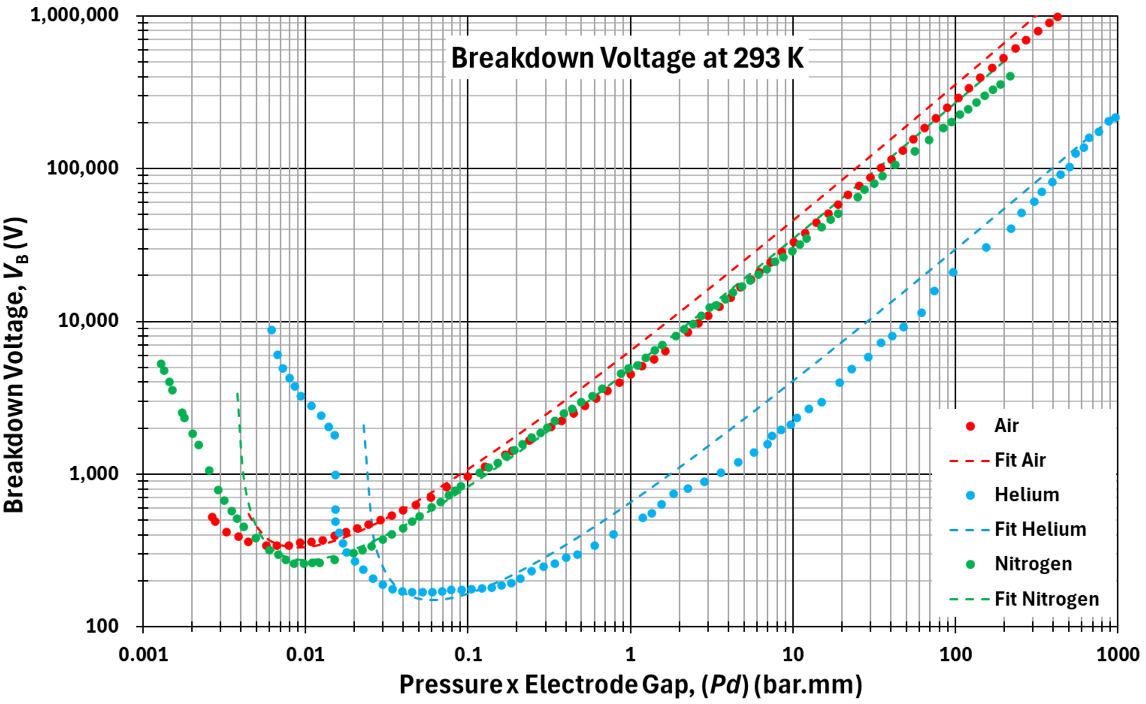

Figure 31: Breakdown voltage as a function of (pressure x electrode gap) for selected gases at room temperature. The points correspond to measurements from the literature, while the dashed lines correspond to fits derived from Eq. (4) and the parameters of **Table 3** (Measurements points are courtesy of D. Polvani and R. Piccin, CERN).

There are deviations between measured data points and fits (in particular, the computed values tend to be overestimated with respect to the measurements), but the general trends are more or less correct. More accurate data fits can be derived for practical applications with the caveat that they rely on parameters with no direct physical meaning. The curves of Figure 31 are referred to as *Paschen curves*. The Paschen curves of air and nitrogen gas are very similar, while that of helium gas is significantly lower.

The first and second Towsend coefficients can be theoretically derived. In the case of an ideal gas, α can be expressed as [159]

$$\alpha = AP\exp\left[-\frac{BPd}{V}\right] \quad , \tag{5}$$

where V is the voltage, and the A and B parameters are the same as those in Eq. (1) and are inversely proportional to the gas temperature.

Let A_0 and B_0 designate the value of A and B at a temperature T_0. Then, at a temperature, T, we can write [160]

$$A(T) = A_0\frac{T_0}{T} \quad , \tag{6a}$$

and

$$B(T) = B_0\frac{T_0}{T} \quad . \tag{6b}$$

The expression of γ is not as straightforward. It depends on the cathode's material and on the sheath of adsorbed gas on its surface. It is higher for dielectric materials than for metals and is not strongly affected by temperature [165]. For our type of applications, it is usually assumed to be constant.

Let γ_0 designate the value of γ at T_0. Combining Eqs. (2), (3), (6a) and (b), shows that $(Pd)_{\min}$ and $V_{\mathrm{B,min}}$ at T can be expressed as a function of $(Pd)_{\min,0}$ and $V_{\mathrm{B,min,0}}$ at T_0

$$(Pd)_{\min} = (Pd)_{\min,0}\frac{T}{T_0} \quad , \tag{7}$$

and

$$V_{\mathrm{B,min}} = V_{\mathrm{B,min,0}} \quad , \tag{8}$$

Equation (8) shows the minimum Paschen breakdown voltage of a gas does not depend on temperature while Eq.(7) shows that the main effect of the temperature on the Paschen curve is a displacement of its minimum.

Figure 32 displays the Paschen curves of helium computed at different temperatures using Eqs. (4), (7) and (8), and the values of $(Pd)_{\min,0}$ and $V_{\mathrm{B,min,0}}$ at room temperature given in Table 3. For (Pd) values above 0.1 bar.mm, the helium breakdown voltage appears to increase as a function of temperature, but still remains below that of air at room temperature.

When developing the high voltage test requirements for HL-LHC Nb_3Sn magnets, it was decided to consider a gap of ~0.5 mm as representative of the turn-to-turn, layer-to-layer and turn-to-quench-heater distances [166]. The green vertical line in Figure 32 illustrates the breakdown voltages corresponding to a pressure of 1 bar and a gap of 0.5 mm and can help getting a feel for the voltage withstand requirements that will be described in Section 2.3.2.

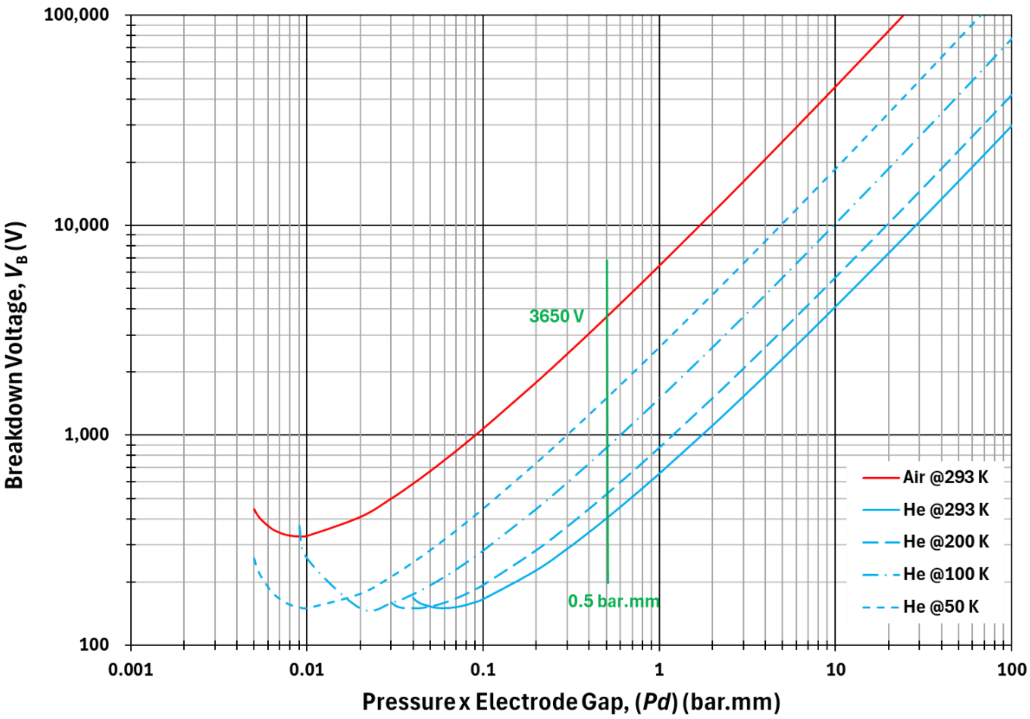

Figure 32: Computed breakdown voltage as a function of (pressure x electrode gap) parameter for air at room temperature and helium at different temperatures. The computation is carried out using Eqs. (4), (7) and (8), and the values of $(Pd)_{\mathrm{min},0}$ and $V_{\mathrm{B,min},0}$ at room temperature given in **Table 3**.

2.3.1.3 Electrical Design and Test Issues for Nb_3Sn HL-LHC Magnets

Given the above considerations, for a superconducting magnet, the most severe condition regarding voltage withstands, occurs during a quench, when significant voltages are generated in the coils, and the heat generated during the event causes a temperature increase of the surrounding helium.

In the case of resin-impregnated magnets like those for HL-LHC, and as discussed in Section 3.5, the problem is further complicated by the fact that thermal contraction differentials result in resin cracks and delamination, which open creep paths where superfluid helium can penetrate. The presence of superfluid helium within a resin-impregnated coil sample was first observed during measurements carried out on a conductor block extracted from a short 11 T dipole magnet coil to assess its transient heat transfer characteristics [167]. This entrapped helium improves cooling. However, in case of a quench, gas helium bubbles and, eventually, warm helium gas pockets are generated. The dimension of these pockets and the local helium pressure are difficult to assess but may lead to internal voltage breakdowns. Furthermore, the pressure rise can enlarge the cracks and result in additional degradation.

Last but not least, once a resin-impregnated coil has been exposed to liquid or superfluid helium, and it is warmed up to room temperature and reopened to air, the gaseous helium that is entrapped in the resin cracks and delamination, may stay entrapped. As a result, the voltage breakdown characteristics of the coil at this stage may end up being determined by the entrapped helium and not by the surrounding air.

The HL-LHC development magnet programs for the 11 T dipole magnets at CERN, and the MQXF quadrupole magnets at LARP/AUP and at CERN have all experienced serious electrical issues, which have required dedicated root-cause analyses. We will not go into the details of all the problems that were encountered and of the recovery/preventive actions that were developed to address them, but we will focus on some key aspects that may be of some use for other projects.

Our selection of topics include:

- the methodology that was followed to establish the electrical test requirements;
- the measurement techniques that are employed for quality control measurements;
- the improvements that were made to enhance quench heater robustness.

Let us stress that electrical withstand levels must be considered from the design phase of a superconducting magnet or of a superconducting system and that it should be treated with the same level of priority as mechanical design, quench protection and field quality (which is rarely the case).

2.3.2 Electrical Test Requirements

2.3.2.1 Metallic Components and Insulation Classification

The metallic parts used in superconducting accelerator magnets can be classified into 3 main categories:

- active parts, which are connected to two different electrical circuits: the coil circuit, made up of the coil windings and of the busbars/current leads and the voltage taps electrically connected to them, and the quench protection heater circuit, made up of the metallic traces of the quench heaters and of the current leads supplying them; quench protection heaters are described in detail in Section 2.3.4, they are mounted on top of the coils but positioned underneath the ground insulation;
- floating parts, which are metallic components within the ground insulation envelope, and which are usually left electrically floating, *e.g.*, for 11 T dipole magnets: copper wedges, Ti-alloy pole pieces, stainless-steel loading plates, stainless-steel winding keys and end spacers; the situation is more complex for MQXFA&B where the Ti-alloy pole pieces are impregnated with the coils;
- external parts, which are metallic components outside the ground insulation envelope, and which are part of the mechanical structure (*e.g.*, for 11 T dipole magnets: stainless-steel collars, low-carbon-steel yoke, stainless-steel outer shell and end plates) or which are part of the He containment vessel and the cryostat; these are electrically connected to the ground.

Also included in the external parts are the capillary tubes and feedthroughs, which are used to route voltage tap wires and quench heater current leads and enable their electrical connections to the outside world at the level of the cold mass (helium containment vessel) and of the cryostat (thermal insulation vacuum).

The various types of insulation used in superconducting accelerator magnets can be classified into five main categories:

- conductor insulation, made up of mica and/or fiberglass braid impregnated with epoxy resin; the mica or braid are applied before coil winding and must sustain the reaction heat treatment (see Section 5.5.2); the resin is applied by impregnation of the heat treated coil (see Section 5.5.6);
- interlayer insulation, made up of fiberglass cloths impregnated with epoxy resin; the fiberglass cloths are mounted on top of the inner-layer winding, and must sustain the reaction heat treatment (see Section 5.5.4); the resin is applied by the same impregnation process as above;
- quench protection heater insulation: the metallic traces of the quench heaters need to be electrically insulated from both coils and ground; as described thereafter, the quench-heater-to-coil insulation has been the source of numerous problems in HL-LHC Nb_3Sn magnets;
- ground insulation, that surrounds the coils and quench protection heaters, and which provides electrical insulation towards the ground potential, *e.g.*: the 11 T coil assemblies are surrounded by five layers of 0.1-mm polyimide foils;

The ground insulation also includes the insulation of the wires and of the feedthrough pins electrically connected to active parts; the insulation of the wires inside the capillaries and of the pins in the feedthroughs must withstand the same voltage requirements as the coils or quench heaters; they have been the cause of various issues in HL-LHC Nb_3Sn magnets (see Section 2.3.5).

- coating of floating parts, *e.g.*, plasma spray of Al_2O_3 on coil end spacers and saddles in MQXF magnets [274].

Each of these insulation categories have specific technical requirements, which need to be qualified in the development phase and quality-control tested during production.

2.3.2.2 *Electrical Test Conditions*

Five different electrical test conditions are considered throughout the magnet life cycle [168][169]:

(1) at room temperature in air before exposure to helium (environmental test conditions defined as 20 ± 3 °C and humidity lower than 60%);

(2) in so-called *normal operating conditions (NOC)* for magnet acceptance on horizontal test bench, corresponding to 1.9 K superfluid helium in the cold mass with all ancillary components (capillary tubes and feedthroughs) connected;

(3) at gaseous helium temperature (GHe), representative of the conditions occurring at the time of peak voltage during a quench, as determined from numerical simulations;

(4) at room temperature in air after helium exposure (same environmental test conditions as in (1));

(5) at NOC after magnet acceptance and tunnel installation.

2.3.2.3 *Voltage Withstand Test Criterions*

In the case of NOC for magnet acceptance on a test bench prior to installation, the test voltage, $V_{\text{test},2}$, is defined as

$$V_{\text{test},2} = 2\,V_{\text{sim}} + V_0 \quad , \tag{8}$$

where V_{sim} is the peak voltage derived from numerical simulations for the so-called *worst-case failure scenario* during magnet operation in the tunnel and V_0 is a constant voltage offset.

A criterion such as Eq. (8) is commonly used for electrical AC voltage tests on rotating electrical apparatus, with a recommended value of 1 kV for V_0 (see for instance [170]). Both SSC [171] and ITER [172] projects use the criterion provided by Eq. (8) with $V_0 = 1$ kV. However, for LHC, which include numerous low-voltage circuits where V_{sim} is in the 60–120 V range, it was decided to reduce the value of V_0 to 500 V [173]. As the LHC operation since 2008 did not reveal any issue with this choice, it was decided to keep the same constant offset of 500 V as well for the HL-LHC.

Once the magnets have been cold tested and accepted and they have been lowered and installed in the tunnel, the test voltage at NOC, $V_{\text{test},5}$, is taken as

$$V_{\text{test},5} = 1.2\,V_{\text{sim}} \quad . \tag{9}$$

A reduction of electrical test voltage on a component that has been thoroughly tested during and after manufacturing, and which has passed the initial acceptance test at nominal operating conditions, is common practice (and usually recommended by the standards for maintenance). The choice of a 20% margin has been made to reduce the risk of overstressing the insulation at a time when it becomes cumbersome and costly to replace a magnet in the tunnel. The 1.2 factor should nevertheless still be sufficient to detect faults that are critical for a safe operation of the machine.

For the tests at room temperature before helium exposure, the test voltage, $V_{\text{test,1}}$, is defined as

$$V_{\text{test,1}} = c\, V_{\text{test,2}} = 2\, c\, V_{\text{sim}} + \text{c}\, V_0 \quad , \tag{10}$$

where c is a scaling factor.

When looking at the curves in Figure 32, it appears that the Paschen curve of dry air at room temperature is 5 to 10 times higher than the Paschen curve of gaseous helium at room temperature and 2 to 3 times higher that Pashen curve of gaseous helium at 50 K. For some applications at CERN, like High Temperature Superconductor (HTS) leads for the LHC and the HL-LHC superconducting link, it has been decided to take $c = 5$ [174]. For HL-LHC magnets, and after discussions with all stakeholders, it has been decided to settle for $c = 2$ so as to limit the test voltage level to moderate values that can be managed in a production workshop [168][169].

Once the magnet has been exposed to helium, and as explained above, there is a risk that gaseous helium remains entrapped in the coils, causing a severe reduction of the voltage breakdown with respect to dry air. As a result, for the tests at room temperature after helium exposure, the test voltage, $V_{\text{test,4}}$, is defined as

$$V_{\text{test,4}} = \frac{1}{10}\, V_{\text{test,1}} = \frac{2\, c\, V_{\text{sim}} + c\, V_0}{10} \quad . \tag{11}$$

The factor of 10 reduction with respect to $V_{\text{test,1}}$ is justified by the aforementioned scale factor between the Paschen curves of dry air and gaseous helium at room temperature (see Figure 32). A similar scale factor was applied to the dipole magnets for the HERA particle accelerator that was operated from 1992 to 2007 at the German Electron Synchrotron (DESY), in Hamburg, Germany [175] and to LHC magnets [173].

The test in gaseous helium intends to qualify the magnet on the test stations at conditions expected to be more representative of those of a quench (although electrical and cryogenic phenomena may occur at different time scales). This test is performed after the magnet has been immersed in superfluid helium, during warm-up, to ensure that only gaseous helium is present, including inside possible insulation pockets. The temperature, T_{sim}, and pressure, P_{sim}, conditions are determined by numerical simulations and need to be kept stable (within specified margins) during the test performance. The test voltage, $V_{\text{test,3}}$, is taken equal to

$$V_{\text{test,3}} = 1.2\, V_{\text{sim}} \qquad \text{at } T_{\text{sim}} \text{ and } P_{\text{sim}} \quad . \tag{12}$$

As for Eq. (9), a 20% margin has been deemed suitable for HL-LHC magnets.

2.3.2.4 Worst Case Scenario for 11 T

For 11 T magnets, the worst-case scenario was analyzed, considering the spread of Residual Resistivity Ratios (RRR) and copper-to-non-copper (Cu-to-non-Cu) ratios measured on the series production magnets and considering a single quench heater failure, at the worst location, out of the 16 quench heater circuits. The quench detection threshold was set to 100 mV, and the heaters were activated after 17 ms (5 ms until quench detection, 10 ms validation time, and 2 ms triggering of quench heater discharge). The results of the simulations for nominal and ultimate currents are presented in Table 4 [168].

In addition, for 11 T magnets, a voltage offset of 430 V at nominal current (466V at ultimate current) need to be considered [168]. As already explained, for tunnel operation, the 11 T dipole magnets are connected in series within one of the eight LHC dipole magnet circuits. In case of a quench, the dipole magnets are discharged over two dump resistors. This offset corresponds to the peak voltage generated by the current discharge over the dump resistors.

Table 4: Peak voltages to ground and hot spot temperatures derived from numerical simulations for 5.3-m-long, 60-mm-two-in-one-aperture, HL-LHC 11 T dipole magnet assembly at nominal protection condition and for the worst case scenario of one quench heater failure [168].

11 T	**No Failure**		**Single Quench Heater Failure**	
Operating Conditions	Nominal	Ultimate	Nominal	Ultimate
Current (kA)	11.85	12.84	11.85	12.84
Hot Spot Temperature (K)	333	358	341	365
Peak Voltage to Ground (V)	305	450	664	797

Table 5: Peak voltages to ground and hot spot temperatures derived from numerical simulations for 7.2-m-long, 150-mm-aperture, HL-LHC MQXFB quadrupole magnet assembly at nominal protection condition and for the worst case scenario of a double failure (one quench heater and one CLIQ failure or two quench heaters) [169].

MQXFB	**No Failure**		**Worst Case Scenario**[a]	
Operating Conditions	Nominal	Ultimate	Nominal	Ultimate
Current (kA)	16.23	17.5	16.23	17.5
Hot Spot Temperature (K)	231	253	375	404
Peak Voltage to Ground (V)	606	776	660	850

[a] 1 QH and 1 CLIQ circuit failure, or 2 QH failures.

In practice, there will be a delay on the energy extraction which should avoid it being activated when the magnet develops its peak nominal voltage, but, to be conservative, it has been decided that, for the determination of V_{sim}, this offset should be added to the peak voltages of Table 4, except for the test in gaseous helium. At nominal current, we therefore get

$$V_{\text{sim,11 T}} = 670 + 430 = 1100\ \text{V} \quad . \tag{13}$$

Let us note that, in a scenario where the quench starts in another magnet of the cell, the resulting voltage-to-ground on the 11T dipole magnet may be higher than if this magnet is first to quench. This scenario has not been analyzed.

2.3.2.5 Worst Case Scenario for MQXF

As already explained in Section 2.2.2, the MQXF magnets rely on two protection systems: quench heaters and CLIQ. Two types of worst-case scenarios have considered in the analysis, which both correspond to a double failure: (1) a failure of one CLIQ circuit, with a failure of one quench heater power supply and (2) a failure of two quench heater power supplies. The analysis also considers conductor parameters varying within the expected tolerances given in Table 1. The results of the simulations for MQXFB are provided in Table 5 and, at nominal current, we get

$$V_{\text{sim,MQXFB}} = 670\ \text{V} \quad . \tag{14}$$

Note that the peak voltage values for single MQXFA magnets are about half those of the longer MQXFB [169].

2.3.2.6 Worst Case Scenario for Quench Heaters

For the quench-heater-to-coil voltage, the worst-case scenario for both 11 T and MQXFB is assumed to correspond to the failure of the mid-point earthing fuse leading to the application of the full capacitor bank voltage between quench heaters and coils. As there are two capacitor banks in series, this gives

$$V_{\mathrm{sim,QH-to-coil}} = 2 \text{ x } 450 = 900 \text{ V} \quad . \tag{15}$$

Once again, for 11 T, one needs to add 430 V to Eq. (15) to take into account energy extraction activation, which yields to a total of 1330 V.

2.3.2.7 Test Voltage Summary Tables

Based on the above considerations, Table 6 and Table 7 present summaries of the test voltage requirements for the electrical acceptance of 11 T dipole and MQXFB quadrupole magnets at CERN.

Once again, let us restate the importance of deriving and implementing a consistent set of test voltages, which enable detection of electrical faults at an early stage while avoiding the risk of overstressing and degrading the magnet electrical insulation. As there is no directly applicable standards, this should be done in a pragmatic manner, relying on the experience of other projects or comparable systems.

2.3.3 Electrical Quality Assurance (ELQA) and Fault Detection and Analysis

Being able to monitor the soundness of the electrical insulation of superconducting magnets, in particular when relying on Nb_3Sn technology, and to detect early signs of degradation, if any, is a key element of electrical quality assurance for accelerator operation. A lot of efforts have been deployed for LHC with the development and implementation of a comprehensive ELectrical Quality Assurance (ELQA) of the LHC superconducting circuits [176]. These efforts were further increased following the LHC incident on 19 September 2008 [177] with the automation of ELQA [178][179][180]. Since then, some new and innovative techniques have also been developed for HL-LHC magnets, such as magnet impedance measurement during a high current quench [181].

Another important task is the detection and localization of electrical faults, at every stage of the magnet life cycle: during production, cold test on a test bench, as well as after installation and during operation in the tunnel. In case of failure during a high voltage test, time domain reflectometry (TDR) has proven to be a very powerful method to identify the origin of the problem, in particular, along instrumentation wires and circuits [182]. This method is based on the principle that a signal propagating along a transmission line will be reflected at the locations where the impedance of the line changes, such as junctions and branches, but also at fault points or at abrupt cross-section changes. The amplitude, shape and polarity of the reflection indicates the nature and magnitude of the discontinuity. The delay between the transmitted pulse and received reflection indicates the distance of the discontinuity and, thereby, its location along the line. TDR has a wide range of applications but is particularly efficient and is being extensively used in the diagnostic of electrical faults on LHC and HL-LHC magnets (see examples provided in Section 2.3.5).

2.3.4 Quench Heaters

2.3.4.1 Introduction and Historical Background

The design of accelerator magnets usually calls for high current densities in the coils for minimizing the amount of superconductors [75][76]. As a result, in case of a quench, one must ensure that it develops quickly throughout the coils, to enable spreading the conductor volume over which the stored magnetic energy is dissipated, accelerate current discharge, and limit hot spot temperature. This is done by relying on a so-called *active quench protection system*, that is activated as soon as a quench is detected.

Table 6: Electrical test values for 5.3-m-long, 60-mm-two-in-one-aperture HL-LHC 11 T dipole magnets at CERN at various stages of the magnet life cycle [168].

11 T	**Test Conditions**	**Test Type**	**Test Voltage (V)**
(1) At room temperature in air prior to Helium exposure	20 ± 3 °C Humidity ≤ 60%	Coil to Ground[a] QH to Coil[b]	~~5400~~ 5000[c] ~~6320~~ 3160[d]
(2) At normal operating conditions in-superfluid Helium on test bench	1.9 K	Coil to Ground[a] QH to Coil[b]	2700 3160
(3) At gaseous Helium conditions	200 ± 20 K 3.0 ± 0.2 bars	Coil to Ground[a] QH to Coil[b]	800[e] 800[e]
(4) At room temperature in air after Helium exposure	20 ± 3 °C Humidity ≤ 60%	Coil to Ground[a] QH to Coil[b]	540 ~~632~~ 640
(5) At normal operating conditions in superfluid Helium in tunnel	1.9 K	Coil to Ground[a] QH to Coil[b]	~~1320~~ 2100[f] 1600
Maximum leakage current (not including test station): 30 µA			
Test voltage duration: 120 s			

[a] Coil connected to positive terminal, ground to negative terminal (QH grounded).
[b] QH to positive terminal, ground to negative terminal (coil grounded).
[c] Reduced from 5400 to 5000 V at the request of production team.
[d] Reduced from 6320 to 3160 V at the request of production team.
[e] Does not include additional 430 V from energy extraction activation.
[f] Increased from 1320 to 2100 V for compatibility with electrical test procedure in tunnel.

Table 7: Electrical test values for 7.2-m-long, 150-mm-aperture HL-LHC MQXFB quadrupole magnets at CERN at various stages of the magnet life cycle [169].

11 T	**Test Conditions**	**Test Type**	**Test Voltage (V)**
(1) At room temperature in air prior to Helium exposure	20 ± 3 °C Humidity ≤ 60%	Coil to Ground[a] QH to Coil[b]	3680 ~~4600~~ 3680[c]
(2) At normal operating conditions in-superfluid Helium on test bench	1.9 K	Coil to Ground[a] QH to Coil[b]	1840 2300
(3) At gaseous Helium conditions	200 ± 20 K 3.0 ± 0.2 bars	Coil to Ground[a] Coil & QH to Ground[d]	~~804~~ 850 ~~804~~ 850
(4) At room temperature in air after Helium exposure	20 ± 3 °C Humidity ≤ 60%	Coil to Ground[a] QH to Coil[b]	368 460
(5) At normal operating conditions in superfluid Helium in tunnel	1.9 K	Coil to Ground[a] QH to Coil[b]	804 1080
Maximum leakage current (not including test station): 10 µA			
Test voltage duration: 30 s			

[a] Coil connected to positive terminal, ground to negative terminal (QH grounded).
[b] QH to positive terminal, ground to negative terminal (coil grounded).
[c] Reduced from 4600 to 3680 V not to exceed coil-to-ground test voltage.
[d] Special configuration chosen to limit stress on insulation between coil and QH.

The most commonly used active systems rely on resistive heaters that are adjacent to the coils and are fired by means of capacitor banks. The quench heater efficiency was first demonstrated on dipole magnets for the Tevatron accelerator that was operated at FNAL between 1983 and 2011 [183][184]. They have been used on subsequent accelerator magnet projects, such as HERA [185], the SSC [186][187], and the LHC [140][188]. As explained in Section 2.2.2, they are also used in HL-LHC magnets, but in the case of MQXF, they are complemented by the CLIQ system [142][145].

The design and implementation of quench heaters raise several issues. To be efficient, one needs to limit the thermal diffusion time between quench heaters and coils, but, on the other hand, one needs a robust electrical insulation between the two with voltage withstand requirements which can be higher than for the coil-to-ground voltages (see Table 6 and Table 7). A compromise must be found between these conflicting requirements, which leads to the selection of an electrical insulation that can be marginal. As a result, and in spite of a lot of efforts in the development, qualification and quality control of quench heaters, they remain a risky item (hence the development of alternative protection systems such as CLIQ).

2.3.4.2 Quench Heater Design and Manufacture

The design of HL-LHC quench heaters is an evolution of the design of the LHC quench heaters [189] and utilizes the progress made in the development of Printed Circuit Boards (PCB) and photolithography [190]. As illustrated in the left side of Figure 33, the base material for the HL-LHC quench heaters is a commercially available laminate (GTS® laminate L960461), produced by GTS Flexible Materials Ltd, located in Rassau, United Kingdom [191], consisting of a 50-µm-thick polyimide film (Kaneka Apical AV) and a 25-µm-thick austenitic stainless-steel (304L) hard temper foil. The steel foil is glued onto the film with a 15-µm-thick epoxy adhesive (GTS® AS1084). The steel surface of the laminate is electrolytically coated with an approximately 10-µm-thick copper layer, using a dedicated coating line at the CERN PCB laboratory. The thickness of the quench heater (without coverlay) is comprised between 95 and 100 µm.

The production of the final traces is realized in two photolithographic steps:

- etching of electroplated copper by nitric acid to create heating stations at regular intervals on the stainless-steel foil (note that nitric acid has no impact on stainless steel;
- etching of metallic stack (electroplated copper and stainless-steel base) by ferric chloride to form the final quench heater traces on top of the polyimide foil.

After a final cleaning step, the quench heater is ready for use (see Figure 33). As detailed thereafter (see Sections 2.3.4.4 and 2.3.4.6), in the early stages of the 11 T and MQXFB programs, the quench heater traces, and electroplated copper were left exposed. Subsequently, it was decided in both programs to glue, on top of the metallic traces, a protection and insulating layer referred to as *coverlay*.

2.3.4.3 Quench Heater Quality Control

The base materials and finished products must be subjected to a tight quality control during and after production, that includes:

- control of the copper plating adhesion onto the stainless steel, and of the electroplated copper geometrical and electrical parameters;
- control of the polyimide foil dielectric strength and that it is devoid of pinholes, which, as illustrated in Figure 34, is a common risk for polyimide insulation (and one of the reasons why an overlap of two layers is often preferred to a single layer).

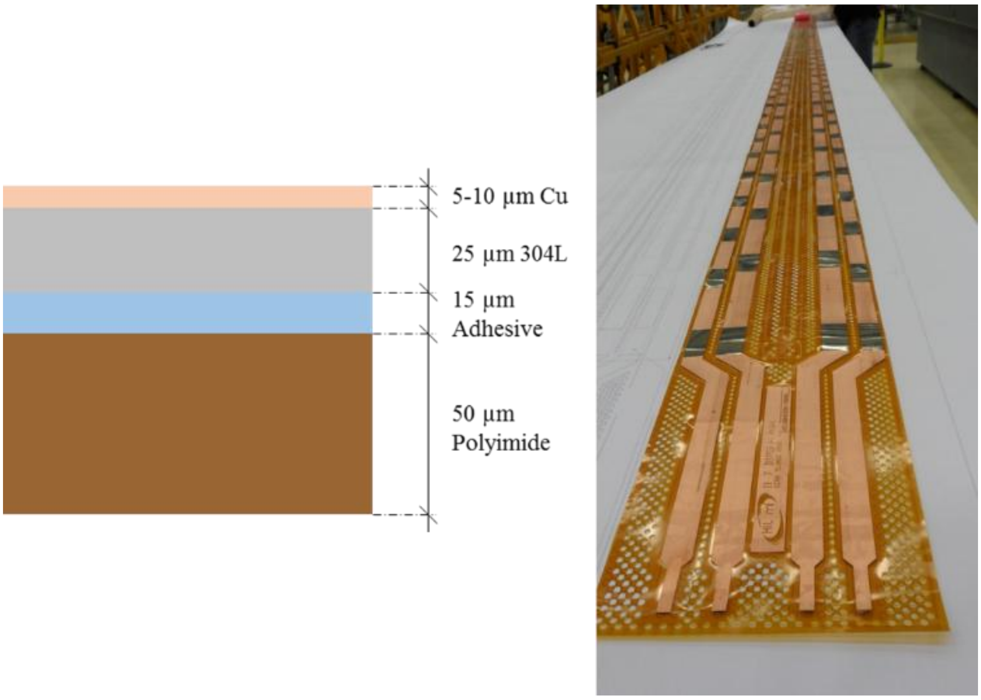

Figure 33: Design and layout of HL-LHC quench heaters. Left: schematic view of laminate structure showing the different layers and their nominal thicknesses. Right: overview of final quench heater after completion of the two photolithographic steps, showing the polyimide base and the copper-electroplated stainless-steel traces etched at regular intervals (Courtesy of C. Scheuerlein, CERN).

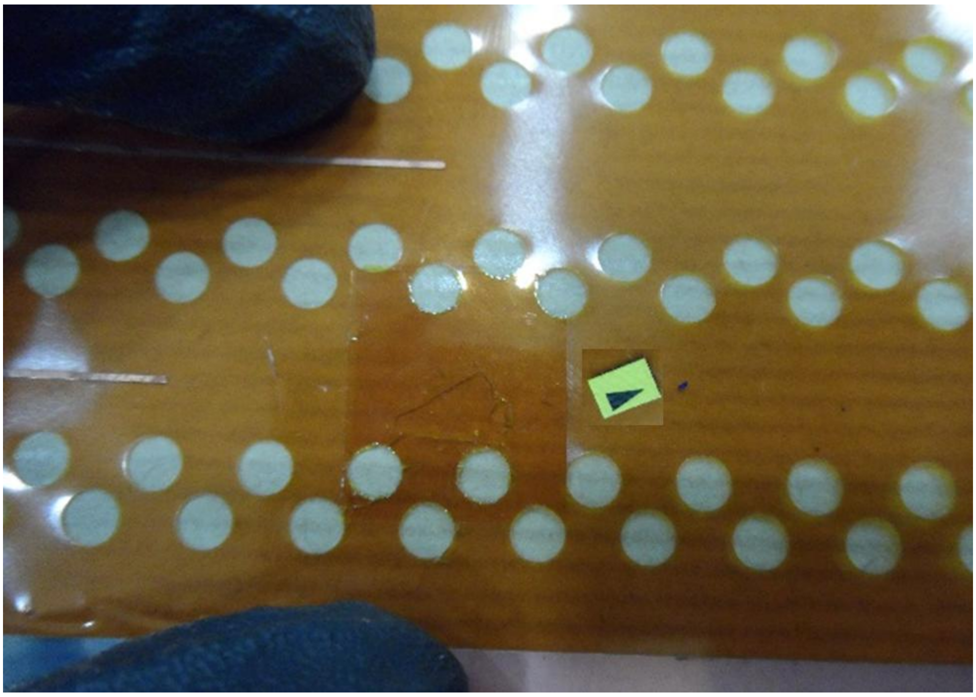

Figure 34: Example of pinhole detected in polyimide foil during high voltage acceptance test of a HL-LHC quench heater (Courtesy of C. Scheuerlein and F. Savary, CERN).

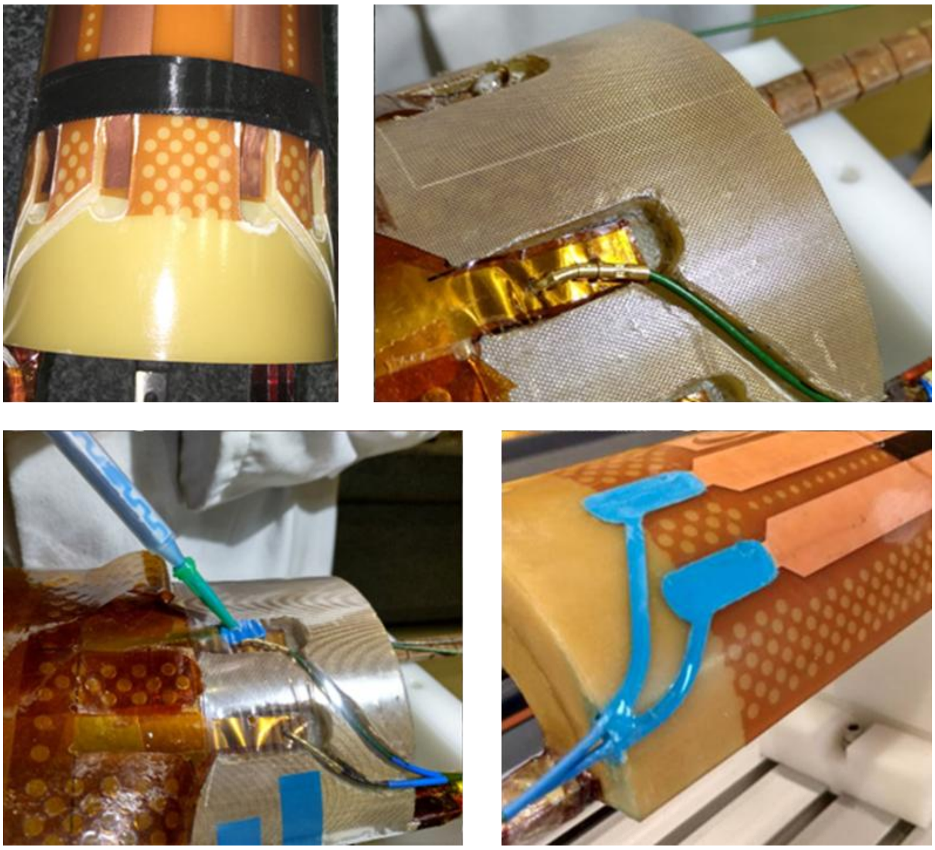

Figure 35: Illustration of the type of procedure that needs to be developed and qualified for electrical connection of current lead wires to quench heater traces. Top Left: housing of heater traces' terminals in cavities machined in G11 coil end saddle. Top right: mounting of connector pin and attachment to terminals. Bottom left: Ecobond® resin injection into terminal housing. Bottom right: finished connection (Courtesy of L. Grand Clément and F. Savary, CERN).

The pinhole check is done through high voltage tests. These tests can be carried out on the polyimide foil used in the laminates and upon acceptance of the final quench heaters.

For HL-LHC, the technical requirements for the tests on the quench heaters are: 4.2 kV DC for 2 min, with a maximum leakage current of 4.2 µA for 11 T dipole magnets, and, initially, 3.7 kV DC for 2 min, with a maximum leakage current of 3.7 µA for MQXFB quadrupole magnets (as explained in Section 2.3.4.6, the test values are now higher). The test is carried out at room temperature and under a small pressure applied on top of the heater (at the time of LHC, a pressure of ~20 MPa was applied using a cylinder rolled over the foil or quench heater as described in Ref. [189]). At the beginning of HL-LHC, it was deemed acceptable to proceed with the repair of small defects with self-adhesive polyimide tapes, but now, the detection of pinholes leads to a rejection of the foil or quench heater, as was the case for LHC.

One particularly critical point for the quench heater installation are the electrical connections at the trace terminals, which need to be mechanically robust and well insulated. Figure 35 illustrates salient steps of the procedure that was followed at the beginning of the 11 T dipole magnet program. In operation, the quench heaters are fired thanks to capacitor discharges and must be able to sustain repeated peak voltages of 900 V and peak currents of up to 150 A, while the current leads attached to their extremities are subjected to various loads during assembly and cooldown/warmup. Detailed engineering and qualification efforts are required in order to develop a suitable and industrial solution.

After this brief introduction let us now review the difficulties that were encountered on both 11 T and MQXF quench protection heaters and describe the solutions that were developed and implemented.

2.3.4.4 Quench Heater Externalization for 11 T Dipole Magnets

The quench protection heaters of the 11 T dipole magnets are mounted over the outer surface of the coil, with the polyimide base facing the coil. For the first short model coils (SD101 to SD109, and SD111 to SD113), the heaters were installed after resin impregnation. For subsequent short and long coils, the heaters were installed after heat treatment completion and impregnated together with the coils, as for MQXF coils. In the latter configuration, the insulation between outer-layer conductors and stainless strips comprises the cable insulation (~0.105 mm under 5 MPa) and the 50-µm-thick polyimide foil at the heater base (~155 µm in total). Although 50 µm of polyimide is expected to ensure a voltage withstand of at least 10 kV at both room and cryogenic temperatures [156], a number of insulation failures between quench heaters and coils were experienced in the course of the 11 T program, most notably on full-length series magnet S2 after ~80 quench heater firings.

As will be presented in detail in Section 3.5, but can also be observed in Figure 36, metallographic observations of magnet coils show that the impregnated fiberglass surrounding the cables cracks and delaminates and, thereby, does not reliably contribute to electrical insulation. As a result, the coil-to-quench-heater insulation only relies on the single polyimide foil, which can present some local defects, such as small thickness variation (see Figure 37), delamination from stainless-steel strip (see Figure 36) or pinholes that may have been missed by QC.

In addition, and as has been observed on MQXFA coils (see Section 2.3.4.5), cracks that develop and propagate in the resin may cause blistering of the polyimide foil, leading to failure. And last but not least, high pot tests carried out on coils disassembled from the 11 T prototype have confirmed the potential risk of generating a direct short between coil and quench protection heaters through a local weak spot as illustrated in Figure 38.

The number of electrical test failures and the aforementioned observations led to the assessment that the coil-to-quench-heater insulation was not robust enough and needed to be increased. Also, it was noted that the fact that the quench heaters are impregnated with the coils prevents any repair and that, in case of problem, the whole coil must be replaced. In comparison, for LHC magnets, it is possible to replace faulty quench heaters and reuse the coil if it has not been damaged.

Based on these considerations, a proposal was developed to externalize the quench protection heaters and to install them on the coil after resin impregnation. The full proposal includes adding a fresh layer of fiberglass tissue on top of the coil outer surface after heat treatment completion, to protect the coil in the impregnation mold, and, since this additional fiberglass layer is fresh and has not been degraded by the heat treatment, to increase the electrical insulation. It also includes adding a polyimide coverlay that is glued on the exposed surface of the quench heater on the electroplated copper side for mechanical protection.

In this new configuration, the insulation between outer-layer conductors and stainless strips comprises the cable insulation (~0.105 mm under 5 MPa), the fresh fiberglass layer (~0.060 mm) and the 50-µm-thick polyimide foil (~215 µm in total). The quench-heater-to-coil insulation dielectric strength was estimated to increase from 10.90 to 11.50 kV, while the hot spot temperature increases by about ~30 K for all scenarios: up to 350 K for a quench at nominal current, 357 K for a quench at nominal current with one quench heater failure, and 363 K for a quench at nominal current with two quench heater failures (note that the hot spot temperatures considered here for the original design are somewhat lower than those given in Table 6 which were derived at an earlier stage with more conservative assumptions) [192].

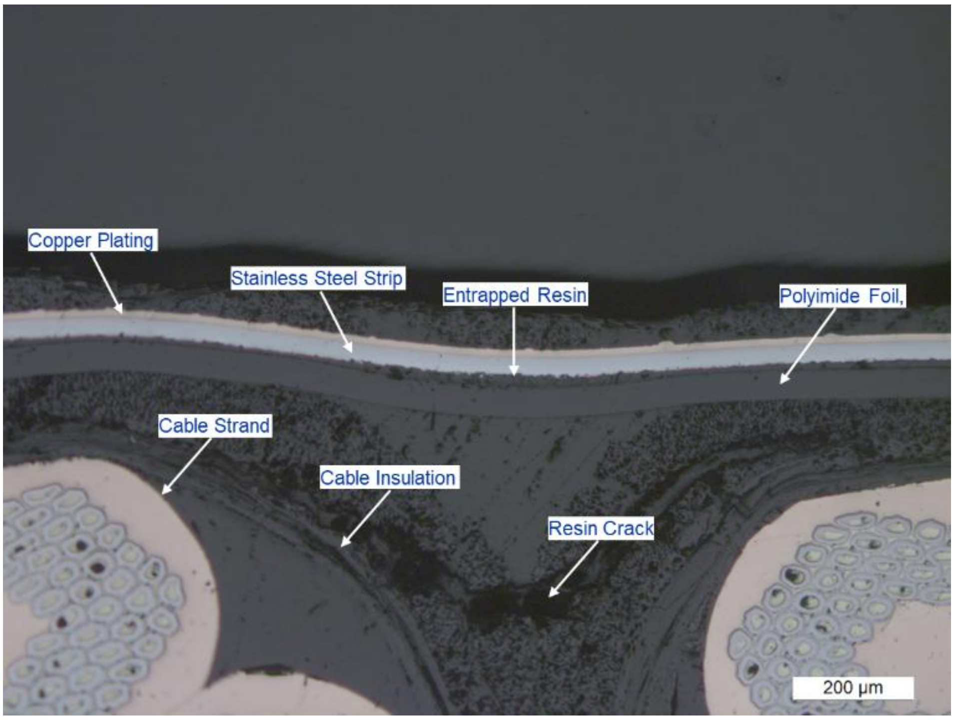

Figure 36: Metallographic analysis of a transverse cross-section of a HL-LHC 11 T dipole magnet coil, illustrating the presence of resin cracks between outer-layer cables and quench protection heater (Courtesy of M. Crouvizier, CERN).

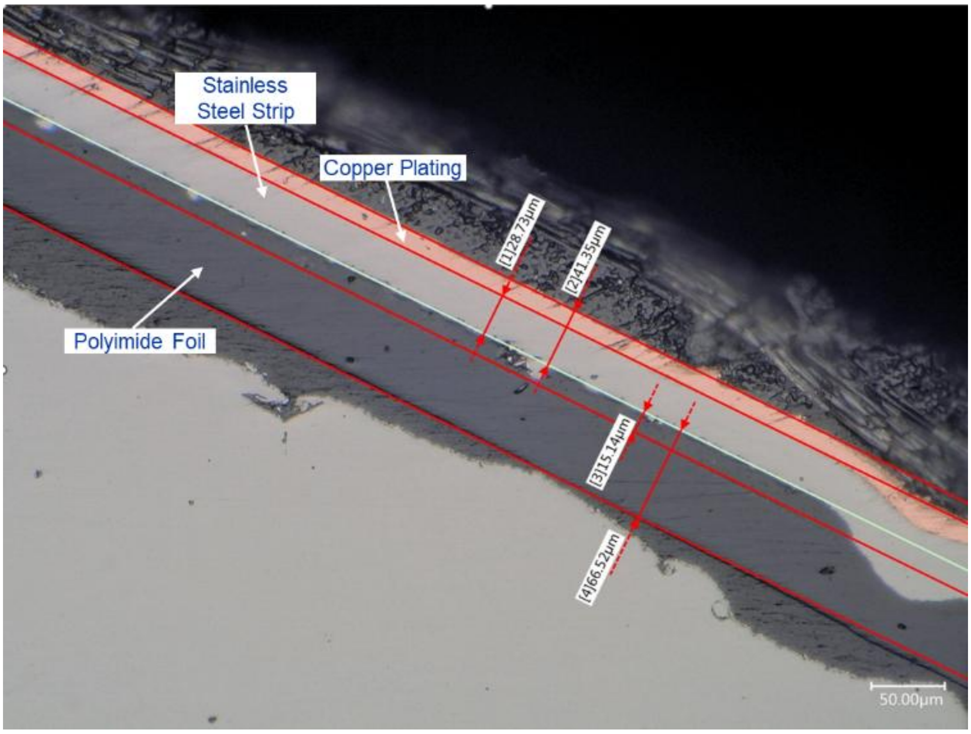

Figure 37: Detailed view of impregnated quench protection heater of a HL-LHC 11 T dipole magnet coil, illustrating the presence local thickness variations of polyimide foil (Courtesy of M. Crouvizier, CERN)

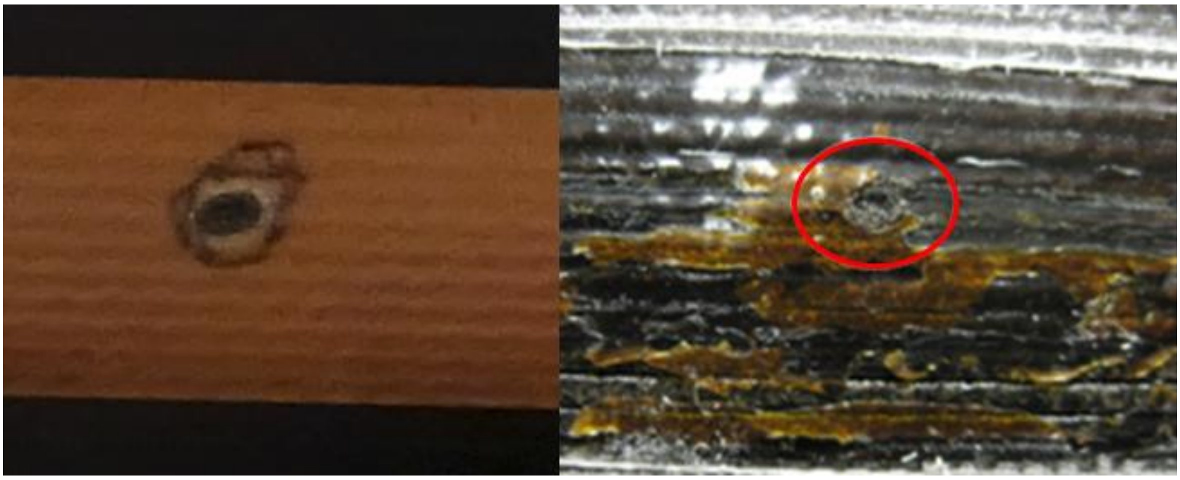

Figure 38: Quench heater failure observed on coil CR06 dismounted from full-length HL-LHC 11 T dipole magnet prototype MBHBP after cold test and after a series of high pot tests carried out at increasing voltage levels until occurrence of an electrical short. Left: view of burn through on top of the electroplated copper. Right: view of burn through after peeling of quench heater layers (Courtesy of A. Foussat and F. Savary, CERN).

The proposal for quench heater externalization was submitted to a technical review on 11 January 2019 which endorsed it. It was implemented on so-called *second-generation* short model coils first used in two-in-one-aperture dipole magnet model MBHDP201, and in 5.3-m-long series coils, starting from coil GE10 and series dipole magnet S3 (see Section 4.2.3).

Let us note that both series dipole magnets S3 and S4, whose quench performances at 1.9 K and 4.5 K are reported in Figure 13, experienced an electrical fault that halted the quench test. The root cause of the fault was traced back to a failure of a junction between the extremity of a quench heater trace and a current lead wire. This led to a redesign of the junction, that was qualified through extensive mechanical and electrical tests and implemented in the last series coils. It is a staunch reminder that hasty implementations under heavy schedule pressure can bear a very high risk and that any type of engineering changes require thoughtful and comprehensive qualifications.

In spite of the difficulties encountered on the 11 T dipole magnets, it seems nevertheless that, for future projects calling for large series production in industry, the use of external quench heaters that are not impregnated with the coils should be given serious consideration in the overall risk analysis.

2.3.4.5 Status Quo for MQXFA Quench Heaters in the USA

The quench heater design and implementation used for MQXFA and MQXFB quadrupole magnets are similar to those used for initial 11 T dipole magnets (including impregnation together with the coils), and, although voltage withstand requirements are significantly lower (see Table 6 and Table 7), questions were also raised regarding the robustness of the coil-to-quench-heater insulation.

As already mentioned in Section 1.5.6.3, the first 4.2-m-long MQXFAP1 quadrupole magnet prototype developed a coil-to-ground short during vertical cold test at BNL. The root-cause analysis that was carried out identified a double short between one quench heater and one coil as the likely origin of the problem, that eventually degenerated into a coil-to-ground short [109][193]. It also concluded that the heater-to-coil double short resulted from excessive and repeated hipot tests that were carried out on this particular heater after the magnet had been warmed up to room temperature following the untimely rupture of a test burst disc during the first quench. Following repair of the burst disc, the magnet was cooled down again, and quenched 17 times, before developing the short to ground.

At the time of MQXFAP1 cold test, the voltage withstand requirements of Table 7 had not yet been fully developed, and although the magnet had been exposed to helium, the quench- heater-to-coil hipot tests after the unscheduled warm up were carried out at the pre-cooldown level of 2.5 kV instead of 460 V. It was concluded that the repeated application of this excessive voltage eventually induced the double short.

To better understand the failure mechanism, a destructive test was carried out on a representative, full-length MQXFA coil that had been cold tested (in a mirror configuration) and exposed to helium. After disassembly of the coil support structure, one of the quench heaters was hipot tested to the coil until the occurrence of a short whose location was determined by thermal imagery. An autopsy was carried out in the electrical short area, which enabled several observations, including the presence of bubbles in the epoxy resin and of blisters on the polyimide base of the quench heater [193]. It is likely that the bubbles originated from cracks in the resin where helium got entrapped and that, during quenches, the temperature rise resulted in a rapid increase of helium pressure that enlarged the cracks and caused blistering of the polyimide. This blistering, in turn, locally reduced the polyimide thickness (by up to 40%), and, upon repeated hipot tests, eventually led to a short.

Having identified the probable mechanism of quench-heater-to-coil failure, LARP/AUP concluded that if the hipot tests are carried out at the recommended value of 460 V, the failure risk remains at a very low level and the decision was taken to keep heater design and implementation as is.

2.3.4.6 Quench Heater Mini-Swap for MQXFB at CERN

Regarding MQXFB at CERN, it was also decided to keep impregnating the quench heaters with the coils, but, based on the corrective actions applied on the 11 T magnets, it was proposed: to add a 50-μm thick fresh layer of E-type fiberglass on the outer surface of the coil upon heat treatment completion and to add a coverlay on the electroplated copper side of the quench heater (0.050-mm-thick polyimide film glued, under pressure and heat, with a 0.025-mm-thick epoxy). In addition, the quench heater polyimide films are cut out 4 mm wider with respect to previous design, enabling the use of higher voltage for quality control tests: the withstand voltage test was raised from 3.7 kV to 8 kV after quench heater production, and from 3.2 kV to 5.6 kV before installation at CERN [194][258].

The hot spot temperature is not affected by the addition of the E-glass layer in normal conditions at nominal current, where CLIQ plays a dominant role in quench development. In the worst-case scenario with one quench heater and one CLIQ circuit failure, the hotspot temperature is estimated to increase by 30 K from 346 K to 375 K at nominal current. These values are similar to those estimated for the 11 T dipole magnets, in particular regarding the impact of adding a fiberglass layer of comparable thickness between the quench heater and the coil.

The proposed change was referred to as *miniswap*, which is a rather odd denomination. It relates to the fact that, in the initial procedure, after heat treatment completion and in preparation for vacuum pressure impregnation, the outer surface of the coil is covered by 1 x layer of ~0.1-mm-thick quench heater and 3 x layers of ~0.130-mm-thick S2 glass fiber sheets. In the new procedure, the outer surface of the heat-treated coil is covered by 1 x layer of ~0.05-mm-thick E glass fiber sheet, 1 x layer of ~0.16-mm-thick quench heater and 2 x layers of ~0.130-mm-thick S2 glass fiber sheets. Therefore, in the pile up of materials on the coil outer surface, 1 layer of S2 glass fiber sheet positioned on top of the quench heater has been swapped with the new layer of E glass fiber sheet and the increased quench hater thickness. The epithet *mini* refers to the fact that, in an earlier proposal, LARP/AUP had considered removing 1 of the 3 layers of ~0.130-mm-thick S2 glass fiber sheet and to place it under the quench heater instead of the ~0.05-mm-thick E glass fiber sheet, which would have been a *full* swap. The miniswap was proposed as a compromise solution for MQXFB at CERN [194].

Figure 39: Examples of capillaries used in the assembly of 7.2-m-long HL-LHC MQXF quadrupole magnets at CERN. Left: capillaries installation on cold mass. Right: capillaries installation on thermal shields during cryostating (Courtesy of O. Housiaux, SERCO, H. Prin and D. Duarte Ramos, CERN).

The miniswap was implemented on two short model coils used in the assembly of quadrupole magnet model MQXFS8, which was cold tested in 2023, and on 7.2-m-long coils, starting with those used in full-length quadrupole magnet MQXFB03. As explained in Section 5.5.10 and illustrated in Figure 145, MQXFB03 was the first MQXFB magnet to achieve the target current of nominal + 300 A at both 1.9 and 4.5 K.

Let us finally note that at the beginning of the MQXF program, it was considered to implement quench heaters on both the inner and outer surfaces of the 2-layer coils [141]. The idea of using quench heaters on the inner surface was dropped because of the difficulties in implementation and of the debonding/delamination observed after cold test. It was decided at the time that the use of CLIQ would offer a more robust and redundant solution.

2.3.5 Capillaries and Instrumentation Feedthrough Systems (IFS)

The electrical design and engineering of superconducting magnets also call for the development and implementation of so-called *capillaries* and *Instrumentation Feedthrough Systems (IFS)*.

Capillaries are small stainless-steel tubes which house instrumentation wires and route them from wherever they are in the magnet to the cold mass envelope and from the cold mass to the cryostat envelope. The capillaries are initially straight, the wires are inserted into the straight tubes, and the tubes are subsequently bent to assume the desired shape for routing. Usually, there a dedicated capillaries for high voltage wires (*e.g.*, voltage taps connected to the coils or current leads feeding the quench heaters) and dedicated capillaries for low voltage wires (*e.g.*, for mechanical instrumentation and temperature sensors). Figure 39 shows examples of capillaries mounted on the cold mass and thermal shields of a full-length MQXFB quadrupole magnet cryo-assembly at CERN. Electrical faults may occur in capillaries due to wear of instrumentation wire insulation caused by friction during capillary shaping or thermal shrinkage differentials during cooldown (see Figure 40).

Instrumentation feedthrough systems rely on connectors mounted on the coldmass and on the cryostat which enable the passage of instrumentation wires signals and currents in and out of the helium containment vessel of the coldmass and in and out of the vacuum enclosure of the cryostat (see Figure 41) [195].

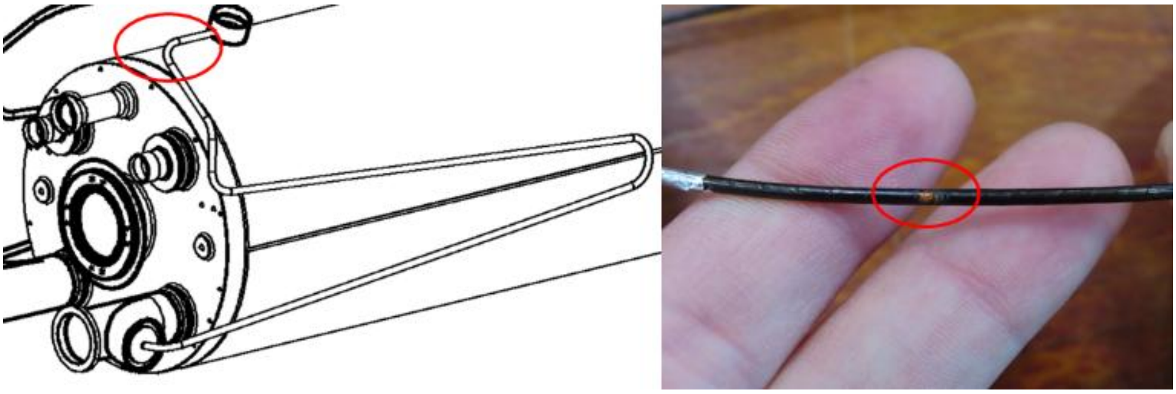

Figure 40: Example of electrical fault detected on an instrumentation wire in a capillary mounted on the cold mass of full-length HL-LHC quadrupole magnet prototype MQXFBP3 at CERN. Left: localization of the fault in a capillary elbow. Right: degradation of instrumentation wire insulation in the elbow area (Courtesy of O. Housiaux, SERCO, and H. Prin, CERN).

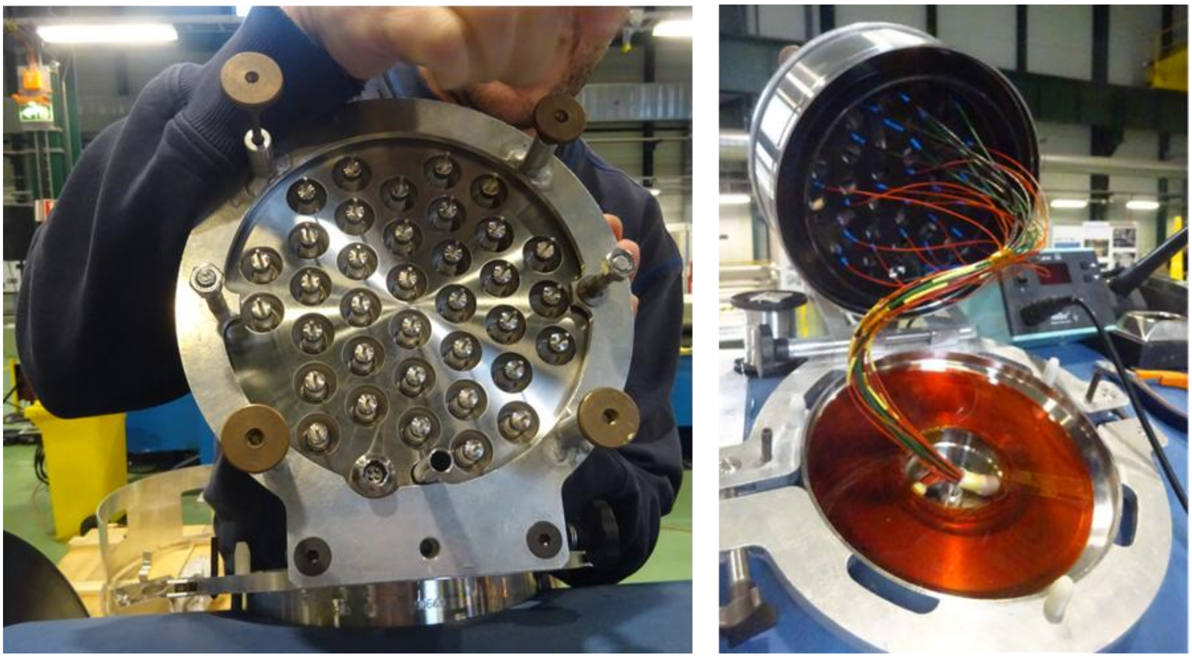

Figure 41: Views of an Instrumentation Feedthrough (IFS) mounted on the cryostat of a HL-LHC MQXFB quadrupole magnet at CERN. Left: external side. Right: internal side with instrumentation wires connected (Courtesy of O. Housiaux, SERCO, and D. Duarte Ramos, CERN).

The IFSs can be quite challenging to design and qualify as they must ensure:

- good electrical connection between the wires on both sides;
- good electrical insulation between wires and ground;
- helium leak tightness (for the cold mass IFS) or vacuum leak tightness (for the cryostat IFS);
- mechanical robustness against mounting/dismounting of connectors and wire pulling.

The IFS development must be qualified through a rigorous program and a high level of QC must be implemented during production.

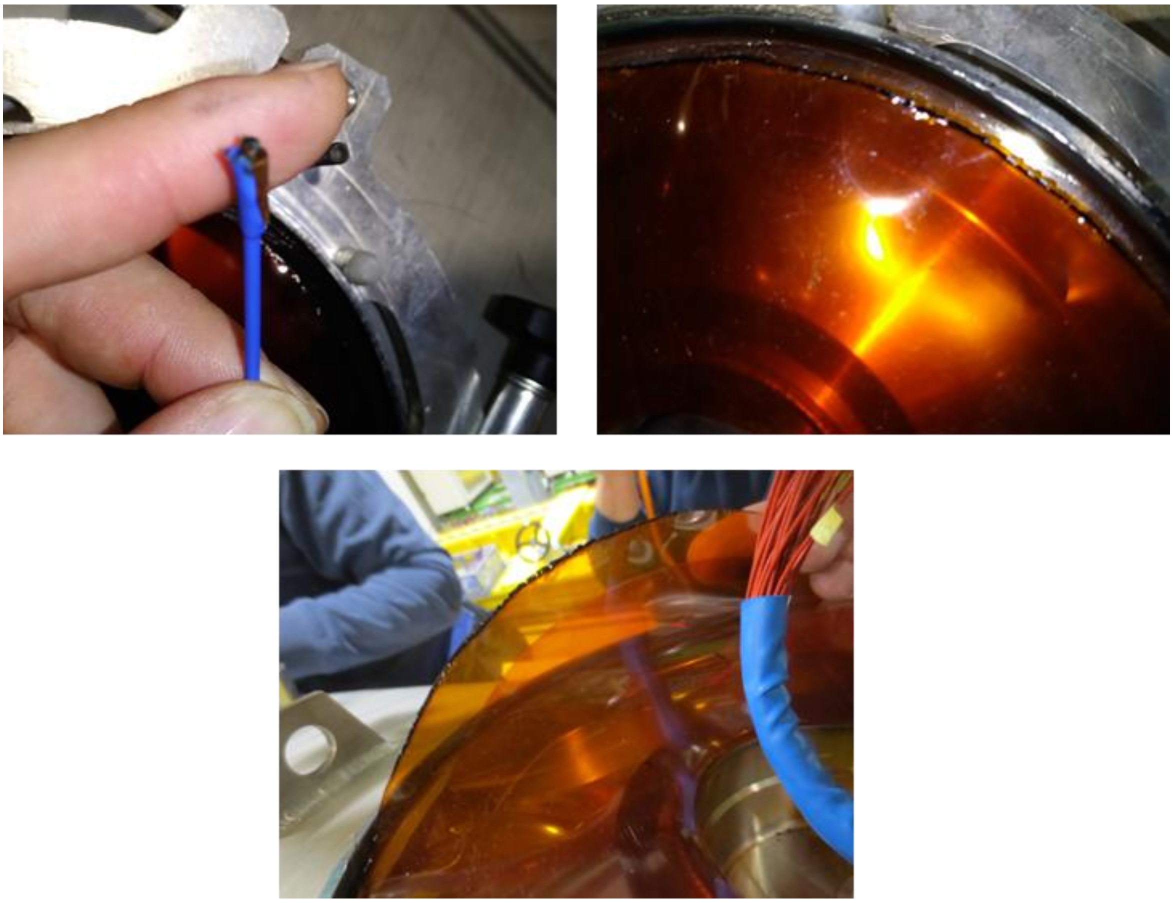

Figure 42: Example of an electrical fault detected in an IFS mounted on the coldmass of full-length HL-LHC quadrupole magnet prototype MQXFBP2 at CERN. Top left: trace of burn on a voltage tap wire insulation. Top right: trace of carbonization on the IFS cover-flange side. Bottom: trace of burn on the rim of the polyimide insulation disc (Courtesy of O. Housiaux, SERCO, and D. Duarte Ramos, CERN).

A common issue during mounting of an IFS on a cold mass or a cryostat is insulation degradation during wire soldering or IFS cover flange welding. As an illustration, Figure 42 shows an example of an electrical fault localized in a cryostat IFS that likely resulted from overheating during cover welding. As for the components themselves, the IFS installation procedures must be qualified, technicians must be trained, and tight QC controls must be applied as the consequences of an electrical fault on such ancillary equipment can be deleterious.

Let us note that the time domain reflectometry method introduced in Section 2.3.3 has proven very efficient in the localization of electrical faults in IFSs or along capillaries.

3 Post-Mortem Examination of Nb_3Sn Conductors and Coils

3.1 Post-Mortem Analyses of ITER CS Cable-In-Conduit Conductors

Following the performance issue encountered on the first two ITER CS CICC qualification samples, the Japanese Atomic Energy Agency (JAEA), located in Naka, Japan, in charge of this program, carried out an autopsy of one of the conductor samples after test in SULTAN [50]. As illustrated in Figure 43, the sample was sectioned into several pieces corresponding to different levels of background field to which the sample is subjected in SULTAN: one from the low-field region, one from the medium-field region and one from the high-field region. The cross-section of the high-field region sample revealed a global displacement and a compression of the rope-type cable inside the conduit along the direction of the Lorentz force. Furthermore, when removing the stainless-steel jacket, the outer surface of the cable displayed evidence of strand buckling and even cracking on the so-called *non-compressive side* of the cable. These observations clearly indicated that there was a problem of strand support against the effect of the Lorentz load.

The fact that strand bending under the effect of the Lorentz load could result in deleterious degradation was further confirmed thanks to metallographic analyses carried out by the Applied Superconductivity Center (ASC), associated with the National High Magnetic Field Laboratory (NHMFL) and Florida State University (FSU), and located in Tallahassee, FL. ASC has been playing a leading role in developing imaging techniques for superconductors over many decades [196]. It was awarded several contracts with ITER Organization to perform metallographic analyses on ITER wires and CICC samples having been subjected to mechanical or electromagnetic loading [197][198]. When the ITER CS crisis arose, it was tasked with carrying out systematic post-mortem analyses of ITER CS conductor samples after testing in SULTAN [199][200][201].

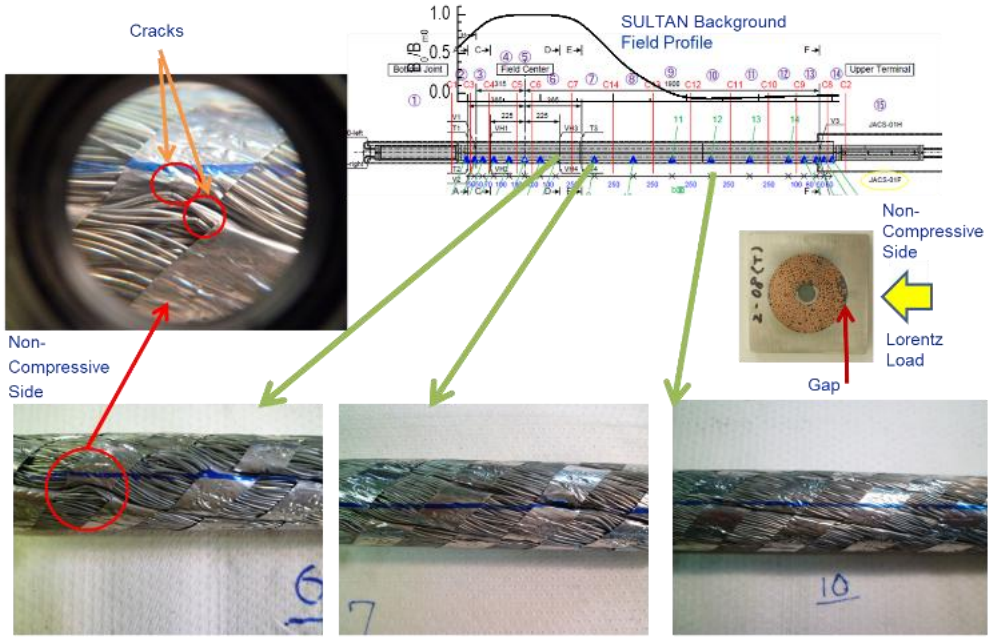

High Field Sample
(many bent strands)

Medium Field Sample
(few bent strands)

Low Field Sample
(no bent strands)

Figure 43: Images from an autopsy of an ITER CS conductor performance qualification sample having exhibited severe degradation upon electromagnetic and thermal cycling during SULTAN test. Top right: Profile of SULTAN background field profile with respect to sample. Middle right: Evidence of cable compression inside the conduit under the effect of the Lorentz force. Bottom Left, Middle and Right: views of cable sections from regions of high, middle, and low background field after jacket removal. Top left: strand buckling and cracking observed on the non-compressive side of high-field cable section (Courtesy of Y. Nunoya, formerly JAEA, now QST [50], 2011).

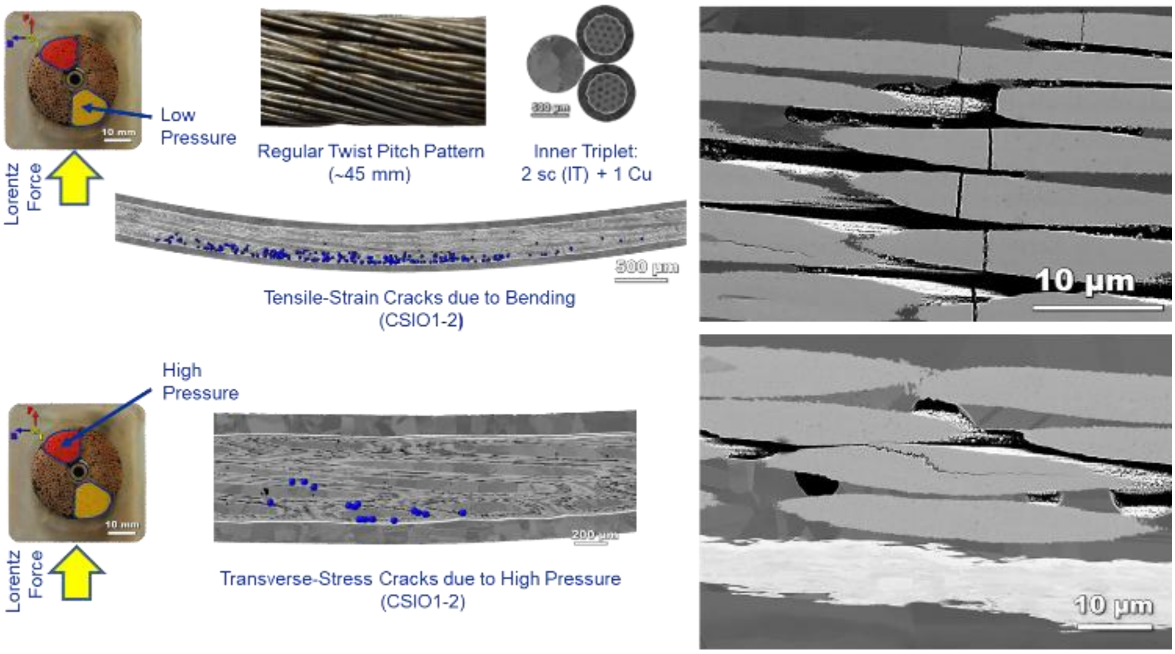

Figure 44: Metallographic analyses carried out on longitudinal cuts of extracted strands from the high-field region of a regular twist pitch ITER CS conductor sample after test in SULTAN. Top: images from a strand in the non-compressive side of cable, exhibiting tensile cracks. Bottom: images from a strand in the compressive side of cable, exhibiting contact stress cracks. Cracks are marked in blue in the central images, while the right images show magnified views of crack morphology (Courtesy of C. Sanabria, formerly ASC).

Figure 44 displays metallographic analyses carried out by ASC on strands extracted from the high-field zone of a SULTAN sample using a Laser Scanning Confocal Microscope (LSCM) or a Scanning Electron Microscope (SEM). Different types of crack morphology are observed, depending on the cable petals from which the strand is extracted [199]. For a petal located on the non-compressive side, the cracks mostly originate from tensile stresses and cut through the filaments transversally. This type of cracks is likely to hinder current transport. For a petal located on the so-called *compressive side*, the cracks also originate from compressive contact stresses. Such types of cracks may have less impact on current transport. Not presented here are also examples of cracks with a so-called *zig-zag* pattern, likely resulting from multidirectional loads.

As explained in Section 1.4.2, the cure to the performance degradation of ITER CS conductors was found by shortening the cable twist pitch, in particular for the inner triplet [15][51]. To confirm the effectiveness of the cure, post-mortem analyses of short-twist pitch CS conductor samples were carried out in a similar manner as above after the test in SULTAN [200]. An example of such analysis is presented in Figure 45: no cracks are visible, neither in strands extracted from the non-compressive side, nor in strands extracted from the compressive side. Such observations were repeated on several conductor samples relying on short twist pitch cables made from both bronze and internal tin strands, confirming, alongside the stable test performances as a function of electromagnetic and thermal cycling, the robustness of the optimized CS conductor design. This is the design that was implemented for series production with good and reproducible results, illustrated in Figure 5 [53].

3.2 Metallographic Analyses of HL-LHC 11 T Coils at ASC

In early 2019, it was suggested to utilize the techniques developed by ASC on ITER CICCs to investigate samples of coils used in the assembly of HL-LHC 11 T dipole magnets that underwent cryogenic testing and energization [202].

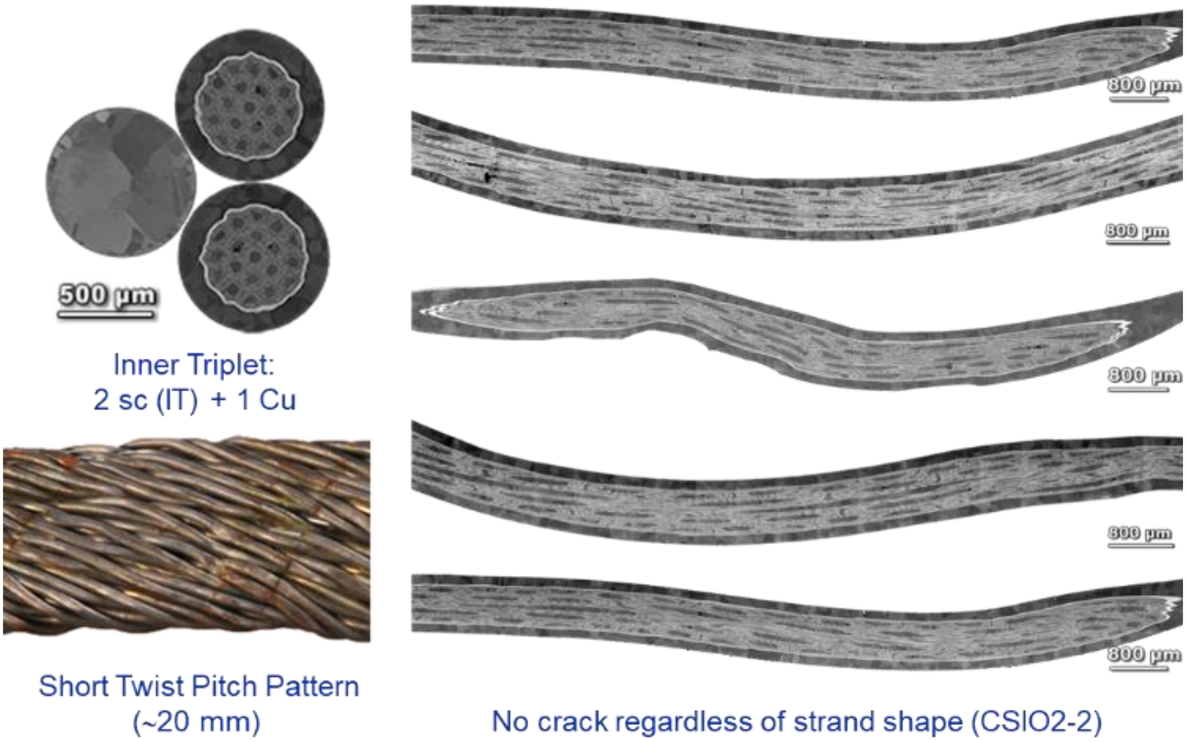

Figure 45: Post-mortem analysis of a short twist pitch ITER CS conductor sample after test in SULTAN. Top Left: cross-sectional views of the strands in the inner triplet. Bottom Left: top view of the short-twist pitch cable. Right: metallographic analyses of longitudinal cuts from (internal tin) strands extracted from the high field zone of the cable devoid of any crack (Courtesy of C. Sanabria, formerly ASC).

Two coil samples were provided to ASC:

- a sample from the straight part of short model coil SD109, used in the assembly of two-in-one-aperture dipole magnet model MBHDP102, that had been identified as an area of quench-start localization with severe performance degradation;
- a sample from the straight part of long series coil GE02, used in the assembly of the hybrid prototype (see Section 1.5.5.3), not associated with an area of quench localization and performance degradation (all quenches in this magnet originated in the connection-side head of coil GE02).

Figure 46 contains Back Scattered Electron (BSE) images recorded with a high-resolution Field Emission Scanning Electron Microscope (FESEM) of Nb_3Sn sub-elements from a strand cross-section selected among those that are visible on transverse cuts from the two coil samples mentioned above. The image taken from the sample of coil SD109 shows several cracks of various morphology, while the image taken from the sample of coil GE02 appears devoid of any crack [202].

Figure 47 shows a micrograph of a longitudinal cut (taken along the coil axis) of the inner layer midplane block of coil SD109. There appear to be numerous cracks in the Nb_3Sn sub-elements, but the crack density varies from turn to turn, with a high concentration towards the midplane turns where the quenches had been localized in this short magnet model. This location corresponds to the coil area where the conductors experience the largest transverse stresses during magnet assembly and energization (peak stresses during the collaring of MBHDP102 could have been as high as ~200 MPa).

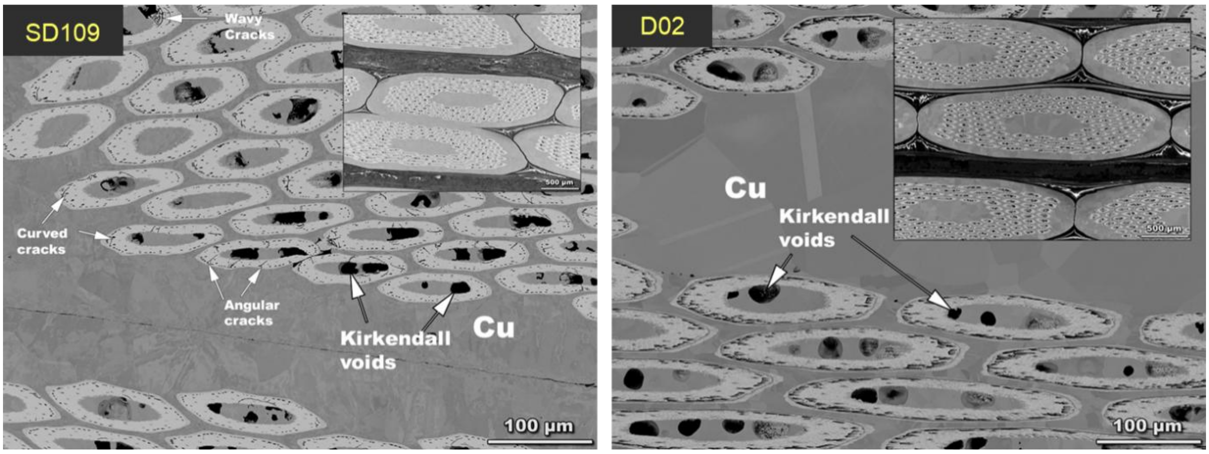

Figure 46: Back Scattered Electron (BSE) images recorded with a high-resolution Field Emission Scanning Electron Microscope (FESEM) of sub-elements in sections of Nb_3Sn RRP® strands selected among those visible on transverse cuts of HL-LHC 11 T magnet coil samples provided to ASC. Top: from short model coil SD109, featuring a large number of cracks of various morphology. Bottom: from long series coil GE02 showing no evidence of cracks (Courtesy of S. Balachandran, formerly ASC [202]).

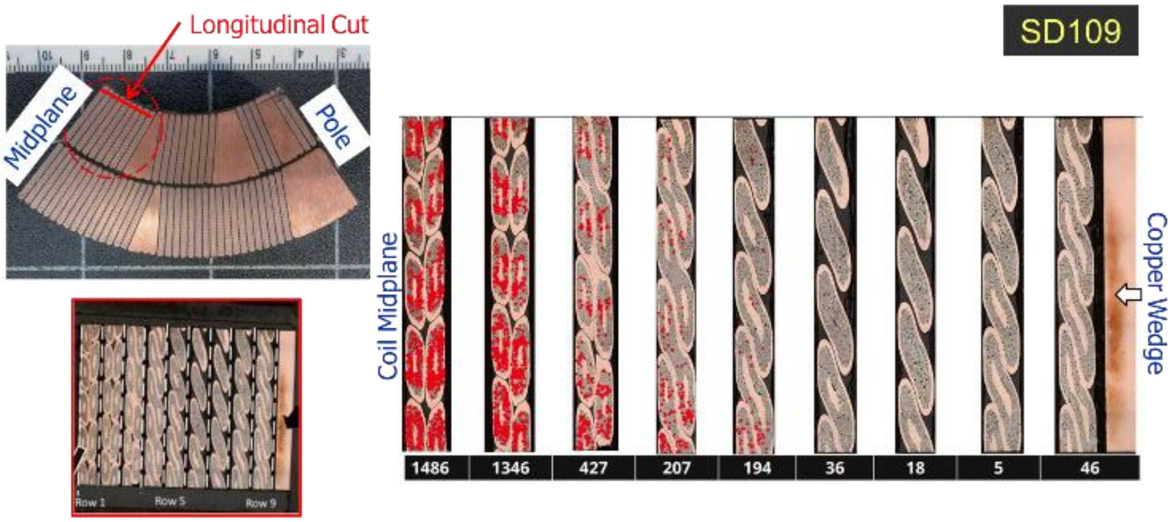

Figure 47: Results of metallographic analysis carried out at ASC on a longitudinal cut from a sample of HL-LHC 11 T model coil SD109 where quenches had been localized; the red marks correspond to cracks observed in Nb_3Sn RRP® strands (Courtesy of S. Balachandran, formerly ASC [202]).

As explained in Section 1.5.5.2, the first 11 T Task Force, which was set up at the end of 2017 to review the performance issue of short HL-LHC 11 T dipole magnet models, identified excessive stress applied during collaring operation as the likely root-cause of the problem and recovery measures were implemented to limit peak collaring stress to less than 150 MPa [100]. The observations reported here clearly confirm that the conductors in high stress areas were severely degraded.

The assembly of the hybrid 11 T prototype benefited from the first Task Force results and its collared coils were assembled following the new procedure. The micrograph at the bottom of Figure 46 confirms the absence of cracks. As observed on ITER CICCs, HL-LHC Nb_3Sn coil areas with large crack concentrations seem to correlate with areas of performance degradation, and it is advisable to undertake corrective actions to eliminate the root cause(s) of Nb_3Sn filaments or Nb_3Sn sub-elements cracking.

3.3 Methodology of Post-Mortem Analyses at CERN

In June 2019, CERN started to develop its own methodology on how to carry out post-mortem examinations of HL-LHC dipole and quadrupole magnet coils that exhibited performance limitation and/or degradation [203][204].

The first step is to identify coil Volumes Of Interest (VOI). Typically, one starts from the coil volumes where the quenches have been localized, using, for instance, the quench antenna results. These volumes are extracted from the coil by cutting methods and the coil samples are subjected to a series of examinations. The examination starts from mesoscale observation of whole coil samples, and progressively zooms in on specific features or events, down to the microscopic scale. The specific features/events of interest are determined based on mechanical discontinuities (*e.g.*, the tip of a sharp component, the junction between pieces, and so on), internal events (*e.g.*, popped-out strands in a cable), geometrical distortions (*e.g.*, cable bulging or displacements), and flaws (*e.g.*, resin crack initiation and/or delamination).

The examination techniques that are applied are [203]:

- high-energy, X-ray Computed Tomography (XCT);
- optical microscopy;
- scanning electronic microscopy;
- Focused Ion Beam (FIB) techniques;
- deep copper etching.

Let us illustrate some of these techniques and the types of findings they lead to.

3.4 High-Energy Xray Tomography

The first novel technique that was identified to investigate the status of magnet coils in a less intrusive manner than by metallography is high-energy X-ray Computed Tomography (high-energy XCT) [203][205]. The system used by CERN is provided by Diondo GmbH, Germany [206]. It relies on a 6 MeV LINear ACcelerator (LINAC) to produce high-intensity X-rays that can pass through dense (metallic) objects and is equipped with a flat panel detector with a resolution of 140 μm (see Figure 48). The maximum sample volume is 700 mm diameter by 1000 mm height.

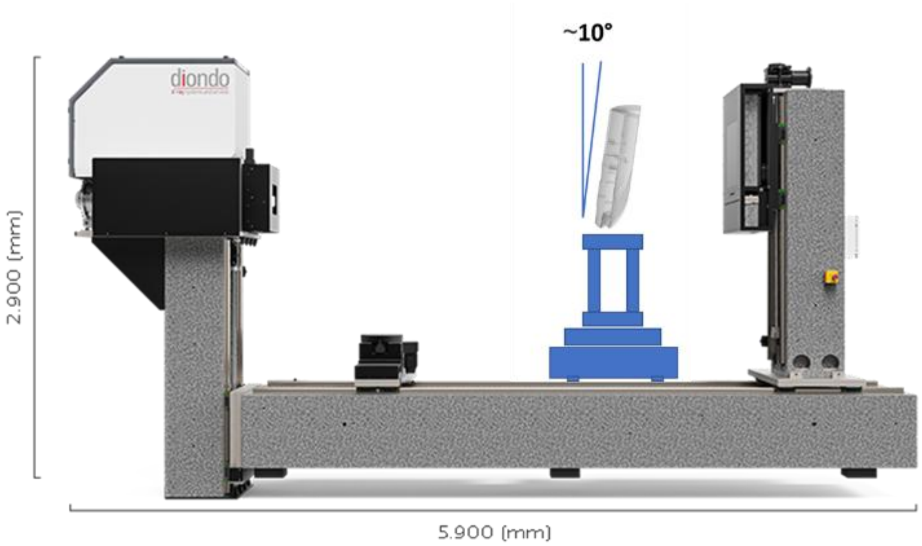

Figure 48: Example of high-energy X-ray tomograph used for analysis of HL-LHC magnet coil samples [206].

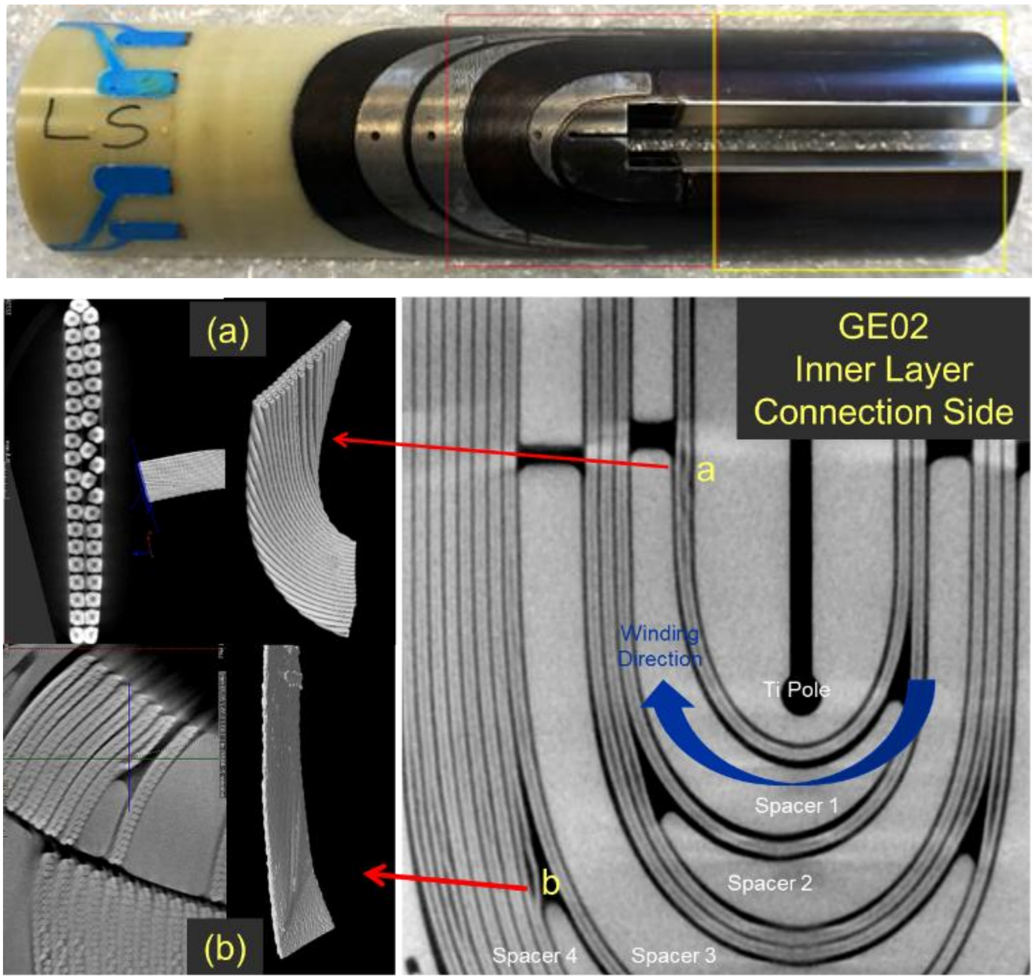

Figure 49: Example of high-energy X-ray computed tomography carried out on the connection-side end of 5.3-m-long HL-LHC 11 T dipole magnet coil GE02 (used in hybrid prototype). Top: top view of coil sample showing the outer surface of the outer layer. Bottom right: XCT scan of coil inner layer, featuring obvious flaws in winding. Bottom left: digital zooms of selected flaws confirming misplacements of strands and bulging of the Rutherford-type cable (Courtesy of M. Crouvizier and S. Sgobba, CERN).

Such system enables radiography of 20-30 cm-long coil samples, including whole coil ends, as illustrated in the top part of Figure 49. The resolution is good enough to carry out in-depts inspections of the coil winding and of the positions of strands in the wound cables.

The bottom part of Figure 49 illustrates computed tomography images of the connection-side end of full-length, 11 T dipole magnet coil GE02. Coil GE02 was used in the assembly of the 5.3-m-long 11 T hybrid dipole magnet prototype. As detailed in Section 1.5.5.3, the hybrid prototype achieved ultimate current upon first cooldown but exhibited a severe detraining after a subsequent warm-up/cooldown cycle, with all detraining quenches (but one) located in the examined connection-side end of coil GE02. The images reveal the presence of popped strands on the pole turn [event (a)] and of cable bulging at the tip of end spacers, such as end spacer 4 [event (b)].

The above example provides a good illustration of the methodology: starting from a coil volume where the quenches were localized during power testing of the magnet, high-energy XCT reveals flaws or defects which can then be examined in more details by metallographic analyses. If one did not know where to look, it would have been difficult to find such defects by performing random cuts on the coil sample.

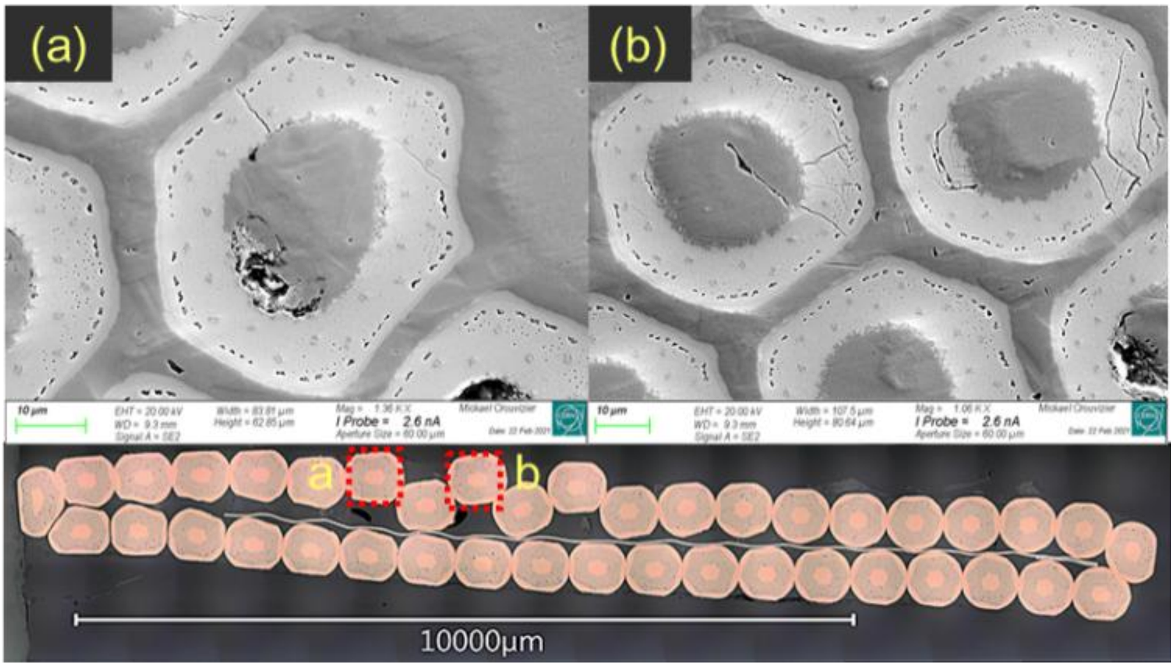

Figure 50: Metallographic analyses of a transverse cut carried out perpendicularly to the conductor axis in the area of event (a) in **Figure 49**. Bottom: cable cross-section, confirming the presence of popped strands, labeled (a) and (b). Top: magnetified views of strands (a) and (b) showing the presence of radial cracks in the tubular Nb_3Sn sub-elements of the RRP® strands (Courtesy of M. Crouvizier and S. Sgobba, CERN).

3.5 Metallographic analysis of Transverse Coil Cross-Sections

After having identified events of interest in the XCT images, the next step is to cut the coil samples in these areas and to carry out metallographic analyses of the cut facies [203].

3.5.1 HL-LHC 11 T Coils

3.5.1.1 Examples of Popped-out Strands

Figure 50 shows a metallographic analysis of a transverse cut carried out perpendicularly to the inner-layer pole turn conductor in the area of event (a) in Figure 49. The image confirms the presence of strands that have popped out of the cable plane. When looking at the cross-section of the popped strands with a higher magnification, one can see large radial cracks in the tubular aggregates of Nb_3Sn filaments in the RRP® strand sub-elements. Such severe cracks are of course not desirable and could well be the cause of the detraining quenches that were localized in that area. (We will present in Section 3.5.2 more striking evidence of strand degradation believed to be the root cause of poor quench performance, but the deep copper etching technique used for MQXFB coil Q108 had not yet been considered at the time of the post mortem analysis of 11 T coil GE02.)

Strands popping out of cables (or even full cable collapsing) are sometimes observed during coil winding (see Sections 4.3 and 5.5.3). They usually occur at the exit of the turns during the winding process (as is the case for event (a) in Figure 49). They are due to a combination of factors but mostly result from the torsion caused by hard way bending of the insulated cable when winding it over the coil heads. During winding, the technicians carefully check the cable to detect the occurrence of popped strands. In case of a defect, they take action to correct it (and to record it in a non-conformity report), but they can inspect only the outer, visible surface of the turns. Defects like those in Figure 50 were localized on the inner, hidden surface of the pole turn and could not be detected at the time of winding.

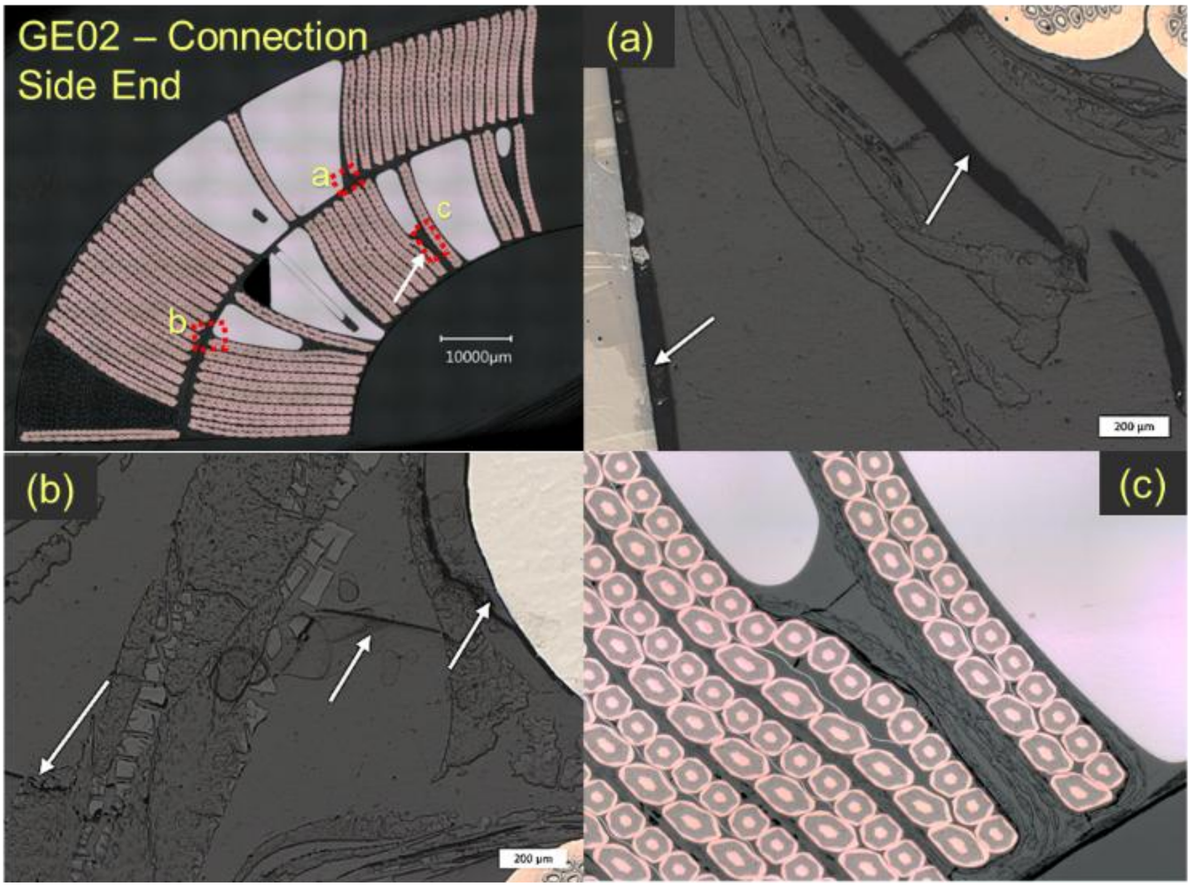

Figure 51: Metallographic analyses of a transverse cut carried out perpendicularly to the coil winding, in the area of event (b) in **Figure 49**. Top Left: overall view confirming cable deformation and bulging at tips of coil end spacers (tip of spacer 4 is marked with a white arrow and labelled "c"). Top Right, Bottom Left and Right: magnetified views of selected resin-rich areas with evidence of cracks and debonding (salient flaws are marked with white arrows; courtesy of M. Crouvizier, CERN).

3.5.1.2 Examples of Resin Flaws

Figure 51 shows a metallographic analysis of a transverse cut carried out perpendicularly to the coil winding in the area of event (b) in Figure 49. The image confirms the observed cable deformation and bulging at the tip of the coil end spacer 4. This is an area where part of the cable is not supported, and which is filled by resin upon coil impregnation. However, as can be seen in the magnified views of selected resin-rich areas, there are porosities and cracks in the resin bulk, debonding at the metallic interfaces (near wedges or end spacers) and delamination of the conductor insulation (in the bulged area).

It would be preferable to prevent the occurrence of such cracks and debonding, but when relying on an epoxy resin system, this can only be achieved by using filler materials (such as chopped glass fibers). Gap filling is routinely done at CERN and AUP for all volumes that are accessible during coil manufacture (see Section 5.5.6.1 and Figure 133), but it is a cumbersome process and sometimes cannot be done. In the example presented here, the small cavities at the tips of the inner layer end spacers become inaccessible after outer layer coil winding and cannot be filled.

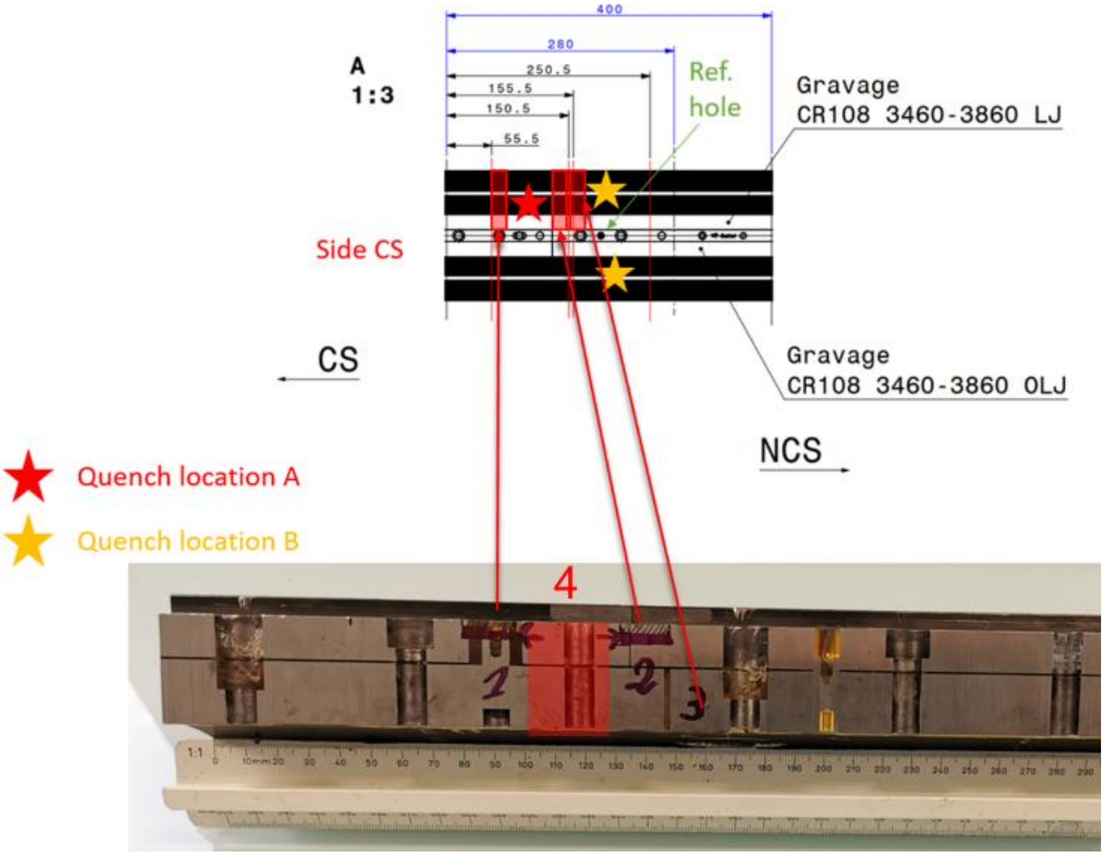

Figure 52: Quench-start localizations and corresponding markings on the sample extracted near the longitudinal center and on the side of 7.3-m-long HL-LHC MQXFBP1 coil Q108 where limiting quenches had been localized (Courtesy of M. Crouvizier and F. Mangiarotti, CERN).

3.5.2 HL-LHC MQXFB Coils

3.5.2.1 Introduction

Similar metallographic analyses of transverse cuts were carried out on samples from 5.3-m-long, HL-LHC MQXFB quadrupole magnet coils. The most extensively analyzed coil is Q108. Q108 was used in the assembly of the first CERN prototype MQXFBP1 and was the coil that limited its performance (see Section 1.5.6.4). The post-mortem analysis of coil Q108 was carried out according to the methodology described in Section 3.3.

3.5.2.2 Volumes of Interest

First, quench-start localization data were used to identify the volumes of interest to be examined. As illustrated in Figure 52, most of the quenches were localized in an area towards the longitudinal center and, predominantly, on one side of coil Q108 [113].

Second, a sample of about 40 cm was extracted and subjected to XCT analyses. Unlike in the case of coil GE02 in Section 3.4, the XCT analysis did not reveal any flaws, neither in conductor positioning within the winding, nor in strand positioning within the cables. This was not a surprise as it is difficult to conceive how conductor/strand misplacement could occur in the middle of the coil straight section.

The next step was to carry out metallographic analyses of transverse cuts at the positions marked as “1” to “4” in Figure 52.

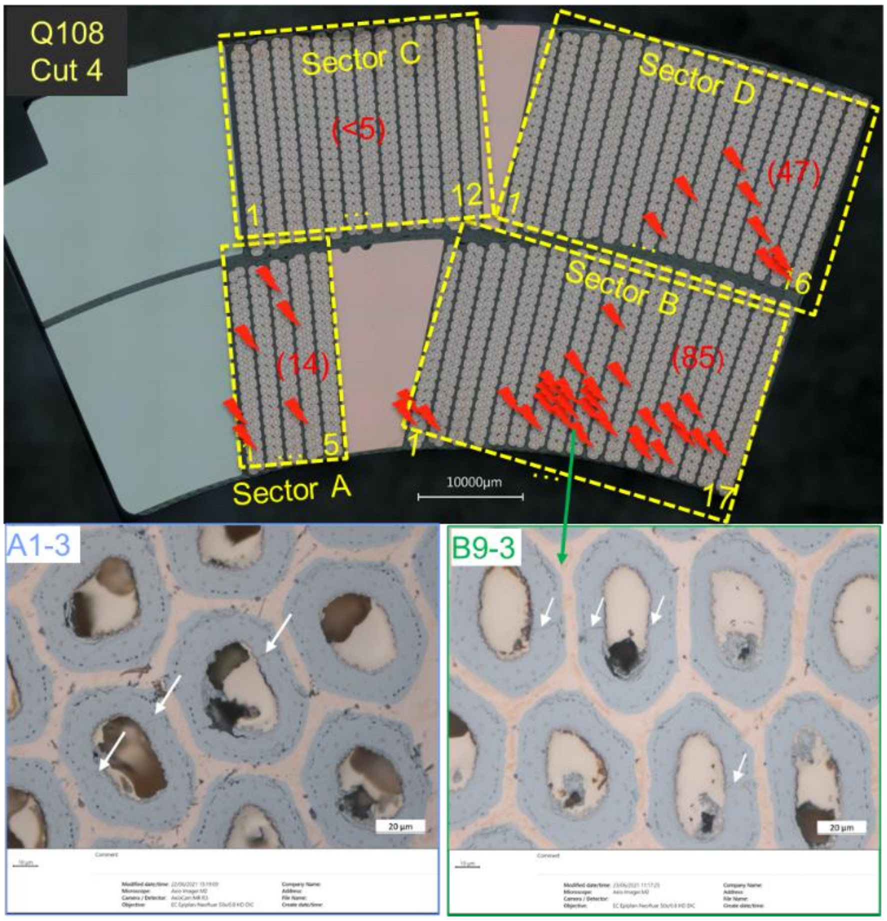

Figure 53: Metallographic analysis of a transverse cut of 7.2-m-long HL-LHC MQXFB quadrupole magnet coil Q108 (used in MQXFBP1), in the area of quench-start localization (towards middle of coil straight section). The magnified views at the bottom reveal the presence of radial micro-cracks in some sub-elements (shown by white arrows); their distribution is marked by red pins in the top image (Courtesy of M. Crouvizier, CERN).

3.5.2.3 Radial Micro-Cracks in Transverse Cross-Sections

Figure 53 shows images from the transverse cut marked as “4” in Figure 52. The magnified views do reveal the presence of radial cracks in some of the strands’ sub-elements. However, compared to those shown Figure 50, the cracks are rather small (*e.g.*, they do not always extend through the thickness of the Nb_3Sn tubes in the sub-elements’) and can be referred to as *microcracks*. The question then arises whether such microcracks are severe enough to explain the observed performance limitations.

Recent studies have been carried out at CERN on impregnated, 11 T and MQXF cable samples subjected to increasing levels of transverse pressure at room temperature (to simulate effects of collaring or bladdering during magnet assembly) [207][208]. They provide two interesting results:

– radial microcracks start to occur in the sub-elements at transverse pressure levels significantly lower than previously thought (below 150 MPa) [207];

– the crack occurrence precedes the transverse pressure level at which critical current and *n*-value degradations are observed [208].

The latter result can be understood when considering that the current is flowing longitudinally in the tubular sub-elements, and, therefore, radial microcracks are likely not sufficient to hinder its transport.

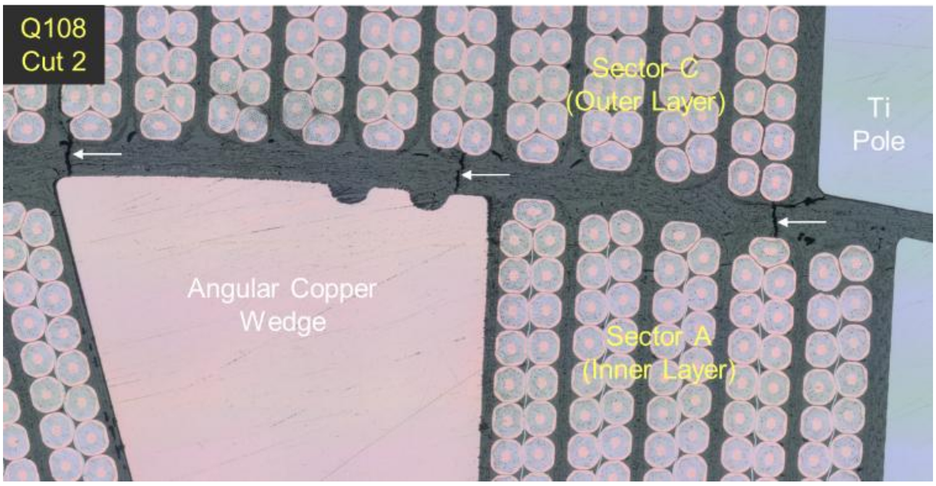

Figure 54: Metallographic analysis of a transverse cut of 7.2-m-long HL-LHC MQXFB quadrupole magnet coil Q108 (used in MQXFBP1), in the area of quench-start localization (towards the middle of coil straight section), illustrating the presence of large cracks having propagated through the interlayer insulation (shown by white arrows; courtesy of M. Crouvizier, CERN).

The above findings raise in turn two more questions:

- At which level of cracking do we start seeing performance limitation or degradation?
- Can we accept microcracks in a magnet?

Some elements for answering to the first question will be given in Section 3.6 The answer to the second question is less easy. Good engineering practices would recommend working in a parameter space that is devoid of cracks, as was achieved for the ITER CS CICCs. From the data in Ref. [207], this would call to limit the transverse pressure applied to MQXF cables to less than ~120 MPa at any time during the magnet life cycle (note that this objective can be met with the new magnet loading procedure described in Section 5.4 and by limiting magnet operation to nominal current).

The above issue is however a point of debate and experiments are being carried out on short magnet models to challenge this conservative requirement [209]. Let us urge caution before stepping back from the recommended good practice: as we have learned from HL-LHC experience, short magnet models are not long prototypes, and crack initiation and propagation are fatigue effects which need to be assessed over the expected lifetime of the magnets.

3.5.2.4 Resin Flaws

As in the case of 11 T coil GE02, the metallographic analyses of MQXFB coil Q108 reveal the presence of cracks in the resin and the conductor insulation. As an illustration, Figure 54 shows an image from the transverse cut marked as “2” in Figure 52. The image features large cracks, which are likely to have originated in the resin and propagated through the interlayer insulation, generating paths between cables of the two layers. Such a situation may become critical if helium gets trapped in these volumes and when large voltage differences generated between the two coil layers, for instance, as a result of a quench.

To address the above concerns, several modifications have been implemented to the vacuum pressure impregnation system and to the procedure applied at CERN on MQXFB coils, which are expected to improve quality (see Section 5.5.6). Metallographic analyses have been carried out on transverse cuts of a coil processed with the improved impregnation procedure, but which has not been used in a magnet assembly and has not been tested at cryogenic temperatures (coil Q126). The images are devoid of cracks in the insulation. However, to be fully conclusive, one would need to carry out a postmortem analysis on a coil that has been assembled and tested in a magnet.

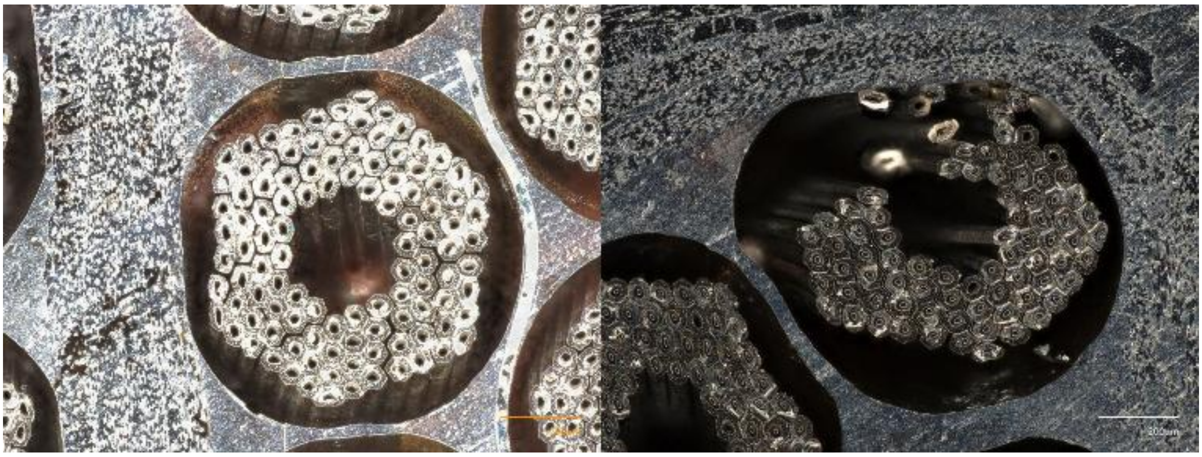

Figure 55: Optical images of resin-impregnated RRP® strands from transverse cross-sections of MQXFBP1 coil Q108 having been submitted to deep copper etching. Left: strand showing no degradation. Right: strand showing a number of broken tubular Nb_3Sn sub-elements (courtesy of M. Crouvizier, CERN).

3.6 Metallographic Analyses of Transverse Cross-Sections of HL-LHC MQXFB Coils After Deep Copper Etching

As explained in Section 3.5, metallographic analysis of transverse cross-sections of conductors or coils is suitable to reveal radial cracks in the Nb_3Sn sub-elements, but these cracks may not be the root cause of transport current limitation. As shown by ASC for ITER CICCs, an additional source of information can be provided by using deep copper etching. Starting from February 2022, CERN started to apply this technique to transverse cross-sections from coil Q108. The etching is done progressively, using HNO_3 diluted at 50% in water, with optical examination between steps. Approximately 400 to 600 µm of copper can be removed by this means.

Figure 55 displays representative optical images of resin-impregnated RRP® strands taken on transverse cross-sections of MQXFBP1 coil Q108 samples having been submitted to a deep copper etching. In the center of each image are the tubular aggregates of Nb_3Sn filaments corresponding to the different sub-elements in the RRP® strand. The void surrounding them corresponds to etched copper, while the white/grey area corresponds to resin or resin-impregnated fiber glass. In the left image, the Nb_3Sn tubes are intact, and the strand is not degraded. In the right image, several tubes, all located on one side of the strand, are missing (the broken pieces are likely to have been washed away by rinsing after copper etching). Unlike radial microcracks, one can expect such severe breakages to hinder current transport and limit performances.

Deep copper etching was applied systematically on the various transverse cuts identified in Figure 52. The results are images like those presented in Figure 56 for Cut 4 (and they are similar for all transverse cuts): among the 2000 strands that are visible in a given cross-section (corresponding to 22 turns for the inner layer, 28 turns for the outer layer, times 40 strands per turn), one, and only one, strand appears degraded. It is always at the same geometrical position in the 2D cross-section: at the top of the inner-layer pole turn, right underneath a small radial extension of the outer Ti-alloy pole spacer, and the degradation always presents the same feature: ~25-30% of the tubular Nb_3Sn sub-elements are missing on the top side of the strand,

The fact that a systematic degradation is observed in the area of quench-start localization and that this degradation is likely to directly impact current transport in the affected strands is of course critical information and a strong pointer to be followed in the determination of the root cause of the problem.

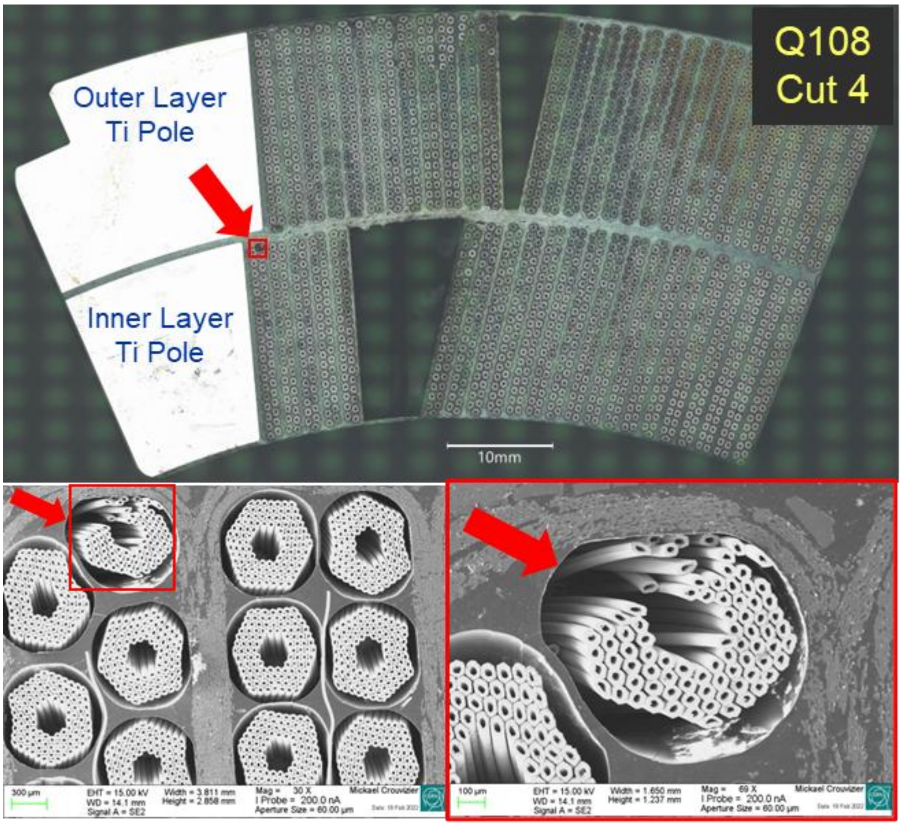

Figure 56: Images from a transverse cut near the longitudinal center of 7.3-m-long HL-LHC MQXFBP1 coil Q108, after deep copper etching; the cut corresponds to the area of quench-start localization marked as "4" in **Figure 52** (Courtesy of M. Crouvizier, CERN).

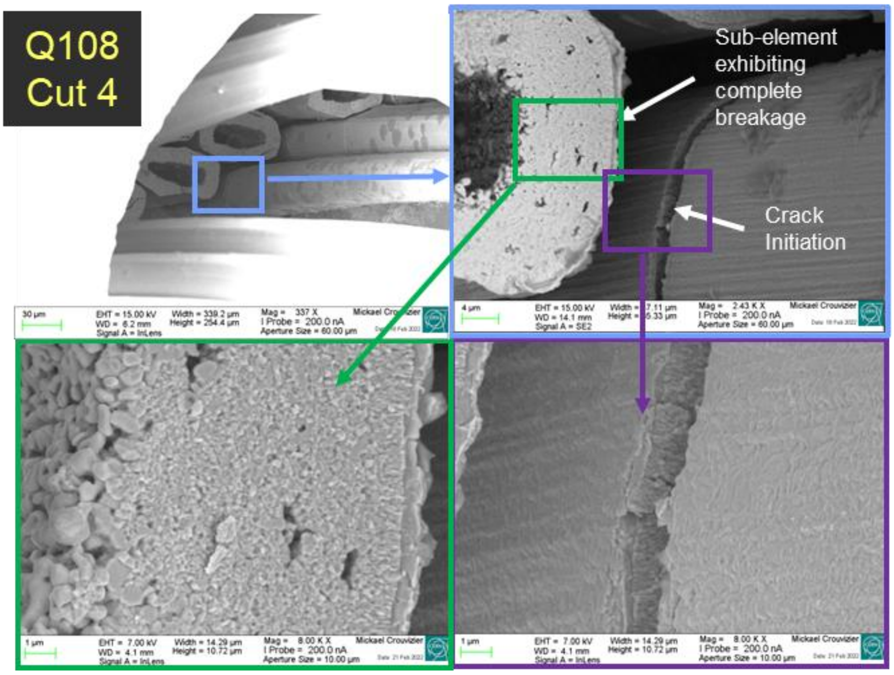

Figure 57: Set of images taken at increasing magnification from a transverse cut near the longitudinal center of 7.3-m-long HL-LHC MQXFBP1 coil Q108, after deep copper etching; the cut corresponds to the area of quench-start localization marked as "4" in **Figure 52** and to the degraded strand at the top of the inner layer pole turn highlighted in **Figure 56** (Courtesy of M. Crouvizier).

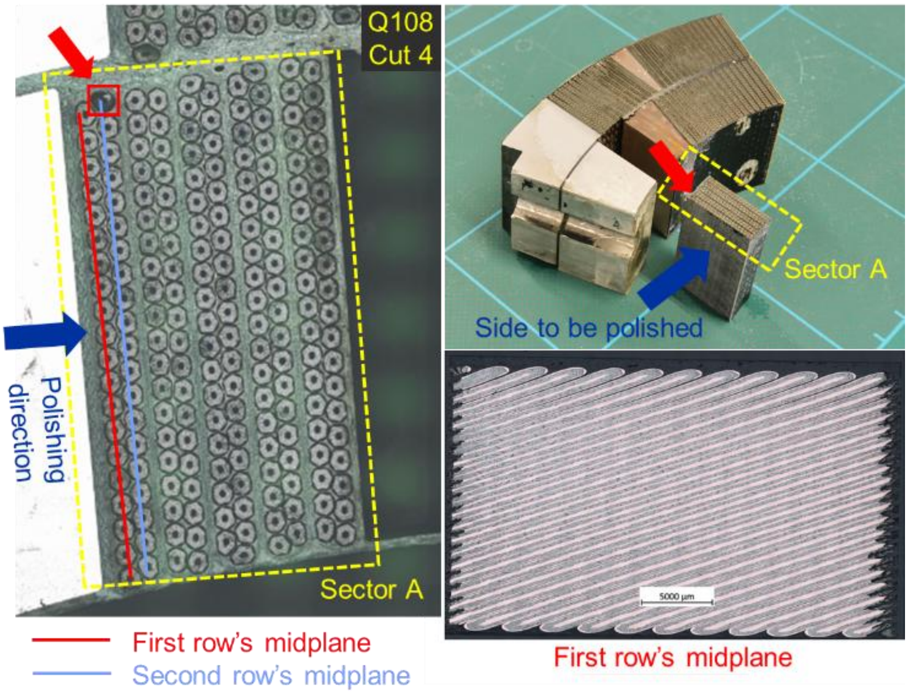

Figure 58: Identification of the longitudinal cuts carried out on a coil sample taken near the longitudinal center of 7.3-m-long HL-LHC MQXFBP1 coil Q108; the sample is the same as the one used for the transverse cross-section examinations in **Figure 56** and **Figure 57** and corresponds to the area of quench-start localization marked as “4” in **Figure 52** (Courtesy of M. Crouvizier, CERN).

3.7 Fractography of Ruptured Nb_3Sn Sub-Elements in HL-LHC MQXFB Coils

Additional information can be obtained by looking at the fracture surfaces of the ruptured tubular sub-elements. Figure 57 shows a set of images taken at increasing magnification for the degraded strand in cut 4 of Figure 56. It appears that the grain morphology at the fracture surface of the ruptured sub-elements is what could be expected from a properly reacted RRP® strand: the grains are uniform, and their size is about 150 nm, which corresponds to the expected grain size in 0.85 mm, 108/123 RRP® strands heat treated according to the temperature cycle applied to MQXFB coils (see Section 5.5.5.2).

The above observation implies that the fracture occurred after completion of the high-temperature plateau of the Nb_3Sn heat treatment. If the fracture had occurred before (for instance, at the time of strand manufacture or cabling), there would have been deformation and even leakage of Sn sources and the grains would not be so regular. This observation provides us with a clear indication of the timing of the rupture.

3.8 Metallographic Analyses of Longitudinal Sections of HL-LHC MQXFB Coils

Having identified one degraded Nb_3Sn strand in the two-dimensional cross-sections examined in Section 3.6, the next question that arises is whether it is a singular event in the longitudinal direction as well, or if the degradation also extends to neighboring strands. This can be examined by carrying out longitudinal cuts and polishing them as it was done on the 11 T coil samples at ASC (see Section 3.2).

Figure 58 illustrates the process that was followed to extract the relevant coil sector from the coil sample used previously and the polishing that was applied to enable the examination of longitudinal sections at the level of the midplanes of the first and second row of strands in the inner-layer pole turn.

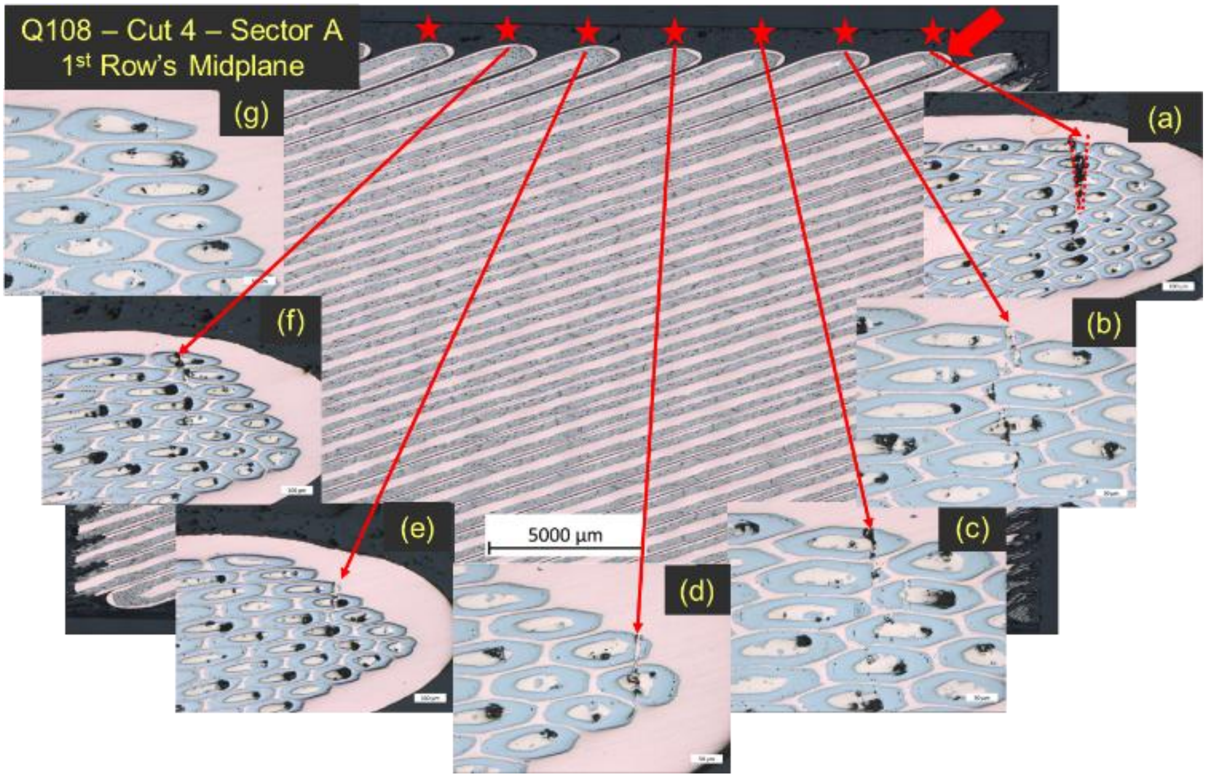

Figure 59: Images taken at the midplane of the first strand row of the inner-layer pole turn conductor of the coil sector that was extracted from the sample taken near the longitudinal center of 7.3-m-long HL-LHC MQXFBP1 coil Q108 as detailed in **Figure 58**; the sample is the same as the one used for the transverse cross-section examinations in **Figure 56** and **Figure 57** and corresponds to the area of quench-start localization marked as "4" in **Figure 52** (Courtesy of M. Crouvizier, CERN).

Figure 59 displays images for a longitudinal section corresponding to the midplane of the first row of strands. The images show that, starting from the degraded strand identified in Figure 56, adjacent strands also exhibit sub-element fractures, albeit with a severity that progressively reduces when moving away in the longitudinal direction. Let us point out that, due to the Rutherford-type cable twist pitch, the strands assume a hairpin-like trajectory at the cable edges. This explains why the degraded strand which appears at the top of the second row of strands in the transverse section in Figure 58 also appears in the longitudinal section of Figure 59 which corresponds to the first row of strands. Let us note also that the observed fractures have a distinctive V-shape (in particular for the degraded strand identified as "a"). Such a V-shape is usually characteristic of a fracture due to bending, which, in the case under examination, would have taken place in the plane of the conductor, *i.e.*, in the so called *hard-way bending* direction.

Examination of the longitudinal sections can also be used to look at the fracture surfaces of the collapsed sub-elements. Figure 60 presents a set of images taken at increasing magnification in the area of the V-shape facture observed on the strand marked as (a) in Figure 59. It appears that the grain morphology is similar to that of Figure 57. Piecing back together the various findings, this leads us to conclude that the cable hardway bending at the origin of the fracture is likely to have taken place after completion of the high temperature plateau of the Nb_3Sn coil heat treatment.

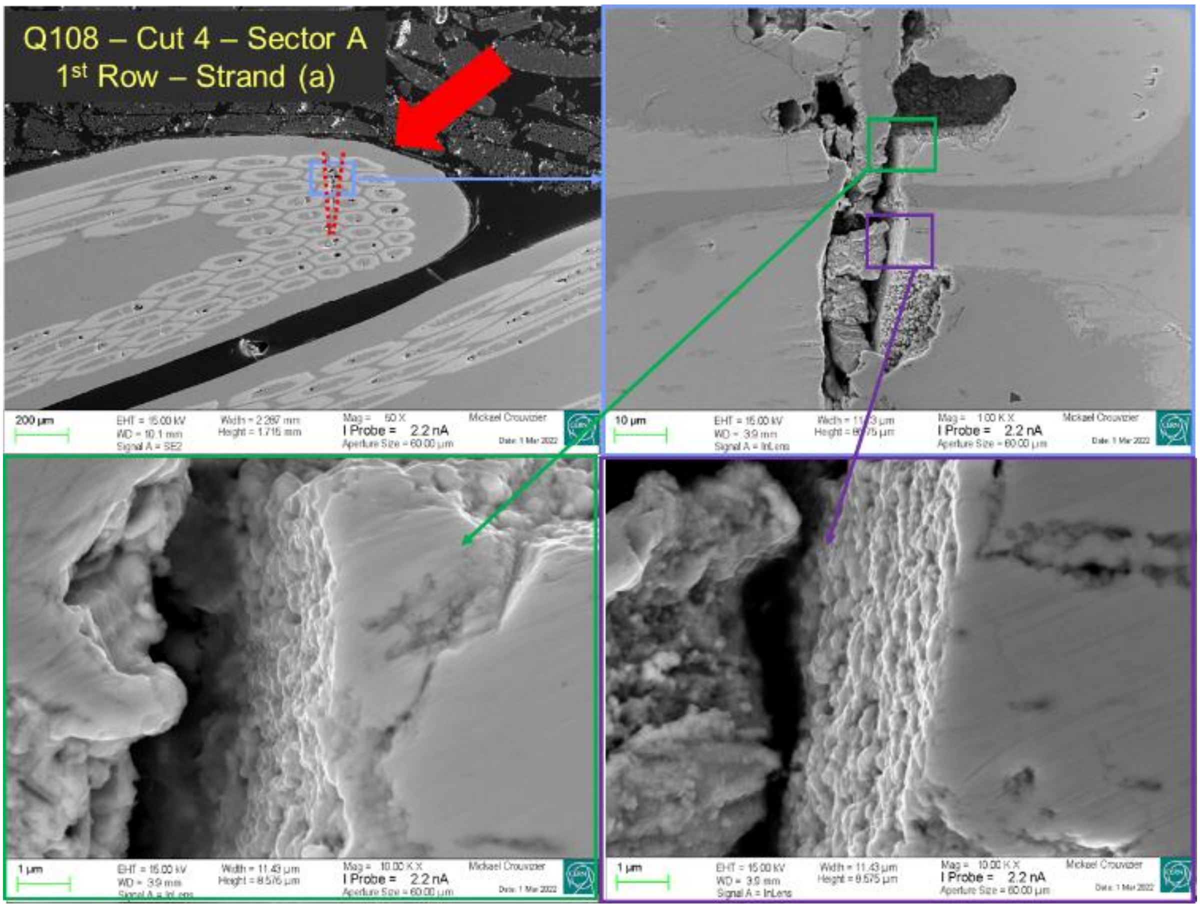

Figure 60: Set of images taken at increasing magnification in the area of the V-shape fracture observed on Strand (a) at the midplane of the 1st row in the longitudinal section of **Figure 59** (Courtesy of M. Crouvizier, CERN).

3.9 Complementary Post-Mortem Analyses

Having identified the timing of the fracture (sometime after completion of the Nb_3Sn coil reaction) and the type of mechanical loading that can produce such a fracture (hard-way bending of the coil inner-layer pole turn), the next step is to try to identify mechanical features and/or manufacturing steps that can produce such loading.

To carry out this analysis, it was decided to cut many transverse slices at regular intervals along the length of coil Q108, and to carry out examination of transverse sections after deep copper etching. Figure 61 shows selected results from this examination (there were many more samples that were examined, leading to the same conclusion): there appears to be a few slices where transverse cross-sections exhibit a degraded strand at the top of the inner-layer pole turn, but the cross-sections with the degraded strand always appear to be in the vicinity of a Ti-alloy pole transition. The longitudinal locations of the transverse cross-sections with a degraded strand are not limited to the area of quench-start localization and occur on both sides of the coils (the so-called *layer-jump side* but also on the *opposite to layer-jump side*). These observations seem to point to a systematic problem on the inner-layer pole turn near the Ti-alloy pole transitions.

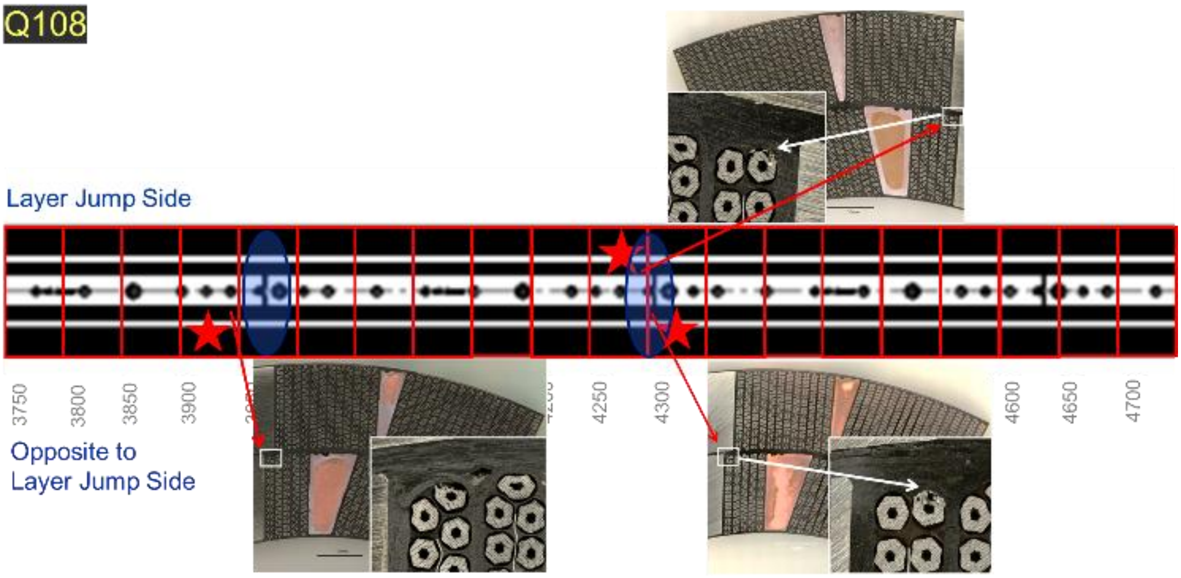

Figure 61: Systematic examinations of transverse cross-sections along the length of 7.3-m-long MQXFBP1 coil Q108, showing evidence of a correlation between cross-section exhibiting a degraded Nb_3Sn strand at the top of the inner-layer pole turn and the transitions between Ti-alloy poles (Courtesy of M. Crouvizier, CERN).

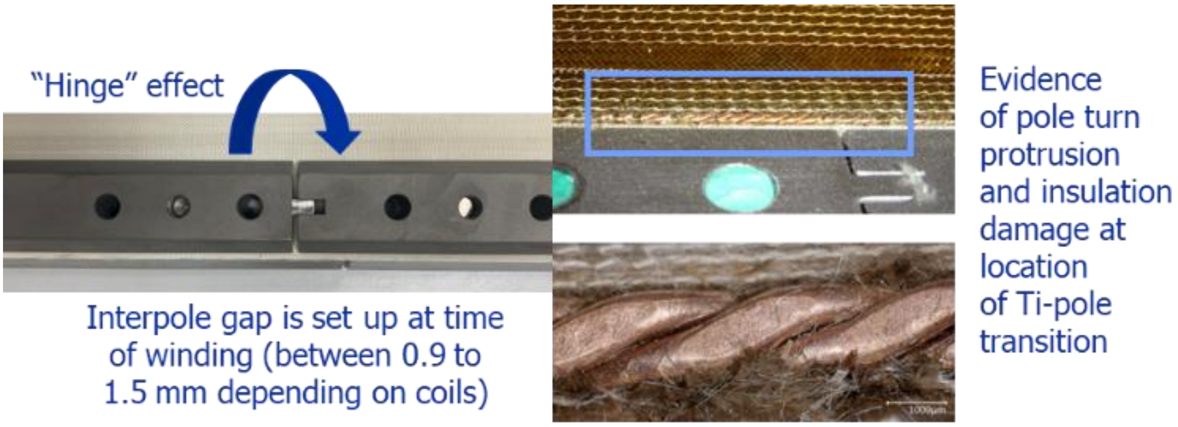

Figure 62: Quality control records after opening the retort used for heat treatment of 7.3-m-long MQXFB coils like coil Q108. Top right: evidence of inner-layer pole turn protrusion at a Ti-alloy pole transition. Bottom right: evidence of insulation degradation at the conductor edge. Left: schematic of "hinge effect" at the Ti-alloy pole transitions (Courtesy of N. Lusa and A. Milanese, CERN).

3.10 Complementary Findings from QC Manufacturing Records of MQXFB Coils

To find a possible explanation for what is happening, a thorough review of quality control records during coil manufacture was carried out, in particular for the process steps between the opening of the heat treatment retort and the closure of the vacuum impregnation mold. A more complete description will be provided in Section 5.5, but some key information can already be derived from the images presented in Figure 62:

- after opening of the heat treatment retort, the inner-layer pole turn exhibits clear evidence of protrusions in the vicinity of Ti-alloy pole transitions, which correspond to cable hardway bending;
- at these longitudinal positions, the fiber glass braid that normally surrounds the cable appears to have been ripped off from the exposed conductor edge, probably by frictional effects;

- at the transitions, Ti-alloy pole pieces are pinned together in a manner that does allow some vertical displacement of one piece with respect to another, resulting in a risk of what can be referred to as a *hinge effect*.

Summarizing the above findings: it is likely that, when opening the heat treatment retort, strain energy stored in the coil is released, which, at the Ti-alloy pole junctions, results in a local hardway bending of the inner pole turn and an outward protrusion. Then, at the time of closure of the vacuum impregnation mold, which is of very accurate dimension, the protruded length of conductor is bent back to its normal position. These two successive hinge effects are likely to be the cause of the observed breakages. Then, the next question is why do we have such localized strain releases in the vicinity of the Ti pole junctions? This issue will be addressed in Section 5.5.

As illustrated in the example above, at the time of coil Q108 manufacturing, there was yet no indication that deviations like the one observed in Figure 62 could have such deleterious impacts. The events were nevertheless carefully recorded, and, afterwards, prove instrumental in the root cause analysis of the quench performance limitation of MQXFB magnets. Other similar examples will be provided in Sections 4 and 5. The lesson to be learned is that, even if at times QA/QC may appear as a burden on the production team, it is a critical and powerful tool, not only to ensure a reliable production, but also to enable problem identification in the case of subsequent non-conformities. Of course, QA/QC should be independent from the organic management line and should be implemented in a top/bottom manner to ensure free information flow and the possibility of triggering alarms.

3.11 Summary of Post-Mortem Analyses and Findings from ITER to HL-LHC

Figure 63(a) and (b) presents a summary in a nutshell of the post-mortem observations made, in the early 2010s, on an ITER cable-in-conduit conductor sample, after testing at the SULTAN facility, and, in the early 2020s, on a HL-LHC MQXFB coil, after assembly and testing in a magnet.

One should, of course, bear in mind that there are significant differences:

- cable type: rope-type for ITER versus Rutherford-type for HL-LHC;
- conductor configuration and cooling: cable inserted into a conduit with a ~30% void fraction and cooled by a forced flow of supercritical helium for ITER versus cable wound into a coil that is resin-impregnated and bathed in superfluid helium for HL-LHC.

However, the observed degradation at the Nb_3Sn strand level are strikingly similar: 20 to 30% of the reacted Nb_3Sn area is broken on one side of the strand, corresponding to breakages of individual filaments in the bronze strand used for ITER CICC shown in Figure 63(a), or corresponding to breakages of tubular sub-elements of aggregated filaments in the RRP® strand used for HL-LHC magnets shown in Figure 63(b).

In the case of ITER CICCs, the root cause of the degradation was attributed to excessive strand bending under the effects of the Lorentz force. The issue was resolved by tightening twist pitches, in particular, that of the triplet of the first cabling stage, to provide better local strand support. As detailed thereafter, for MQXFB coils, the root cause of the degradation is attributed to detailed aspects of the coil manufacturing processes, resulting in local hinge effects causing conductor hard way bending, and the issue was resolved by iterating on the manufacturing processes to avoid these deformation/displacements and achieve better coil size uniformity.

In these two cases, post-mortem analyses on conductor or coil samples have proven instrumental in identifying the root causes of the performance degradation and/or limitation and in devising successful corrective actions plans.

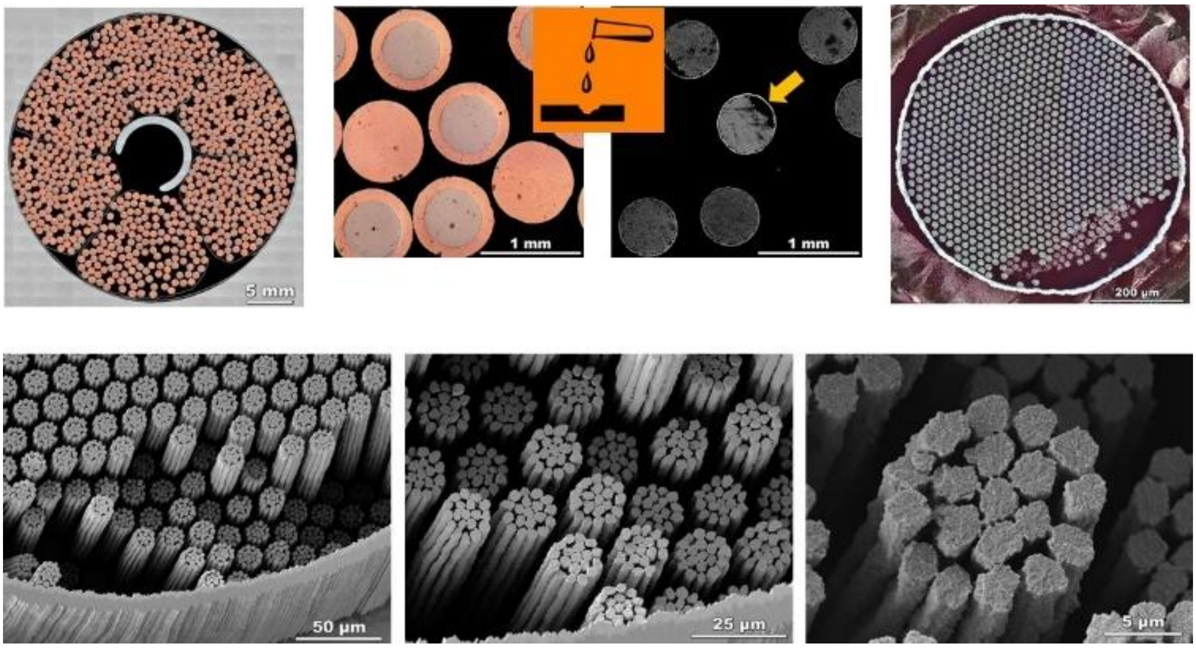

Figure 63(a): Metallographic analysis of a cross-section of a cable-in-conduit conductor for ITER after testing in SULTAN, showing by progressive levels of magnification, Nb_3Sn (bronze) strand degradation down to the level of individual filaments. (Courtesy of C. Sanabria and P. Lee, ASC, 2010s).

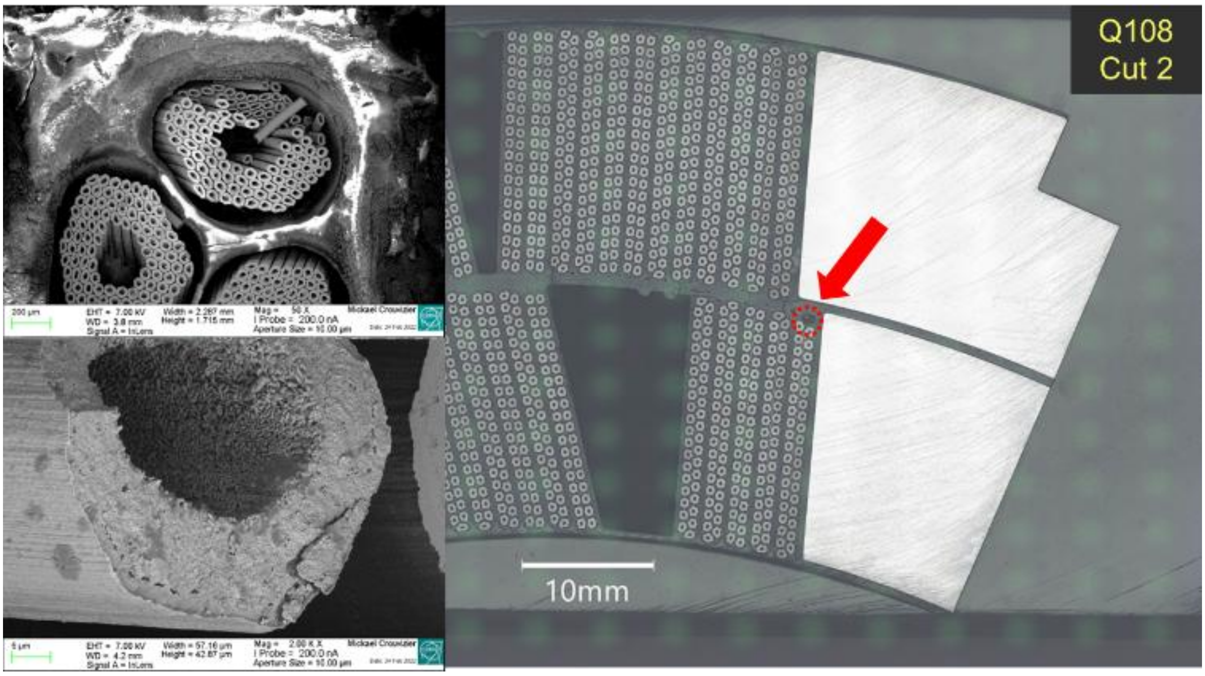

Figure 63(b): Metallographic analysis of a cross-section of a HL-LHC MQXFB coil after testing in a magnet, showing by progressive levels of magnification, Nb_3Sn (RRP®) strand degradation down to the level of individual sub-elements. the cut corresponds to the area of quench-start localization marked as "2" in **Figure 52** (Courtesy of M. Crouvizier and S. Sgobba, CERN, 2020s).

4 Root-Cause Analysis and Recovery Plan for HL-LHC 11 T Dipole Magnets at CERN

4.1 Strategy and 2nd Task Force

As explained in Section 1.5.5.3, in December 2020, the CERN management decided to forsake the installation of 11 T dipole magnets during the Long Shutdown 2 of the LHC. By that time, five 5.3-m-long, 60-mm-two-in-one-aperture magnets had been produced (but only four were cold tested) and a total of 35 coils had been completed, including 8 which were accepted as conforming but had not been assembled (referred to as virgin coils). These 8 coils could potentially be used to manufacture two additional two-in-one-aperture magnets.

At the same time, a 3-phase strategy on how to proceed with the 11 T project was developed and proposed to the CERN management. The strategy was eventually reviewed and endorsed by a special meeting of the CERN Machine Advisory Committee (C-MAC) on 11 March 2021.

As illustrated in Figure 64, the 3-phase strategy was articulated as follows:

- Phase 1: pursuit of investigations to identify root

causes of performance degradation;

- Phase 2: assembly and test of a short model magnet and, if successful, of a full-length prototype, implementing additional mechanical features and instrumentation to improve mechanical support of coil and magnet ends;
- Phase 3: relaunch of production and test of 11 T dipole magnets for tunnel installation.

As part of Phase 1, two families of root causes were considered:

(1) weaknesses/non-conformities internal to the magnet coils;

(2) weaknesses/non-conformities in mechanical support of coil/magnet ends.

Regarding (1), if observations cast serious doubts on conductor placement/support within coils, then, any solution would require re-engineering and re-qualification efforts at coil level which would be beyond HL-LHC project scope, as it would not fit the installation schedule and would need to be supported by another funding source.

Regarding (2), if analyses confirm that there are issues with mechanical support of coil/magnet ends, then, it is worth developing and qualifying corrective/recovery actions.

Phase 1 was to be concluded by an internal technical review to decide whether to proceed with Phase 2.

Phase 2 was to be concluded by an external review to decide whether to proceed with Phase 3.

The scope of Phase 3 –one or two sets of two magnets plus spares– was to be reassessed in due time.

In addition, a 2nd 11 T Task Force was set up in late March 2021 to ensure a proper follow-up of Phase 1 activities and of C-MAC recommendations. A comprehensive report compiling all the analyses that were carried out by the various stakeholders involved in the Task Force was completed on 31 July 2022 [210]. The following sections summarize the main investigation results, based on which it was decided in October 2021 to proceed with Phase 2.

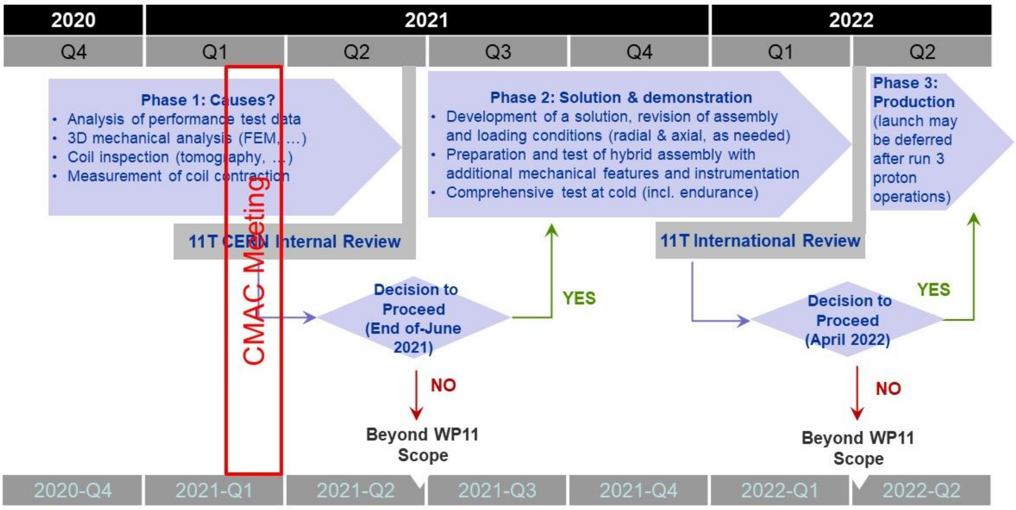

Figure 64: Timeline and decision flow chart for HL-LHC 11 T dipole magnet project at CERN following the decision to forsake tunnel installation during Long Shutdown 2 (Courtesy of F. Savary, CERN).

4.2 Salient Results from Series Production

4.2.1 Production Strategy and Industrial Contract

Before reviewing the various issues that were revealed by magnet/coldmass disassembly and coil post-mortem analyses, let us first present salient results from the series production of 11 T dipole magnet coils at CERN, which provide relevant technical and managerial information on the state of the art of Nb_3Sn technology industrialization.

For the 11 T dipole magnets, it was decided early on to award a contract to an industrial supplier, who would be responsible for the production of coils and collared-coil assemblies, on the CERN premises, using the CERN procedures and following agreed Manufacturing and Inspection Plans (MIPs). The contract was signed with Alstom/GE Steam Power, based in France, on 24 January 2018 and was completed on 31 January 2021 [211].

The initial contract scope included a total of 30 coils (16 for the assembly of 4 two-in-one-aperture magnets for tunnel installation, 8 for the assembly of 2 two-in-one-aperture spare magnets, and 6 additional coils as contingency to cover losses during production) and 12 collared-coil assemblies (8 to produce 4 two-in-one-aperture magnets and 4 to produce 2 spare two-in-one-aperture magnets). The contract was eventually extended to 35 coils and 15 collared-coil assemblies. The additional 5 coils were meant to compensate 5 major non-conformities raised during production (resulting in 4 coil rejections and 1 quarantined coil).

Altogether, and despite the COVID-19 pandemic, which surged in the course of the contract and resulted in a delay of ~3 months, it was a fruitful experience on both sides. The industrial supplier managed to set up a stable core team at CERN and completed its work scope in ~3 years. It also set up a robust QA/QC program that inspired several useful iterations of the CERN-developed execution and control procedures. The poor performances of the 11 T series production magnets are not imputable to the industrial supplier, but to the fact that the technology and manufacturing procedures were still in a development phase and not ready for industrialization. Several issues that were discovered along the way called for stop orders, but thanks to the facts that the production took place at CERN and that there was a good collaboration between CERN and GE, the two teams could work efficiently together in developing suitable recovery actions in a limited time.

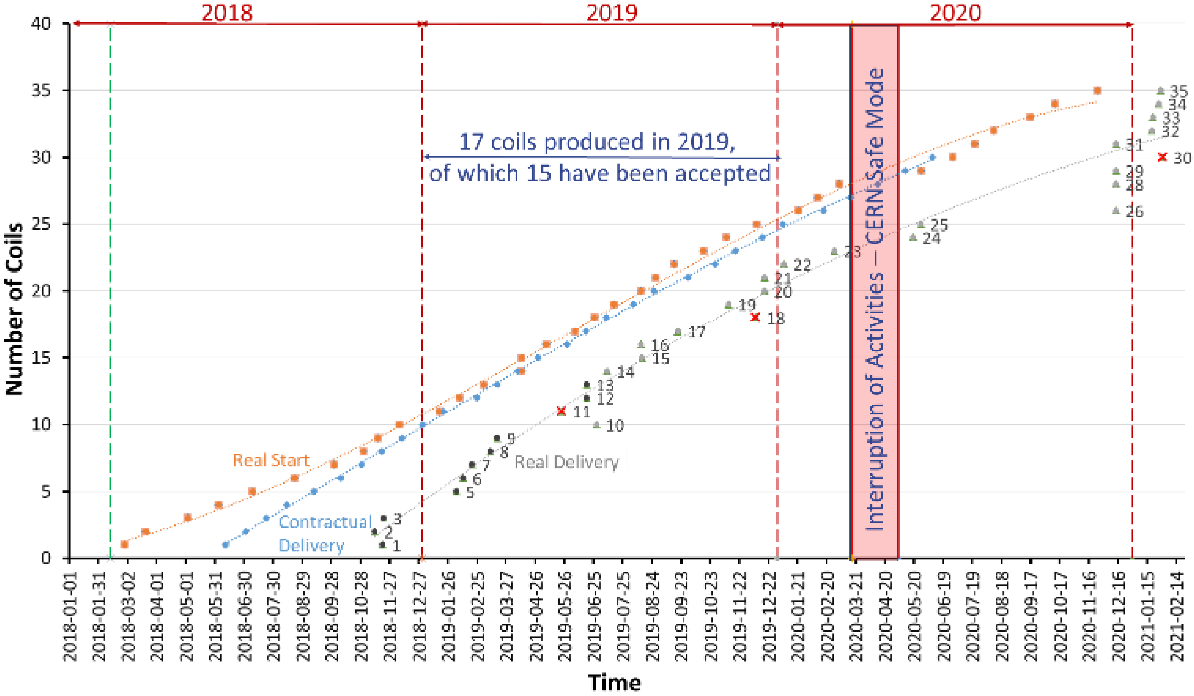

Figure 65: Dashboard of 5.3-m-long, HL-LHC 11 T dipole magnet coil production by industrial supplier on CERN premises with one production line (Courtesy of F. Savary, CERN).

One of the main lessons learned from this experience is that Nb_3Sn accelerator magnet technology is not yet at the required maturity level for industrialization. This consideration was one of the driving reasons for the decision taken in early 2021 to internalize at CERN and by CERN the production of MQXFB coils and magnets, while the initial plan was to carry out a call for tender and to outsource the work. This decision aligned CERN with the strategy of AUP collaborators who had already decided to share among themselves MQXFA magnet production without going to industry (except, of course, for specific procurement of components and/or services). The serious difficulties subsequently encountered and resolved by MQXFB prove that this was the most cost and technically effective solution.

4.2.2 Coil Production Rate and Learning Curve

The supply contract enables us to get some information on the production rate that may be achieved in industry as well as on the learning curve for coil manufacturing.

Figure 65 displays a dashboard of 5.3-m-long, HL-LHC 11 T dipole magnet coil production by the industrial supplier on CERN premises with one production line. We can see the impact of COVID-19 in 2020, but in 2019, the production appears to have reached a stable rate of ~1.5 coils per month. Figure 66 shows the evolution of the duration of the manufacturing process for one coil versus coil sequence. The plot shows a clear learning curve which tends to an asymptotic duration of ~90 days.

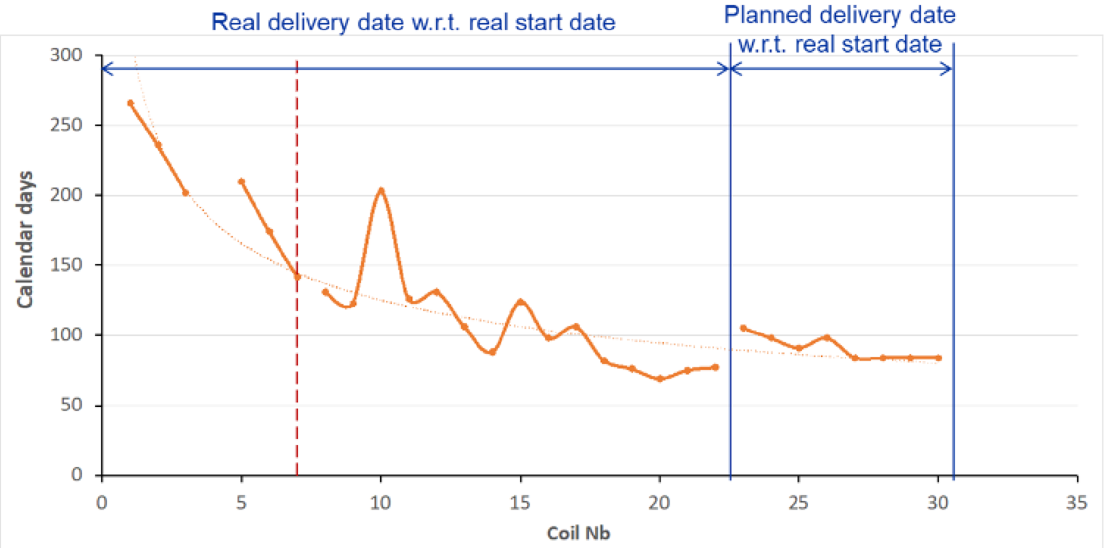

Figure 66: Duration of manufacturing process versus sequential number for 5.3-m-long, HL-LHC 11 T dipole magnet coil production by industrial supplier on CERN premises; data rely on expected delivery dates for last part of production to remove COVID-19 bias (Courtesy of F. Savary, CERN).

4.2.3 Coil Reproducibility Over Series Production

One of the main parameters to judge the quality of an accelerator magnet coil production is the uniformity and reproducibility of azimuthal sizes, which play a critical role in both mechanical assembly [212] and field quality [213][214]. The 7 prototype coils and 35 series production coils provide a good statistical sample for such analysis [215].

As explained in Section 5.5.7, the azimuthal arc lengths (left and right) and radial dimensions (inner and outer) of the coils are measured as part of the final inspections upon manufacturing completion. By aligning the data on the nominal outer coil radius from the CAD model, it is possible to determine azimuthal coil size deviations with respect to nominal, also referred to as excess [101][215][216]. Note that due to the presence of a common, 2-mm-thick, stainless-steel loading plate, placed in the pole region, covering both inner and outer layers, and impregnated with the coil, the azimuthal size measurements correspond to a radial average over the two coil layers. The choice of a common loading plate was made to ensure a more balanced stress distribution between the two coil layers despite their different spring constants. For future applications, it may be preferable to use for the loading plate a material having properties closer to those of the coils and with better resin adhesion.

Figure 67 presents a summary plot of the total (sum of left and right branches) azimuthal excess per coil as a function of coil production sequence. After some large variations during the production of prototype coils, and two outliers due to some data processing issues, the production appears quite stable, with a median value in the ±0.1 mm range (for coil with a 60.7 mm outer radius), and a box size (corresponding to the second and third quartiles) in the 60–165 µm range. These values are comparable, and even slightly better than what was achieved on short model coils [101]. These results confirm the supplier’s ability to implement good quality control and provide a reference on the reproducibility that can be expected over such production. Let us recall that a change was introduced in the coil manufacturing process starting from series coil GE10, where it was decided to stop impregnating quench protection heaters with the coil and to start adding them on top of the impregnated coils at the time of coil assembly (see Section 2.3.4.4). This resulted in a reduction of coil outer diameter from 60.8 to 60.7 mm, which impacted the azimuthal excess median value, but not the box or whisker sizes. The change was implemented to improve the electrical insulation robustness and mitigate failure risks.

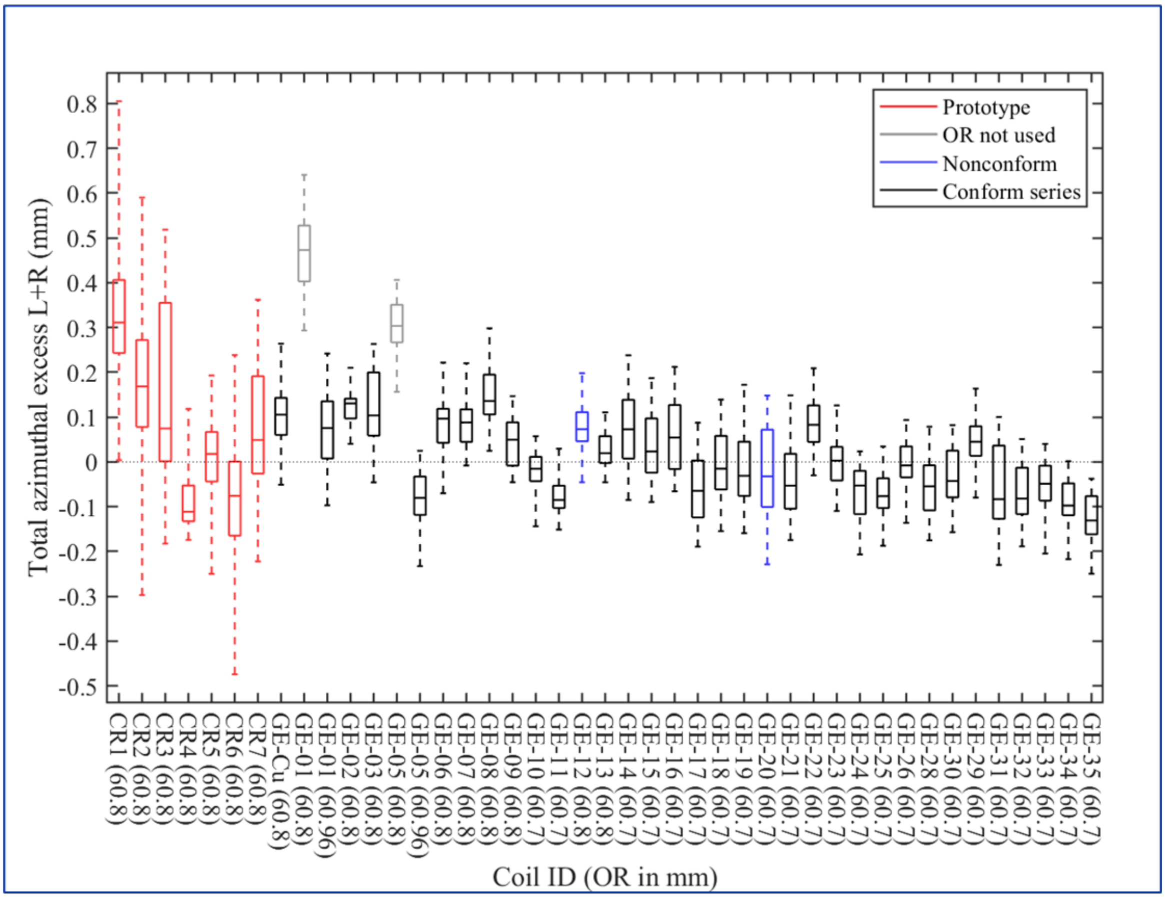

Figure 67: Summary plot of total (sum of left and right branches) azimuthal excess per coil versus coil production sequence for 5.3-m-long, HL-LHC 11 T dipole magnet program at CERN. The coil ID and nominal outer radius are indicated on the horizontal axis. The box displays the second and third quartiles and the median value while the whiskers display the minimum and maximum values along each of the coils. The change of coil outer radius from 60.8 mm to 60.7 mm corresponds to coil with and without impregnated quench heaters (Courtesy of D. Pulikowski, formerly from CERN, and F. Savary, CERN).

4.2.4 Longitudinal Variation of Azimuthal Coil Size and Shimming Plan

In preparation for collaring, two coils are mated together and surrounded by a number of layers of polyimide providing the ground insulation (5 x 0.125 mm for coils with impregnated quench heaters, 4 x 0.125 mm + 1 x 0.075 mm for coil with external heaters –see Section 2.3.4.4). The peak stress experienced by the coil assembly at any given longitudinal location during collaring (at the time of maximum press force) and the residual prestress (after key insertion and press force removal) will depend on the combined azimuthal arc lengths of the mated coils at this location.

As an illustration of azimuthal variations within a coil assembly, the bottom curves of Figure 68 feature estimates of the average combined excess between top and bottom coils on each side of the assembly of coils GE08 & GE09 (used in collared-coil assembly CC04) as a function of longitudinal position. The plots show excess variations along the coil of the order of 150 µm peak-to-peak. Assuming a coil Young's modulus of ~30 GPa, this could result in a variation of up to 90 MPa for the coil inner layer and of up to 65 MPa for the coil outer layer, which is not acceptable.

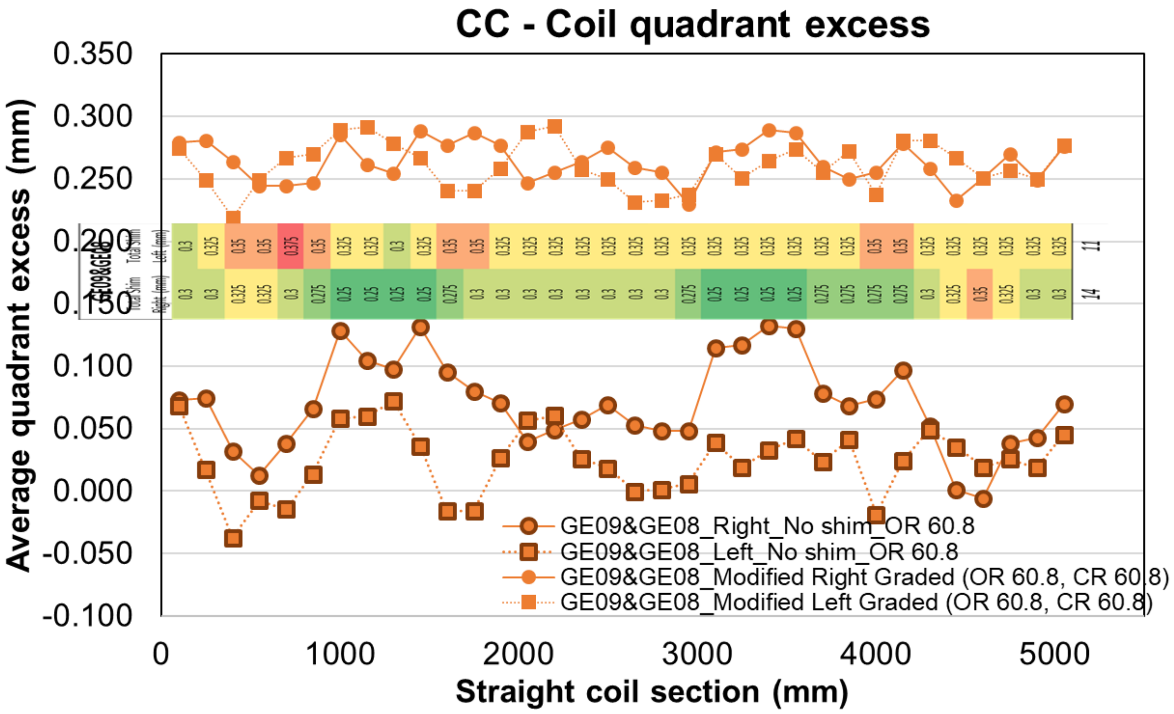

Figure 68: Azimuthal coil size variations and shimming plan for left and right sides of 5.3-m-long HL-LHC 11 T coil assembly made up of series production coils GE08 & GE09 versus longitudinal position. Bottom: combined (top/bottom) average azimuthal excess as derived from coil size measurements. Middle: proposed shimming plan. Top: corrected average azimuthal excess including variable shims (Courtesy of J.-L. Rudeiros Ferńandez, formerly CERN, now LBNL, and F. Savary, CERN).

To compensate for these azimuthal excess variations along the coil assembly, it was decided to rely on longitudinally graded, stainless-steel shims with 25-µm steps. The choice of 25-µm steps was done after qualification tests with pressure-sensitive papers, confirming that the stress concentration at the step edges was limited (< 20 MPa) [217]. The graded shims are assembled and jointed together by tack-welding to form a continuous piece. They are mounted on top of the ground insulation (adjacent to the Ti-alloy pole pieces) and, in a given collared-coil assembly, are identical top/bottom but can be different between left and right.

As an illustration, the middle part of Figure 68 shows the shimming plan for the left and right side of collared coil assembly CC04, while the top curves show the resulting combined azimuthal excess (including shims). The correction allows the peak-to-peak variations to be reduced to a range of ~50 µm, which becomes acceptable in terms of stress range. It can also be seen that the corrected azimuthal coil size excess stays below the target value of 300 µm recommended by the 1st 11 T Task Force to avoid any risk of coil overstress during collaring [100].

To complete this overview, Figure 69 presents a summary plot of corrected combined azimuthal excess for the coil assemblies used in the two short magnet models issued from the 1st 11 T Task Force and for the eleven 5.3-m-long coil assemblies produced by the industrial supplier as part of its contract for series production [217]. Thanks to the stable level achieved in Figure 67, the corrected combined average azimuthal excess for the series production coil assemblies appears also very stable, with a median value within 15 µm, a box size (corresponding to the second and third quartiles) below 40 µm and a maximum value (top of whiskers) below 300 µm. This provides an idea of what can be achieved in an industrial production, which is quite remarkable.

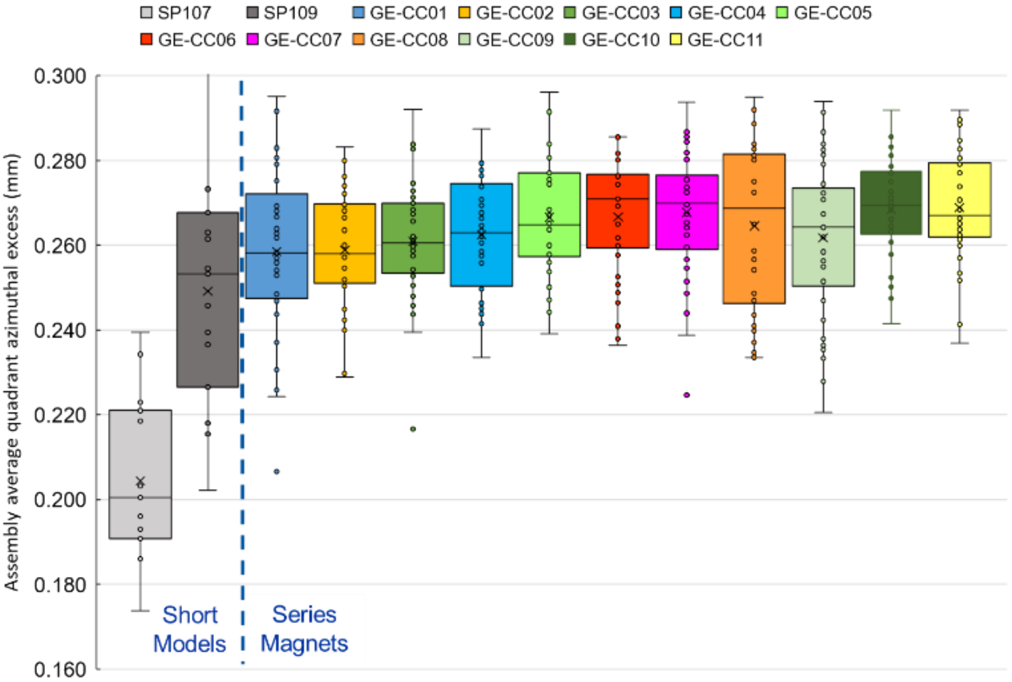

Figure 69: Summary plot of corrected combined (top/bottom) average azimuthal coil excess (including variable shims) for the short model coil assemblies issued from the 1st 11 T Task Force (in light and dark grey) and from 11 x 5.3-m-long coil assemblies produced by the industrial supplier selected for the production of HL-LHC 11 T dipole magnet coils and collared-coil assemblies. The box displays the second and third quartiles and the median value while the whiskers display the minimum and maximum values along each of the coil assemblies (Courtesy of J.-L. Rudeiros Ferńandez, formerly CERN, now LBNL, and F. Savary, CERN [217]).

4.2.5 Comparison Between 5.3-m-long 11 T Coils and 7.2-m-long MQXFB Coils

It is noteworthy that the 5.3-m-long 11 T dipole magnet coils do not exhibit the systematic hump that has been observed towards the longitudinal center of 7.2-m-long MQXFB quadrupole magnet coils (see Section 5.5.8). The 11 T and initial MQXFB coils were produced following similar procedures (see Section 5.5) and relied on ceramic binder application on the outer surfaces of both inner and outer layers. The main differences between the two productions are: coil length, thickness, and radius, material of pole pieces during heat treatment and, probably, radial pile up of materials between coil outer radius and heat treatment retort inner radius. A more detailed analysis would be required to draw any conclusion and explain the different behavior.

4.2.6 How Much Can We Correct by Shimming?

The data reported above clearly demonstrate that undesirable azimuthal coil size variations can be partly corrected by a customized shimming plan. This raised the question of how much variability is tolerable and how much shimming can be applied before we observe performance degradation.

The initial plan of the 1st 11 T Task Force was to build two identical short, single-aperture magnet models, referred to as MBHSP107 and MBHSP108, to qualify the new shimming and collaring procedures and assess reproducibility. For this task, several new short model coils were produced, but among those, two of them (SD118 and SD119) experienced an issue during resin impregnation and came out oversized and highly non-uniform compared to other coils (see Figure 70). To save time, it was decided to assemble MBHSP107 with two nominal-size coils (SD120 & SD121) and to use the other magnet model to experiment with oversized coils [218]. As this was not the intended plan, the model magnet was renamed MBSP109 and was assembled with 1 nominal-size coil (SD123) and 1 oversized coil (SD119) compensated by graded polyimide shims.

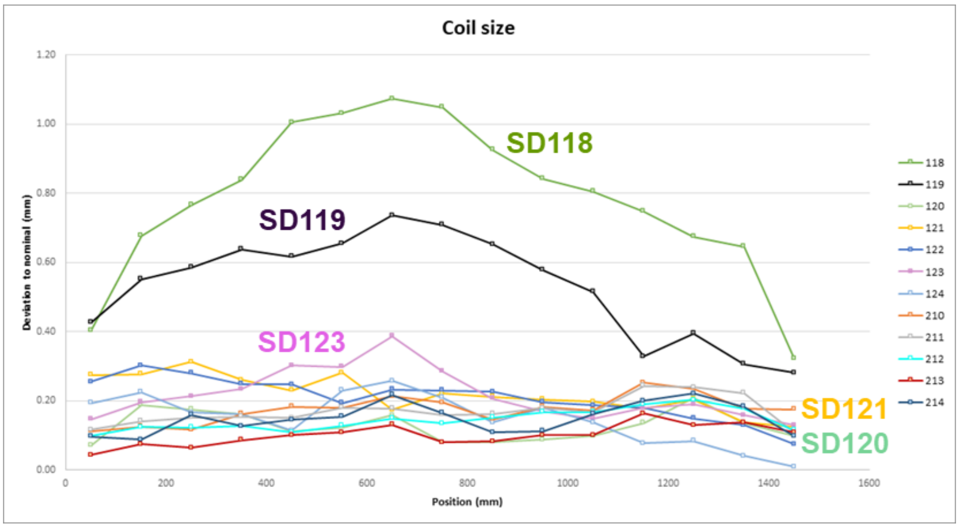

Figure 70: Summary plot of azimuthal coil excess measured on selected short HL-LHC 11 T dipole magnet model coils produced at CERN (Courtesy of J.-C. Perez and F. Savary, CERN).

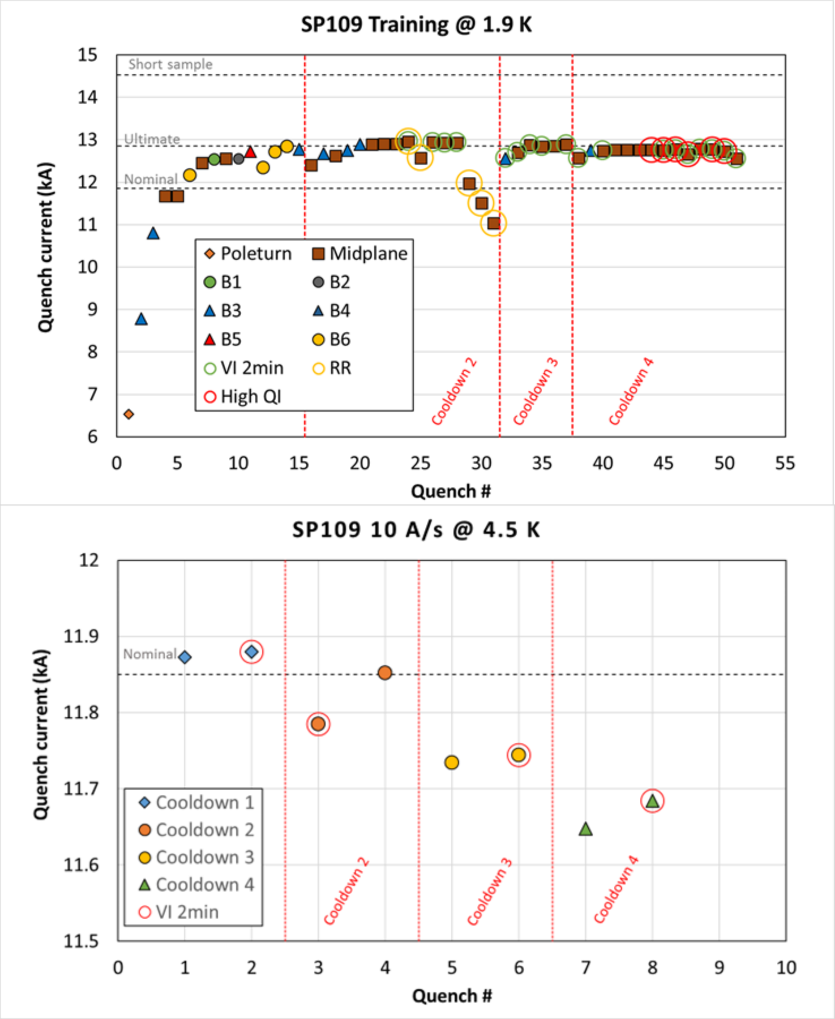

Figure 71: Quench performance of short, 60-mm-single-aperture HL-LHC 11 T dipole magnet model MBHSP109. Top: performance at 1.9 K. Bottom: quench limits at 4.5 K as a function of warm-up/cooldown cycles (Courtesy of G. Willering, CERN).

The top part of Figure 71 summarizes the quench performance of MBHSP109, which was tested at the end of 2019 and in early 2020. The model magnet was trained to a level close to ultimate current at 1.9 K (12.84 kA) and underwent a total of 3 warm-up cooldown cycles to room temperature, after each of which it could be retrained close to ultimate current. However, as can be seen in the bottom part of Figure 71, the quench limit at 4.5 K appears to degrade as a function of the warm-up/cooldown cycle. This performance degradation is confirmed by the progressive degradation of the *V–I* curves displayed in Figure 24. In addition, most of the quenches are located at the coil midplane, like in earlier magnet models, where the highest peak transverse stresses are experienced and where cracks in the Nb_3Sn phase have been observed (see Section 3.5.1). Furthermore, the degradation of both the quench limit and the V–I curve is further enhanced following quenches with hot spot temperature in excess of 300 K (these tests were carried out at the end of the 4th test cycle).

The above results show that MBHSP109 is much less robust than MBHSP107 (note that MBHSP107 was powered to ultimate current after the first, second and fifth cooldown ‒see top of Figure 11). Of course, one cannot draw a direct link between the degraded performance and the reliance on a highly non-uniform coil in its assembly, but one cannot exclude it either and it casts doubts on such practice.

A reasonable conclusion from this experiment is that it is better to keep tight control of coil uniformity during production (at the level demonstrated in Figure 67) and to avoid pairing outliers. Even though a clever shimming plan may enable to partly correct variability, it will not eliminate singularities (see the whiskers' size for SP109 compared to other magnets in Figure 69), adding a level of risk that cannot be quantified. Another outcome from these test results was the decision by the HL-HL project management to cap the testing of full-length 11 T dipole magnets to nominal current + 100 A. This decision was later extended to cap the testing of MQXFA and B quadrupole magnets to nominal current + 300 A, in-line with what is applied for the re-commissioning of the LHC main dipole and quadrupole magnets.

4.2.7 Coil Peak Stress During Collaring

As explained in Section 1.5.5.2, the first 11 T Task Force had concluded that it was critical to control the coil peak stress experienced during collaring, and to limit it below ~150 MPa. This was demonstrated to be achievable by ensuring a maximum coil excess (after shimming) of 300 µm [100]. The question is whether the same target can be achieved on 5.3-m-long collared-coil assemblies.

The Alstom/GE contract introduced in Section 4.2.1, also covered the production of collared-coil-assemblies. The first assembly, referred to as CC01 (which was used in the manufacture of the full-length hybrid magnet ‒see Section 1.5.5.3), was equipped with strain gauges, located on the collar nose, at three different longitudinal locations. These gauges measure the stress applied by the collar nose onto the Ti-alloy pole pieces, which is eventually transferred to the coils (see 4.5.6.1 and Figure 88). At room temperature, the coil azimuthal stress can be estimated to be about 50% of the collar nose stress [100]. Note that none of the subsequent collared-coil assemblies, which were destined to magnets for tunnel installation, had such strain-gauge instrumentation.

Figure 72 presents a time record of the average collar nose stress at the different longitudinal locations for the different phases of the collaring process [217]. It also displays the displacements measured, on both sides, with laser sensors between the top and bottom cradles of the collaring press.

The peak collar nose stresses are observed at the end of Phase 3 in Figure 72, which corresponds to a full closure of the press gap (see Figure 8) and the insertion of lateral keys into the collar keyways and is in the 115‒155 MPa range (corresponding to a coil azimuthal stress in the 57.5‒77.5 MPa range), well below the maximum stress limit. Note also, that, as expected, the larger the coil excess, the higher the stress. These results confirm that the collaring process can be carried out on a 5.3-m-long collared-coil assembly in a controlled and reliable manner.

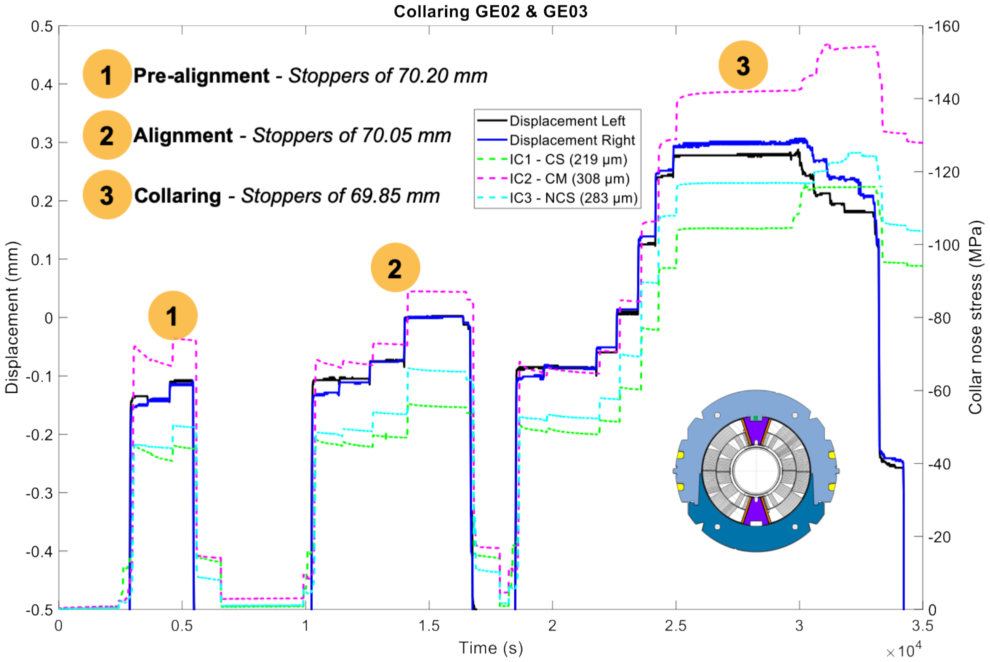

Figure 72: Collar nose stress (dashed lines) and displacement of collaring press cradles (solid lines) recorded as a function of time during the collaring of collared-coil assembly (CC01) used in 5.3-m-long, 60-mm-aperture HL-LHC 11 T "hybrid" dipole magnet prototype (Courtesy of J.-L. Rudeiros Fernández, formerly CERN, now LBNL, and F. Savary, CERN [217]).

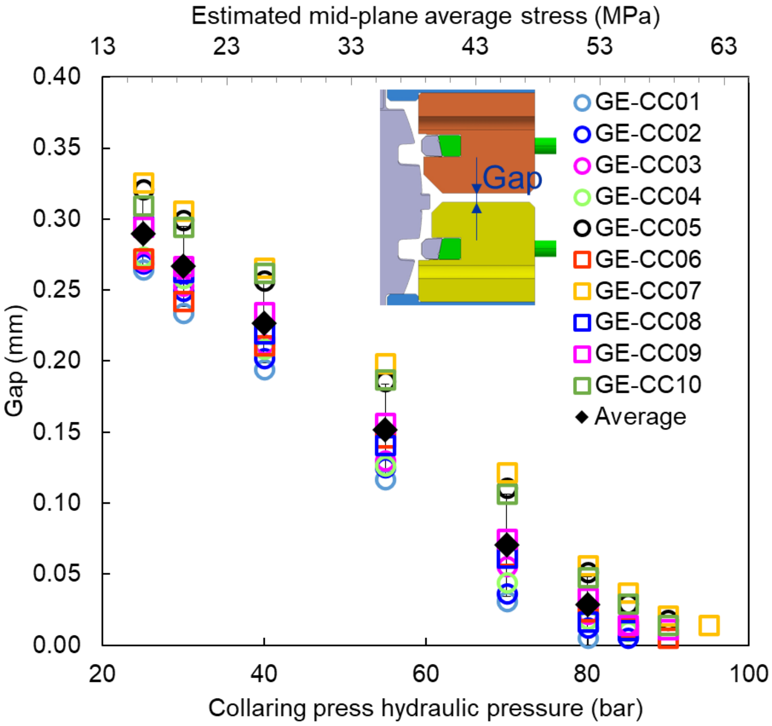

Figure 73: Average collaring press gap versus hydraulic pressure measured during the collaring of 10 x 5.3-m-long, 60-mm-aperture collared-coil assemblies produced by the industrial supplier selected for the production of HL-LHC 11 T dipole magnet coils and collared-coil assemblies (Courtesy of J.-L. Rudeiros Fernández, formerly CERN, now LBNL, and F. Savary, CERN [217]).

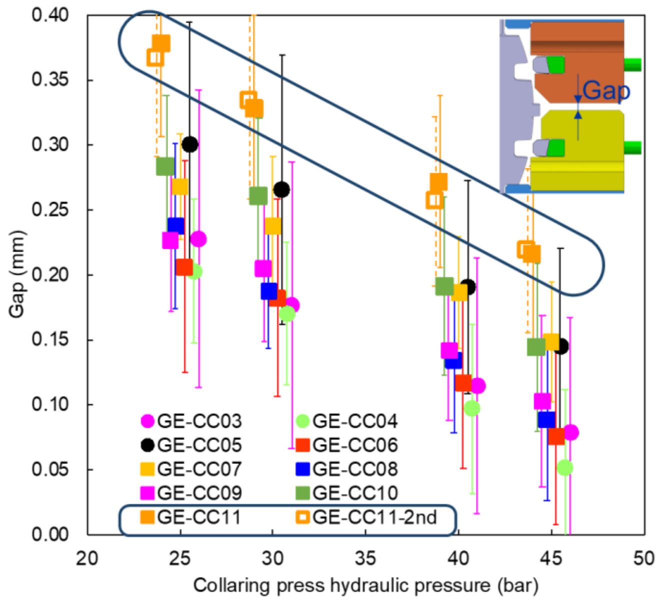

Figure 74: Deviation in measurements of collaring press gap versus hydraulic pressure observed during the initial collaring of 5.3-m-long, 60-mm-aperture HL-LHC 11 T dipole magnet collared-coil assembly CC11 with respect to previous collared-coil assemblies (Courtesy of J.-L. Rudeiros Ferńandez, formerly CERN, now LBNL, and F. Savary, CERN).

4.2.8 Collaring Process Reproducibility Over Series Production

In the absence of strain gauge data, the reproducibility of the collaring process can be assessed by measuring the hydraulic pressure needed to close the gap between the top and bottom parts of the press (see Figure 8). The results are displayed in Figure 73 for 10 collared-coil assemblies (based on the first ten coil assemblies of Figure 69) [217]. The process appears very reproducible, with a gap range of 0.1 mm for a given hydraulic pressure. It exhibits a stiffening at higher pressure, with a peak in the 80 to 95 bars range to fully close the gap. This corresponds to a total press force in the 17.5–21.5 MN range, which, assuming that all hydraulic pressure is transmitted directly onto the coils’ straight section mid-planes, provides a peak stress in the 53–63 MPa range.

The above results confirm that the reproducibility achieved by proper shimming of the coil assemblies ensures a good reproducibility of the collaring process, which can be controlled by measuring simple press parameters (*e.g.*, gap closure and hydraulic pressure). In addition, the hydraulic pressure needed to close the press gap gives a conservative estimate of the peak coil midplane stress, which can be kept well below the maximum target. Also, once the press gap is closed, the coils cannot be over-squeezed, which provides a desirable protection feature in an industrial environment. Although the series production 11 T dipole magnets exhibited performance degradation, they all achieved more or less nominal current at the beginning of their test, and the de-training quenches were mostly localized in the coil heads. This seems to indicate that the stress is properly managed in the magnets’ straight section, further validating the recovery actions of the 1st Task Force and offering a sound methodology for future projects.

4.2.9 Importance of Tolerancing and Metrological Quality Control

A non-conformity that was raised during the collaring of CC11 provides interesting lessons to be learned for future projects. As illustrated in Figure 74, the gaps measured between the top and bottom parts of the collaring press appeared to be larger than on previous collaring. This triggered an alarm; the collaring was stopped, and an investigation was carried out to determine the origin of this deviation.

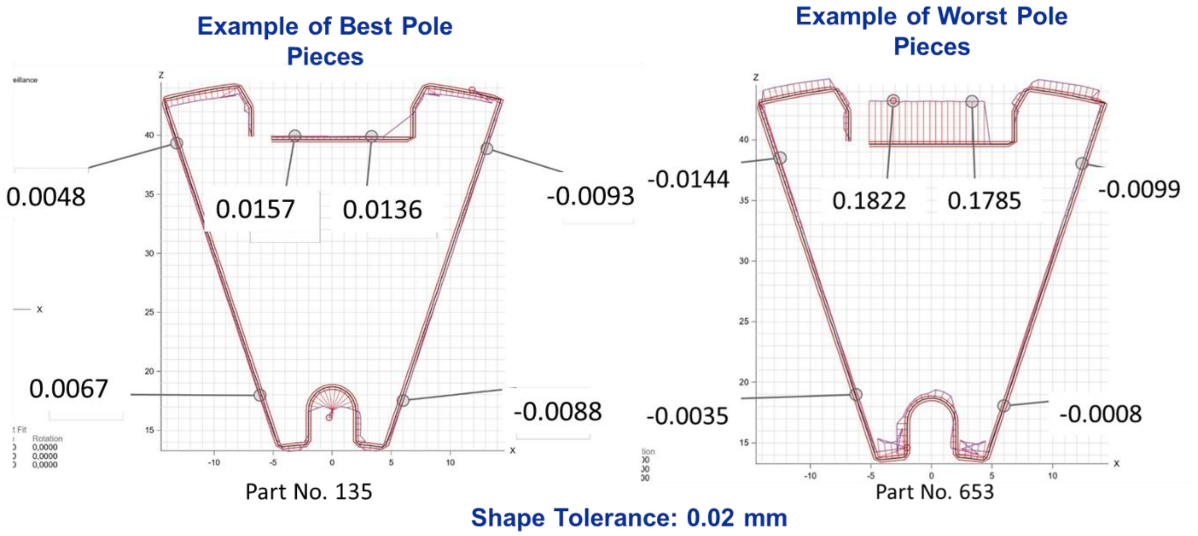

Figure 75: Example of metrology measurements on Ti-alloy pole pieces used in coil manufacturing for 5.3-m-long, 60-mm-aperture HL-LHC 11 T dipole magnets at CERN. All values are in mm (Courtesy of A. Dallocchio, CERN).

The root cause of the problem was traced back to the fact that the coils of this assembly rely on a batch of Ti-alloy pole pieces that were out of tolerance. As illustrated in Figure 75, the drawing imposes a shape tolerance of 0.02 mm on the most critical surfaces (pole faces and bottom of collar nose housing). This tolerance was achieved for the pole faces, but the depth of the collar nose housing at the top of some of the pieces was found to be too small and out of tolerance by up to 0.18 mm. As a result, during collaring, for a given hydraulic pressure, the pile-up of materials under the collar nose is larger, eventually resulting in a wider press gap.

Reaching such tight tolerances on the Ti-alloy pieces is of course tricky, due to high spring back and stress relaxation during machining, as well as high cutting tool wear. The ~750 pieces were subcontracted to one supplier and produced in 5 batches. They were fabricated on the same machine but by different operators and via different machining jigs. Ten percent of the pieces were dimensionally controlled by the supplier, using the same jig. As part of the investigations carried out after the failed collaring, it was found out that the measurement report from the supplier did not include a measurement of the bottom plane of the collar nose housing (this was due to the measurement procedure and the choice of reference). As a result, and since all other measurements were within tolerance, the pieces were considered as conform and accepted, based on the supplier's measurements. It is only after some of the pieces were remeasured at CERN that the deviation of the bottom housing plane was detected, two years after contract closure.

Collared-coil CC11 was eventually disassembled, the out-of-tolerance Ti-alloy pole pieces were replaced, the coils were re-assembled, and a re-collaring was carried out successfully.

The main lessons to be learned from this experience are:

- the importance of tolerancing, which should take into consideration the functionality of the piece, but also its manufacturability and the ability to perform suitable quality control metrology;
- the need to verify/qualify the metrology procedure of the supplier;
- for critical pieces, the need to carry out verification measurements at CERN at a suitable frequency.

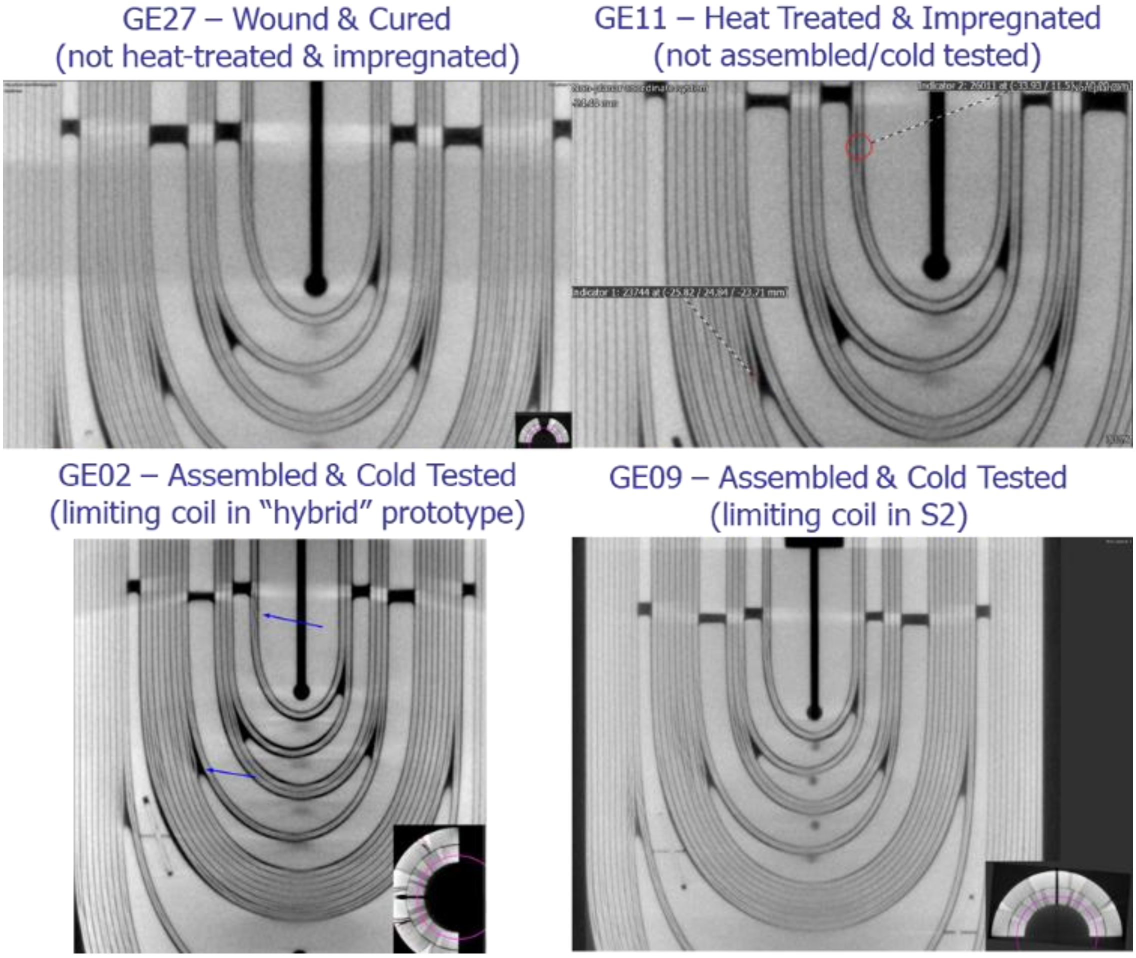

Figure 76: High-energy X-ray computed tomography carried out on the heads of 5.3-m-long, HL-LHC 11 T dipole magnet coils at various stages of manufacture and after assembly and testing: Top left: after winding and curing. Top right: after heat treatment and resin impregnation. Bottom: after assembly and cold testing (Courtesy of M. Crouvizier and S. Sgobba, CERN).

4.3 Salient Findings from Coil Post-Mortem Analysis

The results of computed tomography and metallographic analyses carried out on 5.3-m-long 11 T dipole magnet coils have been presented in detail in Sections 3.4 and 3.5.1. They can be classified into two main categories:

(1) issues with strand pop-outs and conductor bulging in coil heads;

(2) issues with resin cracks, delamination or debonding, in particular, in resin-rich areas.

Both types of issues are internal to the coils and cannot be corrected for the 8 remaining virgin coils available for the assembly of a new full-length 11 T dipole magnet.

Regarding issue (1), further investigations were carried out to identify the manufacturing step at which these events occur. Figure 76 presents a series of XCT analyses of 5.3-m-long HL-LHC 11 T dipole magnet coil heads at various stages of manufacturing and after assembly/cold testing. The images are strikingly similar and indicate that the internal coil defects are already present on cured coils and are likely to originate at the time of winding. Note that a similar analysis on an LHC dipole magnet coil, wound from Nb–Ti cables and issued from the early days of series production at an industrial supplier, does not exhibit such defect [203].

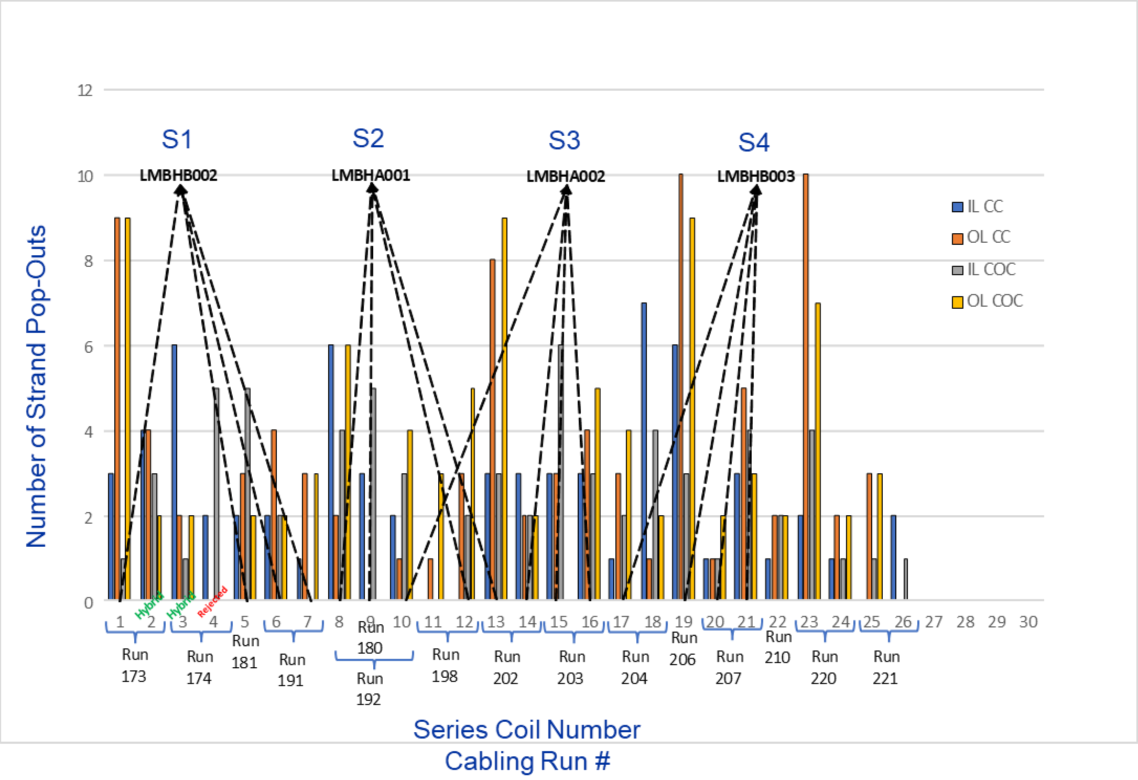

Figure 77: Quality control records during series production of 5.3-m-long, HL-LHC 11 T dipole magnet coils showing the number of strand pop-outs that were identified and corrected during coil winding. The statistics are presented per coil, as a function of coil head (connection side and non-connection side) and coil layer (inner or outer). The dashed lines indicate which coil was used in which magnet. The brackets below the horizontal axis show the cabling runs (Courtesy of O. Housiaux, SERCO, and R. Principe, CERN).

As mentioned in 3.5.1 and explained in more details in Section 5.5.3, popped-out strands as observed in Figure 76 are common occurrences during Nb_3Sn coil winding. Section 5.5.3 lists the various actions that can be taken to mitigate the risks of popped-out strands and cable bulging/collapse, but, in spite of these efforts, the risks have not been eliminated for HL-LHC coils. Let us note that the presence of a stainless-steel core between the two strand layers (see Figure 6) is a factor of mechanical instability during winding.

The procedures for both 11 T and MQXFB coils call for the technicians to carefully check the cables during coil end winding and to record any non-conformity. Figure 77 presents a summary plot of non-conformities issued during the series production of 26 x 5.3-m-long 11 T dipole magnet coils related to strand pop-outs. The data are presented for connection-side and non-connection-side heads of both the inner and outer layers of each coil. Also reported on the plot is the sequence of cabling runs (note that, for 11 T coils, a cabling run usually encompasses 2 x 655-m-long cable unit lengths). There appears to be an average of ~11 pop-outs per coil. The pop-outs are evenly distributed between the two coil heads, and there are ~35% more events for the outer layer, which counts 34 turns, than for the inner layer, which counts 22 turns, showing a correlation with the number of turns. However, there does not seem to be any correlation between the number of pop-outs in coils and the cabling runs.

The number of non-conformities is quite large and is probably underestimated since the hidden surface of the turn being wound (facing the previous turn) cannot be inspected and may also present pop-outs as seen in Figure 49 and Figure 50. As already mentioned, strand pop-outs have also been observed in MQXFB coils [203], but in smaller numbers, probably due to the much larger radii of curvature at which the MQXFB coils are wound.

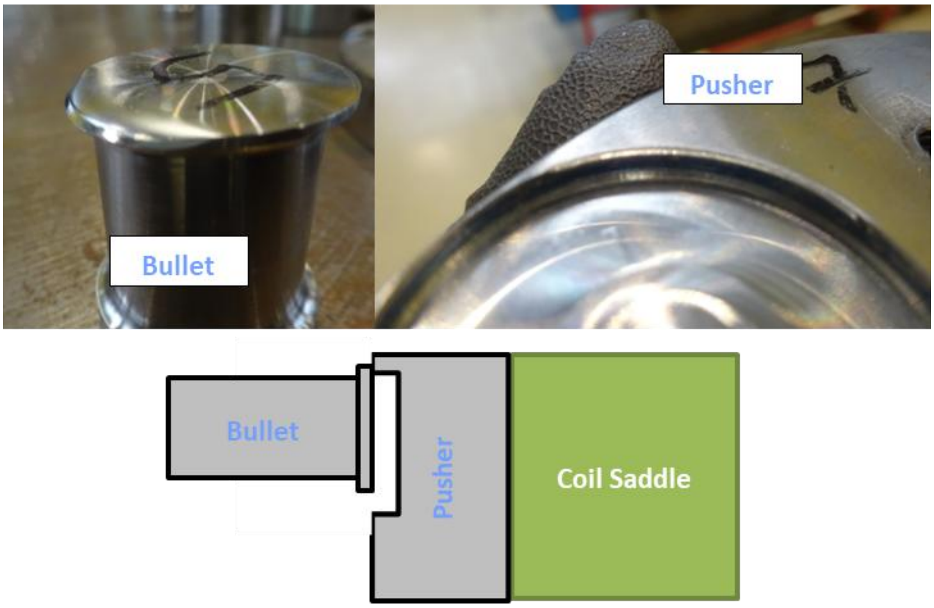

Figure 78: Observation during disassembly of 5.3-m-long, 60-mm-two-in-one-aperture HL-LHC series dipole magnet S3 at CERN. Top left: damaged pusher. Top right: mark left by the damaged pusher on the sector plate. Bottom: sketch explaining the likely root cause of the damage (the damaged pusher corresponds to the external side of upper coil GE15 of Aperture 1, connection-side head; courtesy of O.-Housiaux, SERCO and H. Prin, CERN).

4.4 Salient Observation from Magnet Disassembly

Three series HL-LHC 11 T dipole magnet cold masses (S2, S3 & S4) have been disassembled after cold test and powering and some recurrent non-conformities have been observed [210]. We focus here on the ones that seem the most relevant to the mechanical support of magnet ends.

4.4.1 Loosened Set Screws and Deformed Pushers

As illustrated in Figure 78, S2 and S3 cold masses exhibit an issue with a loosened set screw and a deformed pusher, while no such observation was made during the disassembly of S4. As explained in Section 1.5.5.1, the set screws and the pushers are designed to provide longitudinal pre-compression and support to the coil ends.

It is likely that the pusher corresponding to this screw was not properly engaged in the sector plate’s housing and that the damage occurred during the torque application (see bottom part of Figure 78). Note that the torque is applied to the set screws after completion of end plate orbital welding, at a time when the pushers are not visible anymore. Following this observation, it was decided to add an endoscopic examination of the pushers before torque application.

For both magnets, only one of the set screws was non-conform. In both cases, it was on the connection-side end of the magnet. For S2, it was on the inner side of coil GE13, which is the bottom coil of Aperture 1 and is correlated with the main area of quench-start localization (in particular, after the 4th cooldown). For S3, it was on the outer side of coil GE15, which is the top coil of Aperture 1, where all the quenches were localized, but most of the detraining quenches originated at the opposite non-connection side end (see Figure 104 for the definition of inner and outer sides).

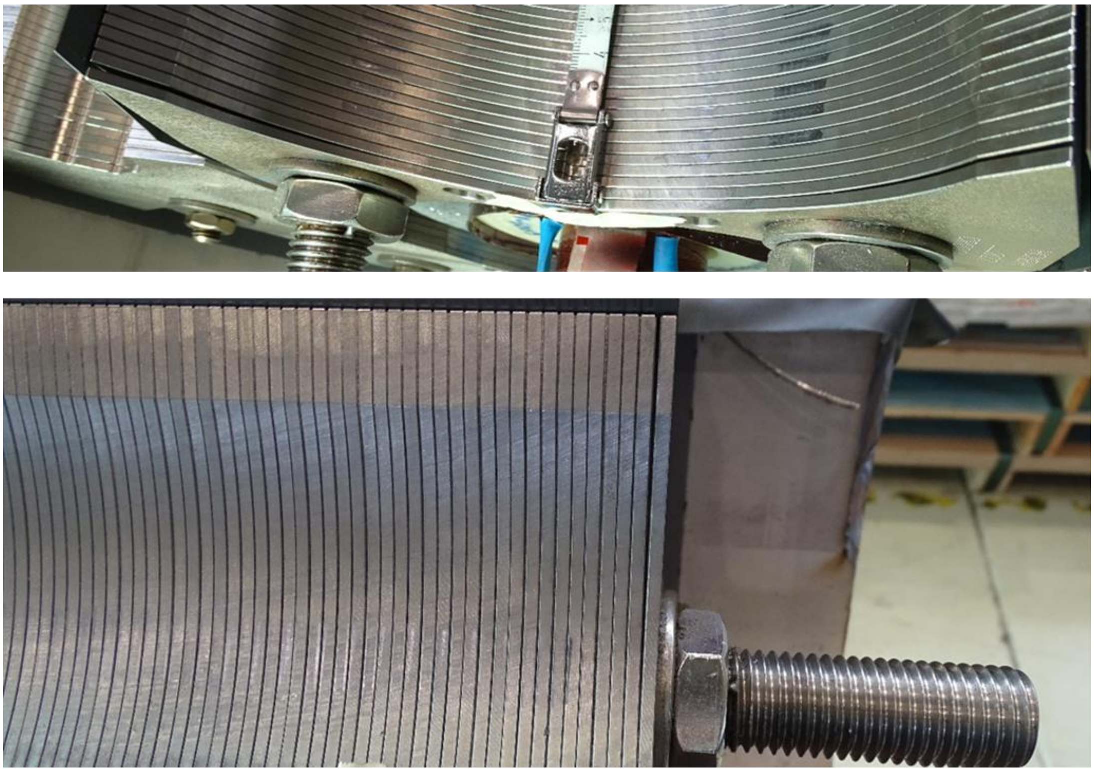

Figure 79: Observation during disassembly of 5.3-m-long, 60-mm-two-in-one-aperture HL-LHC series dipole magnet S2 at CERN showing displacements of central yoke laminations. Top: connection side end. Bottom: non-connection side end (Courtesy of O.-Housiaux, SERCO and H. Prin, CERN).

4.4.2 Displacement of Central Yoke Laminations

As illustrated in Figure 79, S2 and S3 cold masses exhibit an issue with central yoke laminations (those between the two apertures), which are either displaced or deformed at both ends. A similar deformation/displacement, but less pronounced, was also observed on S4. The laminations were properly positioned at the time of assembly and the anomaly was only observed during disassembly after cold testing.

This non-conformity indicates that the end laminations were not rigidly supported and could bend or move, likely under the effect of the axial component of the Lorentz force that tends to stretch the coils outwardly during energization or following a sequence of power and warm-up/cooldown cycles. Of course, on the connection side, the occurrence of this non-conformity may also be linked to the loosened set screw and deformed pusher described in Section 4.4.1.

The above two observations point to weaknesses in the mechanical support of coil and magnet ends, which was not optimal, and which may have contributed to the observed performance degradation.

4.5 Summary from New Finite Element Analyses

4.5.1 Introduction

One of the main actions of the 2nd Task Force has been the development of a new, 3-dimensional (3D), Finite Element (FE) model of the 11 T dipole magnet cold mass to assess local thermo-mechanical stress fields in conductor blocks, in the magnet straight section and in the ends, during assembly (collaring + shell welding), after cooldown and during energization

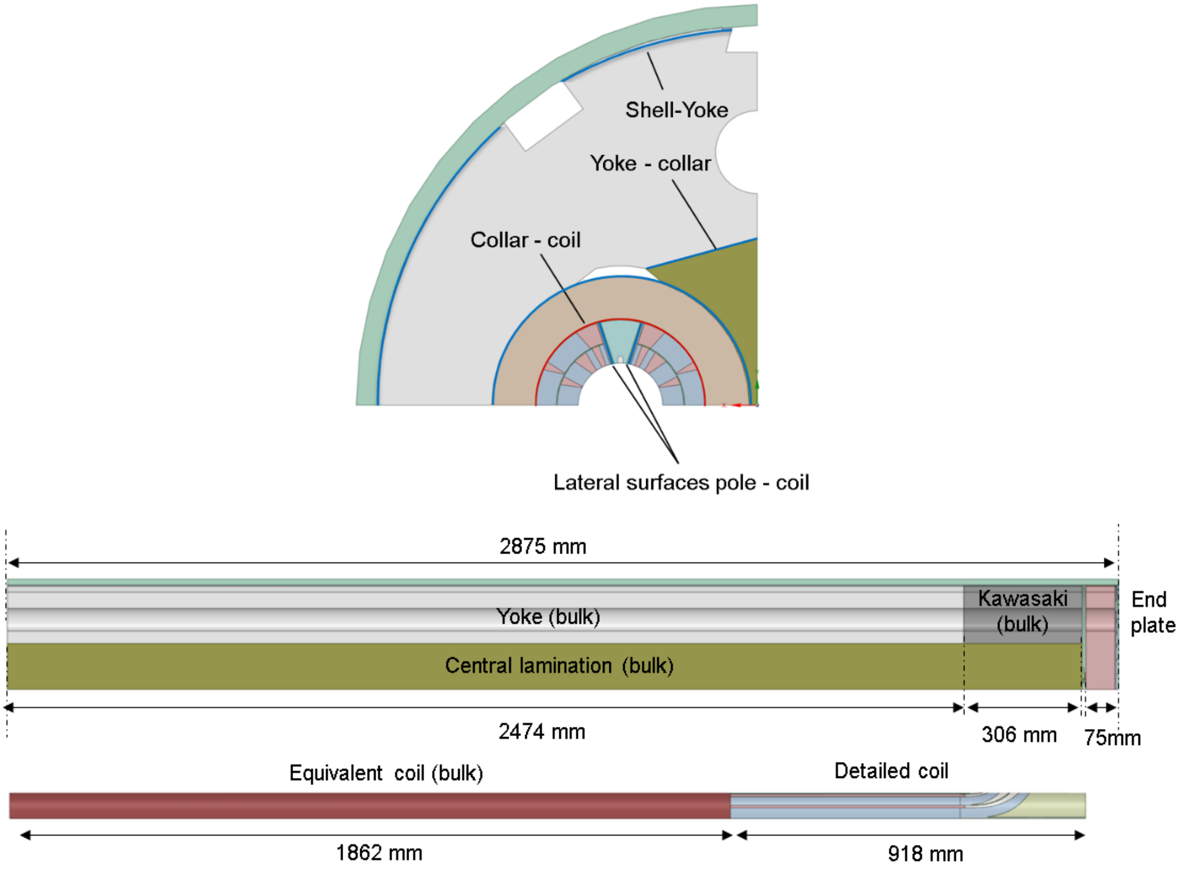

Figure 80: Views of one quarter model of 5.3-m-long, 60-mm-two-in-one-aperture HL-LHC 11 T dipole magnet developed within the framework of 2nd 11 T dipole magnet Task Force at CERN. Top: 2D cross-section, featuring the various interfaces. Bottom: longitudinal section, showing the simplifications in the description of the various components (Courtesy of C. Garion and M. Morrone, CERN [221]).

This FE modelling effort was deemed necessary as there was no such comprehensive analysis tool that remained available at the time of the Task Force launching. Let us now introduce the main features of this new model, which was developed using COMSOL Multiphysics® V5.6 [219], the efforts that were carried out to benchmark it, and its main findings. The full analysis details are provided in Refs. [220], [221] and [222].

4.5.2 Geometry and Mesh

As illustrated in Figure 80, the geometry of the FE model was built starting from the 3D Computer-Aided Design (CAD) model of half the magnet coldmass along the longitudinal axis (connection-side end) and one quarter in the transverse cross-section.

All dimensions are assumed to be nominal (*e.g.*, 15-mm-thick outer stainless-steel shell and 75-mm-thick end plate connected to the shell by a fillet weld). The side-yoke packs, central-yoke packs (between the two collared-coil assemblies), and collar packs are treated as bulk.

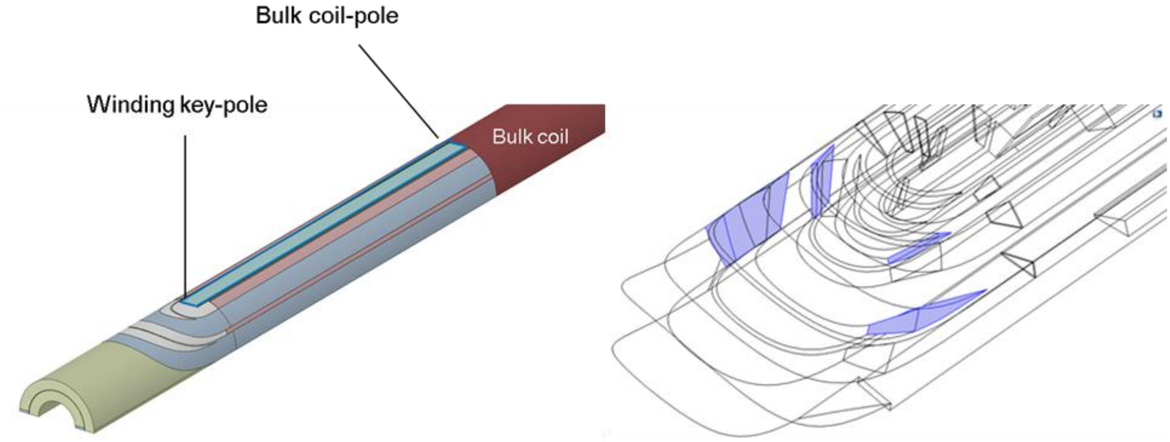

Figure 81: Detailed models of the connection-side end of 5.3-m-long, 60-mm-two-in-one-aperture HL-LHC 11 T dipole magnet developed within the framework of 2nd 11 T dipole magnet Task Force at CERN. Left: Overall view featuring coil head and transition between coil head and coil straight section. Right: Implementation of resin rich areas in selected conductor blocks (Courtesy of C. Garion and M. Morrone, CERN [221]).

The half coil is cut longitudinally into two parts: a first part corresponding to the coil head and the transition region between the coil head and coil straight section, and a second part corresponding to the coldmass straight section.

The first coil part is described in detail and includes: cable blocks, copper wedges, Ti-alloy pole pieces, G11 end saddle, stainless-steel end spacers, and so-called stainless steel *winding keys* (see left part of Figure 81). The winding keys are the last pole pieces, which are implemented at the time of winding and support the pole turn end. There is one for the inner layer and one for the outer layer, and, unlike the Ti-alloy pieces, they are both made of AISI 316L and impregnated with the coil.

The second coil part does not distinguish the different coil components and relies on homogenized properties (including the Ti-alloy pieces).

The cable blocks are also modeled as bulk components, but resin-rich zones are assigned at the extremities of the inner-layer end spacers to simulate the voids that are left between the cable and the spacers during winding. These voids correspond to areas that are subsequently filled by pure resin during the impregnation phase and where degradations have been observed during post-mortem examinations (see Figure 81 and Section 3.5.1).

Around 360,000 second-order tetrahedral elements are used to discretize the geometry.

The sub-modelling technique was applied to refine the mesh in the areas of interest to obtain a higher stress/strain resolution. The underlying assumptions when using sub-models are:

- the global model is accurate enough to give correct displacements on the boundary with the sub-model;
- the improvements introduced in the sub-model are small enough that they do not introduce significant changes in stiffness in the global level.

With such assumptions, it is possible to introduce non-linear material properties, locally in the sub-model.

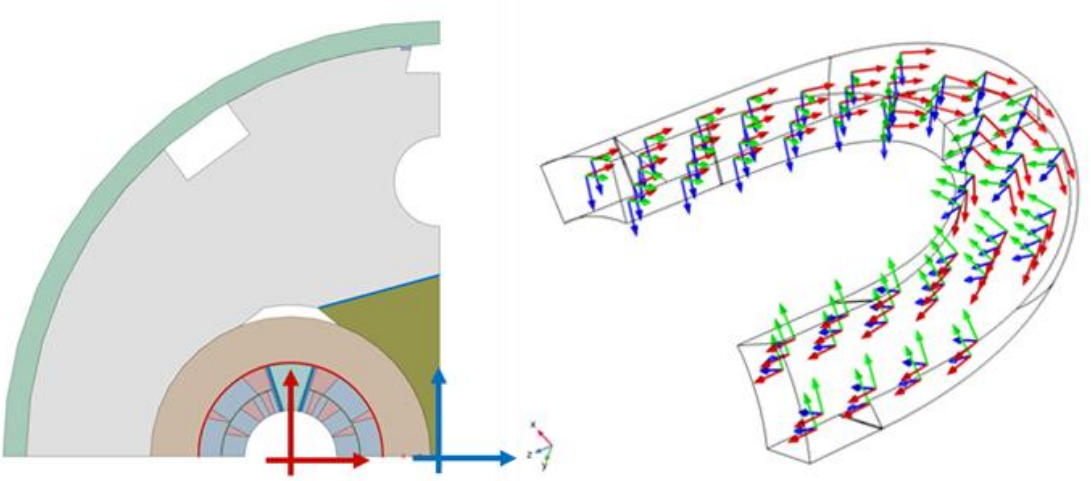

Figure 82: Coordinate systems used in the new model of 5.3-m-long, two-in-one-aperture HL-LHC 11 T dipole magnet developed within the framework of 2nd 11 T dipole magnet Task Force at CERN. Left: cylindrical systems at the center of the coil (red) and at the center of the magnet (blue). Right: curvilinear system following the cable turns in the magnet head featuring azimuthal direction (green), axial direction (red) and radial direction (blue; Courtesy of C. Garion and M. Morrone, CERN [221]).

4.5.3 Coordinate Systems

Four main coordinate systems are used:

(1) a general global cartesian system for the whole geometry;

(2) a cylindrical system at the center of the coil (marked in red in the left part of Figure 82);

(3) a cylindrical system at the center of the magnet (marked in blue in the left part of Figure 82);

(4) a curvilinear system that follows the cable curvature in the coil head (see right part of Figure 82).

The designations transverse (t) and longitudinal (l) directions refer to the global and cylindrical coordinate systems, while the designations axial (a), azimuthal (θ) and radial (r) direction refer to the local coordinate system of the cable. As illustrated in Figure 82, azimuthal corresponds to a direction that is perpendicular to the cable broad face, axial is tangential, and radial is parallel.

4.5.4 Constitutive Laws and Material Properties

A linear elastic constitutive law is considered for all materials of the model. Thermal strain is accounted by considering the integrated thermal strain from room temperature to 4.2 K

A transverse isotropic model is considered for the side-yoke, central-yoke and collar packs. The modelling considers the laminated structure of the yoke and collar packs. It is based on the physical properties in the transverse direction while the Young’s modulus in the longitudinal direction is drastically lowered (~3 GPa). In addition, the transverse Young’s modulus of the collars is halved from the bulk property as only half of the collars contribute to transverse force transfer. For both yoke and collar, the shear modulus of the packs is estimated from the bending stiffness of a single lamination.

The welding phase is simulated by pulling on the edges of the outer stainless-steel shell halves, while the side-yoke packs are free to move to contact the packs on the opposite side. Let us note that the mating faces of the yoke packs have an angle of 0.04° with respect to the vertical axis. This angle compensates for the bending of the yoke during welding and enables a proper closure of the yoke gap.

An orthotropic model is used for the coil. All coil components (impregnated cables, copper wedges, stainless steel loading plates, stainless steel winding key, stainless steel end spacers and G11 end saddle) are assumed to be glued. The Ti-alloy pole pieces, which, for the 11 T dipole magnet coils, are mounted after resin impregnation, with no gap between them, are modeled as a longitudinally continuous component, with frictionless contact to the coil pole faces. Homogenized properties (for the whole coil in the straight section and for impregnated cable blocks in the coil head) are evaluated considering longitudinal properties according to the rule of mixture.

In the coil head, an equivalent Young's modulus is calculated for each cable block. The ratio of resin over plain conductor is estimated over three distinct 30° angular sections. Continuous equivalent properties along the turns are derived by interpolation of these three resin ratios. According to this estimate, the azimuthal Young's modulus of homogenized impregnated cable blocks reduces by ~50% from the straight section to the turn ends. Finally, an orthotropic model is also used for the G11 end saddle at the coil extremity.

Table 8 presents a summary of the material properties used in the new FE model, where E refers to Young's modulus, ν, to Poisson's ratio, G, to shear modulus, and α, to integrated thermal expansion coefficient between room and cryogenic temperatures. The subscripts are self-explanatory. This compilation is the result of a comprehensive review of data available in the literature or determined by *ad hoc* measurements carried out at CERN within the framework of HL-LHC magnet development programs. The simulations reported here all rely on these physical parameters and that there was no iteration on their values to better fit observed behaviors as it is sometimes done.

4.5.5 Loading Steps

The analysis considers five successive loading steps, labeled sequentially A to E.

4.5.5.1 Step A: Collaring

The collaring phase is modeled in one step and corresponds to the state after lateral key insertion and hydraulic press unloading. The shimming is applied by imposing a contact offset between the Ti-alloy pole pieces and collar noses and between the Ti-alloy pole pieces and the stainless-steel loading plates covering the coil pole faces (as explained in Section 1.5.5.1, in the case of 11 T dipole magnets, the stainless-steel pole pieces used for heat treatment are replaced by Ti-alloy pole pieces at the time of coil assembly, and are not resin-impregnated with the coils as for MQXF). The shim between Ti-alloy pole pieces and collar noses is of the nominal thickness (0.2 mm) and is reduced in two steps over the last 55 mm of coil straight section. The azimuthal coil size excess is assumed to be nominal and the shim between Ti-alloy pole pieces and loading plates is uniform and has been tuned to a thickness of 170 μm (see Section 4.5.6.1 for an explanation of how this value was chosen).

4.5.5.2 Step B: Shell Welding

The longitudinal welding of the two half shells is simulated by imposing a 0.6 mm displacement on the horizontal axis at the edges of both half shells.

4.5.5.3 Step C: Longitudinal Loading

A longitudinal prestress is applied to the coil extremity (G11 end saddle) by means of the set screws which are pre-compressed to 30 MPa (see Section 1.5.5.1).

4.5.5.4 Step D: Cooldown

The cool-down phase is modeled by imposing on each component of the cold mass the integrated thermal contraction coefficients from 300 K to 4.2 K listed in Table 8. The impact of magnet cooldown is analyzed at 4.2 K as no further effects are expected between 4.2 K and 1.9 K.

Table 8: Material properties used in new FE model of 5.3-m-long, 60-mm-two-in-one-aperture HL-LHC 11 T dipole magnet developed within the framework of 2nd 11 T Task Force at CERN (Courtesy of C. Garion and M. Morrone, CERN [221]).

Components	**Elastic Parameters at 4.2 K**	**Integrated Thermal Contraction Coefficient from 293 to 4.2 K (x10^{-3} mm/mm)**
Stainless Steel Shell	E = 210 GPA [223] ν = 0.28 [224]	2.95 [225]
Stainless Steel End Plates and Set Screws	E = 210 GPa [226] ν = 0.3 [226]	2.95 [227]
Low-Carbon Steel Yoke Pack (Magnet Central Part)	E_t = 0.98 x 205 = 200 GPa [228] E_l = 3 GPa ν_{tl} = 0.3, ν_{tt} = 0.3 G_{tl} = 2.1 GPa	α_a = 2.95 [227] (rods) α_θ = 2.1 [228] α_r = 2.1 [228]
Stainless-Steel Yoke Pack (Magnet Extremities)	E_t = 210 GPa, E_l = 3 GPa [229] ν_{tl} = 0.3, ν_{tt} = 0.3 G_{tl} = 0.59 GPa	1.85 [229]
Stainless-Steel Collar Pack	E_t = 101 GPa, E_l = 3 GPa [230] ν_{tl} = 0.33, ν_{tt} = 0.33 G_{tl} = 8.62 GPa	α_a = 2.87 (rivet) α_θ = 2.7 [230] α_r = 2.7 [230]
Ti-Alloy Pole Piece	E = 127 GPa, ν = 0.3 [231]	1.74 [231]
ODS Copper Wedges	E = 93 GPa [232]	3.07 [233]
Impregnated Cable Block (cables, fiberglass braids and resin)	E_a = 95 GPa, E_θ = 31 GPa, E_r = 80 GPa [234] $\nu_{a\theta}$ = 0.3, $\nu_{\theta r}$ = 0.3, ν_{ra} = 0.3 $G_{a\theta}$ = 24.2 GPa, $G_{\theta r}$ = 21.3 GPa, G_{ra} = 33.6 GPa	α_a = 2.8 [235] α_θ = 2.5 [235] α_r = 2.5 [235]
G11 End Saddle	E_a = 23.2 GPa, E_θ = 24 GPa, E_r = 15.9 GPa [236] $\nu_{a\theta}$ = 0.21, $\nu_{\theta r}$ = 0.21, ν_{ra} = 0.21 $G_{a\theta}$ = 9.7 GPa, $G_{\theta r}$ = 8.2 GPa, G_{ra} = 6.6 GPa	α_a = 2.5 [237] [238] α_θ = 2.5 [237] α_r = 7 [237]
SS Loading Plate, Winding Key, and End Spacers	E = 210 GPa, ν = 0.3 [226]	2.95 [227]
Homogenized Coil (cable blocks, Cu wedges, SS loading plates and Ti-alloy poles)	E = 100 GPa, ν = 0.3 [220]	2.78 [220]
CTS-101K Resin	E = ~9 GPa, ν = 0.3 [239]	~11 [239]
Polyimid (Kapton®)	E = 5 GPa, ν = 0.34 [240]	4.7 [241]

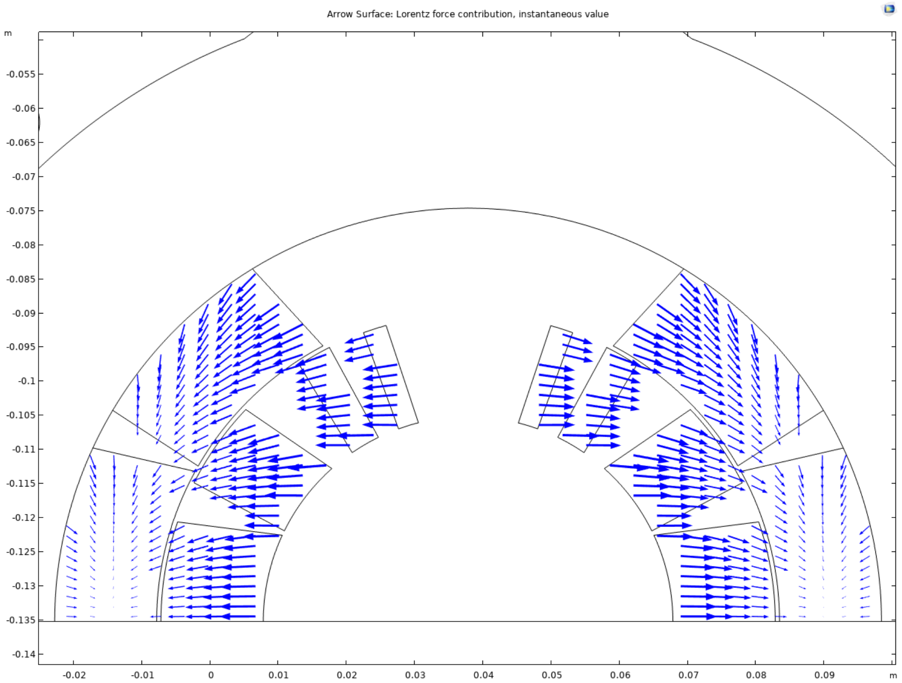

Figure 83: Lorentz force distribution computed at 11.85 kA in the two-dimensional cross-section of the straight part of one 60-mm-aperture of HL-LHC 11 T dipole magnet (Courtesy of M. Morrone and C. Garion, CERN).

4.5.5.5 Step E: Powering

As a first step, the Lorentz forces at nominal current were computed using the CERN-developed ROXIE software [242]. The forces generated in the cable blocks of the coil straight part were computed in 2D whereas those induced in the coil head were calculated in 3D for each turn of each cable block. The 3D computation was used to derive analytical distributions that were implemented into the new FE model (a distribution in $\cos\theta$ for the transverse forces, where θ is the turn orientation with respect to the vertical axis, and a parabolic distribution for the longitudinal forces along the magnet axis). A sanity check was carried out by comparing integrated transverse/longitudinal forces over a half-coil straight section in 2D and a half-coil head in 3D.

In a second step, the new FE model was refined by including an electromagnetic analysis to compute a more accurate volumetric force distribution that could be directly imported into the thermo-mechanical analysis. The magnetic analysis also included iron saturation effects. The results of the electromagnetic computations were compared with ROXIE results for both coil straight part and coil head and differences are in the few percent range.

Figure 83 shows the Lorentz force distribution calculated by COMSOL Multiphysics® in a two-dimensional cross-section of the magnet straight part. As is usually the case for a $\cos\theta$ dipole magnet configuration [75], the Lorentz force has two main components:

- an azimuthal component, which tends to squeeze the coil away from the pole towards the midplane;
- a radial component that tends to bend the coil outwardly with a maximum displacement at the midplane.

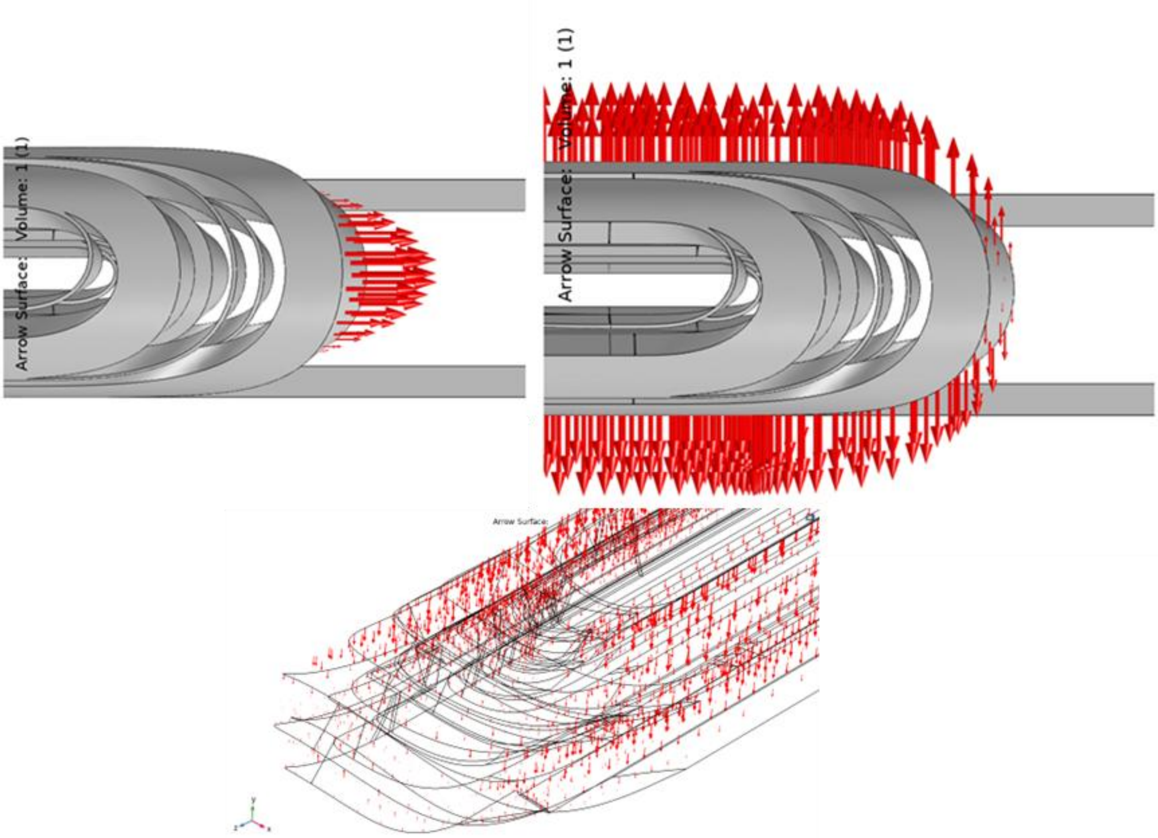

Figure 84: Lorentz force distribution computed at 11.85 kA over the connection-side head of one 5.3-m-long, 60-mm-aperture HL-LHC 11 T dipole magnet coil. Top Left: longitudinal forces. Top Right: lateral forces. Bottom: vertical forces (Courtesy of M. Morrone and C. Garion, CERN).

Integrated values of the Lorentz force components (per half coil, or per aperture) are provided in Table 2. Figure 83 illustrates very clearly the importance of providing robust radial support to the coil assembly and preventing excessive deformation along the magnet's horizontal axis.

Figure 84 shows the Lorentz force distribution in the coil head, which is quite complex. Overall, there are three main components to consider:

- a longitudinal component, which tends to stretch the coil outwardly;
- a lateral component that tends to bend the coil outwardly;
- a vertical component which tends to bend the coil head inwardly (towards the aperture).

The amplitude of the longitudinal component of the Lorentz force integrated over a coil, is: ~65 kN for the inner layer and ~165 kN for the outer layer, with a peak force density localized in the ends of the inner- and outer-layer pole turns and their neighbors (see Figure 85). These areas have been identified as a point of concern, where one needs to prevent conductor detachment from winding keys and end spacers.

Looking at the details of the vertical Lorentz force distribution, and although there is a net overall inward bending effect over the coil head, Figure 86 illustrates that there can be radial gradients across the cable broad faces, and that, for the most external turns of the inner-layer coil head, the force even changes direction and points outwardly

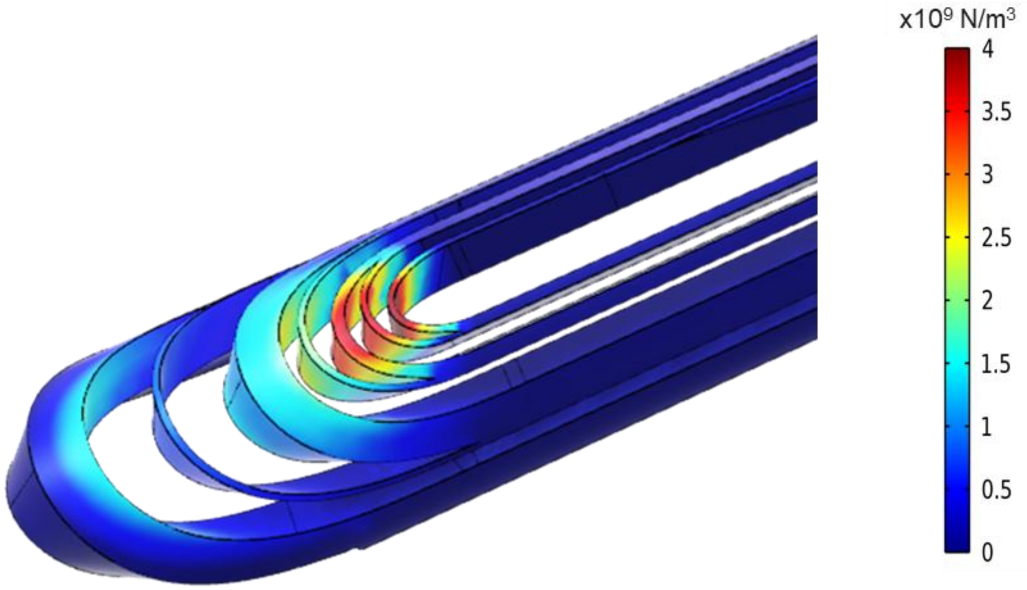

Figure 85: Volumetric density of the longitudinal component of the Lorentz force computed at 11.85 kA over the connection-side head of the inner layer of one 5.3-m-long, 60-mm-aperture HL-LHC 11 T dipole magnet coil (Courtesy of M. Morrone and C. Garion, CERN).

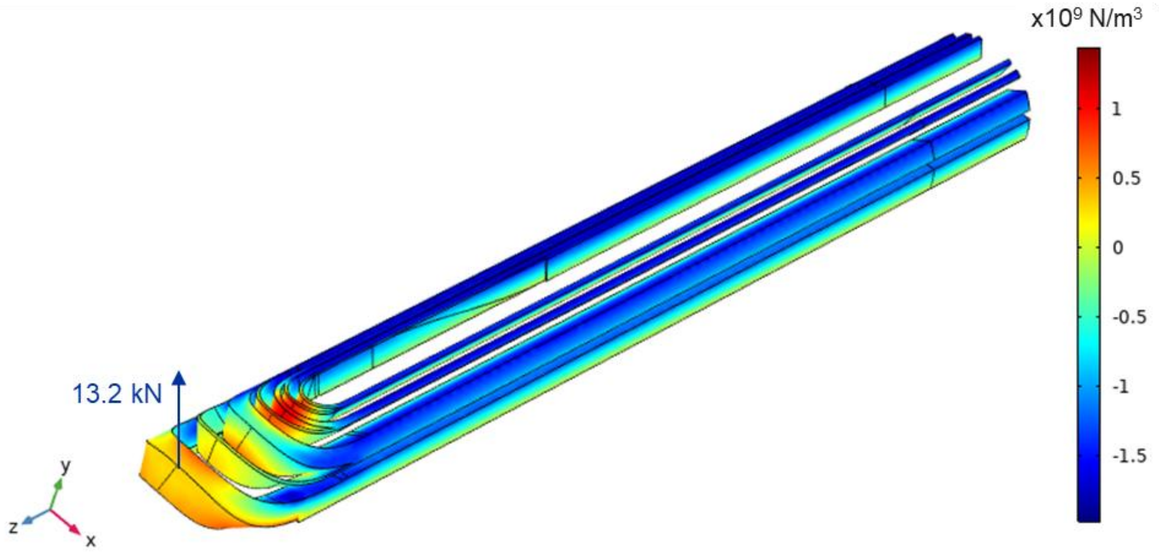

Figure 86: Volumetric density of the vertical component of the Lorentz force computed at 11.85 kA over the connection-side head of the inner layer of one 5.3-m-long, 60-mm-aperture HL-LHC 11 T dipole magnet coil (Courtesy of M. Morrone and C. Garion, CERN).

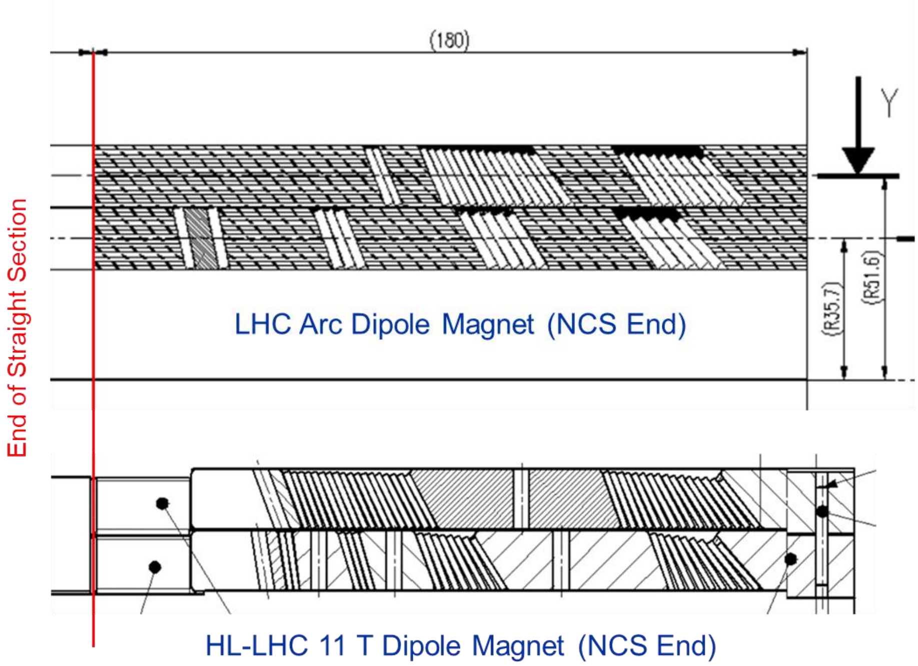

Figure 87: Longitudinal cuts of the non-connection side head of dipole magnet coils. Top: LHC arc dipole magnet (Courtesy of P. Fessia, D. Perini and S. Russenschuck, CERN). Bottom: HL-LHC 11 T dipole magnet (Courtesy of B. Auchmann. Formerly CERN, and D. Smekens, CERN).

The fact that the design optimization of coil ends needs to integrate both electromagnetic and mechanical considerations had already been the object of many discussions at the time of LHC dipole magnet development. Of course, back then, the FE modeling tools were not as sophisticated as today, but significant efforts were put in to couple electromagnetic computations done with ROXIE with an ad hoc mechanical model of conductor blocks and end spacers [243]. This led to iterations on the conductors' layout and on the number and shape of end spacers [244]. Similar efforts were also carried out for designing the ends of the 11 T dipole magnet [245]. Figure 87 displays a comparison between longitudinal cuts of LHC arc dipole magnet and HL-LHC 11 T dipole magnet coil heads (non-connection side). There appears to be significant differences, *e.g.*: the LHC outer coil head is staggered with respect to the inner coil head, while the two 11 T coil heads lay on top of each other. This illustrates that there can be very different solutions to the problem, depending on the objective functions chosen for the optimization, and that more work is needed to comprehensively address this problem.

4.5.6 Benchmarking

Serious efforts have been carried out to benchmark the thermo-mechanical FE model results with available measurement results for each of the loading steps, either from *ad hoc* mock-up tests or from mechanical data from single- and two-in-one-aperture short and long magnets. Such systematic benchmarking is critical to build confidence on the model's suitability and reliability.

4.5.6.1 Collaring (Loading Step A): Coil Azimuthal Stress versus Coil Excess

As part of the first 11 T Task Force set up in November 2017 (see Section 1.5.5.2), a collaring mock-up test was carried out using different short segments cut out from coils representative of 11 T short magnet models and long prototypes. The mock-up relied on so-called *instrumented collars*, which are equipped with electric strain gauges which are glued on the collar nose (Figure 88). These strain gauges measure the pressure exerted by the collar nose onto the Ti-alloy pole pieces. This pressure is eventually transmitted to the coils. The goal of the mock-up was twofold [100]:

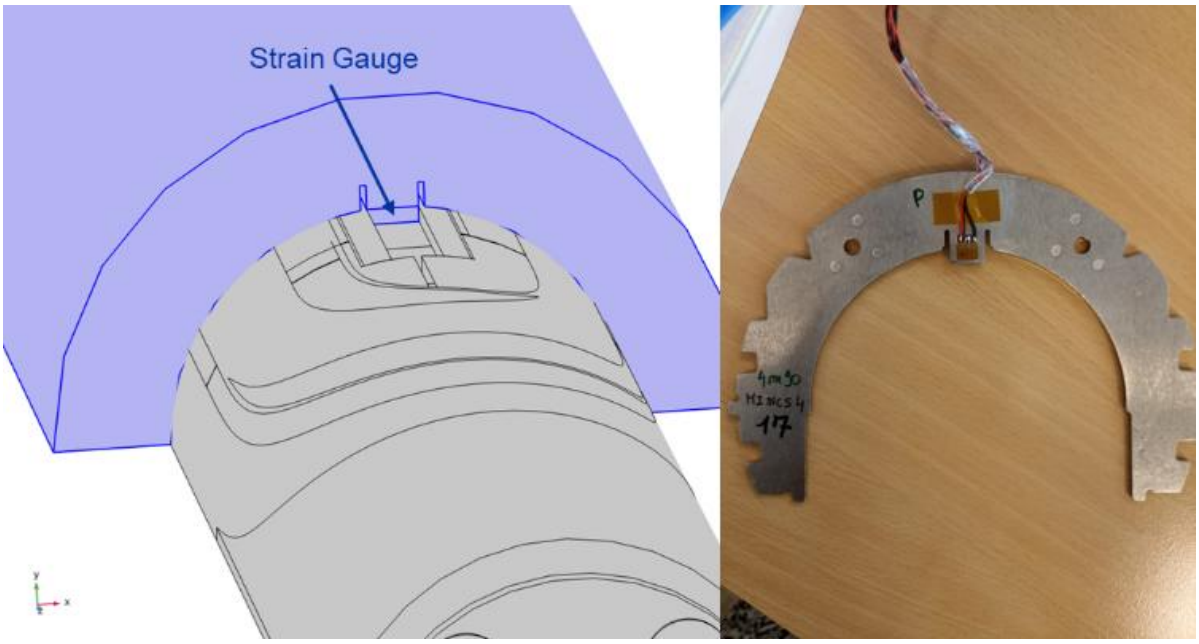

Figure 88: Sketch of collar nose housing on top of Ti-alloy pole piece and location of strain gauge to assess coil azimuthal stress in HL-LHC 11 T dipole magnets (Courtesy of C. Abad Cabrera, formerly CERN, M. Guinchard and M. Morrone, CERN).

- to establish a calibration of collar nose stress versus azimuthal stress at the coil pole;
- to derive relationships between azimuthal stresses at coil pole and at coil midplane versus azimuthal coil sizes, after key insertion and hydraulic force removal upon collaring completion.

As detailed in Section 5.5.7, the azimuthal arc length and the radial dimension of the coils are measured as part of the final inspections upon manufacturing completion. By aligning the data on the nominal outer coil radius from the CAD model, it is possible to determine azimuthal coil size deviations, also referred to as *excess* [101]. The mock-up test results enable two verifications of the collaring loading step of the FE model:

- a comparison of the ratio between coil azimuthal pole stress, $\sigma_{\theta,\mathrm{pole}}$, and collar nose stress, $\sigma_{r,\mathrm{nose}}$: the measured value is ~0.5 [100], while the equivalent ratio derived from the FE model is ~0.6;
- a comparison of the slope of coil azimuthal pole stress versus coil excess: a linear fit of the measurements in Ref. [100] gives a slope of 0.3 MPa/µm while the slope from the FE analysis is 0.34 MPa/µm (see Figure 89).

In both cases, the FE simulation results are well within 15-20% of the measurement results, which is quite reasonable for a model of this complexity. However, one difficulty for the FE model is to reproduce absolute values. As illustrated in Figure 89, one needs to shift the linear fit of the measured data by ~130 µm to force it to cross the origin (as one would expect). Conversely, to be aligned with the measurements, the shim thickness in the model must be equal to 170 µm instead of the nominal value of 300 µm. The discrepancy likely arises from uncertainties on the contact zone between the collar nose and housing in the Ti-alloy pole piece and from accommodation taking place in the different contacts during collaring. Another effect could be initial non-linearities in the coil blocks' stress-strain curve [246], not taken into consideration in this model. This correction will be applied for the rest of the analysis and is the only model parameter that is adjusted.

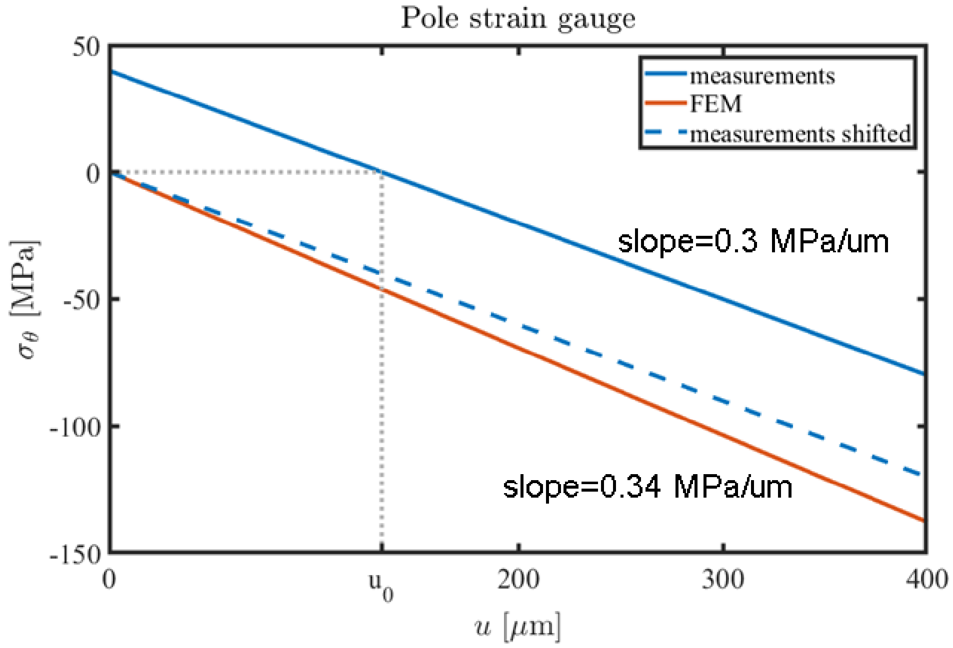

Figure 89: Linear regressions of azimuthal pole stress versus coil excess measured on collaring mock-up of HL-LHC 11 T dipole magnet and computed using new FE mechanical model developed as part of the 2nd 11 T Task Force (Courtesy of C. Garion and M.-Morrone [221]).

4.5.6.2 Shell Welding (Loading Step B): Tensile Stress in Shell

Upon welding completion, measurements of the shell tensile stress were carried out on short two-in-one-aperture HL-LHC 11 T dipole magnet models DP101 and DP102 [101]. The measurements relied on strain gauges placed on the inner and outer radii of the shell, at the level of a cutout in the yoke that accommodates busbars. The measured values range from 225 to 250 MPa. The computed values in the FE model are 230 MPa at the external side of the shell (210 MPa at the level of the busbar cutout) and 225 MPa at the internal side (260 MPa at the level of the busbar cutout). The computed values are again in a reasonable agreement with the measured ones.

4.5.6.3 Cooldown (Loading Step D): Geometry Changes of Short Model Coil

To confirm the value assumed in the simulation for the coefficient of thermal expansion (CTE) of a homogenized magnet coil, a dedicated experiment was carried out in the CERN Cryogenic Laboratory [247].

As illustrated on the left side of Figure 90, a 2-m-long, 11 T dipole magnet coil (SD126) was installed in a metallic container with a plexiglass lid. The coil is placed on three supports (one on the connection side and two on the non-connection side) to create isostatic conditions while being free to contract without any restraint. It is cooled down by the vapors generated by a bath of liquid nitrogen and geometry changes are measured by photogrammetry. The coil is instrumented with 10 temperature sensors and 472 optical targets distributed on its outside surface (see right side of Figure 90). Additional reference targets and scales are located around the pool and outside the cold area at ambient temperature. The measurement uncertainty is between ±15 μm and ±85 μm depending on the location.

Figure 90: Experimental set up at CERN Cryogenic Laboratory to measure geometry changes on 2-m-long, HL-LHC 11 T dipole magnet coil SD122 between room and GN_2 temperature. Left: picture of coil in metallic container with plexiglass lid. Right: picture showing the position of the photogrammetric targets on the coil surface (Courtesy of J. Bremer, T. Koettig, and D. Mergelkuhl, CERN [247]).

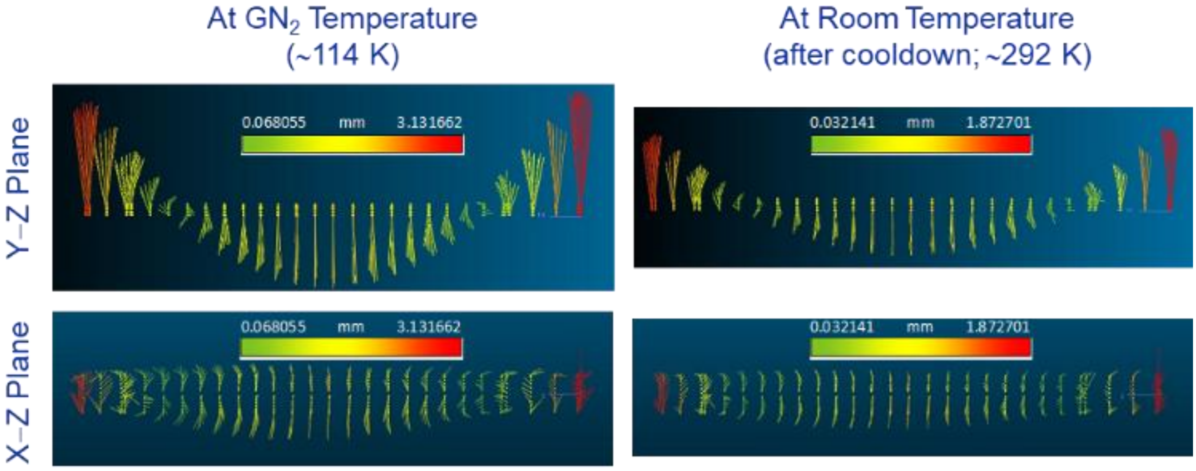

Figure 91: Reconstruction from photogrammetric measurements on 2-m-long, HL-LHC 11 T dipole magnet coil SD122. Left: at GN_2 temperature. Right at room temperature after warm-up. The x-axis is the horizontal axis, the y-axis the vertical axis, and the z-axis the longitudinal axis (Courtesy of J. Bremer, T. Koettig, and D. Mergelkuhl, CERN [247]).

The left part of Figure 91 shows a reconstruction of the measurements at cold conditions with respect to reference measurements at room temperature. It appears that the coil is bending in the vertical plane, with its ends moving upward by ~4.5 mm. Figure 91(right) illustrates that, after warm-up, the coil does not come back to its original shape and remains bent in the vertical plane, with its ends displaced upward by ~2.9 mm [247]. Deformations are also measured in the horizonal plane, but they are much smaller: in the range of ± 0.4 mm at cold and ± 0.25 mm after warm-up to room temperature.

The photogrammetric reconstruction also enables us to derive an estimate of the integrated thermal expansion coefficient (applying a correction for the fact that the coil is bent in the vertical plane at cold conditions). This gives a value of ~2.27 mm/m for a ΔT of 178 K [247].

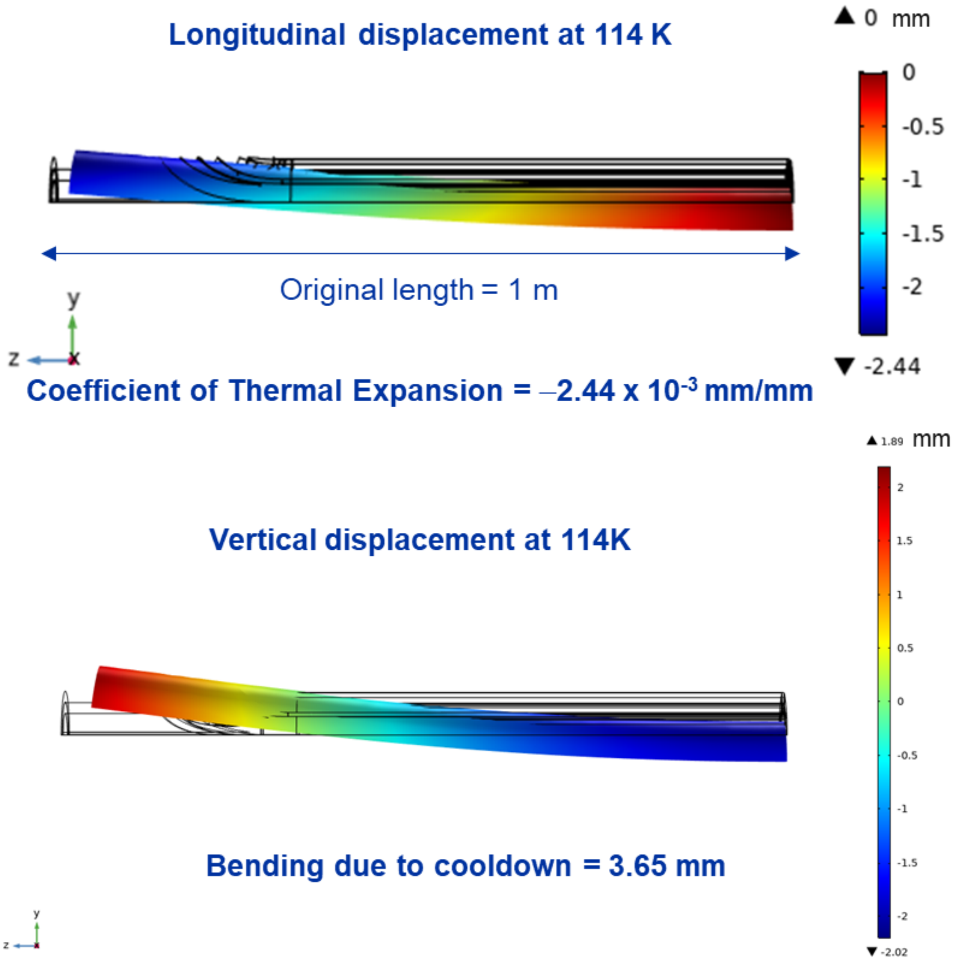

Figure 92: Results from new FE model for HL-LHC 11 T dipole magnet coils applied to simulate the experiment carried out on a 2-m-long coil at CERN Cryogenic Laboratory. Top: computed longitudinal displacement at 114 K. Bottom: computed vertical displacement at 114 K (Courtesy C. Garion and M. Morrone, CERN [221]).

The FE model described above was applied to simulate the experiment on coil SD122. As illustrated in Figure 92, the computed CTE is 2.44 mm/m for the overall coil and 2.3 mm/m for the coil straight section, while the estimated vertical bending due to cooldown is ~3.65 mm. These values are in reasonable agreement with the test results. (Note that the homogenized coil CTE quoted above is different from the one given in Table 8 because it does not include Ti-alloy pole pieces).

Let us stress again that it is critical for the credibility of the FE model to rely on suitable physical parameters, that are derived from first principles and possibly validated by *ad hoc* measurements, rather than on values that are fitted a posteriori to achieve a better match with the observed magnet behavior. This is particularly true for CTEs.

4.5.6.4 Powering (Loading Step E): Axial Mechanics

From the macroscopic point of view, a key element in the axial mechanics of the cold mass is assessing what is the fraction of the longitudinal electromagnetic load that is directly transferred to the set screws mounted on the end plates versus the remaining part that is held by the coil rigidity and the frictional contacts in the system. As explained in Section 1.5.5.1, the force transmitted to the set screws can be measured by bullet strain gauges mounted on the pushers.

Unfortunately, none of the 5.3-m-long 11 T dipole magnets which have been cold tested were instrumented with bullet strain gauges, due to lack of time and schedule pressure. The first long magnet to be instrumented was S5, which has not been cold tested. Therefore, the only available data are those from the short magnet models [101][248]. The most relevant for a comparison with the FE model are those from two-in-one-aperture short model magnet DP201. For this model magnet, the ratio between the force change measured on the bullet strain gauges during energization and the estimated Lorentz force at maximum test current is 38% for aperture SP201 and 46% for aperture SP202. In comparison, the ratio estimated from the FE model is 50%. Again, the agreement between measured and computed values is quite reasonable.

4.5.7 Main Findings from the New FE Model

4.5.7.1 Introduction

Now that we have built confidence in the new FE model through various benchmarking exercises, let us use it to identify areas of undesirable stress concentrations. Of course, we are not expecting the model to be fully accurate, and we should remain circumspect about absolute stress values, but the computed trends and the relative stress distributions are likely to be meaningful and trustworthy.

In a nutshell, in the straight part of the magnet, the new FE model simulations confirm the recommendations of the 1st 11 T Task Force in terms of coil shimming parameters to avoid coil overstress. However, at the transition between the straight part and the end of the magnet and in the magnet head itself, the new FE model reveals a few critical areas that raise concerns and call for correction/preventive actions. Let us review in detail the main findings.

4.5.7.2 Azimuthal Stress in Magnet Straight Section

Figure 93 presents the azimuthal stress distribution in the coil and Ti-alloy pole cross-sections for each of the main loading steps.

Upon collaring completion (loading step A), the peak stress on the conductor occurs in the medium part of the conductor block next to the pole and is of the order of -80 MPa. Let us note the role played by the notch at the inner radius of the Ti-alloy pole to relieve the pole stress. This feature was first introduced in the collar design of the dipole magnets for the Superconducting Super Collider (SSC) project in the USA in the early 1990s [212] and was integrated into LHC dipole magnet collar design [72]. It was omitted in the MQXF design to facilitate the implementation of fiber optics instrumentation.

After cooldown (loading step D), the peak stress in the pole conductor block increases to about -90 MPa because of thermal shrinkage differentials between stainless-steel collars, Ti-alloy pole pieces and coil blocks.

At full energization (loading step E), the coil pole unloads, and the peak stress moves to the midplane of the inner layer and reaches about -100 MPa.

In conclusion, the new FE model confirms that, under nominal assembly conditions, the straight parts of the 11 T dipole magnet coils can be expected to be sufficiently loaded while avoiding overstresses.

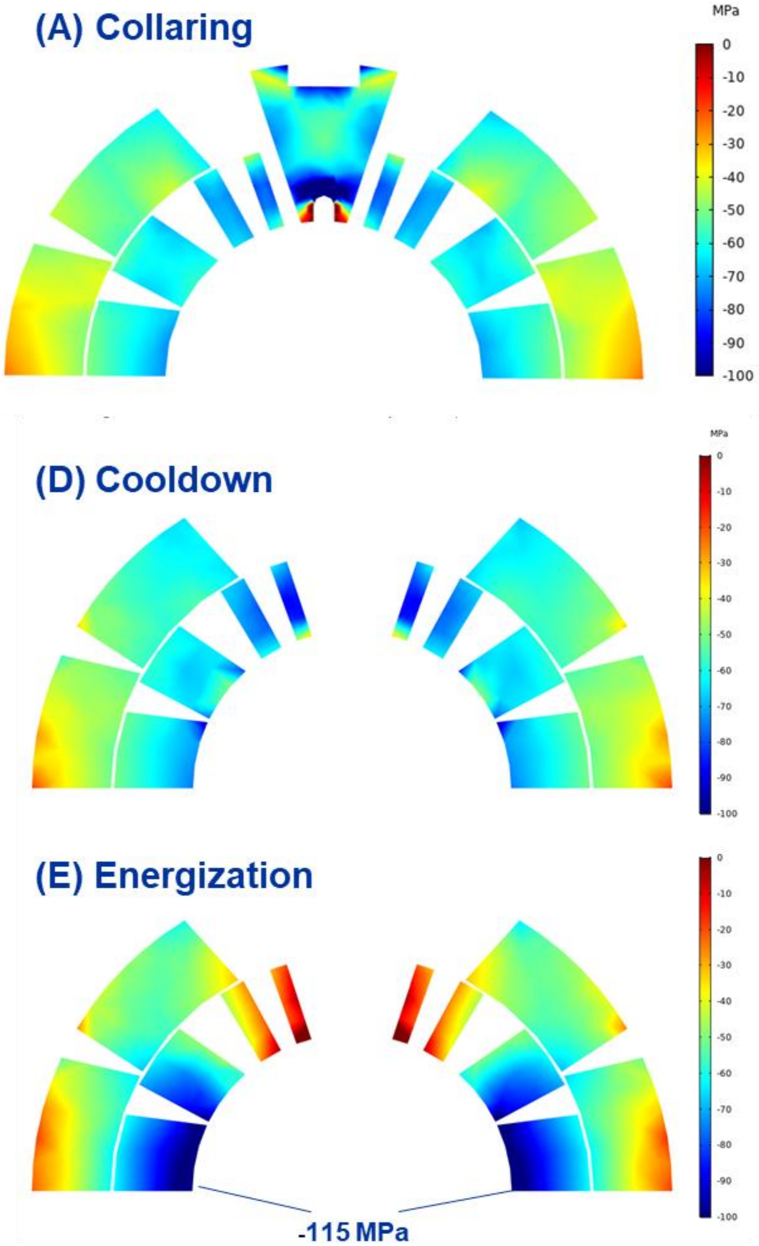

Figure 93: Azimuthal stress distributions in the cross-section of the coil and radial stress distribution in the Ti-alloy pole computed in the straight part of the new FE quarter model of the 5.3-m-long, 60-mm-two-in-one-aperture HL-LHC 11 T dipole magnet at various loading steps. Top: after collaring. Middle: after cooldown. Bottom after energization to 11.85 kA (Courtesy of M. Morrone and C. Garion, CERN [221]).

4.5.7.3 Azimuthal and Radial Stress Concentration in Magnet Coil Head After Collaring

Figure 94 features azimuthal stress distributions over the connection-side coil head after collaring (in the coordinate system of Figure 82, azimuthal refers to a direction perpendicular to the conductor’s broad face).

The simulation shows peak stresses of +120 MPa in the outer-layer pole turn end and of +70 MPa in the inner-layer pole turn end, while the stresses are in the 90–130 MPa range in the transition region between coil head and coil straight section.

Figure 95 features axial stress distributions for the same areas of the connection-side coil head after collaring (in the coordinate system of Figure 82, axial refers to a direction tangential to the conductor's broad face). As in the case of azimuthal distributions, the simulation shows tensile peak stresses at the pole turn ends of +55 MPa in the outer layer and +30 MPa in the inner layer. The simulation also reveals singularities at the extremity of the collaring shim between coil poles and Ti-alloy pole pieces (which also corresponds to the end of the latter and the junction with the stainless-steel winding key) and the occurrence of an overall bending of the coil blocks at the transition between straight section and coil head.

In addition to geometrical discontinuities (*e.g.,* between wedges and spacers), another likely origin of the observed stress concentrations is the fact that the shimming plan implemented on the full-length 11 T dipole magnets calls for an abrupt step between the end of the coil straight part and the beginning of the coil heads. This step is simulated in the FE model by a reduction of the coil excess from +170 µm to 0 µm (let us recall that the reason for the choice of the value of 170 µm in the straight part instead of the nominal value of 300 µm is explained in Section 4.5.6.1). As a result, at the time of collaring, the application of the vertical force from the press in the magnet straight part, where the Ti-alloy poles are in good contact with the coils through the loading plates, results in a longitudinal pulling force on the somewhat looser conductor blocks in the coil heads, resulting in the observed stress concentrations and bending effect at the transition. In reality, the aforementioned effects may not be as dramatic as computed by the FE model, but the model does point to a weakness in the magnet assembly procedure that can be corrected (see Section 4.6).

4.5.7.4 High Compressive Stress on Layer Jump and Likely Cracks in Resin-Rich Areas After Cooldown

Figure 96 features azimuthal stress distributions over the connection-side coil head after cooldown. Compared to Figure 94, one can clearly see an enhancement of the compressive stress on the layer jump (top figures), due to the low CTE of the Ti-alloy pole piece, with a significant area below -150 MPa, which is a concern.

Also, as illustrated in Figure 97, high concentrations of Von-Mises stresses are observed in the resin-rich areas modeled in the coil inner layer (see Section 4.5.2 and Figure 81). These stress concentrations arise during cooldown, due to the high CTE of pure resin, and are further enhanced during energization. They are likely to lead to cracks in the resin (the ultimate tensile strength of pure epoxy resin is ~45 MPa at room temperature and ~90 MPa at 77 K [296]) and/or to delamination of the cable blocks from the metallic wedges and spacers (the double lap shear strength of CTD101-101K® ranges from 8 to 13 MPa at room temperature and 11–15 MPa at 77 K, depending on the metal to which it adheres [297]). These cracks and delamination release and accommodate the high stresses, and this explain the observations made in the metallographic analyses of coil heads (see Section 3.5.1.2).

Similar radial stress concentrations can also be seen at the junctions between copper wedges and stainless-steel end spacer tips. The present FE analysis does not model cracks or delamination.

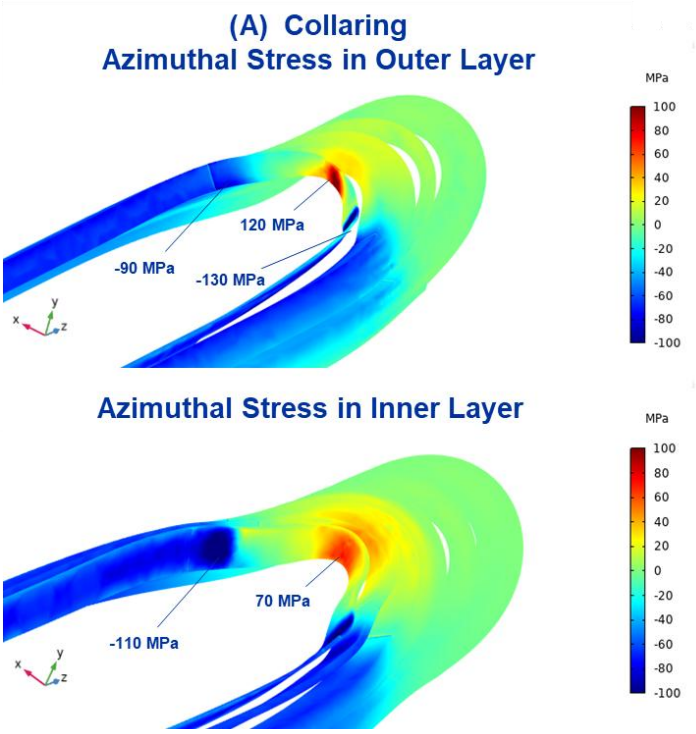

Figure 94: Azimuthal stress distributions in the connection-side coil head computed by new FE quarter model of 5.3-m-long, 60-mm-two-in-one-aperture HL-LHC 11 T dipole magnet after collaring loading step. Top: outer layer. Bottom: inner layer (Courtesy of M. Morrone and C. Garion, CERN [221]).

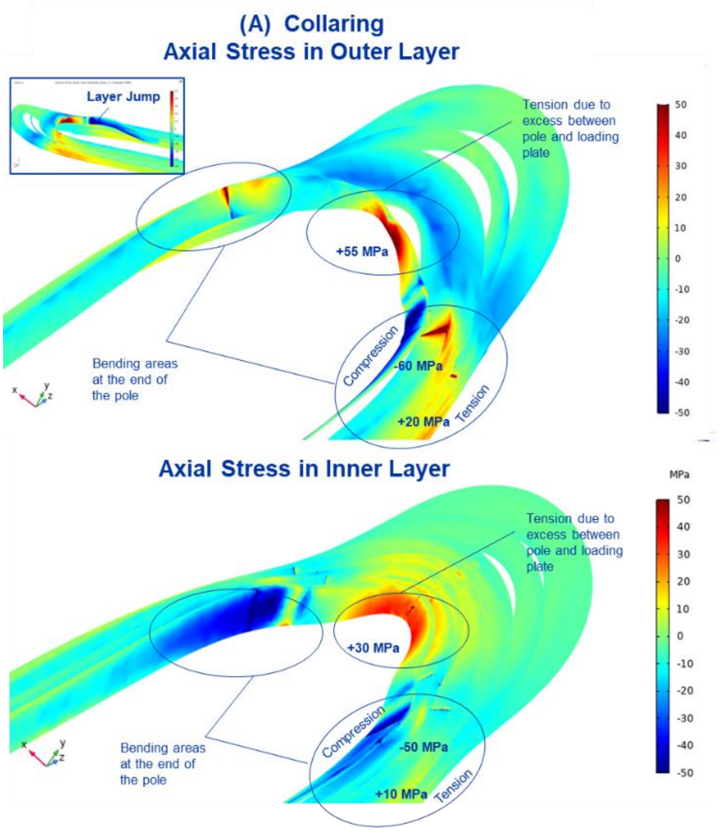

Figure 95: Axial stress distributions in the connection-side coil head computed by new FE quarter model of 5.3-m-long, 60-mm-two-in-one-aperture HL-LHC 11 T dipole magnet after collaring loading step. Top: outer layer. Bottom: inner layer (Courtesy of M. Morrone and C. Garion, CERN [221]).

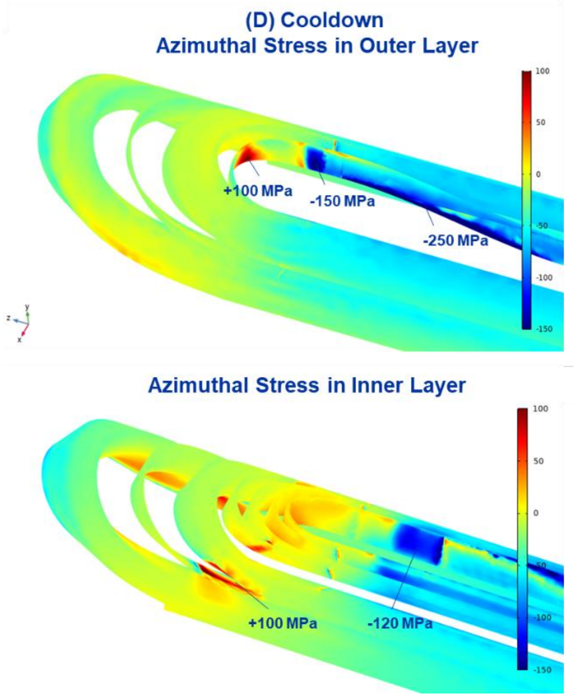

Figure 96: Azimuthal stress distributions in the connection-side coil head computed by new FE quarter model of 5.3-m-long, two-in-one-aperture HL-LHC 11 T dipole magnet after cooldown loading step. Top: outer layer. Bottom: inner layer (Courtesy of C. Garion and M. Morrone, CERN [221]).

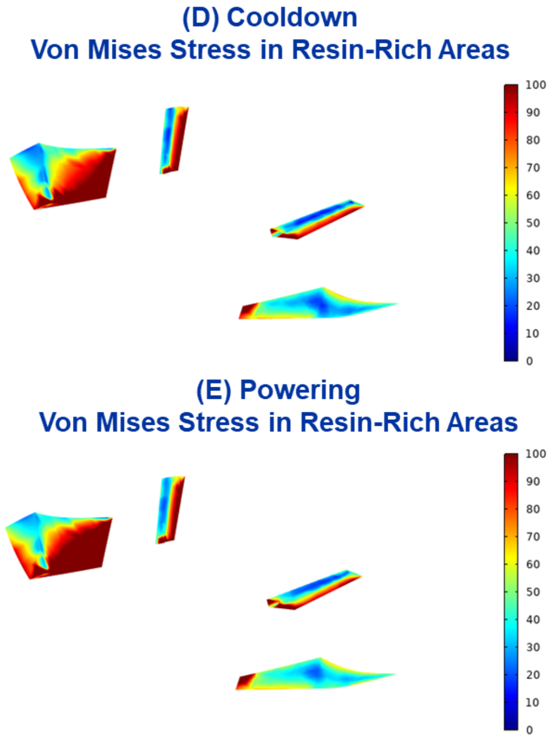

Figure 97: Von Mises stress in resin-rich areas implemented of selected conductor blocks from connection-side head of 5.3-m-long, 60-mm-two-in-one aperture HL-LHC 11 T dipole magnet model developed within the framework of the 2nd 11 T dipole magnet Task Force at CERN (see **Figure 81**). Top: after cooldown. Bottom: after energization (Courtesy of M. Morrone and C. Garion, CERN).

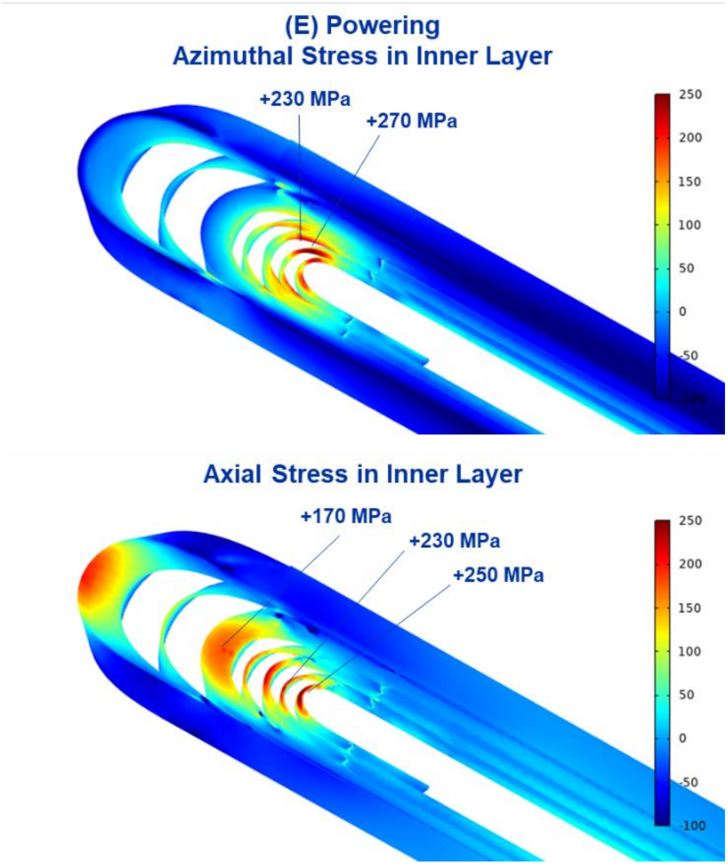

Figure 98: Azimuthal and axial stress distributions in the inner layer of the connection-side coil head computed by the new FE quarter model of 5.3-m-long, two-in-one-aperture HL-LHC 11 T dipole magnet after energization loading step to 11.83 kA. Top: azimuthal stress. Bottom: axial stress (Courtesy of C. Garion and M. Morrone, CERN [221]).

4.5.7.5 Azimuthal Tension in Turn End and Bending of Inner-Layer Coil Head During Energization

As illustrated in Figure 98, the combination of the longitudinal, lateral and vertical components of the Lorentz forces results in complex stress distributions with very high peak values. The azimuthal stress reaches 230 to 270 MPa in the inner-layer turn ends (and up to 240 MPa in the outer-layer turn ends). Conversely, the radial stress distribution shows a strong bending effect due to the vertical and lateral components of the Lorentz force which tends to push the coil head downwardly, with peak tensile stresses in the 170–250 MPa range in the inner layer (and, again, up to 240 MPa in the outer layer).

It is likely that cracks of the brittle resin and delamination of the cables themselves or at their interfaces with end spacers will occur in these areas, enabling stress accommodation to lower and more acceptable levels, but a robust magnet design should not rely on such an uncertain and uncontrollable process, which may vary as a result of warm-up cooldowns.

More design optimization work is needed to limit peak azimuthal and radial stresses in the magnet heads.

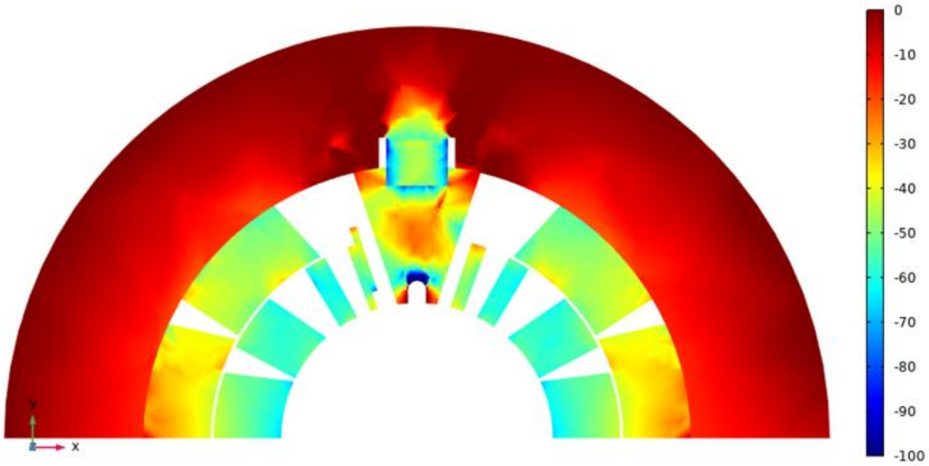

Figure 99: Radial stress distribution in an instrumented collar and azimuthal stress distribution in a half coil computed by new FE quarter model of 5.3-m-long, two-in-one-aperture HL-LHC 11 T dipole magnet after collaring loading step (Courtesy of M. Morrone and C. Garion).

4.5.7.6 Bending of Collar Nose During Energization

As already mentioned in Section 4.5.6.1 and illustrated in Figure 88, and unlike what is done usually in the design of Nb–Ti accelerator magnets [212], the collar nose of the 11 T magnets is not shaped to be directly in contact with the coil pole faces, but has a rectangular tip which is housed in a groove machined on the top of the Ti-alloy pole pieces in contact with the coil. During collaring, the press applies a vertical force onto the collars, whose tips push against the bottom of the Ti-alloy pole housing, eventually providing azimuthal prestress to the coil, as illustrated in Figure 99.

Most 11 T dipole magnet models and prototypes were equipped with instrumented collars at various longitudinal positions. These instrumented collars have strain gauges glued on their noses (see Figure 88). In addition, cutouts are made on both sides of the nose to homogenize the collar nose stress and enable more reliable measurements from the strain gauges. The strain gauge readout is not a direct measurement of the azimuthal prestress at the coil pole, and that there is a transfer function between the two.

As detailed in Section 4.5.6.1, a calibration was carried out on a collaring mock-up at the time of the 1st 11 T Task Force, which established that, for collaring at room temperature, the average azimuthal stress in the coil is about a factor of 2 lower than the collar nose stress [100]. This is also confirmed by the stress distributions displayed in Figure 99 (note that Figure 99 features the radial stress distribution in the collar and the azimuthal stress distribution in the coil.)

The next question arises whether the transfer function remains at a constant value of 2 during cooldown and energization or does it evolve.

Figure 100 shows the stress distribution in an instrumented collar, with a close-up view of the collar nose after cooldown and energization. As can be seen in the plot, the radial component of the Lorentz force results in a bending moment on the collar arms, causing an unloading of the central area of the collar nose. This is associated with the occurrence of a small gap between the nose tip and the housing bottom in the Ti-alloy pole piece (at high magnification), while the lateral faces of the collar nose come into compression against the lateral faces of the housing. This, of course, makes the transfer of force between collar nose, Ti-alloy piece and coil quite cumbersome and calls for a FE model to analyze it. Also, it is likely that the deep cutouts machined on both sides of the instrumented collar nose are exacerbating the effect.

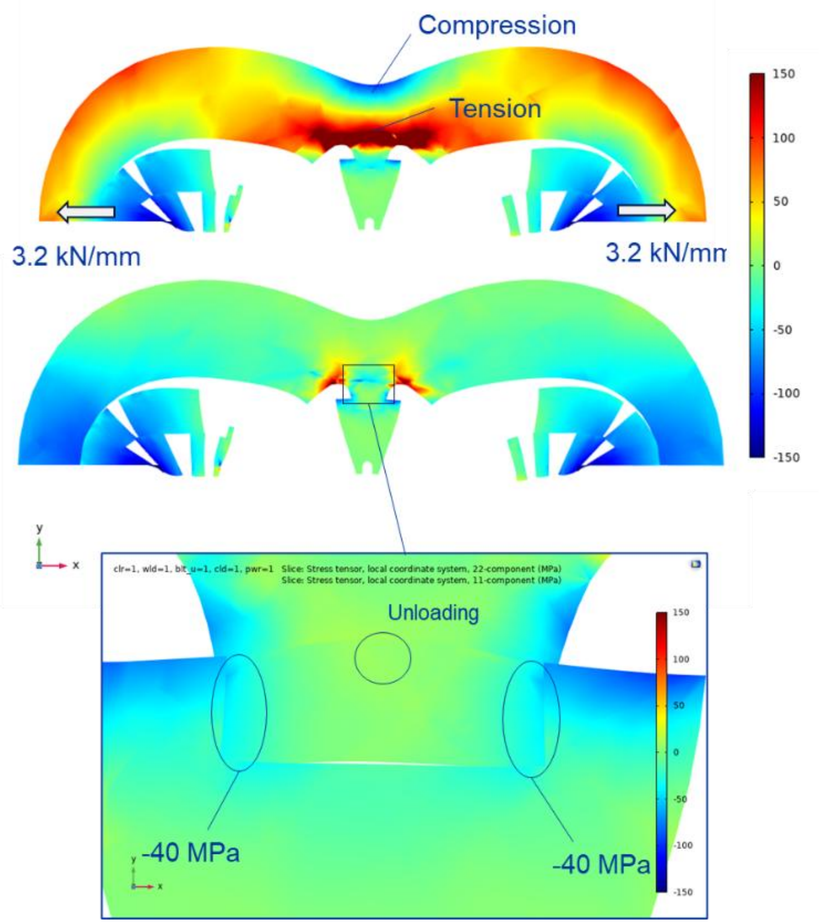

Figure 100: Stress distributions in instrumented collar and adjacent Ti-alloy pole piece computed by new FE quarter model of 5.3-m-long, two-in-one-aperture HL-LHC 11 T dipole magnet during powering. Top: azimuthal stress. Middle: radial stress. Bottom close-up view of radial stress distribution in collar nose and adjacent Ti-pole housing (Courtesy of M. Morrone and C. Garion).

As a consequence, when plotting instrumented collar nose stress as a function of current squared, we do not observe the expected linear decrease from the effect of the azimuthal component of the Lorentz force, which tends to squeeze the coil towards the midplane and to unload the pole (see Figure 101). We, instead, observe a non-linear decrease and a progressive flattening. This is likely due to a superposition of two effects:

- coil pole unloading, caused by the azimuthal component of the Lorentz force;
- aforementioned collar bending and collar nose unloading, caused by the radial component of the Lorentz force.

The three curves of Figure 101 correspond to three different shim thicknesses: nominal value of 170 µm, representing 300 µm in real life, and reduced values of 145 and 95 µm, representing 275 and 225 µm, respectively. The three curves eventually reach the same plateau, which corresponds to full collar nose unloading. As expected, the smaller the shim, the sooner the unloading plateau is reached.

The qualitative description given above shows that the transfer function between collar nose and azimuthal coil stress becomes cumbersome to derive, making the strain gauge measurements during energization arduous to interpret. However, it explains the flattening of the collar nose stress reported in Refs. [101] and [248], for which there was always a strong suspicion that, given the low current level at which it occurred, it was not a sign of coil pole unloading but was likely to have a another origin.

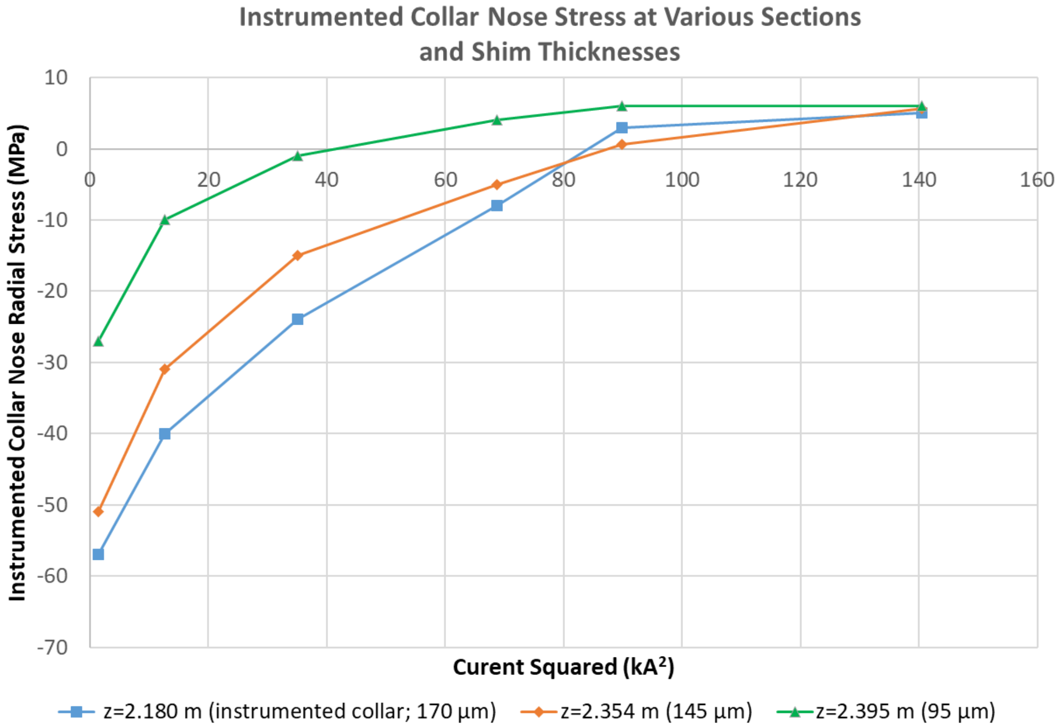

Figure 101: Instrumented collar nose stress versus current squared, computed for 3 different shim thicknesses during powering loading step, by new FE quarter model of 5.3-m-long, two-in-one-aperture HL-LHC 11 T dipole (Courtesy of M. Morrone and C. Garion, CERN).

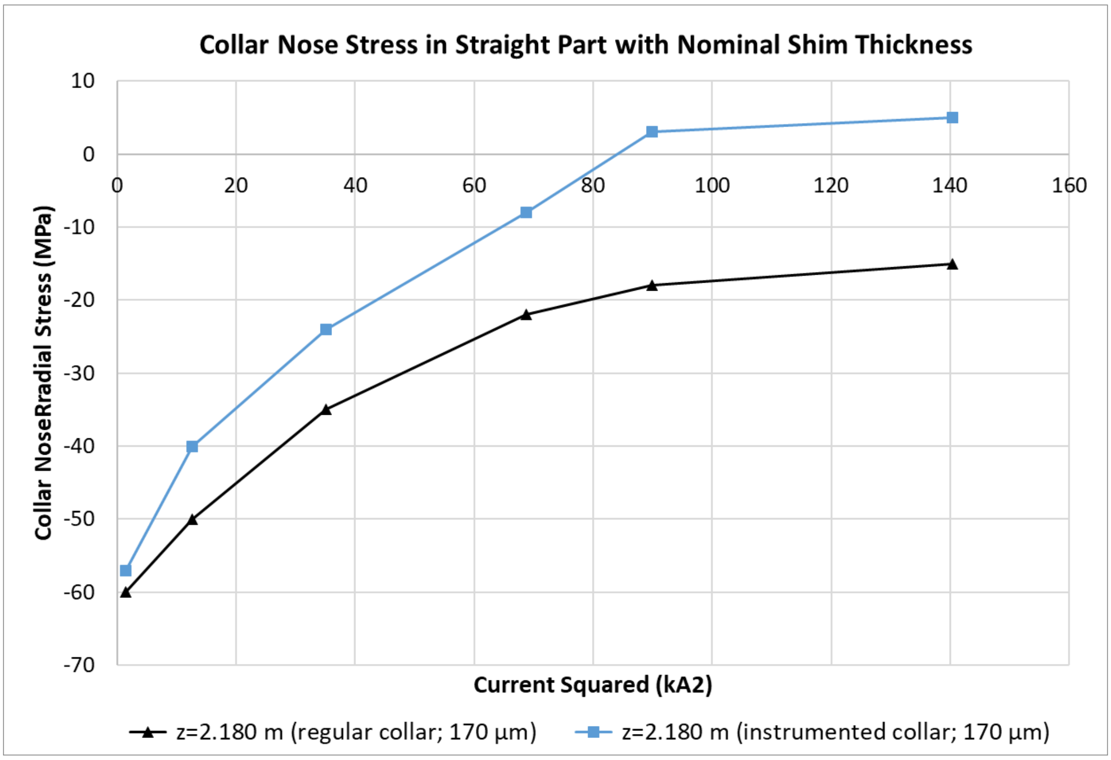

Figure 102: Comparison between instrumented collar nose stress and regular collar nose stress versus current squared, computed for nominal shim thickness during powering step, by new FE quarter model of 5.3-m-long, two-in-one-aperture HL-LHC 11 T dipole (Courtesy of M. Morrone and C. Garion, CERN).

The next question is: is the flattening a specific feature of instrumented collars, because of the deep cutouts on the nose sides, or does it also occur in regular collars without cutout? Figure 102 presents a comparison of computed nose stress versus current squared for an instrumented collar and a regular collar, assuming a nominal shim thickness of 170 µm (corresponding to 300 µm in real life). The regular collar curve exhibits the same non-linear behavior, albeit with a slower rate of decrease, and does not seem to achieve full unloading. The presence of the cutouts exacerbates the phenomenon, but even without them, the effect of collar bending, and the resulting collar nose unloading, are still present (although, they do not lead to the opening of a gap at high magnification as in Figure 100). In summary, the factor of 2 between collar nose and coil pole stress is only valid at room temperature, during assembly, but the transfer function is much more difficult to derive for other loading steps.

This analysis is a reminder that mechanical measurements are tricky and usually call for local design modifications. It is always advisable to carry out a detailed assessment of the impact and of the relevance of the measurements for the various loading steps of the system under assessment. This was studied in detail for the so-called *beam-type strain gauge transducers* developed at BNL and successfully implemented at the time of the Superconducting the Super Collider project [249] or for the so-called *capacitive force transducers* developed at CERN and subsequently at CEA/Paris-Saclay at the time of LHC dipole and quadrupole magnet development [250][251].

4.5.7.7 End Plate Bending During Energization

As illustrated in Figure 103, the FE model shows a slight deformation of the stainless-steel end plate during energization, with a maximum displacement at the center between the two apertures of ~0.35 mm at 11.85 kA. This deformation likely results from the bending of the orbital fillet weld between the end plate and the outer stainless-steel shell.

The occurrence of this deformation is associated with an uneven distribution of the load generated by the longitudinal component of the Lorentz force. In each of the two apertures, the two bullet screws located on the outer side of the structure see a higher load than those located on the inner side (between the two apertures), resulting in a higher force versus current squared slope (see Figure 104). This slight imbalance, may have resulted in the deformation observed on the end laminations of the central yoke pack during the disassembly of full-length 11 T dipole magnets after cold testing (see Section 4.4.2 and Figure 79).

At some point in the design of the 11 T dipole magnet, it was foreseen to rely on a set of tie rods running across the yoke packs and the end plates to provide longitudinal coil pre-compression [220]. Such rods, which are implemented in the MQXF design, may prevent end-plate deformation and result in a more uniform sharing of the Lorentz load. However, a robust solution can also be engineered for the end plate attachment to the outer shell that is not based on a single orbital filet weld that may be prone to bending. Such a solution was, for instance, successfully implemented on the MFISC model magnet (in addition to the *end cage* described in Section 4.6.5) [253]. It was also used on the 11 T magnet models designed and built at FNAL [93].

4.5.7.8 Stress Concentration at Discontinuities (e.g., Copper Wedges/End Spacers)

As illustrated in Figure 98(bottom), tensile stress concentrations are observed in the cable blocks next to interfaces between extremities of copper wedges and tips end spacers. This is a consequence of the presence of singularities in heavily stressed areas, which become more and more pronounced with each loading step, as a result of collaring, cooldown and energization.

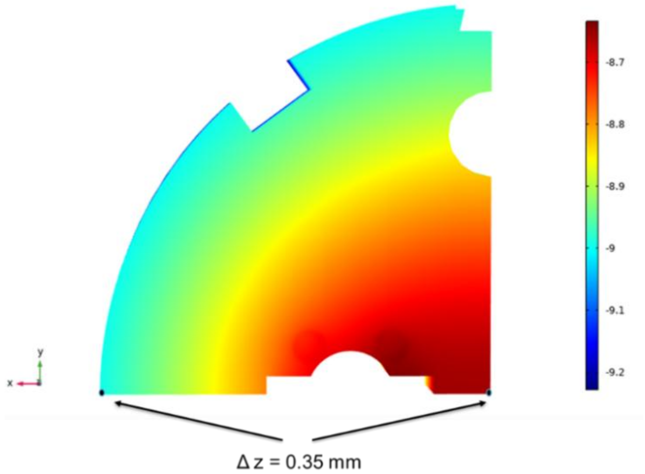

Figure 103: Deformation of connection-side end plate computed by the new FE quarter model of 5.3-m-long, 60-mm-two-in-one-aperture HL-LHC 11 T dipole magnet after energization loading step to 11.83 kA (Courtesy of M. Morrone and C. Garion, CERN).

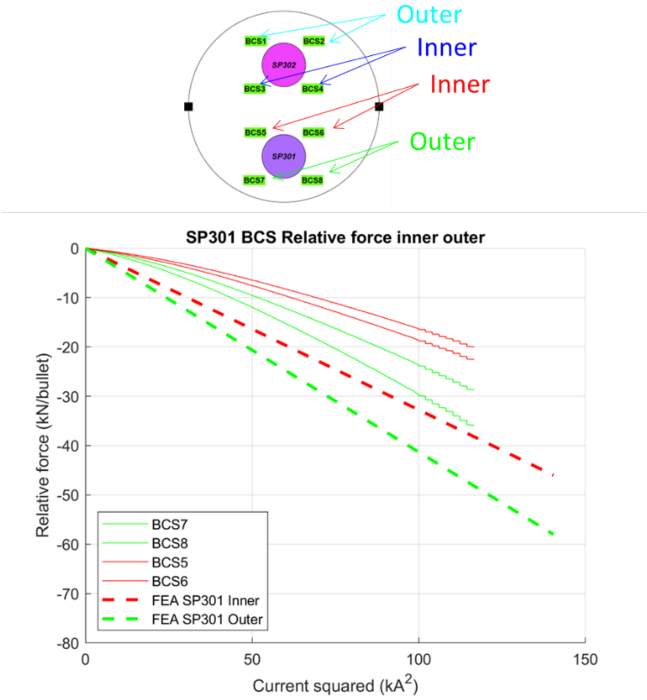

Figure 104: Relative force per set screw vs. current squared measured by bullet gauges on the set screws/pushers at the connection-side of Aperture 1 (SP301) of short magnet model MBHDP301 and computed by new FE quarter model of 60-mm-two-in-one-aperture HL-LHC 11 T dipole magnet during energization loading step to 11.83 kA (Courtesy of C. Abad Cabrera, formerly CERN, with inputs from M. Morrone and C. Garion, CERN).

4.5.7.9 Wrap-Up

We went into many details to present the development, benchmarking and findings of the new FE model that was initiated as part of the 2nd 11 T Task Force, to illustrate how such a model can benefit root-cause analyses and help in the identification of design weakness. Let us now review the recovery actions that were undertaken to address the issues that were identified.

4.6 Recovery Plan

4.6.1 Introduction

Following the investigations of the 2nd 11 T Task Force, it was concluded that, although it was not possible to implement corrective actions on the identified issues internal to the coils, there were still many points related to the external support and loading of the coil and magnet ends to justify enacting the 2nd Phase of the strategy. Therefore, it was decided to proceed with the development of a recovery plan in view of the assembly and test of a full-length, two-in-one-aperture dipole magnet relying on already manufactured virgin coils (having not yet been assembled in a magnet nor tested at cryogenic temperature).

However, before proceeding with the long magnet assembly, it was also decided to qualify the proposed recovery actions on a short, two-in-one-aperture dipole magnet model, with the caveat that, since there was only one short virgin coil available, the magnet model would have to rely on already used coils, with uncertain loading histories. This implies that the quench performance of the reassembled magnet model cannot be guaranteed and that it should be considered mainly as a mechanical model, whose data will serve as validation of the new FE model.

As detailed thereafter and, given that the two apertures of the short model and full-length prototype can be connected electrically to be powered independently during cold testing, it was decided to use this opportunity to evaluate different types of corrective actions. In particular, it was selected to implement so-called *conservative* corrective actions in one aperture and, in addition to these conservative actions, to assess a more *innovative* solution in the other aperture.

The conservative corrective actions, to be applied in both apertures, are meant to address the issues observed during magnet disassembly and the concerns raised by the new FE model. They include:

- use of tapered pole shims at the transition between coil straight section and coil heads;
- replacement of Ti-alloy pole pieces by stainless-steel pole pieces;
- revision of axial preloading system/procedure to minimize risk of set screws misalignment/loosening;
- improvement of laminated yoke structure support to prevent bending/ratcheting at the ends;
- improvement of instrumentation, in particular, for coil/magnet ends.

The innovative solution, to be applied on one aperture only, and in addition to the above corrective actions, is the implementation of a so-called *end cage* over the coil heads (details provided in Section 4.6.5).

Let us now review the main proposals.

4.6.2 Shimming Plan Optimization over Coil Ends

As detailed in Ref. [100], the 1st 11 T Task Force had concluded that a safe value for the lateral shim positioned between the pole piece pole and the stainless-steel loading plate that cover the pole is 300 μm. As explained in Section 4.5.6.1, in the FE model, an equivalent shim thickness of 170 μm is used to correct for the offset in the stress plots of Figure 89.

In the original shimming plan, the shim is constant in the magnet straight section and abruptly ends at the start of the winding key. This abrupt step has been shown to result in undesirable stress concentrations. To mitigate this effect, it was decided to adopt a shimming plan that decreases more progressively from the straight section to the coil ends.

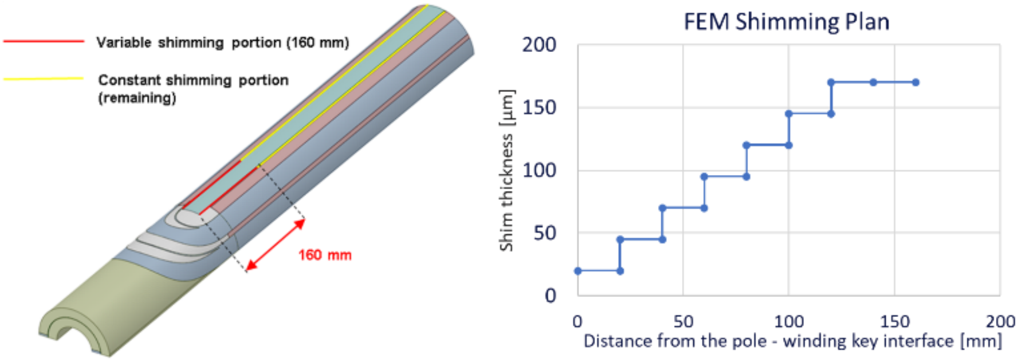

Figure 105: Implementation of the variable shimming plan over the heads of HL-LHC 11 T dipole magnet coils. Left: longitudinal localization of the variable section of the shimming plan. Right: profile of variable shimming plan (note that in FE model an offset of -130 μm is applied; Courtesy of M. Morrone and C. Garion, CERN [222]).

As illustrated in Figure 105, the variable portion of the shimming plan starts from the interface between the winding key and the first Ti-alloy pole piece and extends over a length of 160 mm towards the magnet center. It is implemented by steps of 25 μm every 20 mm. For real coils, the first step is 150 μm, and the staircase ends at 300 μm on the 7th step after which it stays constant. In the FE model, a constant offset of 130 μm is subtracted with respect to real coils, the first step starts at 20 μm while the 7th step ends at 170 μm.

4.6.3 *Change of Pole Piece Material from Ti-Alloy to 316LN Stainless Steel*

In addition to the new shimming plan, it was decided to replace the Ti-alloy pole pieces by pieces made of 316LN stainless steel, whose integrated thermal contraction coefficient between room and cryogenic temperature is closer to that of the coil (see Table 8). The titanium alloy used for the baseline design has an integrated CTE of -1.74x10^{-3} while that of 316LN stainless-steel is -2.95x10^{-3}. Given that the CTE of a homogenized coil is -2.78x10^{-3}, at the end of the cooldown, the Ti-alloy poles end up in longitudinal compression and cause high tension in the coil heads. This effect can be mitigated by relying on stainless-steel pole pieces, which, after longitudinal loading and cooldown end up in moderate compression, mainly due to the longitudinal forces applied by the set screws. Also, the change of pole piece material reduces the stress singularities arising during cool-down between winding keys and pole pieces, and between end spacers' tips and copper wedges.

The expected impacts of the new variable shimming plan and of the change of pole piece material can clearly be seen in the azimuthal and axial stress distributions after collaring in Figure 106 and after cooldown in Figure 107 for the coil outer layer. The plots for the inner layer show a similar trend.

The plots after collaring (Figure 106) shows that the azimuthal stress in the first turn of the outer layer decreases from 120 to 10 MPa. Similarly, the axial stress decreases from 55 MPa to 4 MP. This decrease is likely because the looser shimming in the transition part between coil straight section and coil end results in a greatly reduced pulling force on the conductor blocks. Also, the stress singularities that were observed at the junction between the last pole piece and the winding key are greatly reduced.

The decrease in azimuthal and axial stresses are also confirmed after cooldown. The azimuthal stress in the first turn of the outer layer decreases from +95 MPa to -20 MPa while the high stress area at the layer jump extremity is removed and the peak compressive stress on the layer jump decreases from -150 MPa to -115 MPa. The axial stress in the first turn of the outer layer goes from 60 MPa to -30 MPa and the very high stress singularity that arose at the copper wedge extremity is not present anymore. This, again, is likely to result from the more similar CTEs of pole pieces and coils, which are not inducing additional high tension in the conductor blocks. These results confirm the benefits from the proposed recovery actions.

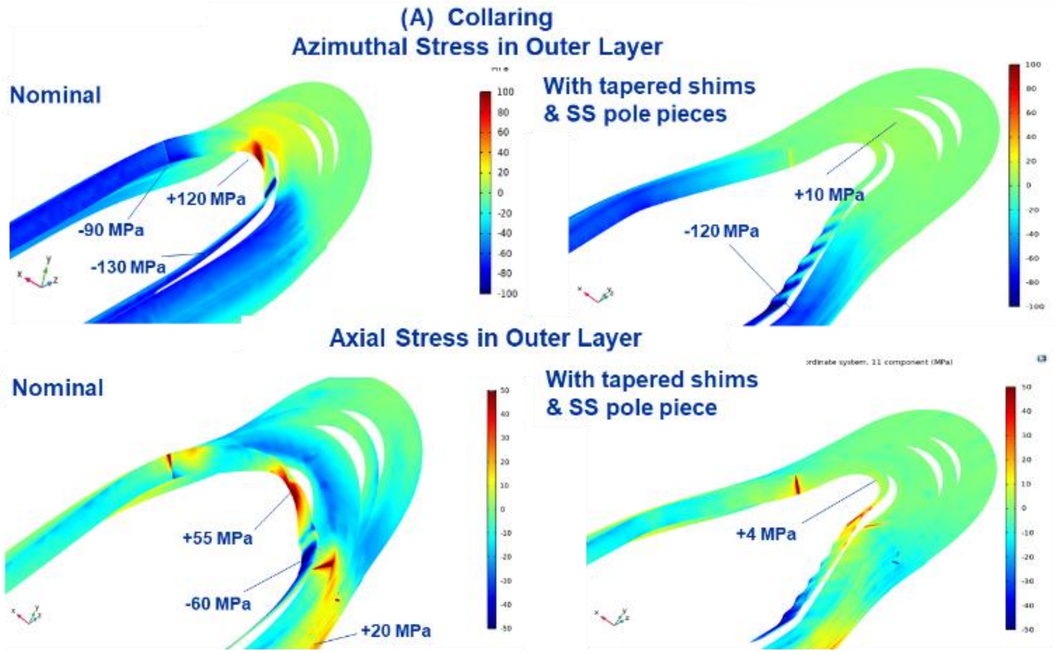

Figure 106: Comparison of azimuthal and axial stress distributions in the connection-side head of the coil outer layer of HL-LHC 11 T dipole magnet at the end of collaring loading step for nominal design (left) and after the implementation of variable shimming plan and stainless-steel pole pieces (right). Top: azimuthal stress. Bottom: axial stress (Courtesy of M. Morrone and C. Garion, CERN [222]).

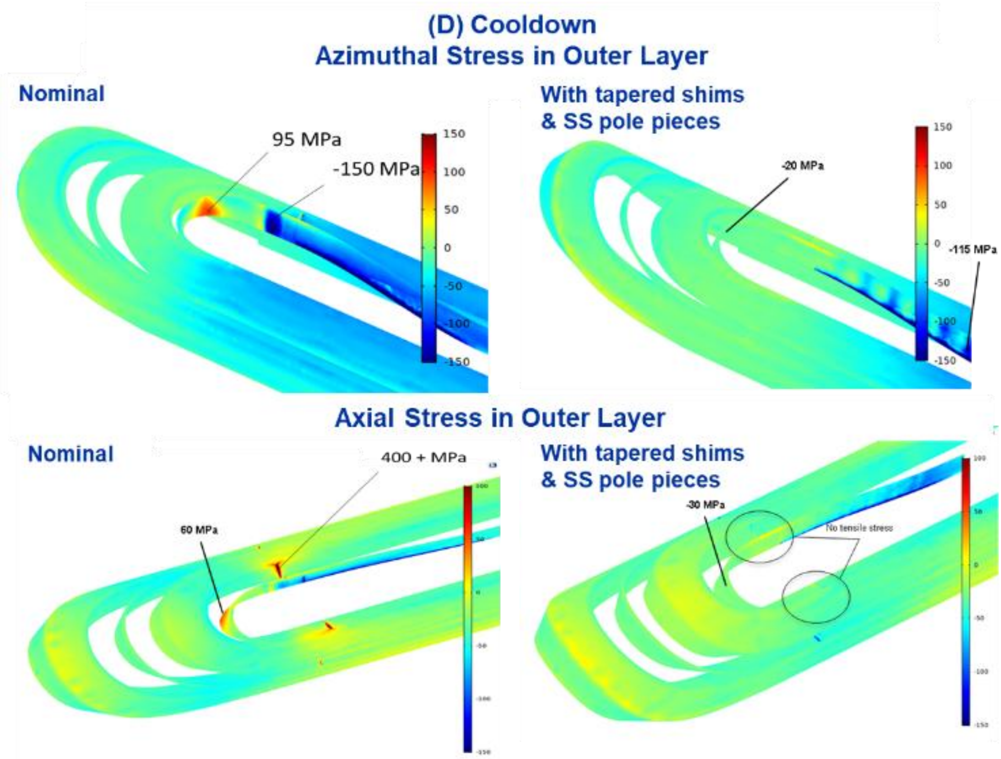

Figure 107: Comparison of azimuthal and axial stress distributions in the connection-side head of the coil outer layer of HL-LHC 11 T dipole magnet at the end of cooldown loading step for nominal design (left) and after implementation of variable shimming plan and stainless-steel pole pieces (right). Top: azimuthal stress. Bottom: axial stress (Courtesy of M. Morrone and C. Garion, CERN [222]).

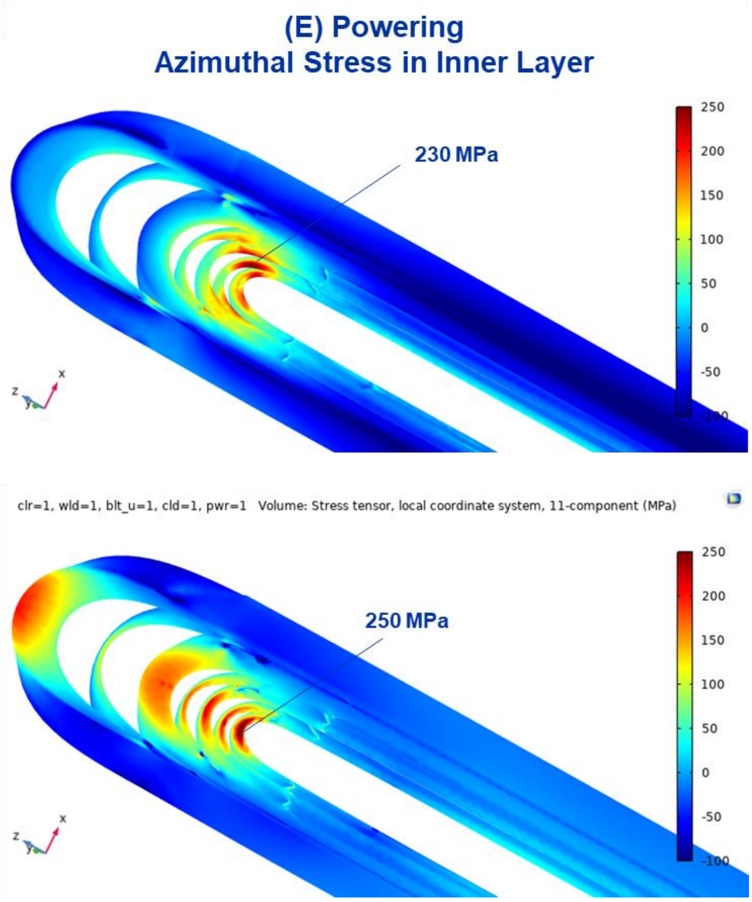

Figure 108: Azimuthal and axial stress distributions in the connection-side head of the coil inner layer of HL-LHC 11 T dipole magnet at the end of energization loading step to 11.83 kA and after implementation of variable shimming plan and stainless-steel pole pieces. Top: azimuthal stress. Bottom: axial stress (Courtesy of C. Garion and M. Morrone, CERN [222]).

After energization to 11.83 kA, and comparing the plots in Figure 98 and Figure 108, the peak azimuthal stress in the inner-layer conductor blocks decreases from 270 MPa to 230 MPa, and the peak axial stress remains of the order of 250 MPa. These high stresses, which, as explained in Section 4.5.7.5, are largely due to the vertical bending of the coils caused by the Lorentz force, are a design feature of the magnet. They remain a serious concern, which can only be mitigated by changing the coil head design. This concern should be addressed in future high-field accelerator magnet programs

4.6.4 Instrumentation of Set Screws and Pushers with Bullet Gauges

A critical piece of information missing from the cold test of full-length 11 T dipole magnets is a measurement of the longitudinal force applied by the set screws to the coil end saddles and its evolution during cooldown and excitation. It was decided that the new magnets to be assembled should all be equipped with calibrated bullet strain gauges mounted on the pushers and to compare measurement and FE model simulation results. Let us recall that, like other types of magnet mechanical instrumentation, bullet gauges were developed at BNL at the time of the SSC [249].

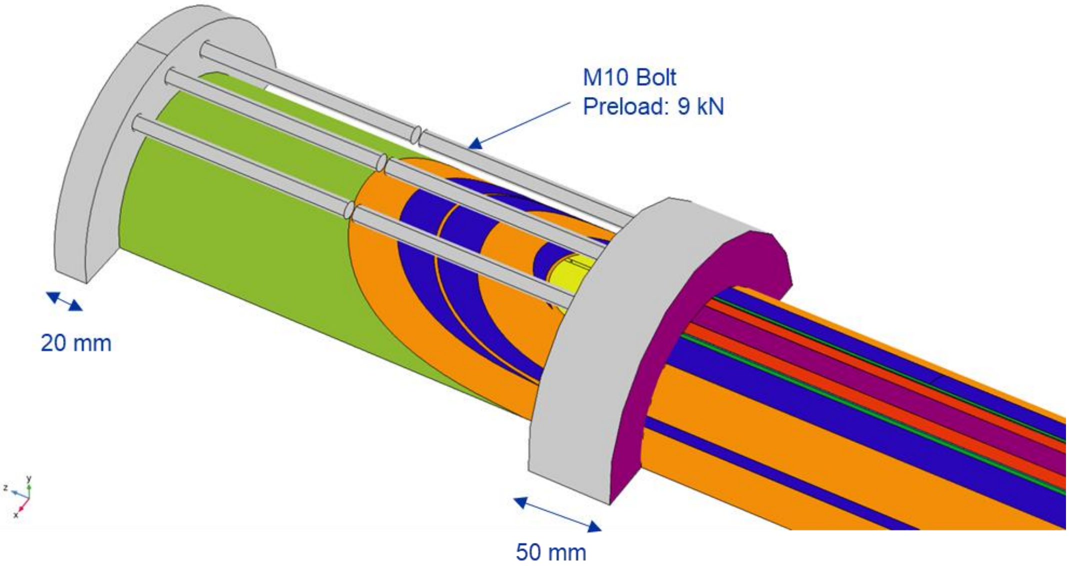

Figure 109: Conceptual design of end cage, to be implemented on the coil heads of 11 T dipole magnets at CERN (Courtesy of D. Perini, G. Spigo, C. Garion and M. Morrone, CERN [222]).

4.6.5 End-Cage Study

A last mitigation solution that has been proposed and investigated in the FE analysis is the integration of a tightening structure over the coil heads known as an *end cage*. The goal of the end cage is to better compact and support the coil ends, in particular: (1) to limit displacement and prevent detachment of conductor blocks from end spacers and winding keys during cooldown and powering and (2) to limit stresses in resin-rich areas and, therefore, reduce risks and impacts of cracking.

The end-cage concept was first developed at CERN in the mid-1990s and implemented in the MFISC and MFRESCA magnets, which both rely on Nb–Ti Rutherford-type cables.

MFISC is a 1-m-long, 56-mm-two-in-one-aperture dipole magnet, with a distance between aperture axes of 200 mm, designed in collaboration with Helsinki University of Technology [252], but built and cold tested at CERN in 1995/1996 [253][254]. The magnet underwent three cooldowns, exhibited little training/retraining and achieved a record field of 10.53 T at 1.77 K.

MFRESCA is a 1.7-m-long, 88-mm-single-aperture dipole magnet that has been implemented and is still operated as a background field magnet for a cable test facility at CERN. The magnet was built under contract by Holec Machine Apparaten (HMA) in the Netherlands and was first cold-tested at CERN in 1999 [255]. It exhibited its first quench at 8.46 T and reached 10.09 T on its 6th quench. It is now routinely excited up to 9.6 T without a problem [256]. The MFISC and MFRESCA magnets are the most successful Nb–Ti accelerator magnets designed and built to date, in terms of both training/retraining and maximum field.

As illustrated in Figure 109, the proposed end cage is made of a 50-mm-long stainless-steel annulus, welded on the last pole pieces at the end of the straight sections of the top and bottom coils and housed in the collar pack. It is completed by a 20-mm-thick stainless-steel circular plate that is mounted at the extremity of the G11 coil end saddle. The coil head comprised between the circular plate and the thick annulus is compressed by means of 2 x 3 M10 rods (3 for the top coil and 3 for the bottom coil), which are tensioned at the time of assembly to a force of 9 kN per rod and a total of 27 kN per coil saddle whose cross-section is 4316 mm^2. The angular positions of the 3 rods are: two lateral rods at an angle of 65° with respect to the midplane and one central rod at 90°.

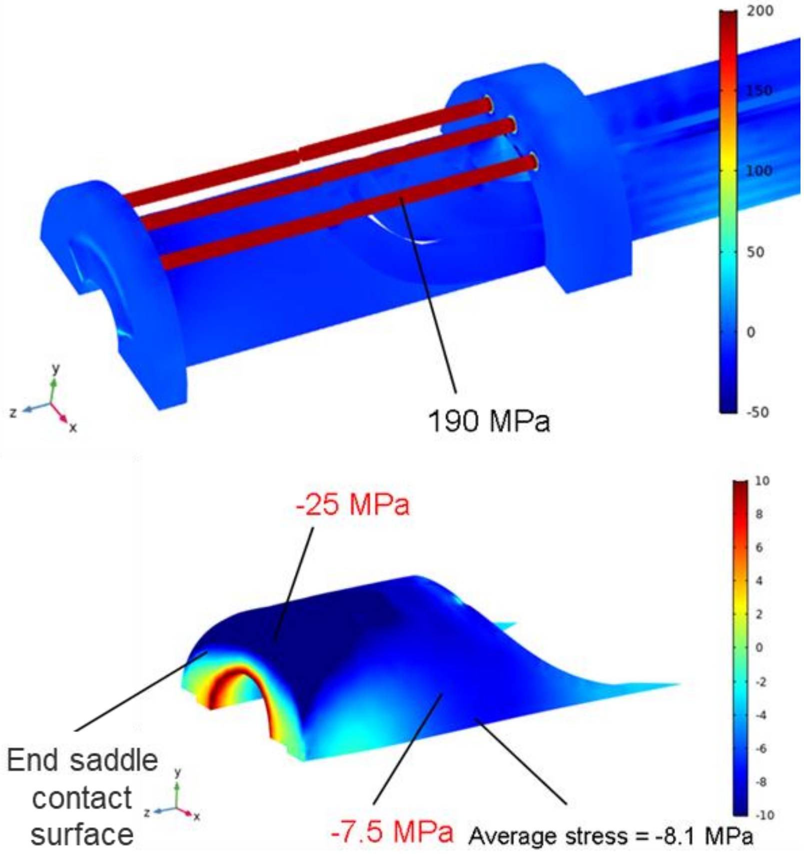

Figure 110: Longitudinal stress distributions resulting from end-cage tie rod tensioning on the coil heads of 11 T dipole magnets at CERN. Top: distribution on tie rods. Bottom: distribution in G11 coil end saddle (Courtesy of M. Morone, C. Garion, CERN [222]).

Figure 110 shows the longitudinal stress distribution in the end-cage tie rods and in the G11 coil end saddle after the application of the tensioning force. The tensile stress in the rods is ~190 MPa and appears to be uniform. However, the longitudinal stress distribution in the G11 end saddle is not uniform, as the circular end plate of the cage appears to bend more on the upper side than at the midplane, resulting in a high compressive zone at the top (with stresses up to 25 MPa), while it is lower towards the midplane. The average stress is -8 MPa, which is comparable to the -6.25 MPa stress applied by the tie rods. This bending and non-homogeneity are not desirable and may reduce the end cage efficiency.

The longitudinal stress in the tie rods is expected to decrease during cooldown (due to thermal shrinkage differentials) and excitation (because the longitudinal component of the Lorentz force compresses the coil head comprised within the end cage). The presence of the end cage, and the associated stiffening of the coil head, is expected to result in a small reduction of the share of the Lorentz load transmitted to the pushers and set screws.

The end cage is designed to compensate for longitudinal effects, it is not expected to help mitigate coil head bending resulting from the vertical component of the Lorentz force. As a consequence, the axial and radial stress distributions computed by the FE model with the end cage are very similar to those computed without it as shown in Figure 108. As already mentioned, given the high stress values computed by the FE model which assumes that all components are glued, it is likely that the resin will crack and that the conductors will delaminate thereby enabling stress accommodation. In such a case, the end cage will keep the head compacted and prevent conductor displacement/ deformation.

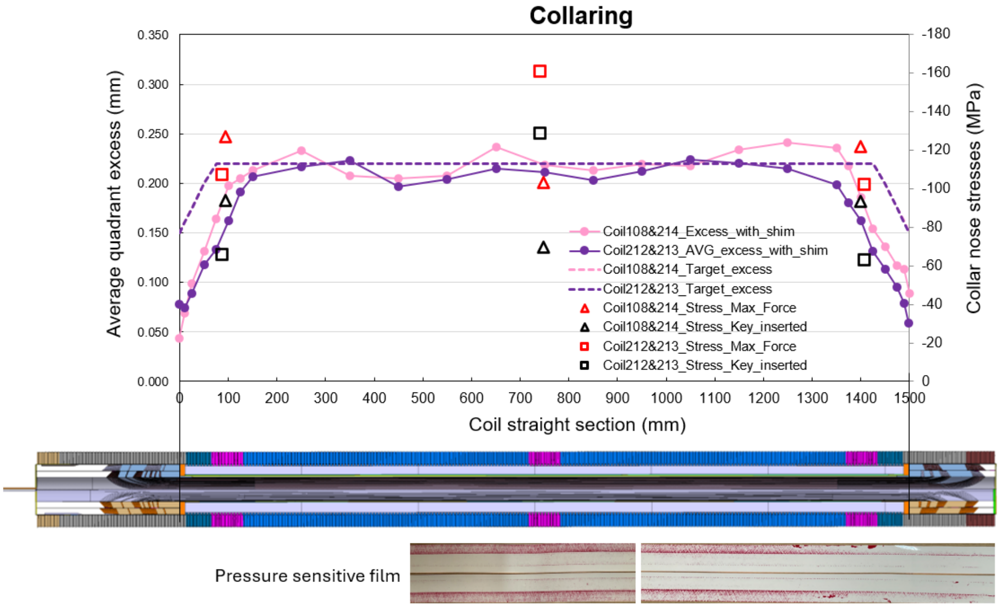

Figure 111: Collaring data from the apertures of short HL-LHC 11 T dipole magnet model MBHDP301 at CERN. Top: corrected combined (top/bottom) average azimuthal coil excess (including variable shims) and measured collar nose stress at maximum collaring force and after key insertion versus longitudinal position. Middle: collared-coil assembly schematics showing the location of instrumented collars. Bottom: results of pressure sensitive test carried out prior to final collaring (Courtesy of C. Abad Cabrera, formerly, CERN, M. Guinchard and D. Perini, CERN).

4.7 Preliminary Results from the Recovery Plan

4.7.1 *Short Model Magnet MBHDP301*

As a first stage, a short, two-in-one-aperture, 11 T dipole magnet model, referred to as MBHDP301, has been re-assembled and cold tested. It relies on existing coils, which, for three of them, SD108 (RRP® strands, 1st generation cable with larger keystone), and SD212 and SD213 (PIT strands, 2nd generation cable with lower keystone) have already been assembled and tested at cryogenic temperatures, while the fourth one, SD214 (PIT strands, 2nd generation cable), is virgin. Aperture 1, referred to as SP301, is assembled with coils SD108 and SD214 and implements a graded shimming plan over the coil heads and stainless-steel pole pieces. Aperture 2, referred to as SP302, is assembled with coils SD212 and SD213, and, in addition to the two new features of SP301, implements end cages at both extremities.

As foreseen, the quench performance of the model magnet is difficult to interpret due to the complicated assembly/disassembly of the coils and apertures. However, the mechanical measurements provide relevant data to assess the implemented recovery actions (at least, within the limits of the measurement uncertainty). In the following, we present a short summary of the main results. More details on this short model magnet assembly and tests can be found in Ref. [257].

4.7.2 *Assembly Data from MBHDP301*

Figure 111 shows the graded shimming plan that was determined based on initial azimuthal coil size excess measurements carried out at the end of coil manufacture. The graph also features collar nose stresses measured at the time of peak collaring force application and after force removal and key insertion. Applying a factor of 2 to derive coil azimuthal stress, it confirms that the coil peak stress during assembly stayed below 80 MPa. Tests were carried out prior to final collaring using a pressure-sensitive film, which shows a smooth decrease of stress over the coil head.

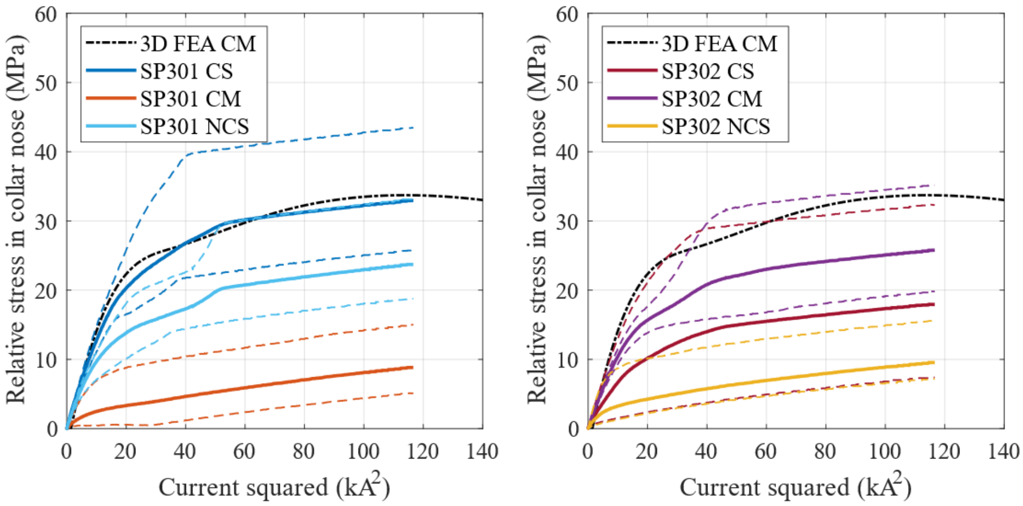

Figure 112: Collar nose stress versus current squared measured on instrumented collars of short, two-in-one-aperture HL-LHC 11 T dipole magnet model MBHDP301 at CERN. Left: Aperture 1 (SP301) with conservative recovery actions. Right: Aperture 2 (SP302) with end cage. The measurements are compared to the computations from the new FE model (Courtesy of C. Abad Cabrera, formerly CERN, M. Guinchard, D. Perini, M. Morrone and C. Garion, CERN).

The strain gauge data from SP302 (with coils SD212 and SD213) exhibit the expected profile after key insertion, with a higher pressure in the center (corresponding to ~65 MPa on the coil) and lower pressures towards the ends (corresponding to 30-35 MPa on the coil). However, the data from SP301 (with coils SD108 and SD214) show some unexpected behavior, with a lower pressure in the middle (corresponding to ~35 MPa on the coil) and higher pressure towards the ends (corresponding to ~45 MPa on the coil). The value in the center is below the target, and the stress profile is not according to expectations, but as we stand on a very conservative side, it was decided to go ahead with these values and profile. The origin of this discrepancy is not understood, but several possible explanations can be put forward: asymmetry in coil assembly made from one virgin and one used coil, effect of the number of collaring trials that were carried out, and so on.

4.7.3 Collar Nose Strain Gauge Measurement during Energization of MBHDP301

Figure 112 presents summary plots of collar nose stress versus current squared measured at the 3 longitudinal locations of instrumented collars in both apertures of magnet model MBHDP301. The measurement results are compared to the results of the FE analysis. In terms of amplitude, the order of the stress curves appears consistent with the pre-compression levels measured after key insertion. In particular, in Aperture 1, corresponding to SP301, the stress at the magnet center remains the lowest compared to the two locations towards the ends, while in Aperture 2, corresponding to SP302, the stress is highest at the center.

The overall shape of the stress evolution as a function of current squared is very similar to that computed by the FE model, with similar inflection and flattening points. As detailed in Section 4.5.7.6, part of this evolution is an artifact caused by collar nose bending that is not representative of actual coil azimuthal stress evolution.

The computed curve shown in Figure 112 corresponds to the smallest shim size in Figure 101 (95 μm in the model, representing 225 μm in real life). This choice was made since the collaring prestress is below target, which indicates that the coil excess might have been overestimated. There is no noticeable difference in behavior between the two apertures, which is not a surprise since the implementation of the end cage should not affect collar nose stress.

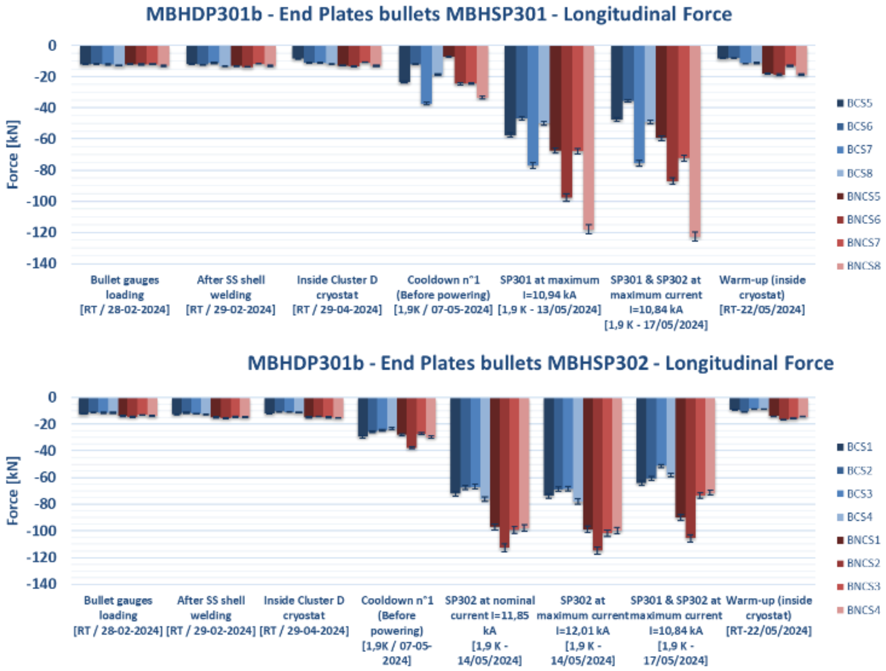

Figure 113: Longitudinal forces measured on set screws/pushers mounted on the end plates of short, two-in-one-aperture HL-LHC 11 T dipole magnet model MBHDP301 at CERN at various stages of assembly and testing. Top: Aperture 1 (SP301) with conservative recovery actions. Bottom: Aperture 2 (SP302) with end cage (Courtesy of C. Abad Cabrera, formerly CERN, M. Guinchard and D. Perini, CERN).

4.7.4 Bullet Gauge Measurements Throughout Magnet MBHDP301 Lifecycle

Figure 113 presents summary plots of longitudinal force measurements from the bullet gauges mounted on the four pushers at both ends of each aperture of short, two-in-one-aperture magnet model MBHDP301 and for each of the main assembly and cold testing phases.

The set screws were all torqued to the same value and retained this value until installation into the vertical test cryostat. The measured longitudinal forces increase during cooldown, but while they remain homogenous for the different bullets of Aperture 2 (the one with the end cage), a larger spread starts to appear between the bullets of Aperture 1.

As expected, the measured forces increase significantly under the effect of the longitudinal component of the Lorentz force during energization, with a noticeably larger spread between the bullets of Aperture 1, while the one between the bullets of Aperture 2 is less pronounced (except for the effect resulting from end plate bending described in Section 4.5.7.7 and illustrated in Figure 104). For both apertures, it also appears that the measured forces on the non-connection side end are larger than on the connection-side end.

Upon warm-up to room temperature, the forces go back to almost the same values before the cooldown, except that the spread in Aperture 1 remains higher than in Aperture 2 and that the non-connection end forces remain slightly higher than the connection-side ones.

Figure 104 presents a comparison of relative force per set screw versus current squared, measured by the bullet gauges on the connection-side of Aperture 1 (SP301) of short magnet model MBHDP301, and computed by the new FE model during energization up to 11.83 kA. Except for the non-linearity at low current, the slopes of the measured data at higher current appear similar to those of the computed ones, with the difference already mentioned and explained in Section 4.5.7.7 between the bullets on the external sides of the apertures, and the bullets in between the two apertures.

In overall, the longitudinal behavior of the apertures with and without end cage appears similar and conforms to what is expected from the FE simulations, at least for the connection-side end. According to these preliminary results, the main difference between the two could be that the end cage ensures a more homogeneous force distribution between the set screws, which would be beneficial. However, before drawing any conclusion, this result would need to be confirmed by additional tests.

4.8 Conclusion

The HL-LHC 11 T dipole magnet work package was plagued by several difficulties: it underwent many technical challenges, which were exacerbated by management changes and a very high schedule pressure that did not enable the implementation of timely feed-back loops after the cold test of the first series magnets. Nevertheless, it achieved some good and results, and the two Task Forces have carried out detailed root-cause analyses and proposed recovery action plans, which benefited the MQXFB program (see Section 5). Also, there are many relevant lessons learned that should be considered for future high-field accelerator magnet development programs. We summarize thereafter some of the main points:

- The 11 T program has offered the opportunity of the first industrial production of 5.3-m-long, Nb_3Sn, accelerator magnet coils, by a supplier working on CERN premises, using CERN tooling and equipment;
- The 11 T program has enabled the development and qualification of a collaring process with graded shims on 5.3-m-long Nb_3Sn dipole magnets, also validated with an industrial partner (let us recall that the performance degradation observed on full-length 11 T dipole magnets is related to problems in the magnet ends but not in the straight section as for MQXFB quadrupole magnets);
- The 1st Task Force has highlighted the importance of controlling coil dimensions and of limiting peak stresses experienced by the coils during collaring. The series production has demonstrated that both goals could be achieved in an industrial environment;
- The root-cause analysis carried out by the 2nd Task Force clearly points to issues with the design of coil ends: both electromagnetically (volumetric distribution of Lorentz force resulting in deleterious bending) and mechanically (high frequency of strand pop-outs during winding). Efforts should be made to further optimize and dilute the Lorentz force distribution and the shape of coil end spacers, which will be validated through extensive winding trials;
- There are also issues with the mechanical support of the coil and magnet ends, which is not robust enough;
- The 2nd Task Force has also highlighted the importance of having a detailed FE model to accompany/support root-cause analyses and to guide the choice of recovery actions. FE model needs to rely on physical parameters and to be thoroughly benchmarked;
- The FE model also reminds us of the importance of good engineering practice and that material choices need to be carefully considered since it may result in significant thermal stresses during cooldown (and subsequent warm-up);
- The present analysis shows that resin cracks and conductor delamination/debonding are likely to occur in critical areas to enable local stress accommodation. This does not seem a sound and robust approach. The mechanical design should be iterated to limit the risks of such occurrence;
- The collar nose design and the implementation of strain gauge instrumentation on the collar nose needs to be reconsidered;

- The implementation of end cages over the coil heads does not seem to add value to the present 11 T dipole magnet design, as the dominating problem is bending of coil head due to the transversal and lateral components of the Lorentz force. However, it may still be an interesting concept to consider for other magnet designs;
- Complex R&D programs call for a dedicated core team working in a continuous manner. Team changes and stop and go in the executions require significant relearning and retraining efforts.

Of course, lessons learned on Nb_3Sn dipole magnets are relevant for Nb_3Sn quadrupole magnets.

The next question is, based on the assessment from the Task Forces and on the test results from short model magnet MBHDP301, is it worth proceeding with the next stage and the assembly and test of a full-length prototype?

It appears that the full-length prototype is not likely to address all uncovered issues and that it may not be robust enough for tunnel installation. However, such prototype will be useful to close the loop on several issues. Also, it provides a last opportunity before a long time to perform R&D on a long Nb_3Sn accelerator magnet. Furthermore, in view of FCC-hh development, it could be a good vehicle to study supercritical helium cooling around 4.5 K. The recommendation is thus to proceed with the full-length prototype, but with a clear design of the experiment in view of future projects, such as the 12 T robust dipole magnet program initiated at CERN and INFN/Genova, and with well-identified and measurable goals.

5 Root-Cause Analysis and Recovery Plan for HL-LHC MQXFB Quadrupole Magnets at CERN

5.1 Root-Cause Analysis

As already explained in Section 1.5.6, after the unsuccessful test of the first two full-length MQXFB quadruple magnet prototypes, it was decided to put the magnet manufacturing at CERN on hold and to carry out a thorough root-cause analysis to determine the origin or origins of the performance limitation. This 360-degree effort, led to the identification of three possible root causes [258]:

(1) Issue with cold mass assembly: non-optimum mechanical coupling between welded outer stainless steel and magnet structure (in particular, aluminum shrinking cylinders;

(2) Issue with magnet loading: non-optimum magnet assembly parameters and processes (*e.g.*, during bladder pressurization, referred as *bladdering*, and key insertion, referred to as *keying*, operations) leading to unbalanced and/or excessive peak stresses on coils;

(3) Issue with coil manufacturing: problems during production processes and/or handling, leading to local or global non-uniformities and/or reacted conductor displacements/deformation.

Of course, it could be a combination of the three root causes, or there could be one predominant cause, and the other two may exacerbate the problem.

5.2 3-Stage Recovery Plan

Having identified the above root causes, a 3-stage recovery plan was developed to address them one by one. However, due to production lead times, it was not possible to carry out the work in the most effective sequence, *i.e.*, first improving the coils, then improving the magnet assembly, and then improving the cold mass assembly. Instead, the work was carried out in reverse order, starting with the coldmass assembly, then the magnet assembly, and finally the coil manufacturing. There was also hope among some stake holders that the cure would be found quickly and that one would not need to go all the way to a revision of the coil manufacturing procedures, which was perceived as heavy and risky. This did not happen, and one needed the full-fledged recovery plan to cure the problem. Although the recovery actions were decided stage by stage, the results of each stage were naturally fed back to the subsequent one.

Let us now review in detail the three sets of recovery actions and their impact on magnet performance.

5.3 Stage 1: Cold Mass Assembly

As illustrated in Figure 114, the initial design requirements called for welding the two halves of the outer stainless shell longitudinally without specific consideration about the interface and possible mechanical coupling, both radially and longitudinally, between the outer stainless-steel shell and the aluminum cylinders of the magnet structure. The only specification was to limit the additional coil overstress due to welding to 8 ± 8 MPa [258].

Given the extent of weld shrinkage, it is likely that upon longitudinal welding completion, the stainless-steel shell is in good radial contact with the aluminum cylinders of the magnet structure. Then, given the large difference in integrated thermal shrinkage coefficients from room to cryogenic temperatures between stainless steel (~$3\text{x}10^{-3}$ mm/mm) and aluminum (~$4\text{x}10^{-3}$ mm/mm), the aluminum cylinder structure tends to shrink away from the shell in the radial direction and will also try to contract in the longitudinal direction. However, longitudinally, there can be a high friction coefficient between aluminum cylinders and shells, preventing respective motion and possibly resulting in uncontrolled stick-slip situations during energization.

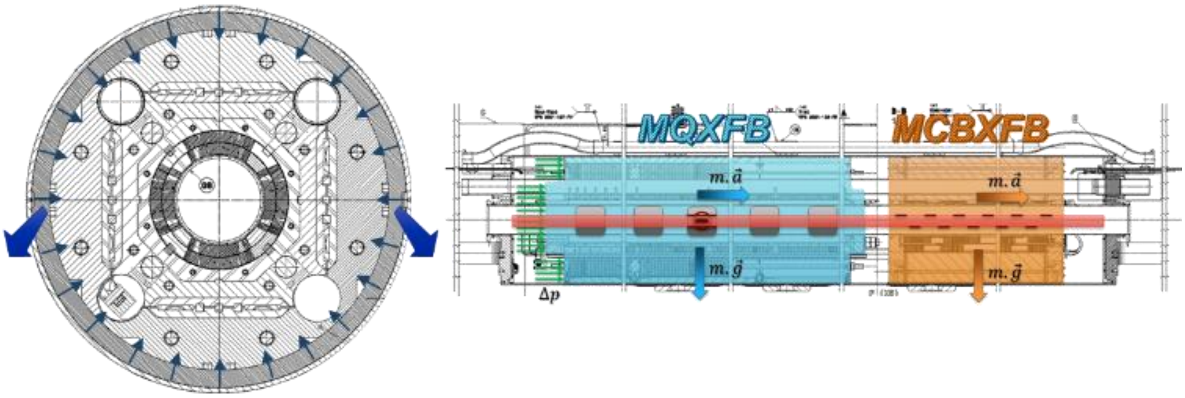

Figure 114: Schematic of HL-LHC MQXFB quadrupole magnet cold mass assembly. Left: cold mass cross-sectional view, highlighting the radial pressure that the outer shell may apply to the aluminum cylinders of the magnet structure as a result of weld shrinkage. Right: longitudinal view of Q2 cold mass assembly in final configuration with one Nb_3Sn MQXFB quadrupole magnet and one Nb–Ti, nested dipole magnet corrector (Courtesy of H. Prin, CERN).

After the test results of MQXFBP1 and MQXFBP2 prototypes, it was assessed that mechanical coupling between the stainless-steel shell and magnet structure could present a risk, eventually impacting magnet performance. It was decided at that time, to go back to the sound engineering practice of clearly separating the functions and limiting the risks that ill-defined interfaces may entail.

In the MQXFB design, the function of coil mechanical support is provided by the aluminum cylinder structure, which is sturdy enough to take up all the Lorentz forces on its own (which is why MQXFA magnets can be tested vertically at BNL prior to shell welding). As for the function of helium pressure vessel, it is provided by the welded outer shells and end domes. In practice, the outer shell is not expected to play any role in the mechanical support of the coils, and there is no strong requirement for the shell to be in close contact with the aluminum cylinders. Note that the need of coping with these two functions is common to all accelerator magnet cold masses. In the design of LHC quadrupole magnets, it was addressed by implementing a so-called *inertia tube*, providing mechanical rigidity and precise alignment to the magnet, while also playing the role of outer He vessel [259].

The first recovery action that was decided was to iterate on the outer shell design and welding parameters aiming at minimizing mechanical coupling with the aluminum cylinder structure. As illustrated in Figure 115, the proposal was to increase the arc lengths of the two half shells, taking into consideration the outer envelope of the deformed aluminum cylinder structure after magnet loading and the expected weld shrinkage [260]. The goal is to ensure that, at the end of longitudinal welding, the shell does not add any constraints on the aluminum cylinders at room temperature and, thereby, enable them to shrink more or less freely during cooldown. Quantitatively, the requirement on additional coil overstress due to welding was lowered to 0 -0 /+8 MPa [258][260].

The proposed solution imposed tighter requirements on the shell manufacturing to achieve the desired arc length and tolerances, which were discussed and agreed upon with the shell supplier. It also called for the introduction of a fixed point between the magnet structure and the outer shell. A fixed point is usually implemented between the magnet cold mass and its cryostat, for instance, towards the longitudinal center, to prevent the cold mass from moving longitudinally during transportation and in case of a quench or of a pressure wave originating from the quench of a neighboring magnet in a string of cryogenically connected magnets. As in the new design, the magnet structure is now “floating” within the outer shell, such fixed point is needed between the two (note that a MQXFB cold mass is ~11 tons).

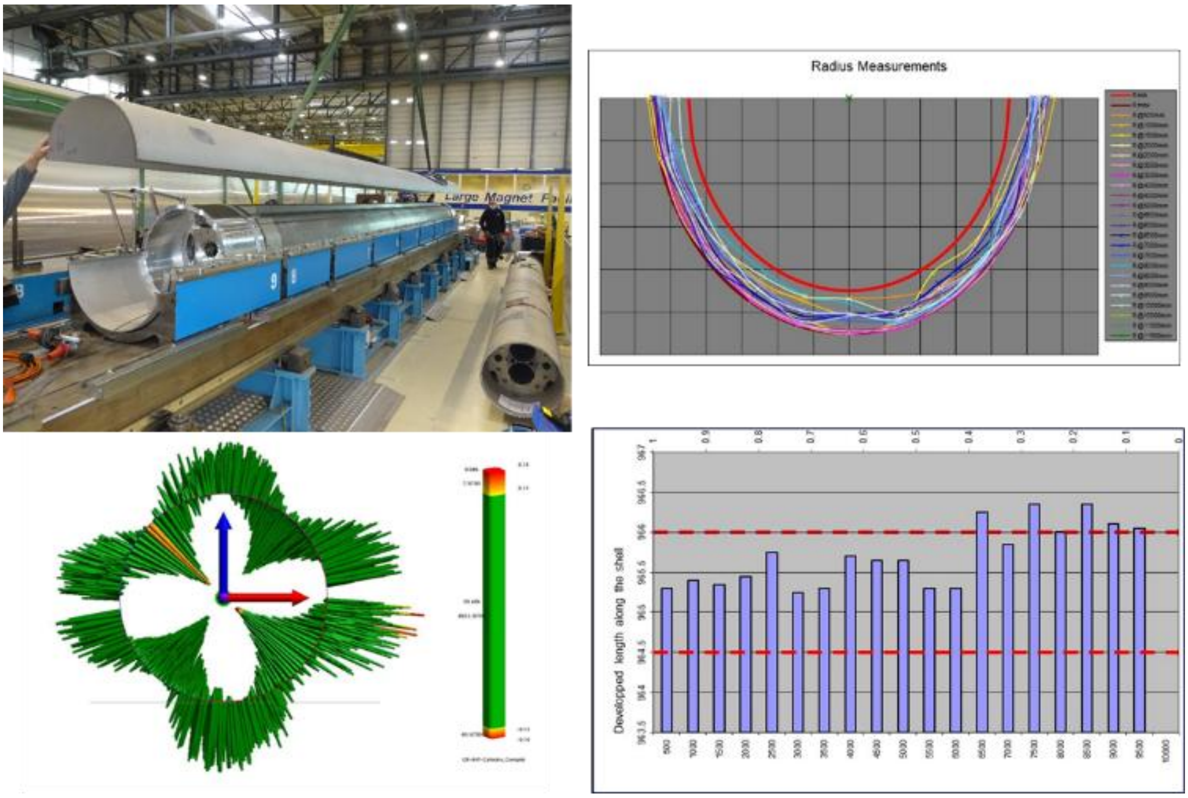

Figure 115: Optimization of outer shell developed length for 7.2-m-long HL-LHC MQXFB cold-masses at CERN. Top Left: Picture of two full-length half shells. Bottom Left: measured deformations of aluminum cylinder structure after magnet loading. Right: control of half shell geometry at shell supplier after implementation of new requirements (Courtesy of H. Prin, CERN).

The fixed-point requirements were defined as follows [258]:

- During transport, the maximum acceleration that shall be carried by the fixed point is 0.5 x g, resulting in a load of 55 kN for MQXFB;
- During operation of the cryogenic system, the MQXFB magnet inside the cold mass shall withstand 4 bar differential pressure between its ends (induced by cryogenic operation or by quench of other magnets), resulting in a load of 96 kN.

Note that different requirements apply to MQXFA cold masses, because of different length and configuration (two magnets in the same cold mass), as well as different modes of transportation (by ship in addition to truck).

At CERN, it was decided to rely on a single fixed point at the longitudinal magnet center [260]. As illustrated in Figure 116, the fixed point is implemented by means of two 316LN pins with a diameter of 30 mm, one on each side of the magnet. The pins are fitted into holes machined in the iron yoke and their top parts are plug-welded to the backing strips used for longitudinal shell welding.

The new shell design and welding parameters were implemented in the 7.2-m-long quadrupole magnet prototype MQXFBP3. MQXFBP3 was manufactured by cutting out the shell and end domes of full-length magnet MQXFB01, which had already been assembled following the same procedure as for MQXFBP1 and MQXFBP2. The magnet itself was left untouched and new half-shells were welded around it following the new procedure. Therefore, MQXFBP3 is relying on existing coils, which were manufactured, assembled and loaded like the first two prototypes, and only the shell design and welding parameters are new.

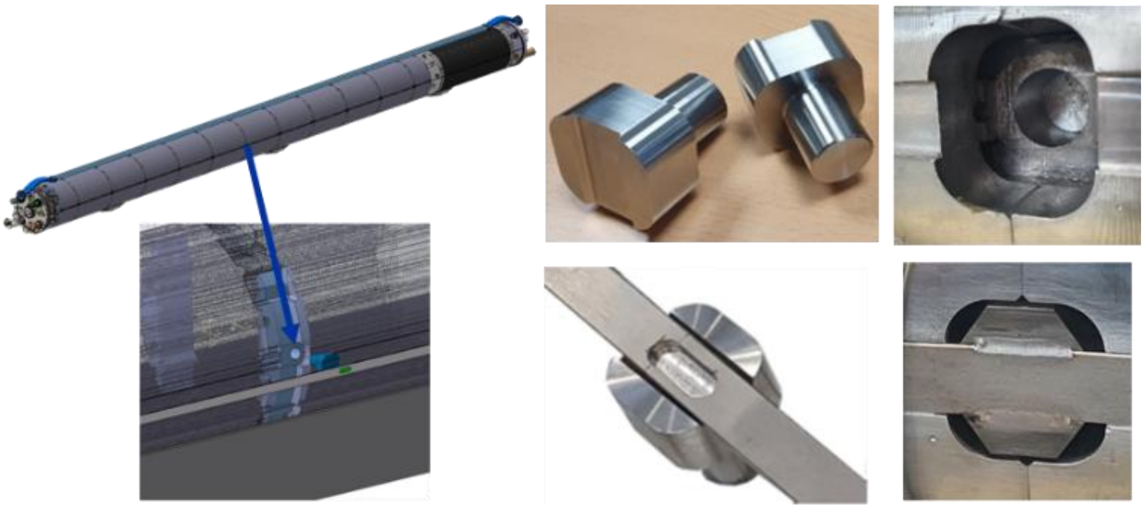

Figure 116: Implementation of fixed point between magnet structure (iron yoke) and welded outer shell for 7.2-m-long HL-LHC MQXFB cold mass at CERN. Left: location of fixed point. Right: detailed of fixed-point components and installation (Courtesy of H. Prin, CERN).

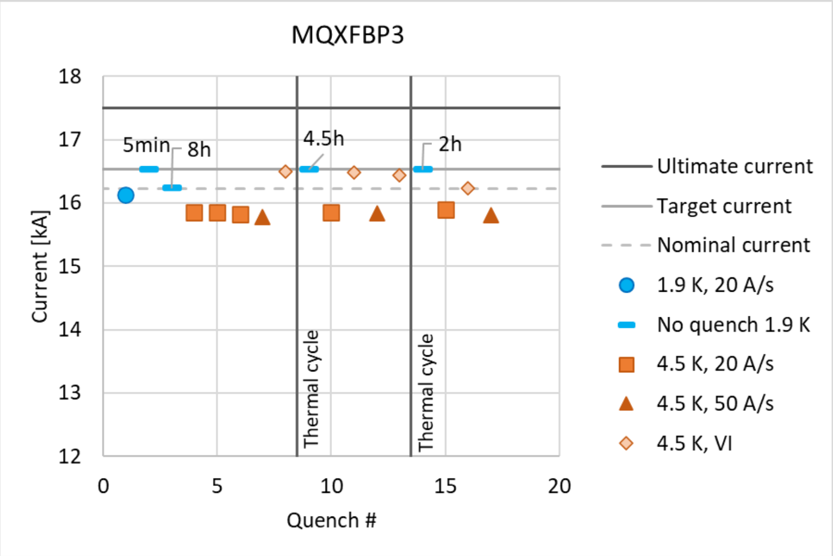

Figure 117: Quench Performance of 7.2-m-long, 150-mm-single-aperture HL-LHC MQXFBP3 quadrupole magnet prototype at CERN, in a test cold mass configuration and test cryostat, integrating the first-stage recovery actions: new shell design and welding parameters and new fixed point, but existing coil manufacturing and magnet loading procedures (Courtesy of F. Mangiarotti, CERN).

Figure 117 shows the quench performance of MQXFBP3, which was tested in Spring/Summer 2022 in a test cold mass configuration (without nested MCBXFB dipole magnet corrector). We can observe a clear improvement with respect to MQXFBP1 and MQXFBP2 since this prototype achieved the target current (nominal +300 A) after only one training quench at 1.9 K. However, when tested at 4.5 K, it exhibited the same type of limitation with the same phenomenology as the previous prototypes (in particular, with quenches localized towards the mechanical center of the magnet), albeit at a higher current level. The magnet was subjected to two warm-up/cooldown cycles and the quench performance appears stable. Since then, the magnet has been reassembled into a final Q2 cold mass configuration (including a nested MCBXFB dipole magnet corrector) and was retested in March 2024, confirming a good reproducibility of both quench performance and quench localization [261].

The results of MQXFBP3 did trigger some discussions at CERN on whether such magnet is acceptable for tunnel installation as, from the legalistic point of view, it meets the HL-LHC project requirements, which did not include performance checks at 4.5 K. However, the test results also show that the root cause of the limitation observed on the first two prototypes has not been cured. Therefore, it is likely that the magnet has damaged strands in its cross-section like those displayed in Figure 56 and Figure 59. The applied corrective action on shell design and welding may have improved the situation but it did not fully resolve the problem. In the end, it was decided to pursue the second stage of the recovery plan. One can also be hopeful that the conservative approach of not installing this magnet in the tunnel will be followed.

5.4 Stage 2: Magnet Loading

As already introduced in Section 1.5.6 and shown in Figure 14, MQXF magnets rely on a so-called *coil pack assembly* made up of 4 $\cos 2\theta$ coils which are held together by means of aluminum collars outfitted with low-carbon steel pads on the outside. The coil pack is inserted into a structure made of low-carbon steel yoke surrounded by segmented, precisely machined, 7075 T6 aluminum shrinking cylinders. After insertion and alignment, metallic bladders are positioned between pads and yokes and are inflated to put the Al cylinders into tension and apply pre-compression onto the coils [262][263]. The bladder pressure is increased in a step wise manner, and on the plateaus, keys of gradually larger sizes are inserted into keyways machined on the sides of the pads and yokes. Once the desired level of cylinder tension and coil azimuthal pre-compression have been achieved and final dimension keys have been inserted, the bladders are deflated and removed, and the structure, which is locked by the keys, remains in a loaded condition. During cooldown, the Al cylinders shrink more than the other materials, and their tension increases, resulting in an increase of coil azimuthal pre-compression up to the level needed for compensating the effects of Lorentz forces during powering [262].

This design presents two specific features:

- the reliance on tensile stress in the aluminum shrinking cylinders to control the coil loading and on the higher integrated thermal contraction coefficient of aluminum between room and cryogenic temperatures to limit the coil loading requirement at room temperature;
- the reliance on “bladders and keys” to load the magnet structure at room temperature, thereby eliminating the need for an expensive collaring press as that required for the more traditional collaring operation applied, for instance, to 11 T dipole magnets (see Section 1.5.5.1).

The use of inflatable bladders is a conventional assembly technique that was, for instance, applied in the assembly of the ATLAS toroidal field coils [266]. The “bladder & key” procedure associated with an aluminum shrinking cylinder was pioneered in the assembly of short magnet models at LBNL in the early 2000s [267][268]. It was subsequently used by LARP [88] and became the baseline for HL-LHC MQXF magnets [103][263].

Even though one of the initial goals of the “bladder & key” technique was to minimize and possibly eliminate coil overstress at the time of bladdering, its implementation on 7.2 m long magnet structures was not so straightforward. As an illustration, Figure 118 shows coil azimuthal stress data recorded during the bladdering and keying of MQXFBP3 (which was carried out following the standard procedure). It appears that for each of the successive plateaus of bladder pressurization, there is a significant stress overshoot between the time when the bladders are inflated to enable insertion of the bigger keys, and the time when the bladders are deflated with the bigger keys in position. The largest overshoot is for the last plateau (insertion of the final dimension keys) and can be up to 30%.

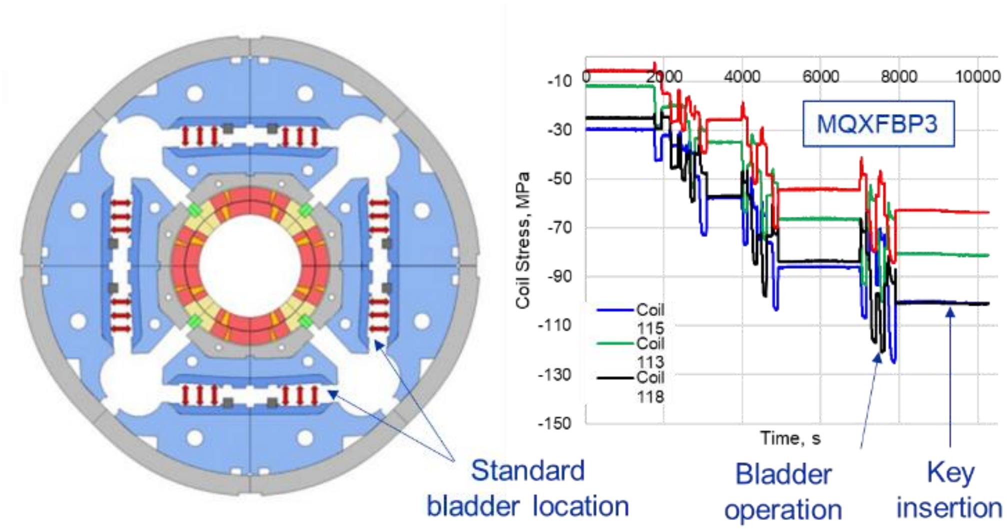

Figure 118: Standard bladdering & keying operation at CERN. Left: a cross-sectional view of HL-LHC MQXF quadrupole magnet showing the bladders' location between iron pad and yoke. Right: coil azimuthal stresses measured in different quadrants of quadrupole magnet prototype MQXFBP3, showing a clear overshoot at the time of bladdering (Courtesy of J. Ferradas and S. Izquierdo Bermudez, CERN).

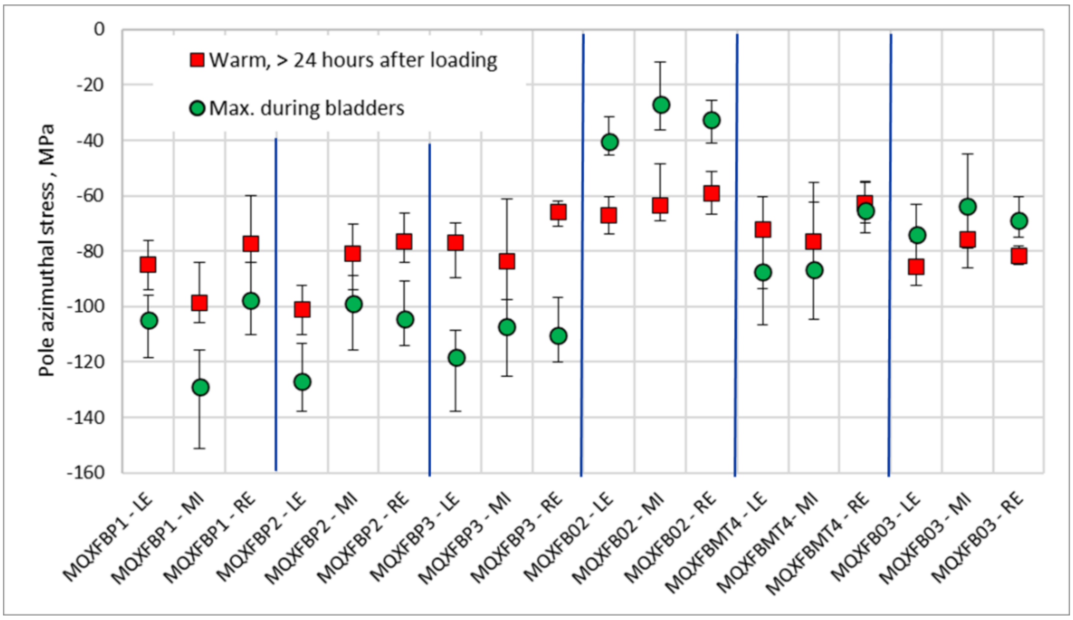

Figure 119: Summary plot of maximum coil stress during bladdering operation and residual coil stress after final-size key insertion measured at 3 longitudinal locations on the 5.3-m-long MQXFB quadrupole magnet assemblies at CERN (Courtesy of J. Ferradas and S. Izquierdo Bermudez, CERN).

Figure 119 presents a summary plot of stress during final bladdering plateau and the residual stress after final key insertion as measured on all full-length MQXFB magnets. It appears that all first 3 prototypes, which relied on the same bladdering & keying procedure, presented the same features. Such stress overshoot starts to resemble the kind of effects observed during a traditional collaring and puts into question one of the advertised benefits of the bladder & key technique. In addition, stress imbalances are also recorded between different coil quadrants. Such imbalances are not desirable as they increase the risks of uncontrolled overstress during bladdering operation [262].

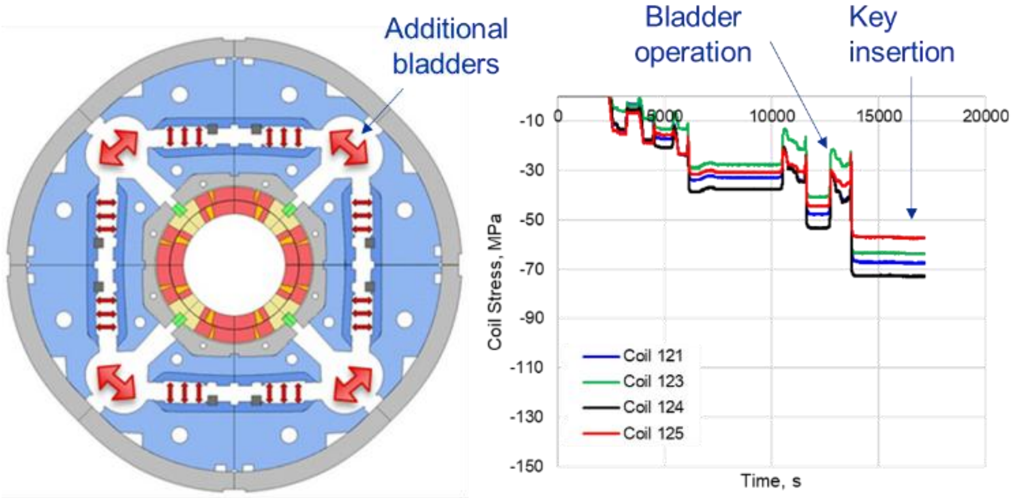

Figure 120: Optimized bladdering and keying operation at CERN. Left: cross-sectional view of HL-LHC MQXF quadrupole magnet showing additional bladder location in yoke cooling holes. Right: coil azimuthal stresses measured in different quadrants of quadrupole magnet prototype MQXFB02 demonstrating the elimination of the stress overshoot at the time of bladdering (Courtesy of J. Ferradas and S. Izquierdo Bermudez, CERN).

Although there was not a consensus on the potential deleterious impacts of the observed coil stress overshoots, it was argued that:

- some of the peak stresses are in the range or even exceed the 120 MPa threshold above which radial micro-cracks have been observed to occur in the tubular aggregate of Nb_3Sn filaments of MQXF strands (see Section 3.5.2 and [207]);
- the stresses are measured very locally at 3 positions along the magnet coils and there might be areas of higher peak stresses.

Taking these elements into account, it was decided to build contingencies and mitigate risks by devising a mean to reduce, and possibly eliminate, the stress overshoots. The technical requirements for bladdering and keying were revised as follows [258]:

- the maximum azimuthal coil pole compression shall not exceed 100 MPa during magnet assembly;
- room temperature targets for average azimuthal stress on coils and aluminum shrinking cylinders are set to −70 ±10 MPa and +58 ±6 MPa, respectively.

The above goals were achieved by introducing additional bladders into the yoke cooling holes as illustrated in the image of Figure 120 [263]. The new bladders enable to stretch iron yokes and Al cylinders outward rather than to push onto the collared coils inwardly, thereby enlarging the gaps between pads and yokes and offering the needed clearance for key insertion. Note that this type of bladder configuration was used in the past at CERN for the assembly of magnet models relying on similar design features [264][265].

The new procedure was first validated on a 5.3-m-long, HL-LHC mechanical test magnet referred to as MQXFBMT3, which was assembled in early 2022 with pressure-sensitive paper up to full force. MQXFBMT3 demonstrated that the stress overshoot can be eliminated so that the peak stress during assembly is the residual stress after final-size key insertion. As illustrated in the image of Figure 120, the coil stress measured during bladder pressurization becomes lower than the coil stress measured after key insertion because of the outward opening of the yoke/cylinder structure, confirming the soundness of this procedure.

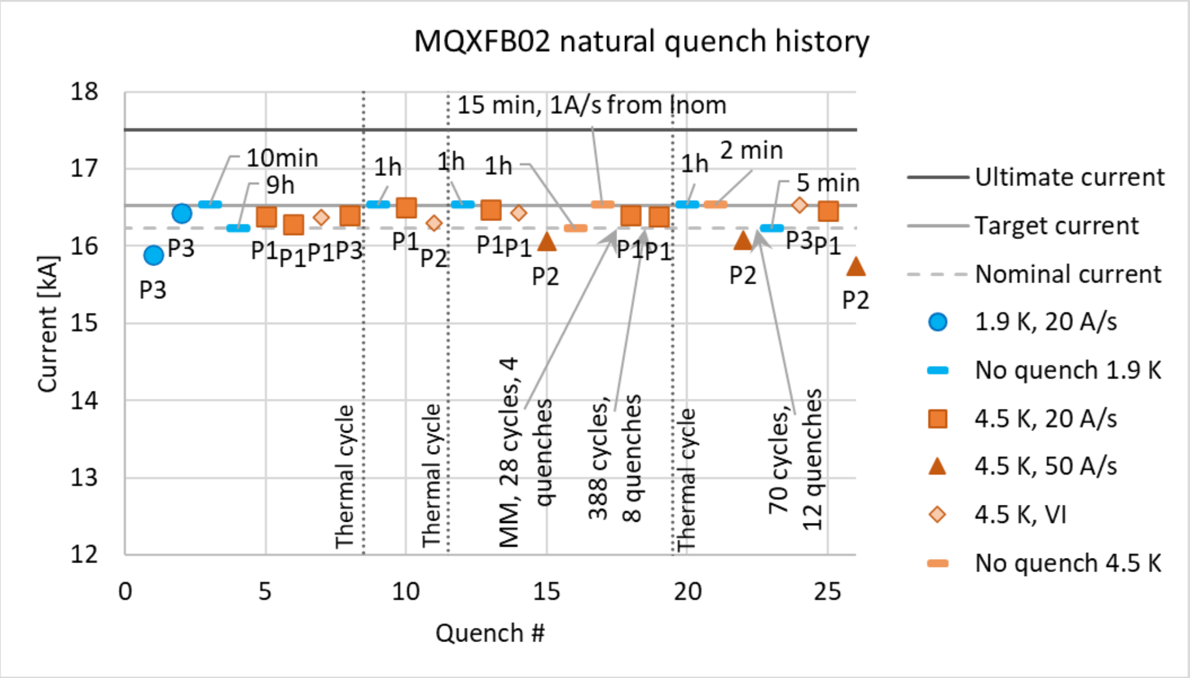

Figure 121: Quench Performance of 7.2-m-long, 150-mm-single-aperture HL-LHC MQXFB02 quadrupole magnet prototype at CERN, in a test cold mass configuration and test cryostat, integrating the first- and second-stage recovery actions: new shell design and welding parameters and new fixed point, new magnet loading procedures, but already manufactured coils (Courtesy of F. Mangiarotti, CERN).

Following the success of the mechanical test magnet, it was decided to proceed with the assembly of MQXFB02. MQXFB02 relies on already manufactured (virgin) coils, but it was loaded with the newly optimized bladdering & keying procedure, and it was assembled into a test cold mass and cryostat configuration using the optimized shell design and welding parameters previously qualified on MQXFBP3.

Figure 121 displays the quench performance of MQXFB02, which was first tested at the end of 2022, and further endurance-tested at the beginning of 2023. Similarly to MQXFBP3, MQXFB02 achieved target current (nominal + 300 A) at 1.9 K, but exhibited a limitation at 4.5 K, with the same phenomenology and quench-start localization as before. However, the quench limitation is, again, at a slightly higher current level than the previous prototype (this time, it is between nominal and target current). As for MQXFBP3, the test results of MQXFB02 demonstrated some improvement with respect to its predecessors, but they also showed that the root cause of the limitation had not yet been eradicated.

The test results of MQXFB02 reinitiated the debate about whether the implementation of the first two stages of recovery actions was sufficient to meet HL-LHC project requirements on future magnets, although there were still signs of limitations and, possibly, of cracked Nb_3Sn strands in some of the coils.

An ultimate confirmation of the risks associated with not curing the root cause of the limitation was provided by the assembly and test of another full-length, mechanical test magnet, referred to as MQXFBMT4. MQXFBMT4 relies on 3 coils salvaged from MQXFBP1 (the ones that were not limiting) and one new coil, Q127, produced with similar procedures, but at a much later stage than the coils used in previous prototypes. It was assembled with the optimized loading procedure, and with the optimized shell design and welding parameters.

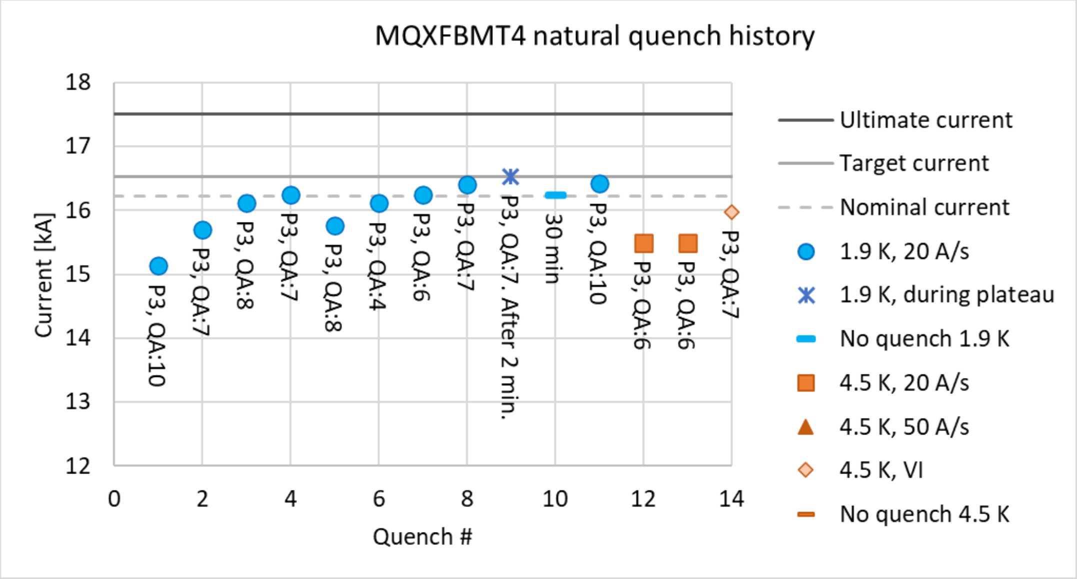

Figure 122: Quench performance of 7.2-m-long, 150-mm-single-aperture HL-LHC mechanical test quadrupole magnet MQXFBMT4 made from 3 coils salvaged from MQXFBP1 and one new coil produced with similar processes as previous coils but at a much later stage (Courtesy of F. Mangiarotti, CERN).

The assembly and test of MQXFBMT4 were requested to assess whether the experience accumulated in coil production over the previous couple of years had been enough to cure the problem [269]. The cold test took place in July 2023 and the test results are presented in Figure 122. The training is significantly slower than on MQXFBP3 and MQXFB02 and was not completed up to target current at 1.9 K due to lack of time. The performance at 4.5 K appears limited at a current level below the ones achieved on MQXFBP3 and MQXFB02. All quenches are in the new coil, with plateau quenches at the usual localization, near the longitudinal magnet center.

The test results of MQXFBMT4 confirm that, as long as the root cause is not cured, the risk of performance limitation remains, and that the limitation level may vary from coil to coil in an uncontrolled fashion. This gave an a posteriori justification to the decision taken in March 2023 to proceed with stage 3 of the recovery plan.

Like any engineering solution, the aluminum shrinking cylinder and “bladder & key” design option has its pros and its cons. However, in recent years, it has unfortunately become an ideological mantra that is presented by some stake holders as the ultimate and superior solution to any kind of problems, without discernment, comparative analyses, and assessment of limitations. This posture is reminiscent of other “ideological battles” that have plagued accelerator and fusion magnet development over the years:

- vertically-split versus horizontally-split yoke for the design of dipole magnets for the Superconducting Super Collider (SSC) project in the USA in the early 1990s [212];
- aluminum versus stainless steel collars for the design of LHC dipole magnets at CERN in the late 1990s [270];
- rectangular versus circular geometry for cable-in-conduit conductors in various fusion magnet projects [271].

It astonishing how such technical details can lead to heated debates and tensions, particularly as engineering problems usually have more than one solution that can all be made to work. Consequently, the choice of one solution over another should be based on facts, for instance, by assessing the respective weight of the following objectives or constraints:

- mechanical tolerances and sensitivity/forgiveness to discrepancies;
- manufacturability and ease of reliable inspections/quality controls;
- system integration and the additional technical requirements it may impose;
- performance qualification and scalability;
- number of items to be produced;
- maturity and suitability for industrialization (if required);
- cost (for large series).

In the case of the MQXFA and MQXFB quadrupole magnets, the number of units is limited, the production is carried out by expert laboratories and the cost optimization is not a major driving factor. This implies that, as long as the designs and production processes are qualified, one does not need to care about large quantities and industrialization. However, for future projects one would need to carry out more thorough analyses of available design options, rely on mock-up tests for comparison, and establish an unbiased assessment along the aforementioned seven objectives.

5.5 Stage 3: Coil Manufacturing

5.5.1 Introduction

We learned from the postmortem examinations presented in Section 3 that there are damaged strands in MQXFB coils. The damaged strands are at a specific location in the coil 2D cross-section: at the top of the inner layer pole turn, right underneath a radial extension of the outer layer Ti-alloy pole (see Figure 56). In the longitudinal direction (along the coil axis), the damaged strands are in the vicinity of the Ti-alloy pole junctions (see Figure 61). Examination of the facies of the ruptured sub-elements enables us to conclude that the fracture occurs after completion of the Nb_3Sn reaction heat treatment (see Figure 57 and Figure 60).

In addition, QC records during MQXFB coil manufacturing reveal that the areas of strand damage correspond to areas where protrusions of the coil inner pole turn are observed upon opening of heat treatment retort (see Figure 62). Last but not least, postmortem inspections carried out on coil Q126, a full-length coil that was manufactured using standard procedures but not assembled in a magnet and not cold tested, confirm the presence of damaged strands at several inner layer pole turn locations, thereby corroborating the fact that strand breakages occur during coil manufacture. The next questions are: what causes the pole turn protrusions and how can they be avoided?

The main steps of coil manufacture are as follows:

- cable insulation;
- inner-layer coil winding;
- ceramic binder painting on outer surface of coil inner layer and curing;
- outer-layer coil winding;
- ceramic binder painting on outer surface of coil outer layer and curing;
- coil reaction heat treatment;
- coil vacuum pressure impregnation;
- coil final inspection and size measurements.

Let us briefly review the main features and challenges of these different steps.

5.5.2 Cable Insulation

Prior to winding, the MQXF cable is braided with 66-tex, S2 glass fiber yarns with 933 sizing, with a target thickness of 0.145 mm ± 0.005 mm under 5 MPa. This braid is the structuring element of the turn-to-turn insulation [272].

In the case of 11 T, the cable insulation is made up of 0.08 mm mica tape that is folded around the cable in a C-shape covering one broad side and the two edges, completed by a 0.07 mm layer of 11-tex S2 glass fiber yarns with 636 sizing braided over the mica [97].

Unlike what was done in the past [36], there is no step in the process for removing the organic sizing that coats the fiberglass filaments forming the yarns. As a result, during reaction heat treatment, the organic sizing is burnt leaving electrically conducting carbon residues that affect the dielectric strength of the insulation and change its color from white to greyish/brownish. This carbonization was not considered to be a serious issue for HL-LHC magnets.

5.5.3 Coil Winding

For both 11 T dipole and MQXF quadrupole magnets, the choice was made early on of winding the two coil layers in one go, one on top of the other, using a single unit length of cable. The advantage of this choice is that it avoids the interlayer splice that was required in LHC dipole magnets, which would have to be performed on reacted conductors after heat treatment. The drawback is that the cable for both inner and outer layer is the same and there is no possibility of so-called *grading*, which enables to rely on a smaller amount of superconductor in the lower-field, outer layer for cost optimization [75]. This is not an issue for HL-LHC, which requires only a limited number of Nb_3Sn magnets, but would need to be re-assessed for future large accelerator projects like FCC-hh. For 11 T, the cable unit length is ~655 m, while for MQXFB, it is ~760 m (see Table 2).

As illustrated in Figure 123, the winding at CERN is carried out in a clean room, with a slight overpressure and access control, using a shuttle-type machine. One particular difficulty is the winding of coil ends and the design of coil end spacers, which, for $\cos\theta$ or $\cos 2\theta$ coils, assume complex 3-D shapes [75][76]. In addition to conductor peak field, Lorentz force distribution, and integrated field quality considerations, the winding and end spacer parameters need to be optimized to prevent the occurrence of strands popping out of the cable plane when bending it to turn around the ends. This operation may result in a hard way bending component (in a direction parallel to the cable midplane and perpendicular to the cable small edges) which can lead to strand pop-outs or even a total cable collapse on the turn exit.

To mitigate the risks of popped-out strands and cable collapses, 3 types of actions can be undertaken:

- the end spacer design usually undergoes several iterations validated through representative winding trials;
- a specific set of clamps is used to hold the conductors in place when winding the coil ends (see Figure 124 for MQXFB at CERN);
- the technicians are requested to check visually and with their fingers if there is any pop-out.

However, regarding the third action, the technicians can only inspect the outer surface of the braided cable, and, as illustrated in Section 3.5.1.1 and Figure 50, strand pop-outs can also occur on the inner surface of the cable and go undetected during winding. (Note that the illustrations presented there were for a 11 T coil, but similar observations were also made on MQXF coils, albeit not as frequently). These findings indicate that, for future accelerator projects, more work is needed on the coil end spacer design. One can also think of additional pieces of tooling to better control the mechanical integrity of cable upon end winding.

Figure 123: Winding of a 7.2-m-long HL-LHC MQXFB quadrupole magnet coil at CERN (Courtesy of R. Berthet, FOSELEV, and R. Principe, CERN).

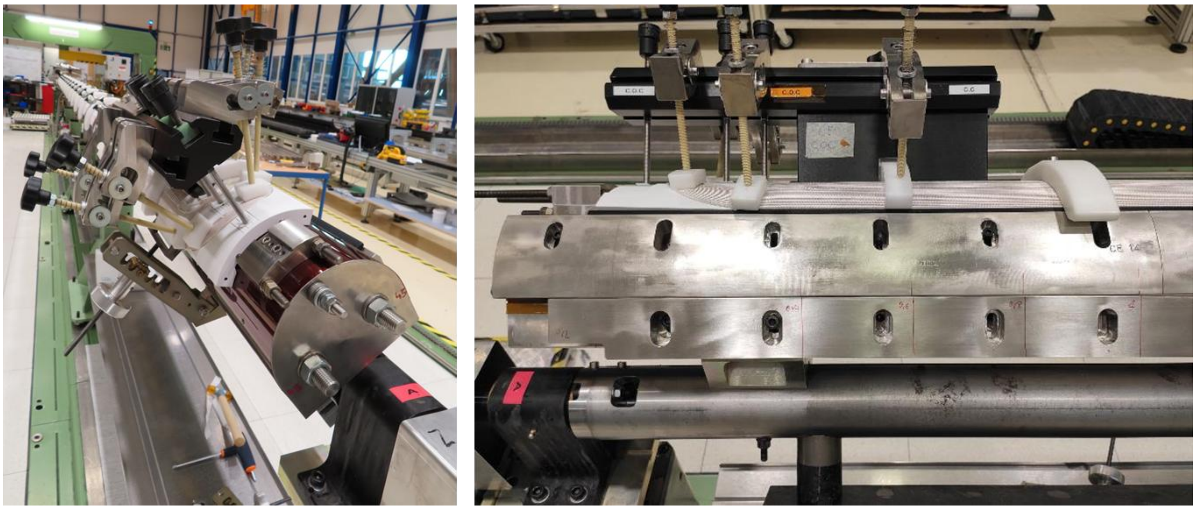

Figure 124: Clamping tools used during the winding of 7.2-m-long HL-LHC MQXFB quadrupole magnet coil ends at CERN (Courtesy of R. Berthet, FOSELEV, and R. Principe, CERN).

Figure 125: Application of ceramic binder on the outer surface of a wound 7.2-m-long HL-LHC MQXFB coil at CERN. The operation requires the use of personal protection equipment due to health and safety reasons (Courtesy of R. Berthet, FOSELEV, and R. Principe, CERN).

5.5.4 Ceramic Binder Application

Upon completion of inner layer winding, the S2 glass fibers on the outer surface are painted with a thin layer of a polymer-derived ceramic binder, CTD-1202®, produced by Composite Technology Development, Inc., in the USA [273]. Next, the inner layer is heated up to 120 °C in a mold of accurate dimension for binder curing. The ceramic binder, which was qualified as part of the LARP program in the USA, is applied to provide mechanical rigidity to the coil, thereby facilitating subsequent handling [274]. It also defines a solid reference surface onto which the outer layer is wound. Personal protection equipment is required for health and safety reasons (see Figure 125).

Before the start of outer layer winding, the inner layer is covered by a stack of S2 glass fiber cloths wetted with CTD-1202® binder. This stack is formed and cured prior to installation on a dedicated mandrel and is the structuring element of the interlayer insulation. It comprises 2 x 0.250 mm layers, woven from 66-tex S2 yarns with 933 sizing, plus 1 x 0.175 mm layer, woven from 33-tex S2 yarns with 493 sizing.

In the standard procedure, upon completion of outer layer winding, the S2 glass fibers of the cable insulation are also painted with CTD-1202® binder, and the whole 2-layer coil is cured again. Although this last operation is not strictly necessary, it was thought to facilitate the next operations and the preparation for reaction heat treatment [274].

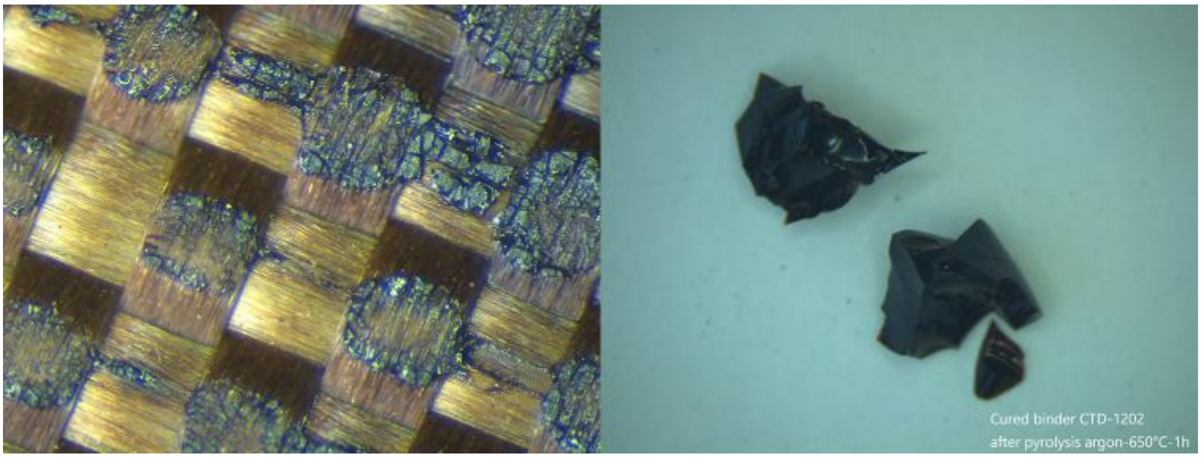

Figure 126: Observation of SiOC formation on a sample of S2 glass fiber cloth painted with CT1202® binder and having been subjected to a curing at 150 °C in air and a heat treatment at 650 °C in Argon for 5 days (Courtesy of D. Ternova and C. Scheuerlein, CERN, 2022).

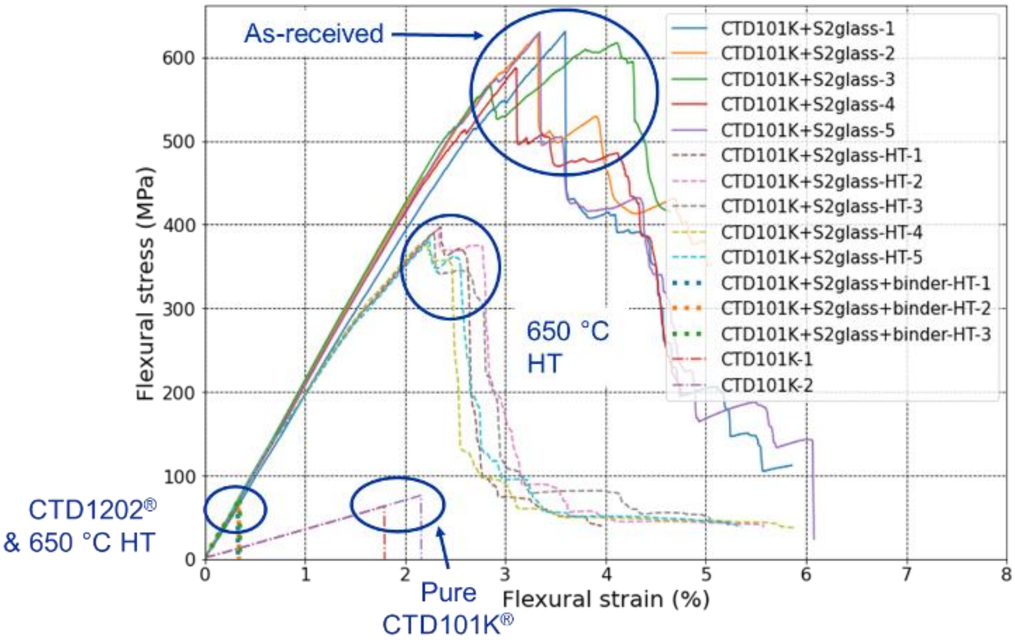

Figure 127: Impact of CTD-1202® binder and reaction heat treatment on the mechanical strength of S2 glass laminates impregnated with-CTD101K® resin (courtesy of A. Gaarud and C. Scheuerlein, CERN, 2022).

The application of the ceramic binder is an assembly aid and is not expected to play any reinforcement role in coil electrical insulation. As a matter of fact, and as illustrated in Figure 126, it has been observed recently that during the 665 °C reaction heat treatment that is applied to the coil (see Section 5.5.5), the binder undergoes a pyrolysis that produces a dark and tough ceramic structure called silicon oxicarbide (SiOC). The SiOC formation likely causes the dramatic loss of mechanical strength measured on S2 glass laminates, painted with CTD-1202® binder, heat treated to 650 °C, and impregnated with CTD-101K® resin as in the final coil (see Figure 127) [275]. This fragility may explain why cracks can propagate through the interlayer insulation as observed in Figure 54. A program was initiated at CERN in 2023 to improve the robustness of the interlayer insulation by looking for alternative solutions.

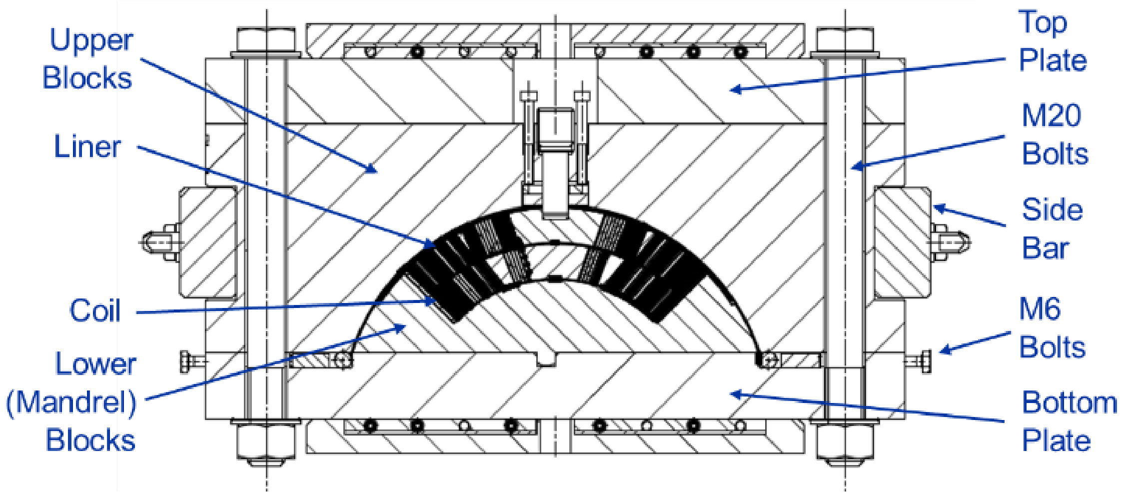

Figure 128: Cross-sectional view of retort used for reaction heat treatment of 7.2-m-long HL-LHC MQXFB quadrupole magnet coils at CERN (Courtesy of O. Housiaux, SERCO, and R. Principe, CERN).

5.5.5 Reaction Heat Treatment

5.5.5.1 Heat Treatment Preparation

As explained in Section 1.2, in the wind & react process, the heat treatment required to react the Nb_3Sn phase is applied after completion of manufacturing steps that could result in potentially harmful mechanical deformations of wires and cables. For both accelerator and fusion magnets, this corresponds to winding completion (hence, the terminology of “wind-and-react”).

In preparation for heat treatment, the coil is mounted inside a retort, whose main components are (from bottom to top): a *base plate*, lower (mandrel) blocks that support the coil, a *liner* positioned on the coil outer surface to protect it, upper blocks, and a *top plate* (see Figure 128).

In the case of MQXFB, the liner is kept in position by silver coated M6 screws pushing laterally against the base plate. The assembly is held together by means of 20 x silver coated, M20 bolts and side bars. The retort defines a cavity of accurate dimensions that constrains the coil in the 2-D cross section while supposedly letting it expand in the longitudinal direction. In addition, it integrates features enabling pure Argon flow through the coil.

As illustrated in Figure 129, once the assembly is completed, the retort is inserted into a furnace providing a good uniformity through the temperature cycle (typically ± 5 °C). Note that strand witness samples are mounted at both extremities of the lower mandrel blocks for quality control checks on critical current and residual resistivity ratio.

5.5.5.2 Heat Treatment Parameters

For RRP® 108/127 wire at 0.85 mm diameter, the heat treatment calls for 3 temperature steps:

(1) ramp to 210 °C at 25 °C/hour, plateau for 48-hours;

(2) ramp to 400 °C at 50 °C/hour, plateau for 48 hours;

(3) ramp to 665 °C at 50°C/hour, plateau for 50 hours.

The first two steps are to enable Cu-Sn mixing while the third step is for Nb_3Sn reaction [276].

Figure 129: 7.2-m-long HL-LHC MQXFB quadrupole magnet coil in its retort ready for loading into heat treatment furnace. The foreground features a bottle of pure argon that will be connected to enable a flow through the coil (Courtesy of O. Housiaux, SERCO, and R. Principe, CERN).

The level of the first temperature plateau is selected to be below the Sn liquidus (227 °C eutectic) to protect against Sn burst. During this stage, Sn from the sub-element cores diffuses into the surrounding copper and forms Cu–Sn bronze phases that extend until the first rows of Nb filaments in the Cu/Nb arrays. The bronze phases that form are predominantly higher-Sn content η phase (Cu_6Sn_5), on the Sn core side, and lower-Sn content ε phase (Cu_3Sn), on Cu/Nb side [276]. At the end of the plateau, a significant fraction of the initial Sn (~30%) remains and will subsequently liquify.

The level of the second temperature plateau is selected to be below the melting point of the η phase (~408 °C), to prevent dissolution of Nb filaments. During this stage, a ring of ternary phase, $Nb_{0.75}Cu_{0.25}Sn_2$, referred to as *nausite*, named after the researcher who first observed it [277], develops at the periphery of the sub-element Cu–Sn cores and at the contact of the inner rows of Nb filaments in the Cu/Nb arrays. The discovery of the nausite phase called for a remodeling of the Cu-Nb-Sn phase diagram [278]. In the meantime, inter-filament copper migrates into the Cu-Sn core, enriching its ε phase content significantly, while Sn diffuses into the multifilament area [279].

During the subsequent temperature ramp, the nausite phase decomposes (typically, around 550 °C) to form a ring of $NbSn_2$, which, in turn, decomposes (typically, around 650 °C) to form Nb_6Sn_5. As a result, during the third and final plateau, a small inner ring of coarse and poorly connected Nb_3Sn grains is formed from Nb_6Sn_5, while fine and well connected Nb_3Sn grains are directly formed from the Nb filaments that were not transformed into $NbSn_2$ or Nb_6Sn_5 [280].

The temperature and duration of the third plateau determine the volume fraction, stoichiometry, grain size and upper critical field (B_{C2}) of the Nb_3Sn phase. These parameters, in turn, determine the shape of the critical current density versus the applied field curve, J_C(B), the residual resistivity ratio, RRR, and the electromechanical characteristics of the wire [18][33][281] [282]. They must be optimized for each specific wire layout [283].

As explained in Section 1.1 and illustrated in Figure 2 and several Figures of Section 3.5, at the end of the heat treatment, the densely packed array of reacted filaments in the sub-elements of RRP® wires is aggregated, resulting in a tubular Nb_3Sn phase whose outer diameter determines the effective filament diameter for magnetization and hysteresis loss.

5.5.5.3 Volume Change and Thermal Shrinkage Differentials

One of the main challenges for the reaction heat treatment of Nb_3Sn accelerator magnet coils is the amplitude and the management of conductor volume changes. The overall coil volume changes are hard to predict and depend on the thermomechanical properties of other coil components (wedges, spacers, retort, and so on) during the ramp-up and the ramp-down of the temperature cycle [224]. In addition, friction between coil components and between coil and retort can be expected to play a role. All these effects become more pronounced on longer coils, eventually leading to non-homogenous physical properties.

When left unconstrained, measured data for 11 T and MQXF cables made from RRP® strands show that both wires and cables undergo an increase of transverse cross-section and a length shortening upon reaction heat treatment [280][284]. Note that the change in longitudinal direction is not monotonic during the temperature ramp up. These results are consistent with previous measurements on other strand types and cable geometries [285][286]. However, the constraints applied during heat treatment strongly affect the cable dimensional changes [287][288]. For instance, it has been observed that, for an insulated cable, the constrains applied on the cable cross-section by its insulation can result in a smaller longitudinal contraction than for a bare cable. This effect is more pronounced for a braided insulation [287].

To cope with thermal shrinkage differentials between conductors and coil components, the latter are usually segmented in the longitudinal direction. This is the case of the copper wedges, which delimit the conductor blocks in the two-dimensional cross-section and are used to tune field quality (see Figure 7 and Figure 14). This is also the case of the pole pieces. For MQXFB, the pole pieces are 400 mm long in the coil central part, and between 520 mm and 560 mm long at the extremities and are made of annealed Ti6Al4V. The pole pieces are mounted at the time of winding and are never removed. For 11 T, the pole pieces used for heat treatment are 240 mm long, with an 87.5 mm long piece at the longitudinal center of the coil and are made of annealed 316LN. They are replaced by annealed Ti6Al4V pole pieces at the time of coil assembly.

As illustrated in Figure 130, at the time of winding, the pole pieces are mounted on the winding tooling with gaps between them. The gaps are in the 1–1.5 mm range for MQXFB coils and 2.5–2.7 mm range for 11 T coils. The gaps are expected to be more or less closed at the end of reaction heat treatment.

5.5.5.4 Opening of Heat Treatment Retort

The most critical step of the procedure is undoubtedly the opening of the retort upon reaction heat treatment completion. It is usually accompanied by a spring back of the reacted coil, in both transverse and longitudinal directions. The opening procedure starts with unbolting of M20 screws, then lifting of top plate, then removal of upper blocks, and finally, unbolting of M6 screws and removal of liner. Each of these steps is accompanied by vertical displacements of the structure and pole pieces, as well as coil longitudinal elongations, which, as illustrated in Figure 131 are now routinely measured at both ends by means of dial gauges.

Figure 130: Layout of segmented Ti-alloy pole pieces in preparation for the winding of the inner layer of a 7.2-m-long HL-LHC MQXFB quadrupole magnet coil at CERN. The gap intentionally left between pole pieces is clearly visible at the picture center (Courtesy of N. Lusa, CERN, 2022).

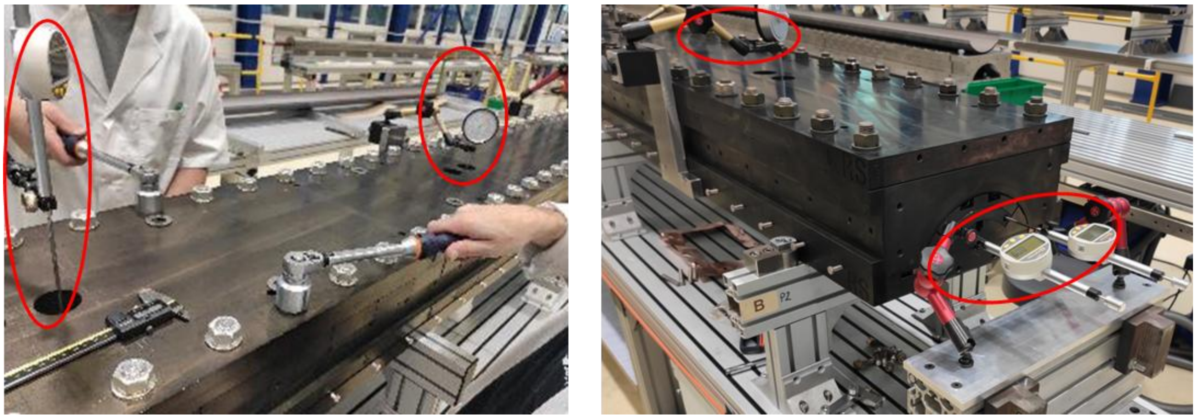

Figure 131: Dial gauge measurements carried out at various steps of retort opening after reaction heat treatment of 7.2-m-long HL-LHC MQXFB quadrupole magnet at CERN. Left: coil vertical displacement measurements. Right: coil elongation measurements. The largest displacements/elongations occur at the time of unbolting of M20 screws (Courtesy of N. Lusa, CERN).

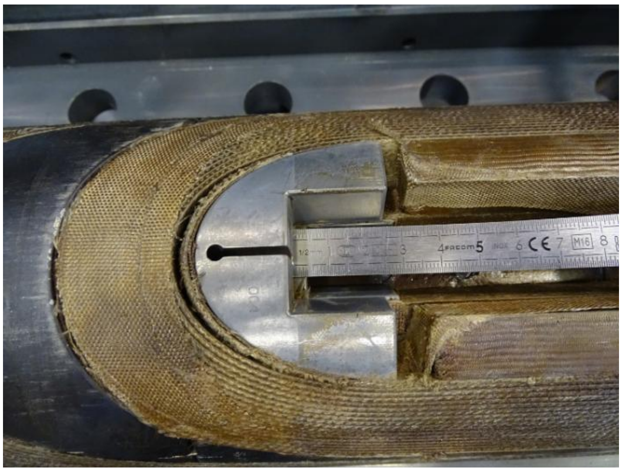

Figure 132: Observation of severe displacements at the non-connection side of 5.3-m-long HL-LHC 11 T dipole magnet coil CR07 after opening of RHT retort (Courtesy of F. Savary, CERN).

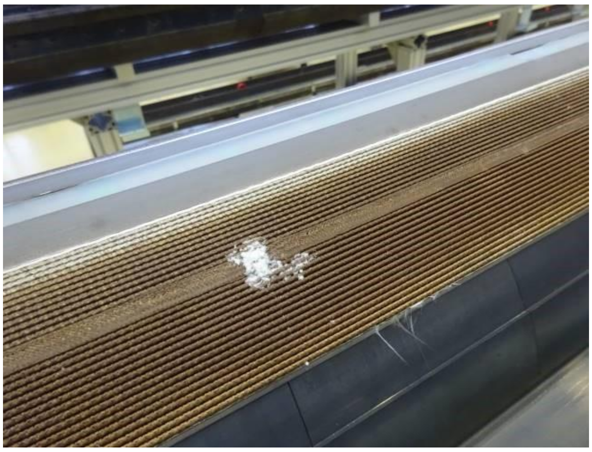

Figure 133: Top view of a reacted 7.2-m-long HL-LHC MQXFB quadrupole magnet coil after heat treatment. The white powder at the picture center is crushed glass fiber packed into a gap between segmented angular wedges. This gap will eventually be filled with epoxy resin during impregnation (Courtesy of O. Housiaux, SERCO and R. Principe, CERN).

The observation of such displacements and elongations upon retort opening is a clear indication that, although the coil is supposedly free to expand longitudinally in the retort, the system still has some significant stored energy, which is then progressively relaxed. Even in the ideal case of a longitudinally free-to-expand system, there may still be some stored energy, and thereby residual stresses, due to the heterogeneity of the materials (and of the materials' coefficients of thermal expansion) that make up the coil.

In the early stage of HL-LHC development at CERN, the above phenomenon had been underestimated and very significant spring back were observed. As an illustration, Figure 132 shows the non-connection side of 5.3-m-long HL-LHC 11 T dipole magnet coil CR07 after retort opening, where severe displacements/delamination can be seen. The conductors and end spacers were put back in place by hand, the coil manufacture was completed, and it was assembled in full-length dipole magnet prototype MBHBP. As already reported in Section 1.5.5.3, MBHBP exhibited poor performances, with all quenches localized in coil CR07 ends. It was concluded that this uncontrolled longitudinal spring back, and the subsequent hand repair, were the likely root causes of the poor magnet performances. Note that this is an extreme but very illustrative case.

Following this experience, a number of corrective actions have been implemented for subsequent 11 T and MQXFB coils. Among them are a revision of the radial pile up of materials in the heat treatment retort, as well as the sequences which are followed for bolting/unbolting of screws and mounting/removal of upper blocks. For MQXFB, the most recent procedures call for starting in the longitudinal center and moving towards the ends in a symmetric way at the time of retort closure and for starting in the extremities and moving towards the middle, also in a symmetric way, at the time of retort opening.

5.5.6 Vacuum Pressure Impregnation (VPI)

5.5.6.1 Gap Filling

Upon heat treatment completion and as illustrated in Figure 133, all the gaps visible on the outer surfaces of the reacted coil assembly are filled with AGY Glass 463-AA-750 fiberglass powder in preparation for resin impregnation. This filling is carried out to limit the occurrence of resin-rich areas after impregnation, which, if not reinforced, will be prone to cracking during cooldown owing to the limited fracture toughness of the resin [239].

In the case of HL-LHC Nb_3Sn coils, the outer layer is wound on top of the inner layer, and heat treatment and impregnations operations are carried out on the two layers together. Thus, the outer surface of the inner layer cannot be visually inspected (only the inner surface of the inner layer and the outer surface of the outer layer are accessible). As a result, gaps, particularly in the coil ends or at the transition between straight section and coil ends, will remain unfilled. This likely explains the resin cracks discussed in Section 3.5.1.2 and observed in Figure 51. Such a problem can only be addressed if the inner and outer layers are processed independently and joined together after heat treatment and even, possibly, after impregnation completion, by an internal splice. Such a design is worth studying for future high-field magnet applications.

5.5.6.2 Impregnation Mold and Resin Mix

The coil impregnation is carried out in a mold of accurate dimensions, with very tight geometrical tolerances. The mold is made of austenitic stainless steel (304L in the case of 11 T, 316L for MQXFB). The impregnation has 3 main goals [36]:

– to complement coil electrical insulation;

– to provide mechanical rigidity to the coil for subsequent handling and loading operations;

– to control coil geometry for field quality purposes.

Both 11 T and MQXFB rely on the same resin mix, that was qualified by LARP [289]: CTD-101K®, developed by CTD in the USA in the early 2000 for fusion magnet applications [273][290]. The CTD-101K® mix is made of three parts: a Bisphenol A Diglycidyl Ether compound, referred to as *DGEBA* (Part A), that is commonly found in epoxy resins, an anhydride-type hardener (Part B), and an accelerator of non-disclosed chemical nature (Part C). The resin mix offers low viscosity (400 cP at 40°C and less than 100 cP at 60 °C), long pot-life (60 hours at 40 °C) and has high radiation resistance [291][292].

5.5.6.3 Impregnation Process

The resin mix is applied to the coils by what we shall refer to as a *Vacuum Pressure Impregnation (VPI)* process. The VPI process is a refined version of the more widely known Vacuum Assisted Resin Transfer Mold (VARTM) process, which has become the most common process for consolidating the electrical insulation of large superconducting magnets [293].

The CERN VPI system consists of 3 main parts: a resin mixer and feeder tank (60 l) with a disposable resin bucket (maximum resin capacity of 16 kg), a large vacuum vessel with the impregnation mold containing the coil, and a resin outflow tank (40 l) with another disposable resin bucket. All three components can be independently pumped and vented and are instrumented with vacuum gauges. The injection and outflow tanks can be pressurized by nitrogen gas at 3.5 bars.

As shown in Figure 134, the CERN VPI system is highly automated, and a large number of online measurements are performed and monitored in order to guarantee a high-quality level of impregnation. The process is carried out in 12 steps [294]:

(1) loading of mold (with coil inside) into vacuum vessel and room temperature tests (including, pressure test and electrical test of heating system);

(2) vacuum vessel tilting at 18° (see Figure 135); the tilting is a common practice for such system; it helps having a regular and homogeneous propagation of resin that moves from bottom to top by capillarity along the coil, with the mold having been evacuated beforehand (see step (4)) and the weight of the resin column providing an additional push;

(3) mold heating and pressure test to check ability to withstand pressurization at warm (at 80 °C and 3.5 bars for 11 T coils, and 110 °C and 2.5 bars for MQXFB coils);

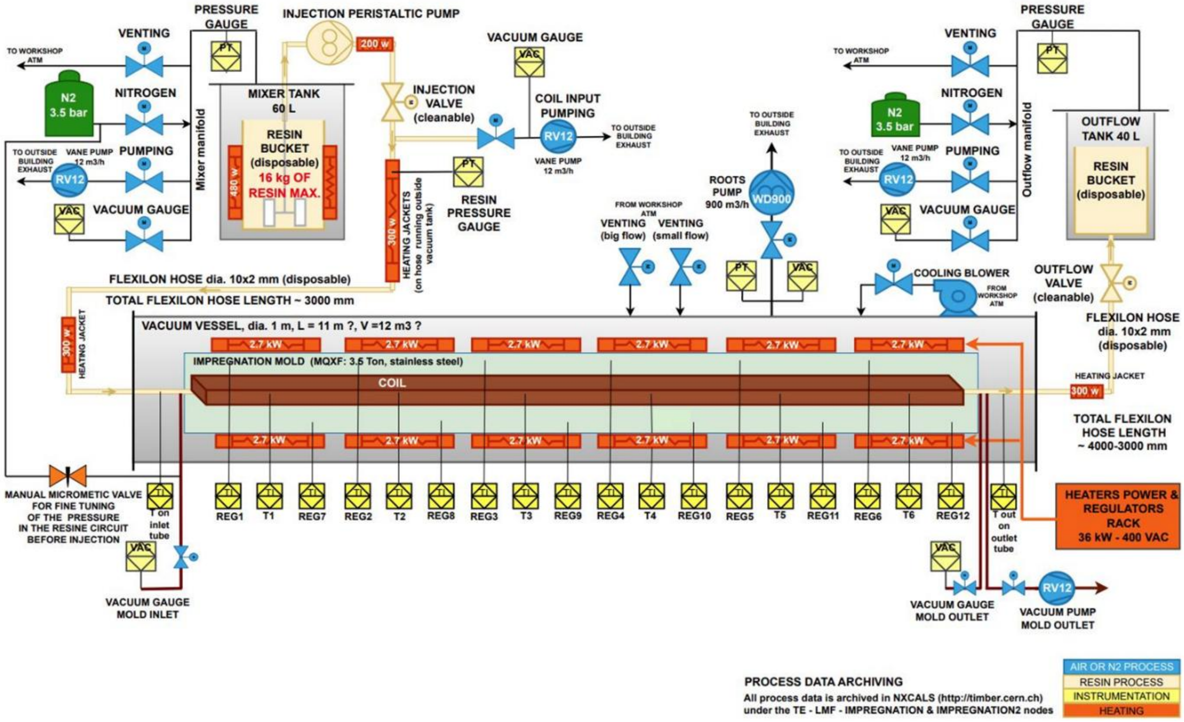

Figure 134: Schematic of Vacuum Pressure Impregnation (VPI) system for 7.2-m-long HL-LHC MQXFB quadrupole magnet coils at CERN featuring the positions of valves and thermocouples (Courtesy of J. Axensalva and D. Tommasini, CERN, 2022).

Figure 135: View of VPI station at CERN with vacuum tank tilted at 18° before start of resin impregnation (Courtesy of J. Axensalva, CERN).

(4) in parallel to temperature ramp, nitrogen rinsing of mold to evacuate air and to dry the coil (repeated 60 times for MQXFB coils);

(5) mold outgassing at high temperature (110 °C for MQXFB) and atmospheric pressure for 8 hours;

(6) mold cooling and vacuum pumping for 48 hours to achieve a final mold temperature and pressure of ~60 °C and ~0.15 mbar, respectively;

(7) resin mixing for 2 hours and degassing for another 2 hours at a temperature of ~65 °C and a pressure of ~0.2 mbar in mixer;

(8) resin injection at ~60 °C, from mixer, initially at ~0.2 mbar, into pre-heated mold, whose pressure is raised to 1-2 mbar to prevent resin outgassing in the mold; injection process lasts ~100 min for 7.2-m-long MQXFB coils and ~60 min for 5.3-m-long 11 T coils; at the end of this step, the resin has reached the outflow tank;

(9) resin soaking for 2 hours minimum at ~60 °C and under vacuum conditions;

(10) milking: once the resin has passed through the coil under vacuum conditions, the outflow tank is pressurized with dry nitrogen by steps of 0.5 bar up to 2 bars for MQXFB coils and 2.7 bars for 11 T coils for 30 minutes; the milking process is repeated several times and aims at enhancing resin penetration in the coil and reducing entrapped bubbles (if any);

(11) resin curing in 2 steps: 110 °C for 5 hours (curing step), followed by 125 °C for 16 hours (post curing step); temperature ramp of 15 °C/hour); measurements carried out during the impregnation of a 5.3-m-long 11 dipole magnet coil (GE-12) whose mold was specifically instrumented shows longitudinal temperature variation below 5 °C, with a downward trend from mold inlet to outlet [295];

(12) passive cooldown (for about 2 days).

The curing cycle described in Step (11) is the one recommended by CTD. It was determined empirically to achieve a high density of cross-links between macromolecules and a high glass transition temperature while keeping a reasonable duration. As for the Nb_3Sn reaction heat treatment, it could likely be further optimized but one needs to bear in mind the constraints imposed by the large thermal inertia of the mold and the coil.

As illustrated in Section 3.5.1 and Figure 51 and in Section 3.5.2 and Figure 54, in spite of all the efforts to prevent resin-rich areas and to ensure high-quality resin impregnation, significant cracks, debonding and delamination are observed in the insulation of coils, in particular for those having been exposed and tested in helium.

To improve the situation, one would need to identify resin systems that are less prone to cracking and debonding, in particular, during cooldown and warm-up temperature cycles. A number of developments are presently being carried out in this domain, comparing physical properties of different resin systems [239][292][296], as well as their adhesion properties [297], looking for improvement of existing resin mixes (*e.g.*, by including additives for increasing toughness) [292][298], looking for alternatives to polymer resins [296][299], and exploring other innovations on insulation materials and processes [300].

5.5.7 Final Inspection and Coil Size Measurement

Upon VPI completion, the coil undergoes a very thorough quality control, including visual inspections, electrical tests, and dimensional metrology. The dimensional measurements are particularly critical for determining the coil assembly and magnet loading parameters.

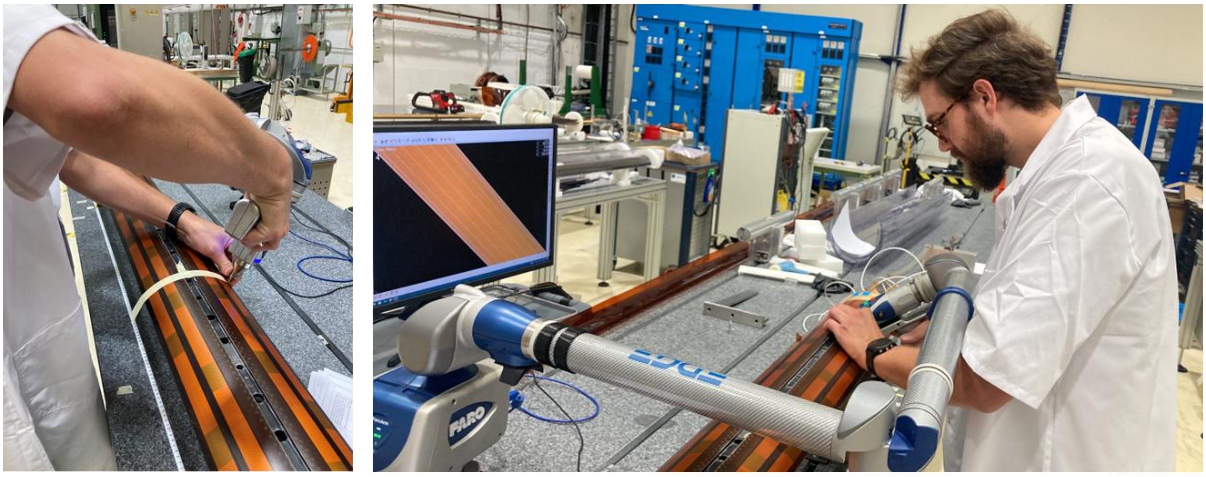

Figure 136: Final size measurements of impregnated Nb_3Sn coils for HL-LHC magnets measured using a FAROarm® (Courtesy of O. Housiaux, SERCO, and S. Straarup, CERN).

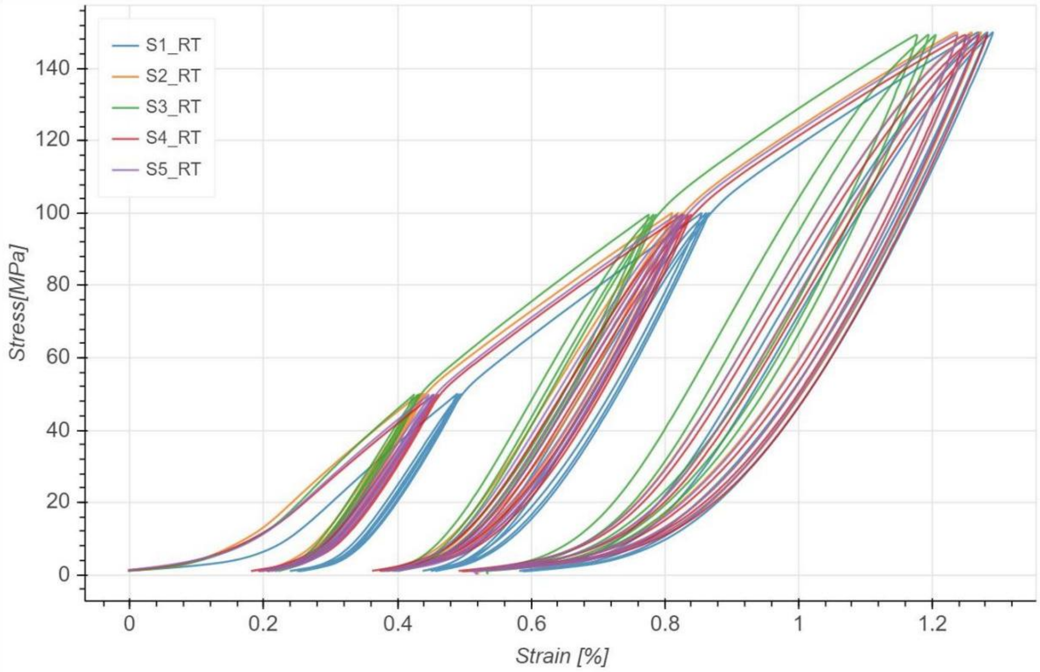

Figure 137: Stress-strain curves measured on resin-impregnated stacks of reacted HL-LHC 11 T dipole magnet cables at room temperature (Courtesy of Ó. Sacristán, CERN [310]).

As illustrated in Figure 136, the final sizes of impregnated Nb_3Sn coils for HL-LHC magnets are measured at rest using a portable articulated Coordinate Measuring Machine (CMM), developed by FARO Technologies, Inc., headquartered in Lake Mary, Florida, USA, and referred to as *FAROarm®* [301]. The FAROarm®, which was first used at LBNL in the early 2010s [302] and was adopted by LARP [272], is very handy and cost effective, but it is labor intensive and does require some caution when used for a long coil where its base must be moved to different positions. Also, it calls for careful post-processing in order to realign the measured data with the nominal outer coil radius from the CAD model [215][303].

One issue, however, is that the coil sizes are measured at rest, while, for previous accelerator magnet applications, the coil sizes were measured in a so-called *Young's modulus press*, under the target coil azimuthal pre-compression for magnet loading. See, for instance, the procedure applied to SSC dipole magnet coils [212][304]; a similar procedure was followed for LHC dipole and quadrupole magnet coils [305][306][307].

For Nb–Ti coils, the measurements were done under compression to avoid the large non-linearity of the coil stress-strain curve at low stress and to achieve the near-linear regime at higher stress, which is more representative of the coil behavior during collaring [308][309]. Although, a similar procedure was used for the coils of the short Nb_3Sn quadrupole magnet built at CEA/Saclay in the 2000s (see Section 1.6 and [119]), limiting the stress applied to the coils to 50 MPa, it was deemed too risky to apply this procedure to HL-LHC magnet coils and the decision was taken to carry out size measurement on coils at rest.

As illustrated in Figure 137 and similarly to Nb–Ti cable stacks, the stress-strain curves of Nb_3Sn cables stacks do exhibit non-linearities at low stress, upon initial loading and upon subsequent reloading [309][310]. In addition, the Young's modulus of resin-impregnated Nb_3Sn coils is 4 to 5 times higher than the one of polyimide-insulated Nb–Ti coils, thereby requiring tighter tolerances and parameter control during manufacturing and assembly and calling for more accurate coil size measurements. As more experience and confidence have been acquired on coil production, it may be a good time to revisit this issue and the coil size measurement procedure to be applied to Nb_3Sn magnet coils.

5.5.8 Findings from MQXFB Coil Manufacturing Data: Coil "Hump" and "Belly"

5.5.8.1 Introduction

The main findings from dimensional measurements carried out at various stages of coil manufacture are [311]:

- coil *hump* towards mechanical center and coil longitudinal elongation with respect to the ends of the base plate of the reaction heat treatment retort at time of opening;
- inner-layer pole turn *protrusions* at junctions between Ti-alloy pole pieces;
- coil *belly* towards mechanical center after vacuum pressure impregnation.

5.5.8.2 Coil Hump

As illustrated in Figure 138, after unbolting of the reaction heat treatment retort, lifting of top plate and removal of upper blocks, it appears that the top of the coil pole pieces move upward with respect to the bottom plate, with a maximum displacement in the 1.5–2 mm range towards the coil longitudinal center. This effect, referred to as hump, is observed on all coils manufactured with the standard procedures described in the above sections. Looking more closely at the details, one can also see some jumps between adjacent pole pieces, which can be as high as 250 μm.

In addition, as illustrated in Figure 139, the various steps of retort dismounting are accompanied by a coil longitudinal elongation with respect to the retort ends, which is of ~5 mm (most of the elongation occurs while unbolting M20 screws). The lifting of the Ti-alloy pole pieces and the coil elongation both confirm that there is stored energy in the coil which is released at the time of retort opening.

The existence of the hump is confirmed when, in preparation for impregnation, the coil is rotated by 180° and rests on its Ti-alloy pole pieces and outer surface. The vertical position of the coil midplanes can be measured by using a standard CMM. The position appears to vary longitudinally (along the coil axis), in a similar fashion as in Figure 138, with a maximum of 1.5-2 mm towards the coil center [311].

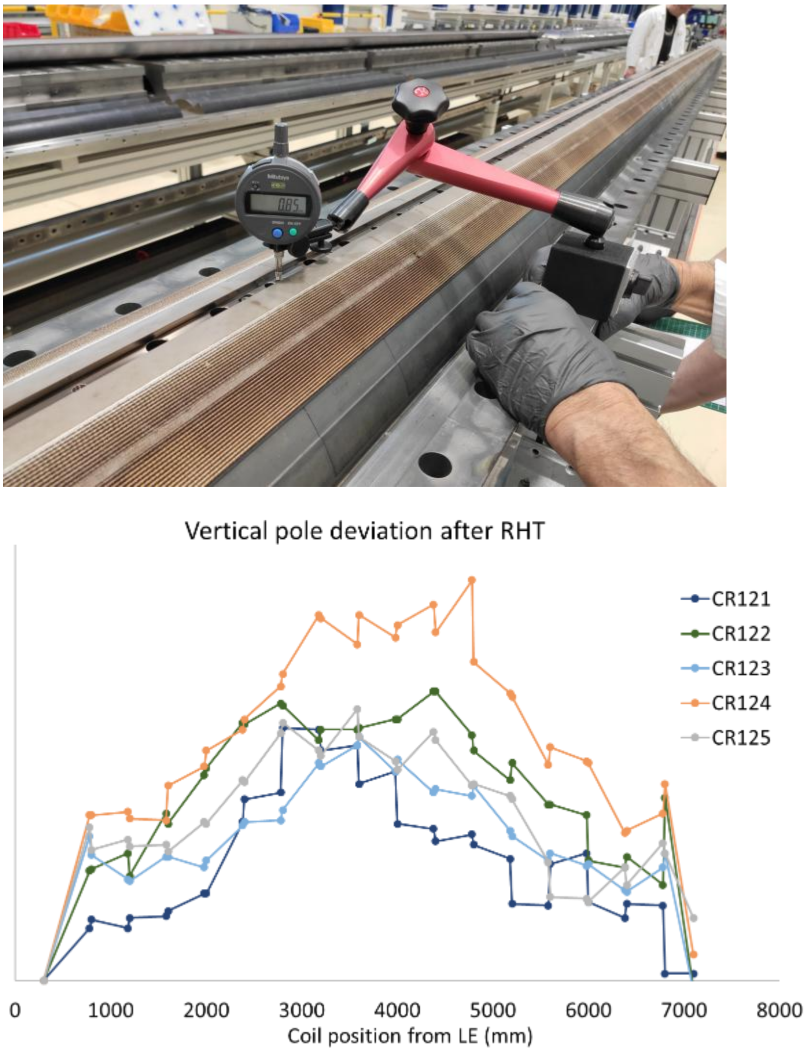

Figure 138: Summary plot of vertical Ti-alloy pole displacement with respect to base plate, as measured with dial gauges on 7.2-m-long HL-LHC MQXB quadrupole magnet coils produced according to standard procedures, after completion of reaction heat treatment and dismounting of retort (Courtesy of N. Lusa, CERN).

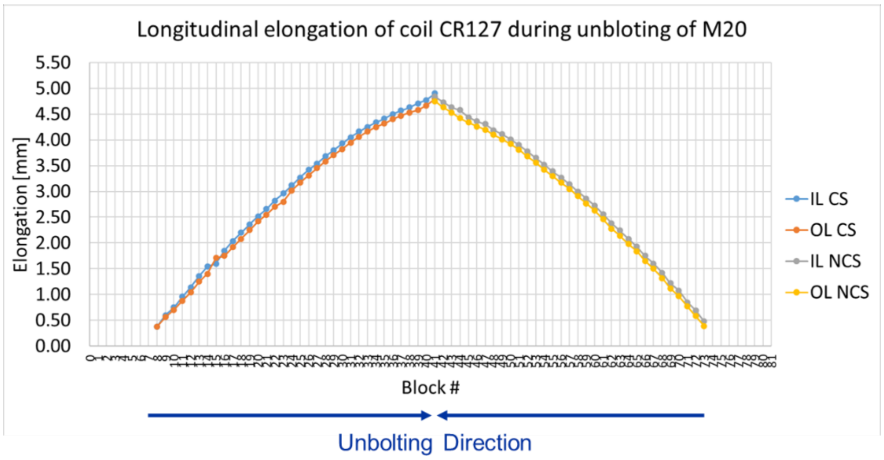

Figure 139: Vertical coil elongations with respect to reaction heat treatment retort ends as measured by dial gauges on 7.2-m-long HL-LHC MQXB quadrupole magnet coil Q127 during unbolting of M20 screws (Courtesy of N. Lusa, CERN).

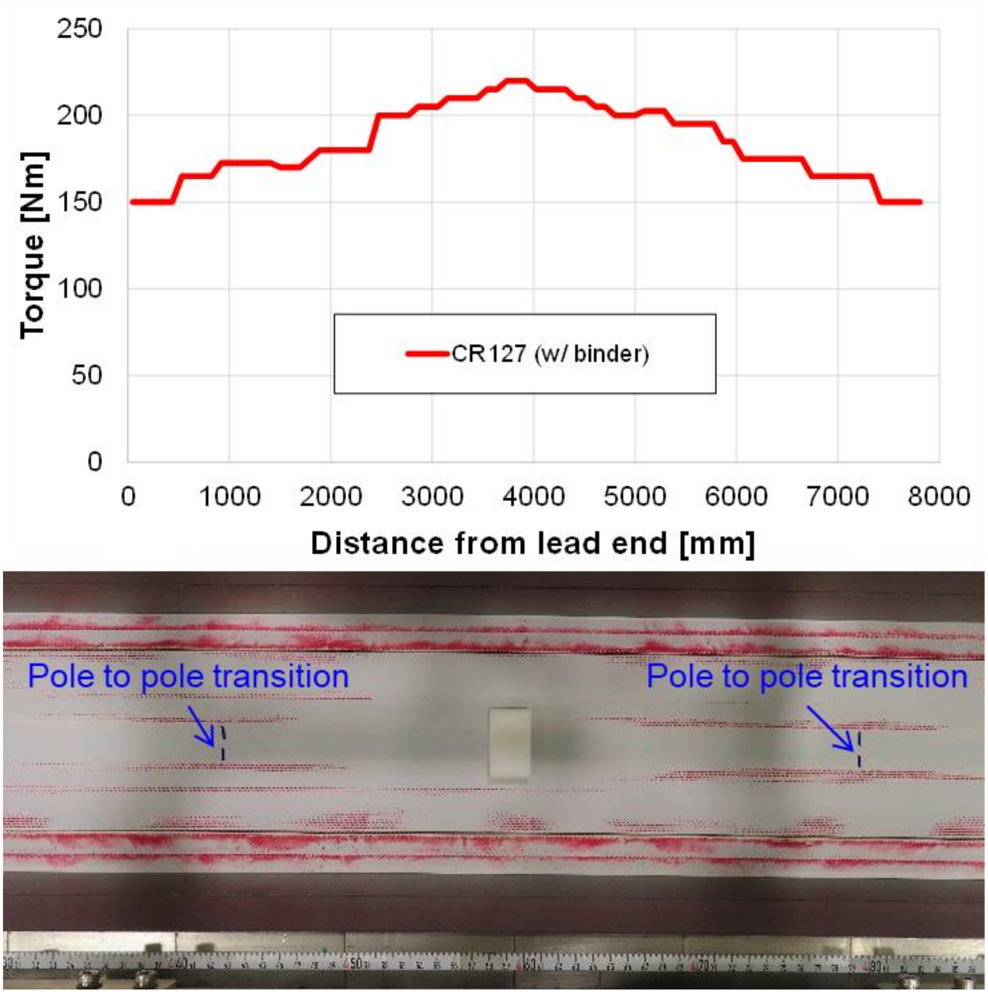

Figure 140: Observations during a VPI mold closure test on 7.2-m-long HL-LHC MQXB quadrupole magnet coil Q127, which had been equipped with pressure sensitive paper on its inner surface. Top: torque needed to close mold as a function of longitudinal position. Bottom: marks on pressure sensitive paper after test completion (Courtesy of N. Lusa, CERN).

5.5.8.3 Inner-Layer Pole Turn Protrusion and Hinge Effect

As detailed in Section 3.10 and illustrated in Figure 62, evidence of inner-layer pole turn protrusions and of local insulation damages has been observed at various locations along the coils corresponding to Ti-alloy pole transitions.

Another interesting verification was carried out by placing pressure-sensitive paper in the VPI mold, particularly on the inner coil surface, where the protrusions have been observed, and to record what happens upon mold closure. As illustrated in the bottom of Figure 140, the VPI mold closure results in clear stress concentration marks at the locations of the protruded turns. This confirms that this operation is applying stress on the conductors to force them back into place. Also, the top part of Figure 140 shows that the torque required to bolt the VPI mold is not uniform along the coil, but increases by nearly 50% towards the coil center, which is consistent with the above observations [311].

In summary, the hump and the pole turn protrusions both result from the coil spring back at the time of retort opening, while the misalignment of adjacent Ti-alloy pole pieces, and the associated hinge effect, are likely the cause of the observed strand breakages, which occur either at the time of RHT retort opening or at the time of VPI mold closing.

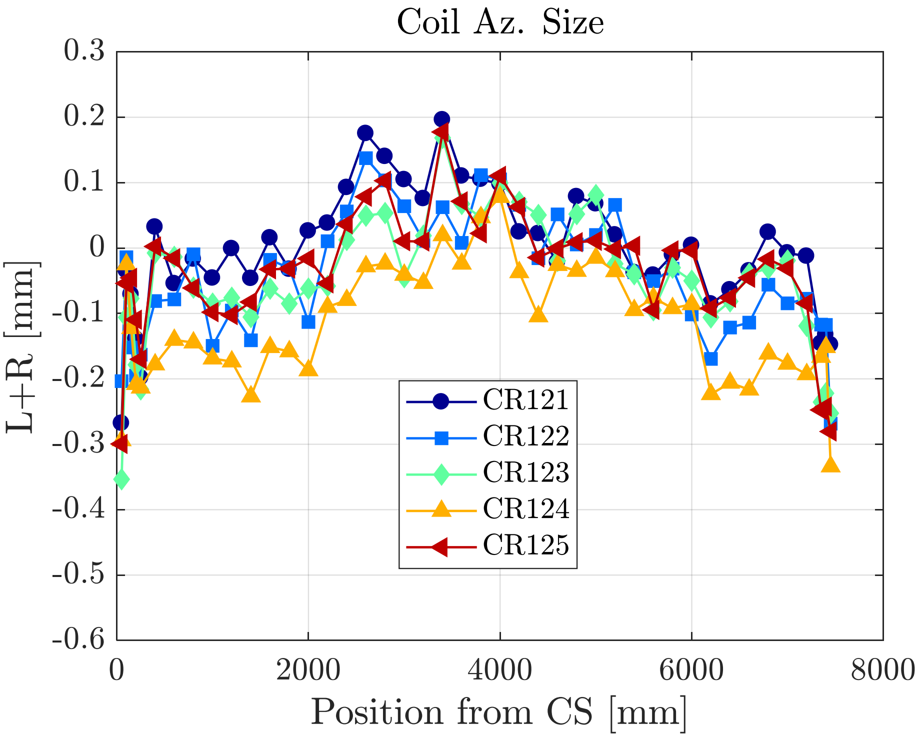

Figure 141: Summary plot of azimuthal sizes as measured on 7.2-m-long HL-LHC MQXB quadrupole magnet coils produced according to standard procedures, after completion of vacuum pressure impregnation (Courtesy of N. Lusa, CERN).

5.5.8.4 Coil Belly

As illustrated in Figure 141, and even though the coils have been impregnated in a mold of accurate dimensions, the final azimuthal coil size measurements, also exhibit a bell shape, referred to as *belly*, with a fatter size in the 0.1–0.2 mm range towards the coil longitudinal center.

The belly is again a systematic effect observed on all coils. When this was first observed, a thorough review of VPI tooling dimensions and tolerances, and of assembly procedures was carried out, but the review did not reveal any issue with respect to tooling design and assembly parameters.

Comparing the humps in Figure 138 and the bellies in Figure 141, one can now establish that they are correlated [311], and that the coil belly is likely a consequence of the hump.

5.5.9 Stage-3 Corrective Actions

The main findings in Section 5.5.8 enable us to establish the chain of events that eventually leads to strand breakages and to trace back its origin to excessive energy stored in the coils due to reaction heat treatment. The next and last point to elucidate is: why do we have so much stored energy in MQXFB coils, while we do not observe similar phenomena in shorter MQXFA or 11 T coils? This points towards frictional effects between coil and retort during reaction heat treatment, which can be expected to be more pronounced on longer coils.

Once again, a systematic review of design and assembly parameters and of manufacturing procedures was carried out to determine what could be done to reduce frictional effects. Several trials were performed to give more breathing space to the coils inside the retort cavity, *e.g.*, by increasing gaps between Ti-alloy pole pieces and by removing one layer of fiberglass cloth on the outer coil surface.

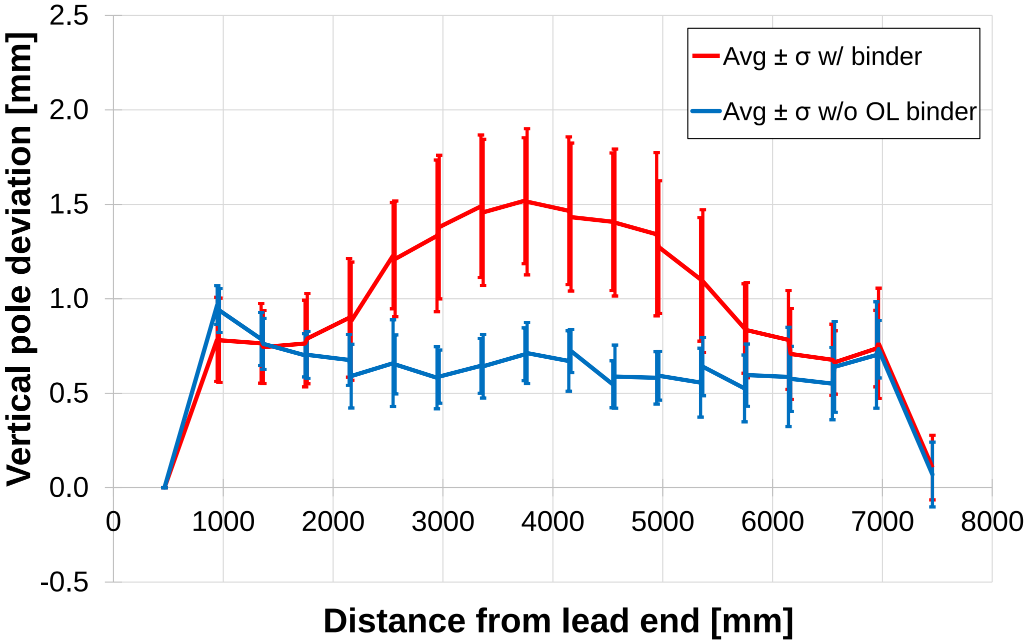

Figure 142: Comparison of vertical Ti-alloy pole displacement with respect to base plate, as measured with dial gauges on 7.2-m-long HL-LHC MQXFBP3 quadrupole magnet coils manufactured with (red data points and line) and without (blue data points and line) ceramic binder application on the coil outer surface, after completion of reaction heat treatment and dismounting of retort (Courtesy of N. Lusa, CERN [311]).

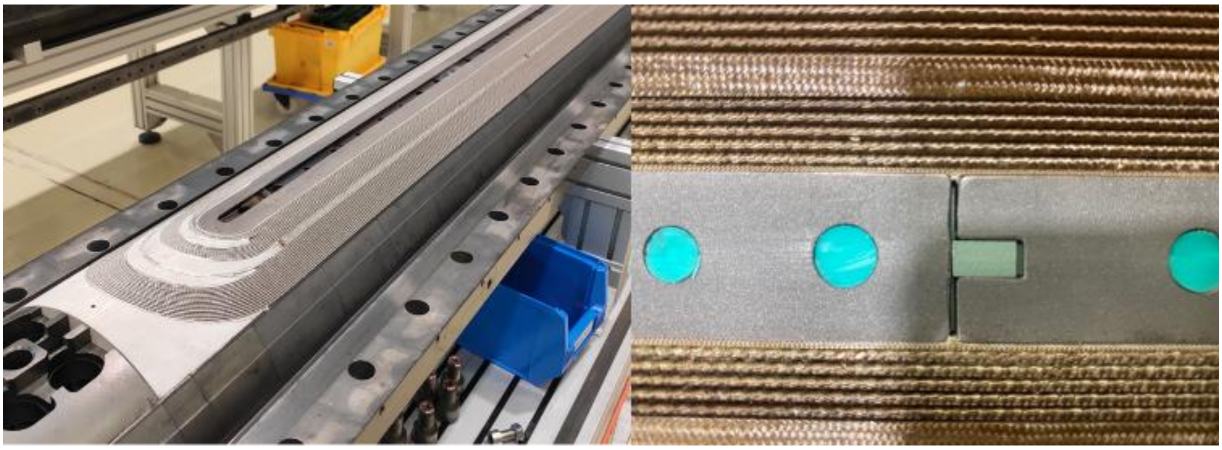

Figure 143: Pictures of reacted 7.2-m-long HL-LHC MQXB quadrupole magnet coil Q128 manufactured without ceramic binder on its outer surface. Left: view of outer coil surface, which appears more silverish and cleaner than before. Right: view of inner coil surface in the vicinity of a Ti-alloy pole junction, with no evidence of inner pole turn protrusion and of insulation degradation (Courtesy of N. Lusa, CERN).

These two changes were, among others, applied on coil Q127, which was assembled and tested in MQXFBMT4 without benefit (see Section 5.4 and Figure 122). What eventually proved to be successful is the removal of the ceramic binder application on the outer surface of the coil outer layer (while still keeping the binder application on the outer surface of the coil inner layer) [311]. As illustrated in Figure 142, the coils manufactured without ceramic binder on their outer surface, come out flat from the reaction heat treatment and do not exhibit any hump.

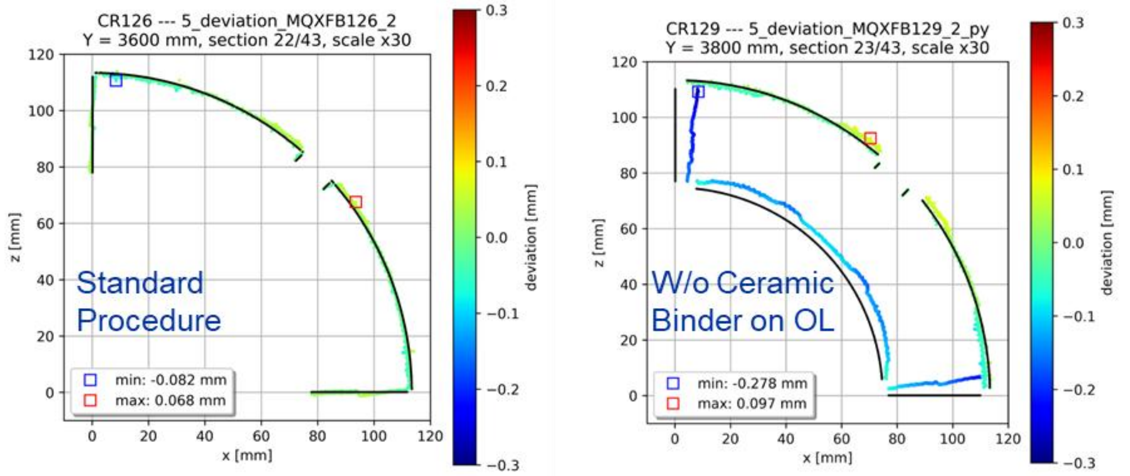

Figure 144: Comparison of 2-dimensional geometry of 7.2-m-long HL-LHC MQXBP3 quadrupole magnet coils manufactured with (left side) and without (right side) ceramic binder on coil outer surface, after completion of vacuum pressure impregnation (Courtesy of N. Lusa and S. Izquierdo-Bermudez, CERN).

In addition, the coil longitudinal elongation measured as result of unbolting the M20 screws on the retort is 20-25% smaller than on previous coils. Also, when inspecting the inner-layer pole turn conductors in the vicinity of the Ti-alloy pole junctions, one does not observe any significant protrusion anymore (see Figure 143). Subsequently, the torque needed to close the VPI mold is almost 50% smaller than before and it is much more uniform along the coil axis, while the impregnated coils do not exhibit any marked belly anymore. In short, all the undesirable effects that had been observed on coils produced by the standard procedures, have been eliminated.

Of course, any engineering process change results in adverse effects whose impacts and potential risks need to be assessed and mitigated. As illustrated in Figure 144, the removal of the ceramic binder on the coil outer surface results in a slight change in the two-dimensional geometry: the coil angular extent decreases from 90° to ~89.5° while the inner radius increases by ~0.2 mm. The change in arc length can be compensated by shimming, the change of inner radius will result in a small loss of transfer function (estimated to ~2.5 x 10^{-3}), which does not need compensation and will offer a larger clearance for beam tube insertion. In addition, the data reported in Ref. [312] indicate that the removal of the ceramic binder on the coil outer surface introduces differences of integrated thermal contraction coefficients between inner and outer coil layers, in particular, in radial and azimuthal directions (the difference in axial direction is not significant).

The differences in coil geometry and thermomechanical properties are likely to arise because, as explained in Section 5.5.4, during heat treatment, the ceramic binder reacts with the fiberglass insulation that is braided around the conductor and severely degrades its physical properties. As a result, when the ceramic binder is applied to the inner layer but not to the outer layer, one can expect that the inner-layer insulation braid is degraded, while the outer-layer insulation braid keeps its mechanical integrity, resulting in slightly different thermomechanical behaviors.

When considering the pros and cons of eliminating the binder application on the coil outer surface, it was concluded that the benefits of avoiding the hump and belly outweigh the other risks, and it was decided to proceed with the assembly of a full-size magnet made from such coils.

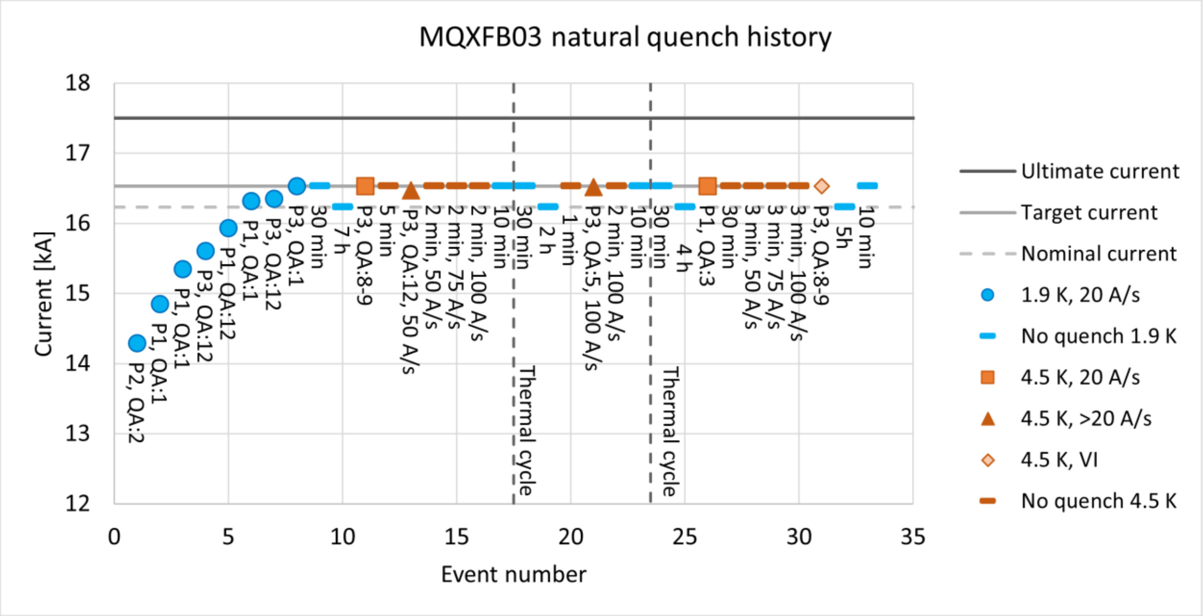

Figure 145: Quench Performance of 7.2-m-long, 150-mm-single-aperture HL-LHC MQXFB03 quadrupole magnet prototype at CERN, in a test cold mass configuration and test cryostat, integrating the first-, second- and third- stage recovery actions: new shell design and welding parameters and new fixed point, new magnet loading procedures, and new coil manufacture procedures without ceramic binder on outer coil surface (Courtesy of F. Mangiarotti, CERN).

5.5.10 Assembly and Test of MQXFB03

MQXFB03 is the first magnet that integrates the actions from all 3 stages of the recovery plan: it relies on 4 new coils, manufactured without ceramic binder on their outer surface, it was loaded with the optimized bladdering & keying procedure validated on MQXFB02, and it was assembled into a test cold mass and cryostat configuration using the optimized shell design and welding parameters qualified on MQXFBP3.

MQXFB03 was tested in the third and fourth quarter of 2023 and, as illustrated in Figure 145, and it is the first 7.2-m-long MQXFB magnet to achieve the target current of 16.53 kA (nominal +300 A) at both 1.9 K and 4.5 K. It exhibits good endurance after two warm-up/cooldown cycles with no retraining at 1.9 K. The initial training quenches at 1.9 K are all in the coil heads, in stark contrast with previous full-length MQXFB magnets. At 4.5 K and nominal 20 A/s ramp rate, there is one training quench (after initial cooldown and 1.9 K training) and one retraining quench (after 3rd cooldown and ramps to target and nominal current at 1.9 K), both above nominal and very near target current. There are two additional retraining quenches at 4.5 K and higher ramp rates, also near the target current. In addition, and as illustrated in Figure 146, MQXFB03 can be ramped up to target current with ramp rates up to 100 A/s at 4.5 K without quenching, while all previous full-length MQXFB magnets exhibited a noticeable ramp rate degradation below target current. This element, again, confirms the robustness of this magnet.

In short, the performance limitation and phenomenology that had been observed on previous, full-length, MQXFB magnet straight sections (near the apex of coils' hump and belly) have been overcome and we can finally conclude that, with the implementation of the stage-3 recovery actions, the root cause of the problem has been eradicated.

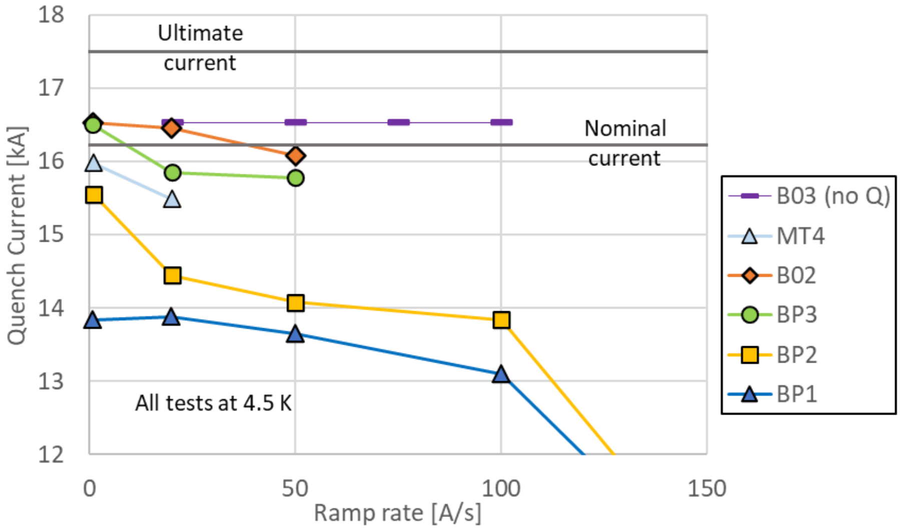

Figure 146: Ramp rate sensitivity at 4.5 K of 7.2-m-long, 150-mm-single-aperture HL-LHC MQXFB quadrupole magnets at CERN, in a test cold mass and cryostat (Courtesy of F. Mangiarotti, CERN).

Since then, a second full-length quadrupole magnet, referred to as MQXFB04, was manufactured following the same procedures as for MQXFB03 and integrating the recovery actions from all 3 stages. It was assembled with a nested MCBXFB dipole magnet corrector in a final Q2 cold mass and cryostat configuration and was cold-tested in the second quarter of 2024 [261]. The performances of MQXFB04 are similar to those of MQXFB03, including after the warm-up cooldown cycle, confirming the success of the recovery plan.

5.6 Conclusion

We followed a chain of targeted diagnostic steps that led us to the identification of possible root causes for the performance limitation observed on the first two MQXFB prototypes, and to the definition and implementation of suitable recovery actions. Starting from accurate quench-start localizations in both transverse and longitudinal directions, we defined coil volumes of interest to be inspected. Using different techniques, from high-energy X-ray computed tomography to metallography in both transverse and longitudinal directions and deep copper etching, we were able to zoom in on specific flaws in the magnet coils, down to the level of local Nb_3Sn strand damages, likely at the origin of the quench limitation. We could also determine the timing at which the damages occurred. Knowing the localization of the damages, we were able to establish correlations with specific mechanical features of the coil assembly, and knowing their timing, we could trace back the manufacturing process that produced them. An in-depth analysis of this specific manufacturing process and of related non-conformities led us to an understanding of the chain of events resulting in the observed behavior, which, in turn, gave us clear guidance on what needed to be improved. The elaboration and implementation of pointed corrective actions eventually enabled us to mitigate the identified risks one after another and resolve the quench limitation issue in the magnet straight section. None of the above would have been possible, without precisely knowing where to look.

In the case of ITER cable-in-conduit conductors, the issue of performance degradation as a function of electromagnetic and thermal cycling was resolved by tightening the twist pitches of the first stages of the rope-type cable. This short twist pitch sequence dramatically reduced the risks of reacted Nb_3Sn strand bending under the effect of the Lorentz forces, and the robustness of this new cabling pattern was confirmed by post-mortem analyses of conductor samples after testing in SULTAN which were devoid of any Nb_3Sn filament crack.

In the case of 7.2-m-long MQXFB quadrupole magnets, the issue of performance limitation in the magnet straight section was resolved by achieving a better control of coil uniformity and, thereby of reacted conductors' placement, by limiting deformations during manufacturing and by preventing subsequent coil overstressing during magnet and cold mass assembly. To close the loop, it would of course be interesting to verify that coils manufactured by the new procedure are also devoid of cracks in the vicinity of the Ti-alloy pole transitions, after assembly completion and following cold testing.

Let us stress that, for both projects, the root causes were related to specific detailed mechanical engineering issues, that could be resolved by rather simple changes in design or process parameters and that there was nothing inherently wrong with Nb_3Sn technology, save that it requires more care and is less forgiving than Nb−Ti technology.

From the human and management points of view, the lessons learned from the MQXFB crisis are similar to those learned during the ITER CS conductor crisis. The three main keys to the success are:

- having the right people at the right place (in particular, engineering should be done by engineers), bringing together all required expertise, regardless of affiliation, and getting them to work together in a collaborative and transverse manner;
- development and implementation of a rigorous and systematic methodology, that addresses all issues and considers all options, without exclusive, and reliance on good engineering practices, to build confidence and contingencies;
- enforcement of a decision-making process based on rational technical and scientific facts and on logical deductions rather than on opinions or beliefs.

The efforts reported in Section 5 were concentrated on MQXFB magnet straight sections to address the specific issue of performance limitation observed on MQXFBP1 and MQXFBP2. However, as experienced with the 11 T dipole magnet program at CERN (see Section 4) and the MQXFA magnet production at AUP [111], a similar review of design features and assembly procedures may be required for the magnet end parts and longitudinal loading. The assembly and test of the following MQXFB magnets at CERN will be critical to assess whether this should be a concern or not.

6 Key Take-Away Points

The main take-away points from the comprehensive review of ITER and HL-LHC experiences presented in the above sections can be summarized in ten bullet points:

(1) Conductor: it is essential to develop and rely on robust Nb_3Sn strands, which can be produced in large quantities and in a cost-effective manner. The root-cause analyses carried out for both ITER and HL-LHC crises were eventually successful because there was no suspicion about local defects in the strands themselves. If it had not been the case, disentangling strand from cable and magnet issues would have been very challenging.

(2) Electromagnetic design: except for solenoids, most magnet designs are 3-dimensional and critical areas are ends and transition regions. For high-field accelerator magnets, it is critical to integrate in the electromagnetic design optimization the volumetric distribution of the Lorentz force in the coil heads and to try to minimize deleterious bending effects. Also, the shape of the end spacers should be optimized to reduce/prevent strand pop outs during winding.

(3) Mechanical design: while Nb–Ti strands and cables may tolerate deformation/displacement of a few tens of millimeters, reacted Nb_3Sn strands and cables need to be supported with an accuracy better than, typically, 0.05 mm. All mechanical design aspects must be assessed at this scale. Also, the mechanical design should include from the start consideration of the full magnet system, including cold mass and cryostat as these may impact the loads experienced by the coils and the conductors. Finally, any mechanical engineering problem has usually more than one solution, each of these solutions should be carefully assessed, and the final choice depends on the program goal, *e.g.*, manufacturing of a short model magnet relying on existing and limited infrastructure, or production of series magnets in an environment where investment on heavy tooling can be considered.

(4) Electrical design and insulation: the electrical design of wind & react magnets must integrate the application of the heat treatment that can cause both mechanical and electrical degradations. In case of resin impregnation, the choice of the resin system must be optimized to limit the impact of cracking and debonding during cooldown and energization (in relation with the mechanical design).

(5) Finite element modeling: the development of comprehensive finite element models, that describe the full magnet life cycle, that can be used as tools to identify weak or stress concentration points, and that can guide the choice of design solutions is indispensable. The models should rely on physical parameters, deduced for known material properties and should not be adjusted to fit observed behaviors. The models should be benchmarked and validated on mock-ups and *ad hoc* experiments to build confidence in their suitability.

(6) Manufacturing processes: tooling and processes should be optimized to prevent: (i) deformations/displacement of conductors, or strands within conductors, in particular after heat treatment, and (ii) application of unnecessary stress overloads on reacted conductors. For accelerator magnet coils, this implies that coil handling and assembly require tolerances that correspond to fitting rather than mounting.

(7) Instrumentation & diagnostics: instrumentation and diagnostics should be integrated from the start into the magnet design to be able: (i) to accurately determine quench-start localization, (ii) to monitor performance evolution and, eventually, degradation, and (iii) to measure key mechanical parameters in the most direct way possible. If the implementation of instrumentation requires design modifications, a local FE model should be developed to assess the modification impact.

(8) Post-mortem analyses: the post-mortem analyses developed for ITER and HL-LHC have proven to be very efficient tools in root-cause analyses. However, they do require some time and need to be applied in a proper sequence to enable proper zooming into each problem type.

(9) Good engineering practices: the application of a systematic and rigorous methodology that addresses all problems one after another, without short cuts, has been key in resolving the ITER and HL-LHC crises. Also, good engineering practice calls for addressing all issues that arise, and if a cost- and schedule-effective solution can be found, to implement it, as this will help build contingencies and increase operation margin.

(10) Design of experiments and decision-making processes: a development program, in particular for an immature technology, should be built step-by-step, starting from material samples and mock-ups, to demonstrators, to short models, to full-length prototypes. This enables, at every step, qualification/validation of key design concepts, technological choices, manufacturing processes, and numerical models. Achieving maturation and understanding requires time, but skipping intermediate steps may lead to confusion in case of failure or unexpected results, calling for time- and resource-consuming crash programs. And last but not least, it is critical to implement a decision-making process based on thorough root cause and risk analyses and shielded, as much as possible, from schedule and management pressure.

Despite the setbacks that were encountered on the path of Nb_3Sn magnet development for ITER and HL-LHC, which were not exclusively due to technical issues, and which have been overcome, we can conclude that Nb_3Sn has been demonstrated to be a viable and robust technology for fusion and accelerator magnet applications. We can even go beyond and state that, thanks to ITER and HL-LHC, Nb_3Sn technology is reaching maturity, and that far from being prehistoric, it is now history in the making. As new large-scale projects of fusion reactors and particle accelerators are emerging, Nb_3Sn remains a valid option to consider, bearing in mind the hard lessons learned from ITER and HL-LHC.

Acknowledgements

The authors are greatly indebted to the CERN Director General, F. Gianotti, who enabled the TE-MSC Group to complete the “validation of the full inner triplet quadrupole manufacturing process” by setting this goal as one of the top five objectives for the laboratory in her January 2023 New Year presentation.

The authors express their utmost appreciation to the technical staff of the TE-MSC Group, for their hard work and dedication and for keeping their motivation throughout these troubled times. Sincere gratitude as well to the technical staff of other Groups at CERN, within the TE-Department, TE-CRG, TE-MPE, TE-RAS and TE-VSC, but also outside, in particular, EN-MME, for their continuous and proactive aid.

The authors are grateful to A. Milanese who, as responsible of the Large Magnet Facility (LMF), oversaw with meticulousness and perseverance the implementation of the 3-stage recovery plan for MQXFB until its complete fulfilment. They are thankful to the selfless but efficient role played by D. Tommasini, in addressing a number of engineering issues, in a rational and pertinent manner, and to the support of H. Felice in promoting the exchange and the diversity of opinions. They acknowledge the contributions of J.-C. Perez to the 11 T and MQXF short magnet model programs and of S. Izquierdo-Bermudez to the large body of analyses that were carried out for both programs. Susana also became a key stakeholder in the recovery plan implementation when she took over the responsibility for MQXFB production at LMF. The authors are appreciative of the driving role of A. Ballarino in the development and production of high-quality Nb_3Sn wires and cables, and of her cautious advice on the in-coil performance of Nb_3Sn conductors under transverse load.

This work would not have been possible without the steadfast support of O. Brǜning, HL-LHC Project Leader and M. Zerlauth, HL-LHC Deputy Project Leader.

Special mentions to Lucio Rossi, formerly CERN, now University of Milan, who launched the HL-LHC project and associated collaborations circa 2010, with gusto and charisma, and fostered the first application of Nb_3Sn dipole and quadrupole magnets in a machine, and to F. Bordry, who as Director of the CERN Accelerators and Technologies Sector at the time, understood the benefits of such developments and became a staunch supporter of the 11 T dipole magnet program. The MQXFB crisis reported here fell under the ATS Directorship of M. Lammont, who entrusted the TE and TE-MSC management to address the issue until achievement of the objective set by the CERN DG.

Special mentions as well to the US pioneers who have played key roles in the development of HL-LHC Nb_3Sn technology, in particular at LBNL and FNAL, and later on, at BNL, and who contributed to many vivacious but fruitful discussions, first as part of LARP and then as part of AUP, under the leadership of G. Apollinari. Acknowledgement to individual contributions is given through the numerous references provided in the report.

Warm thanks to P. Védrine, CEA/Paris-Saclay, and S. Gourlay, formerly LBNL now FNAL, who, as CERN MAC member and former member, readily understood what was at stake and were supportive of the ongoing efforts, and to A. Yamamoto, who as CERN SPC member, always exerted an independent mind but eventually became convinced that Nb_3Sn accelerator magnets could be made to work.

The authors are thankful to L. Bottura and E. Todesco, CERN, who played a significant role in moving the 11 T and MQXF projects forward and for their participations to dynamic discussions, thanks to their singular ideas and opinions. This is a reminder that constructive confrontations and peer reviews are essential elements in any significant scientific or technological endeavor, as they force to be more rigorous and are instrumental to the consolidation of recovery plans.

More specifically, the authors acknowledge L. Bottura for:

- advocating the placement of an industrial contract for the manufacture of 11 T dipole magnet coils and collared coil assemblies;
- supporting the 1st 11 T Task Force that was established in November 2017 and disbanded in Summer 2018;
- promoting the externalization of the quench protection heaters mounted on the 11 T dipole magnet coils to improve electrical robustness;
- launching the analyses of the complex electrodynamic effects associated with interstrand current redistribution in a damaged Rutherford-type cable;
- forewarning that the difficulties encountered on the 11 T magnets would not be unique and that MQXF magnets might also call for attention.

The authors also acknowledge E. Todesco for:

- being the corresponding author of the initial 11 T dipole magnet requirements;
- contributing to the definition of the HL-LHC interaction region magnet layout and parameters;
- accompanying the Nb_3Sn technology transfer from LARP to CERN and for applying a strong filtering on any proposed change;
- coordinating, with P. Ferracin, formerly CERN, now LBNL, the short MQXFS magnet model program and the production of the first two full-length MQXFBP magnet prototypes;
- defining the HL-LHC project acceptance criteria for MQXF magnets;
- identifying, with P. Ferracin, the potential issue of mechanical coupling between stainless steel outer shell and aluminum cylinder structure in MQXF cold mass (1st stage of recovery plan);
- promoting the assembly and test of MQXFBMT4, which confirmed the issue with coil manufacture (3rd stage of recovery plan).

Arnaud Devred is much obliged to M. Sumption, Ohio State University, who induced him to write this report based on the series of seminars he gave at various institutes, universities and suppliers throughout 2023 and 2024. He is also grateful to M. Meddahi, CERN, who encouraged him to persist in the objective and comprehensive writing of the present report, as a reference for the younger generation.

References

[1] A. Devred, “Practical low-temperature superconductors for electromagnets,” CERN-2004-006, Geneva, Switzerland: CERN (2004).

[2] B. T. Matthias, T. H. Geballe, S. Geller and E. Corenzwit, “Superconductivity of Nb_3Sn,” *Phys. Rev.*, Vol. 95 No. 6, p. 1435 (1954).

[3] N. Mitchell, D. Bessette, *et al.*, “Conductor development for the ITER magnets,” *Proceedings of 15th International Magnet Technology Conference, L. Liangzhen, S. Guoliao and Y. Luguang (eds)*, pp. 347-352, Beijing, China: Science Press (1998).

[4] J.L. Duchateau, M. Spadoni, *et al.*, “Development of high-current high-field conductors in Europe for fusion application,” *Supercond. Sci. Technol.*, Vol. 15 No. 6, pp. R17-R29 (2002).

[5] R.M. Scanlan, “Conductor development for high energy physics ─ plans and status of the US program,” *IEEE Trans. Appl. Supercond.*, Vol. 11 No. 1, pp. 2150-2155 (2001).

[6] P.J. Lee and D.C. Larbalestier, “Advances in superconducting strands for accelerator magnet application,” *Proceedings of 2003 Particle Accelerator Conference, J. Chew, P. Lucas and S. Webber (eds.)*, Vol. 1, pp. 151-155, Piscataway, NJ, USA: IEEE (2003).

[7] A. Devred, B. Baudouy, *et al.*, “Status of the next European dipole (NED) activity of the collaborated accelerator research in Europe (CARE) project,” *IEEE Trans. Appl. Supercond.*, Vol. 15 No. 2, pp. 1106-1112 (2005).

[8] T. Boutboul, A. den Ouden, *et al.*, “Nb_3Sn conductor development and characterization for NED,” *Journal of Physics: Conference Series*, Vol. 97, 012211 (9pp; 2008).

[9] O. Napoly, R. Aleksan, *et. al.*, “The CARE Accelerator R&D Programme in Europe,” *Proceedings of 2005 Particle Accelerator Conference*, Vol. 1, pp. 749-751, Piscataway, NJ, USA: IEEE (2005).

[10] A. den Ouden, H.H.J. ten Kate, *et al.*, “Analysis of the mechanical behavior of an 11.5 T Nb_3Sn dipole magnet according to the ring collar concept,” *IEEE Trans. Magn.*, Vol. 26 No.1, pp. 331-334 (1992).

[11] A. den Ouden, S. Wessel, *et. al.*, “An experimental 11.5 T Nb_3Sn LHC type of dipole magnet,” *IEEE Trans. Magn.*, Vol. 30 No. 4, pp. 2320-2323 (1994).

[12] A. den Outen, S. Wessel, *et. al.*, “Application of Nb_3Sn superconductors in high-field accelerator magnets,” *IEEE Trans. Appl. Supercond.*, Vol. 7 No. 2, pp. 733-738 (1997).

[13] H.H.J. ten Kate, A. den Ouden and D. Schoerling, “The UT-CERN cos-theta LHC-Type Nb_3Sn dipole magnet,” in *Nb_3Sn Accelerator Magnets, D. Schoerling and A.V. Zlobin (eds)*, pp. 105-132, Cham, Switzerland: Springer (2019).

[14] A. den Ouden, H.H.J. ten Kate, *et al.* “Retest of MSUT at CERN,” presented at the 2022 Applied Superconductivity Conference, Honolulu, Hawaii, USA, 23-28 October 2022.

[15] A. Devred, I. Backbier, *et al.*, “Challenges and status of ITER conductor production,” *Supercond. Sci. Technol.*, Vol. 27, 044001 (39pp; 2014).

[16] A. Vostner, M. Jewell, *et al.*, “Statistical analysis of the Nb_3Sn strand production for the ITER toroidal field coils,” *Supercond. Sci. Technol.*, Vol. 30, 045004 (14 pp; 2017).

[17] T. Miyatake, Y. Murakami, *et al.*, “Influence of wire parameters on critical current versus strain characteristics of bronze processed Nb_3Sn superconducting wires,” *IEEE Trans. Appl. Supercond.*, Vol 22 No. 3, 4805005 (5pp, 2012).

[18] J.A. Parrell, Y. Zhang, *et al.*, “High field Nb_3Sn conductor development at Oxford Superconducting Technology,” *IEEE Trans. Appl. Supercond.*, Vol 13 No. 2, pp. 3470-3473 (2003).

[19] J.A. Parrell, M.B. Field, *et al.*, “Advances in Nb_3Sn strands for fusion and particle accelerator applications,” *IEEE Trans. Appl. Supercond.*, Vol 15 No. 2, pp. 1200-1204 (2005).

[20] O. Brüning and L. Rossi (eds), The High Luminosity Large Hadron Collider, Advanced Series on Directions in High Energy Physics, Vol. 24, World Scientific (2015).

[21] O. Brüning and L. Rossi (eds), The High Luminosity Large Hadron Collider –Second Edition, Advanced Series on Directions in High Energy Physics, Vol. 31, World Scientific (2024).

[22] L. D. Cooley, A. K. Ghosh, *et al.*, "Conductor specification and validation for high-luminosity LHC quadrupole magnets," *IEEE Trans. Appl. Supercond.*, Vol. 27 No. 4, 6000505 (5pp; 2017).

[23] Bruker OST, LLC, 600 Milik St, Carteret, NJ 07008, USA is a subsidiary of Bruker Energy & Supercon Technology (BEST), headquartered in Billerica, MA, USA.

[24] J. Levitan, J. Lu, *et al.*, "Verification testing of MQXFA Nb_3Sn wires procured under LARP," *IEEE Trans. Appl. Supercond.*, Vol. 29 No. 5, 6000904 (4pp; 2019).

[25] B. Bordini, A. Ballarino, *et al.*, "The bundle barrier PIT wire developed for the HiLumi LHC project," *IEEE Trans. Appl. Supercond.*, Vol. 27 No. 4, 6000706 (6pp; 2017).

[26] M. Benedikt, M. Capeans, et al. (eds), FCC-hh: The Hadron Collider, Future Circular Collider Conceptual Design Report Volume 3, The European Physics Journal, Vol. 228 No. 4 (2019).

[27] A. Ballarino and L. Bottura, "Targets for R&D on Nb_3Sn conductor for high energy physics," *IEEE Trans. Appl. Supercond.*, Vol. 25 No. 3, 6000906 (6pp; 2015).

[28] X. Xu, "A review and prospects for Nb_3Sn superconductor development," *Supercond. Sci. Technol.*, Vol. 30 No. 9, 093001 (20pp; 2017).

[29] A. Ballarino, S.C. Hopkins, *et al*, "The CERN FCC conductor development program: a worldwide effort for the future generation of high-field magnets," *IEEE Trans. Appl. Supercond.*, Vol. 29 No. 5, 6000709 (9pp; 2019).

[30] C.B. Müller and E.J. Saur, "Influence of mechanical constraints on the superconducting transition of Nb_3Sn-coated niobium wires and ribbons," *Advances in Cryogenic Engineering*, Vol. 8, pp. 574-578, Boston, MA, USA: Springer (1963).

[31] E. Buehler and H.J. Levinstein, "Effect of tensile stress on the transition temperature and current-carrying capacity of Nb_3Sn," *J. Appl. Phys.*, Vol. 36 No. 12, pp. 3856-3860 (1965).

[32] J.W. Ekin, "Strain effects in superconducting compounds," *Advances in Cryogenic Engineering Materials*, Vol. 30, pp. 823-836, Boston, MA, USA: Springer (1984).

[33] N. Cheggour, T. S. Stauffer, *et al*, "Implications of the strain irreversibility cliff on the fabrication of particle accelerator magnets made of restacked-rod process Nb_3Sn wires," *Sci. Rep.*, Vol. 9, 5466 (14 pp, 2019).

[34] D. Evans, J.T. Morgan, and G.B. Stapleton, "Epoxy resins for superconducting magnet encapsulation," RHEL/R-251, Chilton, England: Science Research Council (1972).

[35] A.B. Brennan, T.M. Miller, *et al.*, "Thermomechanical properties of a toughened epoxy for impregnating superconducting magnets*," Cryogenics,* Vol. 35 No. 11, pp. 783-785 (1995).

[36] A. Devred, "Insulation systems for Nb_3Sn accelerator magnet coils manufactured by the wind & react technique," *IEEE Trans. Appl. Supercond.*, Vol. 12 No. 1, pp. 1232-1237 (2002).

[37] W. B. Sampson, "*Superconducting magnets for beam handling and accelerators,"* BNL-11394; CONF-670705-3, Upton, NY, USA: Brookhaven National Laboratory (1967).

[38] N. Mitchell, D. Bessette, *et al.*, "The ITER magnet system,*" IEEE Trans. Appl. Supercond.*, Vol. 18 No. 2, pp. 435-440 (2008).

[39] D. Clery, *A Piece of the Sun: the Quest for Fusion Energy*, London, New York: Overlook Press (2013).

[40] A. Bonito-Oliva, P. Aprili, *et al.*, "About the first 6 toroidal field coils and 2 poloidal field coils completed by EU for ITER," *IEEE trans. Appl. Supercond.*, Vol. 32 No. 6, 4203905 (5pp; 2022).

[41] N. Koizumi, M. Nakamoto, *et al.*, "Progress of ITER TF coil fabrication in Japan," *IEEE Trans. Appl. Supercond.*, Vol. 30 No. 4, 4202106 (6pp; 2020).

[42] P. Libeyre, T. Schild, *et al.*, “From manufacture to assembly of the ITER central solenoid,” *Fusion Engineering and Design,* Vol. 146, pp. 437-440 (2019).

[43] N. Martovetsky, K. Freudenberg, *et al.*, “Testing of the ITER CS module #4,” *IEEE Trans Appl. Supercond.,* Vol. 34 No. 5, 4200206 (6pp; 2024).

[44] Y. Ilyin, F. Simon, *et al.*, “Completion and factory acceptance test of ITER PF1 coil,” *IEEE Trans Appl. Supercond.,* Vol. 34 No. 5, 4205005 (5pp.; 2024).

[45] X. Zhang, W. Wen, *et al.,* “ITER PF6 Double pancankes stacking,” *Fusion Engineering and Design,* Vol. 147, 111240 (4pp; 2019).

[46] F. Simon, Q. Hua, *et al.*, “Manufacturing and assembly of the ITER correction coils,” *IEEE Trans. Appl. Supercond.,* Vol. 34 No. 5, 4200405 (5pp; 2024).

[47] M.O. Hoenig and D.B. Montgomery, “Dense supercritical-helium cooled superconductors for large high field stabilized magnets,” *IEEE Trans. Magn.*, Vol. MAG-11 No. 2, pp. 569-572 (1975).

[48] D. Ciazynski, “Review of Nb_3Sn conductors for ITER,” *Fusion Engineering and Design,* Vol. 82, pp. 488-497 (2007).

[49] A. Devred, D. Bessette, *et al.*, “Status of conductor qualification for the ITER central solenoid,” *IEEE Trans. Appl. Supercond.,* Vol. 23 No. 3, 6001208 (8pp; 2013).

[50] T. Hemmi, Y. Nunoya, *et al.*, “Test results and investigation of T_{cs} degradation in Japanese ITER CS conductor samples,” *IEEE Trans. Appl. Supercond.,* Vol. 22 No. 3, 4803305 (5pp; 2013).

[51] G. Brumfiel, “Cable test raises fears at fusion project,” *Nature,* Vol. 471, p. 150 (2011).

[52] D. Bessette, “Design of a Nb_3Sn Cable-in-Conduit Conductor to withstand the 60 000 electromagnetic cycles of the ITER central solenoid,” *IEEE Trans. Appl. Supercond.,* Vol. 24 No. 3, 4200505 (5pp; 2014).

[53] M. Breschi, A. Devred, *et al.*, “Performance tests of ITER CS conductor samples from series production,” *Supercond. Sci. Technol.*, Vol 36, 035007 (15pp; 2023).

[54] N. Martovertsky, T. Isono, *et al.*, “ITER central solenoid insert test results,” *IEEE Trans. Appl. Supercond.*, Vol. 26 No. 4, 4200605 (5pp; 2016).

[55] N. Martovertsky, K. Freudenberg, *et al*, “Testing of the ITER Central Solenoid Modules,” *IEEE Trans. Plasma Sci.*, Vol. 50 No. 11, pp. 4292-4297 (2022).

[56] M. Breschi, A. Devred, *et al.*, “Results of the TF conductor performance qualification samples for the ITER project,” *Supercond. Sci. Technol.,* Vol 25, 095004 (17pp; 2012).

[57] M. Breschi, D. Macioce and A. Devred, “Performance analysis of the toroidal field ITER production conductors,” *Supercond. Sci. Technol.*, Vol 30, 055007 (13pp; 2017).

[58] N. Mitchell, M. Breschi and V. Tronza, "The use of Nb_3Sn in fusion: lessons learned from the ITER production including options for management of performance degradation," *Supercond. Sci. Technol.*, Vol. 33, 054007 (21pp; 2020).

[59] G. Zhuang, G.Q. Li, *et al*., “Progress of the CFETR design,” *Nuclear Fusion,* Vol. 59, 112010 (14pp; 2019).

[60] Y. Wu, Y. Shi, *et al.*, “Basic design and progress of Central Solenoid Model Coil for CFETR,” *IEEE Trans. Appl. Supercond.,* Vol. 28 No. 3, 4200205 (5pp; 2018).

[61] J.G. Qin, Y. Wu, *et al.*, “Manufacturing of Nb_3Sn sample conductor for CFETR Central Solenoid Model Coil,” *IEEE Trans. Appl. Supercond.,* Vol. 27 No. 4, 4200805 (5pp, 2017).

[62] Yu Wu, ASIPP, private communication (2025).

[63] X. Liu, F. Wu, *et al.*, “Progress in the conceptual design of the CFETR toroidal field coil with rectangular conductors,” *Nuclear Fusion,* Vol. 60, 046032 (10pp; 2020).

[64] C. Dai, Y. Wu, *et al.*, “Performance test and analysis of the first large-scale cable-in-conduit conductor with high J_c Nb_3Sn strand for fusion reactor. *Nuclear Fusion*, Vol. 61, 036044 (10pp; 2021).

[65] C. Dai, Y. Wu, *et al.*, “Conceptual design of 15 tesla conductor test facility for future fusion reactor,” *IEEE Trans. Appl. Supercond.*, Vol. 30 No. 4, 9500305 (5pp; 2020).

[66] C. Dai, Y. Wu, *et al.*, “Performance of the Cable-in-Conduit Conductor for Super-X Test Facility,” *IEEE Trans. Appl. Supercond.*, Vol. 33 No. 2, 9500105 (5pp; 2023).

[67] L. Evans (ed.), *The Large Hadron Collider: a Marvel of Technology*, Lausanne, Switzerland: EPFL Press (2009).

[68] R.N. Cahn and C. Quigg, Grace in All Simplicity: Beauty, Truth and Wonders on the Path to the Higgs Boson and New Laws of Nature, New York, NY, USA: Pegasus Book (2023).

[69] H. ten Kate, “ATLAS Superconducting toroids – the largest ever built,” *International Journal of Modern Physics,* Vol. 25 No. 15, pp. 2933-2954 (2010).

[70] A. Yamamoto, Y. Makida, *et al.*, The ATLAS central solenoid, *Nuclear Instruments and Methods in Physics Research A*, Vol. 584, pp 53-74 (2008).

[71] B. Curé, G. Le Godec, *et al.*, “Fifteen years of operation of the compact muon solenoid detector superconducting magnet,” *IEEE Trans. Appl. Supercond.*, Vol. 34 No. 5, 4500208 (8pp; 2024).

[72] L. Rossi, “Superconducting magnets for the LHC main lattice,” *IEEE Trans. Appl. Supercond.*, Vol. 14 No.2, pp 153-158 (2004).

[73] R. Ostojic, “Superconducting magnets for LHC insertion,” *IEEE Trans. Appl. Supercond.*, Vol. 14 No.2, pp 181-186 (2004).

[74] D.B. Thomas and N.M. Wilson, “Filamentary superconductors for pulsed magnets,” in *Proc. of 4th International Conference on Magnet Technology (Y. Winterbottom ed.)*, Upton, NY, USA: Brookhaven National Laboratory, pp. 493-497 (1972).

[75] A. Devred, “Superconducting magnets for particle accelerators and storage rings,” *Wiley Encyclopedia of Electrical and Electronics Engineering*, Vol. 20, pp. 743-762 (1999).

[76] S. Russenschuck, Field Computation for Accelerator Magnets: Analytical and Numerical Methods for Electromagnetic Design and Optimization, Weinheim, Germany: Wiley-VCH (2011).

[77] T. Shintomi, A. Terashima, *et al.*, “Development of large keystone angle cable for dipole magnet with ideal arch structure,” *Adv. Cryog. Eng. (Materials)*, Vol. 36(A), pp. 323– 328, 1990

[78] A. Vervweij, B. Auchmann, *et al.*, “Retraining of the 1232 main dipole magnets in the LHC,” *IEEE Trans. Appl. Supercond.*, Vol. 26 No.4, 4000705 (5 pp.; 2016).

[79] E. Todesco, G. Villering, *et al.*, “Training of the main dipole magnets in the Large Hadron Collider toward 7 TeV operation,” *IEEE Trans. Appl. Supercond.*, Vol. 28 No. 3, 4006905 (5pp; 2018).

[80] G. Ambrosio, G. Bellomo, and L. Rossi, “Study of a high gradient, large aperture, Nb_3Sn quadrupole for the low beta insertions of the LHC,” *Proceedings of 4th European Particle Accelerator Conference (EPAC 94)*, pp. 2268-2270 (1995).

[81] E. Todesco, H. Bajas, et al., “The High Luminosity LHC interaction region magnets towards series production,” *Supercond. Sci. Technol.*, Vol. 34, 053001 (38pp; 2021).

[82] S.A. Gourlay, G. Ambrosio, *et al.*, “Magnet R&D for the US LHC Accelerator Program (LARP),” *IEEE Trans. Appl. Supercond.*, Vol 16 No. 2, pp 324-327 (2006).

[83] P. Wanderer, “Overview of LARP Magnet R&D,” *IEEE Trans. Appl. Supercond.*, Vol 9 No. 3, pp 324-327 (2009).

[84] G. Ambrosio, N. Andreev, *et al.*, “Progress in the long Nb_3Sn Quadrupole R&D by LARP,” *IEEE Trans. Appl. Supercond.*, Vol. 22 No. 3, 4003804 (4pp; 2012).

[85] D. Dell'Orco, R. Scanlan, and C.E. Taylor, "Design of the Nb_3Sn dipole D20," *IEEE Trans. Appl. Supercond.*, Vol. 3 No. 1, pp. 82-86 (1993).

[86] D. Dell'Orco, R. Scanlan, *et al.*, "Fabrication and component testing results for a Nb_3Sn Dipole Magnet," *IEEE Trans. Appl. Supercond.*, Vol. 5 No. 2, pp. 1000-1003 (1995).

[87] A.D. McInturff, R.Benjegerdes, *et al.*, "Test Results for a high field (13 T) Nb_3Sn dipole," *Proceedings of. 1997 Particle Accelerator Conference, M. Comyn, M.K. Craddock, et al. (eds.)*, pp. 3212–3214, Piscataway, NJ, USA: IEEE (1998).

[88] P. Ferracin, G. Ambrosio, *et al.*, "Mechanical performance of the LARP Nb_3Sn quadrupole magnet LQS01," *IEEE Trans. Appl. Supercond.*, Vol. 21 No. 3, pp 1683-1687 (2011).

[89] G. Ambrosio, N. Andreev, *et al.*, "Test Results of the first 3.7 m long Nb_3Sn quadrupole by LARP and future plans," *IEEE Trans. Appl. Supercond.*, Vol. 21 No. 3, pp 1858-1862 (2011).

[90] E. Todesco, H. Allain, *et al.*, "A first baseline for the magnets in the high luminosity LHC insertion regions," *IEEE Trans. Appl. Supercond.*, Vol. 24 No. 3, 4003305 (5pp; 2011).

[91] G. de Rijk, A. Milanese, and E. Todesco, "11 Tesla Nb_3Sn dipoles for phase II collimation in the Large Hadron Collider," sLHC Project Note 0019, Geneva, Switzerland: CERN (2 July 2010).

[92] A.V. Zlobin, N. Andreev, *et al.*, "Design and fabrication of a single-aperture 11 T Nb_3Sn dipole magnet model for LHC upgrades," *IEEE Trans. Appl. Supercond.*, Vol. 22 No. 3, 4001705 (5pp; 2012).

[93] A.V. Zlobin, N. Andreev, *et al.*, "11-T two-in-one-aperture Nb_3Sn dipole development for LHC upgrades," *IEEE Trans. Appl. Supercond.*, Vol. 25 No. 3, 4002209 (5pp; 2015).

[94] A.V. Zlobin, "Nb_3Sn 11 T dipole for the high luminosity LHC (FNAL)," in *Nb_3Sn Accelerator Magnets, D. Schoerling and A.V. Zlobin (eds)*, pp. 193-222, Cham, Switzerland: Springer (2019).

[95] M. Karppinen, N. Andreev, *et al.*, "Design of 11 T two-in-one-aperture Nb_3Sn dipole demonstrator magnet for LHC upgrades," *IEEE Trans. Appl. Supercond.*, Vol. 22 No. 3, 4901504 (4pp; 2012).

[96] F. Savary, E. Barzi, *et al.*, "The 11 T dipole for HL-LHC: status and plan," *IEEE Trans. Appl. Supercond.*, Vol. 26 No. 4, 4005305 (5pp; 2016)

[97] B. Bordini, L. Bottura, *et al.*, "Nb_3Sn 11 T Dipole for the High Luminosity LHC (CERN)," in *Nb_3Sn Accelerator Magnets, D. Schoerling and A.V. Zlobin (eds)*, pp. 223-258, Cham, Switzerland: Springer (2019).

[98] J. Fleiter, A. Ballarino, *et al.*, "Optimization of Nb_3Sn Rutherford cables geometry for the high-luminosity LHC," *IEEE Trans. Appl. Supercond.*, Vol 27 No. 4, 4004305 (5pp, 2017).

[99] G. Willering, M. Bajko, *et al.*, "Comparison of cold powering performance of 2-m-long Nb_3Sn 11 T model magnets," *IEEE Trans. Appl. Supercond.*, Vol. 28 No. 3, 4007205 (5pp; 2018).

[100] P. Ferracin, L. Bottura, *et al.*, "Mechanical analysis of the collaring process of the 11 T dipole magnet," *IEEE Trans. Appl. Supercond.*, Vol. 29 No.5, 4002705 (5pp; 2019).

[101] S. Izquierdo-Bermudez, E. Nilsson, *et al.*, "Mechanical analysis of the Nb_3Sn 11 T dipole short models for the High Luminosity Large Hadron Collider," *Supercond. Sci. and Technol.*, Vol 32 N. 8, 085012 (18pp; 2019).

[102] J. Golm, S. Arguedas Cuendis, *et al.*, "Thin film (high temperature) superconducting radiofrequency cavities for the search of axion dark matter," *IEEE Trans. Appl. Supercond.*, Vol. 32 No. 4, 1500605 (5pp; 2022).

[103] P. Ferracin, G. Ambrosio, *et. al.*, "Magnet design of the 150-mm aperture low-β quadrupoles for the high luminosity LHC," *IEEE Trans. Appl. Supercond.*, Vol. 24 No. 3, 4002306 (6pp; 2014).

[104] J. Fleiter, A. Bonasia, *et. al.*, "Status of high-field Rutherford cable production for the HL-LHC project," presented at *the Applied Superconductivity Conference (ASC 2024), Salt-Lake City, USA,* 1-6 September 2024.

[105] S. Stoynev, G. Ambrosio, *et al.*, “Summary of test results of MQXFS1—the first short model 150 mm Aperture Nb_3Sn quadrupole for the high-luminosity LHC upgrade,” *IEEE Trans. Appl. Supercond.*, Vol. 28 No. 3, 4001705 (5pp; 2018).

[106] F. Mangiarotti, H. Bajas, *et al.*, “Test results of the CERN HL-LHC low-beta quadrupole short models MQXFS3c and MQXFS4,” *IEEE Trans. Appl. Supercond.*, Vol. 29 No. 5, 4001705 (5pp; 2019).

[107] F.-J. Mangiarotti, J. Ferradas-Troitino, *et al.*, “Powering performance and endurance beyond design Limits of HL-LHC Low-Beta quadrupole model magnets,” *IEEE Trans. Appl. Supercond.*, Vol. 31 No. 5, 4000805 (5pp; 2021).

[108] J. Muratore, K. Amm, *et al.*, “Test results of the first two full-length prototype quadrupole magnets for the LHC Hi-Lumi upgrade,” *IEEE Trans Appl. Supercond.*, Vol. 30 No. 4, 4004205 (5pp; 2020).

[109] G. Ambrosio, K. Amm, *et al.*, “Lessons Learned from the prototypes of the MQXFA low-beta quadrupoles for LHC and status of the production in the US,” *IEEE Trans. Appl. Supercond.*, Vol. 31 No. 5, 4001105 (5pp; 2021).

[110] J. Muratore, G. Ambrosio, *et al.*, Test results of the first pre-series quadrupole magnets for the LHC Hi-Lumi upgrade,” *IEEE Trans. Appl. Supercond.*, Vol. 31 No. 5, 4001804 (4pp; 2021).

[111] G. Ambrosio, K. Amm, *et al.*, “Challenges and lessons learned from fabrication, testing and analysis of eight MQXFA low beta quadrupole magnets for HL-LHC,” *IEEE Trans. Appl. Supercond.*, Vol. 33 No. 5, 4003508 (8pp; 2022).

[112] M. Baldini, G. Chlachidze, *et al., “*Quench performance of the first pre-series AUP cryo-assembly*” IEEE Trans Appl. Supercond.*, Vol. 34 No. 5, 4005204 (4pp; 2024).

[113] F.-J. Mangiarotti, G. Willering, *et al.*, “Power test of the first two HL-LHC insertion quadrupole magnets built at CERN,” *IEEE Trans. Appl. Supercond.*, Vol. 32 No. 6, 4003305 (5pp; 2022).

[114] A. Asner, C. Becquet, *et al.*, “Development and successful testing of the Nb Sn wound, in situ-reacted, high field superconducting quadrupole of CERN”, *IEEE Trans. Magn.*, Vol. MAG-19 No. 3, pp. 1410-1416 (1983).

[115] A. Asner, R. Perin, *et al.*, “First Nb_3Sn, 1 m long superconducting dipole magnet models for LHC break the 10 Tesla field threshold,” T. Sekiguchi, S. Shimamoto (eds.), *Proceedings of 11th International Conference on Magnet Technology,* Vol. 1, pp. 36-41, Dordrecht, The Netherlands: Springer (1989).

[116] R. Perin, “CERN-ELIN Nb_3Sn dipole model,” in *Nb_3Sn Accelerator Magnets, D. Schoerling and A.V. Zlobin (eds),* pp. 87-104, Cham, Switzerland: Springer (2019).

[117] A. Devred, M. Durante, *et al.*, “Development of a Nb_3Sn quadrupole magnet model,” *IEEE Trans Appl. Supercond.*, Vol. 11 No. 1, pp. 2184-2187 (2001).

[118] M. Durante, A. Devred, *et al.*, “Development and manufacturing of a Nb Sn quadrupole magnet model at CEA/Saclay for the TESLA interaction region,” *IEEE Trans Appl. Supercond.*, Vol. 14 No. 2, pp. 357-360 (2004).

[119] L. Quettier, M. Durante, *et al.*, “Manufacturing and test of a short Nb_3Sn quadrupole magnet model at CEA/Saclay,” *IEEE Trans Appl. Supercond.*, Vol. 19 No. 3, pp. 1121-1124 (2009).

[120] N. Schwerg, C. Vollinger, *et al.*, “2D Magnetic Design and Optimization of a 88-mm Aperture 15 T Dipole for NED,” *IEEE Trans Appl. Supercond.*, Vol. 17 No. 2, pp. 1043-1046 (2007).

[121] F. Toral, A. Devred, *et al.*, “Comparison of 2-D Magnetic Designs of Selected Coil Configurations for the Next European Dipole (NED),” *IEEE Trans Appl. Supercond.*, Vol. 17 No. 2, pp. 1117-1121 (2007).

[122] P. Loveridge, D.E. Baynham, *et al.*, “Mechanical Design of the Next European Dipole,” *IEEE Trans Appl. Supercond.*, Vol. 18 No. 2, pp. 1487-1490 (2008).

[123] J.H. Rochford, D.E. Baynham and A. Devred, “An Evaluation of the Helical Winding Method Applied to the Next European Dipole Project,” *IEEE Trans Appl. Supercond.*, Vol. 18 No. 2, pp. 1541-1544 (2008).

[124] D.I. Meyer and R. Flask, “A new configuration for a dipole magnet for use in high energy physics applications,” *Nuclear Instruments and Methods*, Vol. 80, pp. 339-341 (1970).

[125] B. Auchmann, D.M. Araujo *et al.*, “Test Results from CD1 short CCT Nb_3Sn dipole demonstrator and considerations about CCT technology for the FCC-Hh main dipole,” *IEEE Trans Appl. Supercond.*, Vol. 34 No. 5, 4000906 (6pp, 2024).

[126] A. Milanese, M. Devaux, *et al.*, “Design of the EuCARD high field model dipole magnet FRESCA2,” *IEEE Trans Appl. Supercond.*, Vol. 22 No. 3, 4002604 (4pp, 2012).

[127] P. Manil, B. Baudouy, *et al.*, “Development and coil fabrication test of the Nb_3Sn dipole magnet FRESCA2,” *IEEE Trans Appl. Supercond.*, Vol. 24 No. 3, 4001705 (5pp, 2014).

[128] F. Rondeaux, P. Ferracin, *et al.*, “Block-type” coils fabrication procedure for the Nb_3Sn dipole magnet FRESCA2,” *IEEE Trans Appl. Supercond.*, Vol. 26 No. 4, 4002604 (5pp, 2016).

[129] E. Rochepault, N. Bourcey, *et al.*, “Fabrication and assembly of the Nb_3Sn dipole magnet FRESCA2,” *IEEE Trans Appl. Supercond.*, Vol. 27 No. 4, 4002604 (5pp, 2017).

[130] E. Rochepault, N. Bourcey, *et al.*, “Mechanical analysis of the FRESCA2 dipole during preload, cool-down, and powering,” *IEEE Trans Appl. Supercond.*, Vol. 28 No. 3, 4002405 (5pp, 2018).

[131] N. Bourcey, A. Carlon Zurita, *et al.*, “Assembly of the Nb_3Sn dipole magnet FRESCA2,” *IEEE Trans Appl. Supercond.*, Vol. 28 No. 3, 4007505 (5pp, 2018).

[132] G. Willering, C. Petrone, *et al.*, “Cold powering tests and protection studies of the FRESCA2 100 mm bore Nb_3Sn block-coil magnet,” *IEEE Trans Appl. Supercond.*, Vol. 28 No. 3, 4005105 (5pp, 2018).

[133] R. Keijzer, G. Succi, *et al.*, “Modelling V-I measurements of Nb_3Sn accelerator magnets with conductor degradation,” *IEEE Trans. Appl. Supercond.*, Vol. 32 No. 6, 4001105 (5pp; 2022).

[134] R. Keijzer, G. Willering, *et al.*, “Effect of strand damage in Nb_3Sn Rutherford cables on the quench propagation in accelerator magnets,” *IEEE Trans. Appl. Supercond.*, Vol. 33 No. 5, 4700605 (5pp; 2023).

[135] B. Turck, “Influence of a transverse conductance on current sharing in a two-layer superconducting cable,” *Cryogenics*, Vol. 14, pp. 448-454 (1974).

[136] A.A. Akhmetov, A. Devred and T. Ogitsu, “Periodicity of crossover currents in a Rutherford-type cable subjected to a time-dependent magnetic field,” *J. Appl. Phys.*, Vol 75 No. 6, pp. 3176-3183 (1994).

[137] A. Verweij, “Modelling Boundary-Induced Coupling Currents in Rutherford-type Cables,” *IEEE Trans. Appl. Supercond.*, Vol. 7 No. 2, pp. 723-726 (1997).

[138] G. Succi, L. Bottura, *et al.*, “On the effect of strand damage on the operating margin of a Nb_3Sn Rutherford cable,” *Cryogenics*, Vol. 125, 103458 (11pp; 2022).

[139] R. Keijzer, G. Willering, *et al.*, “Effect of strand damage in Nb_3Sn Rutherford cables on the quench propagation in accelerator magnets,” *IEEE Trans. Appl. Supercond.*, Vol. 33 No. 5, 4700605 (5pp; 2023).

[140] F. Rodriguez-Matteos and F. Sonnenman, “Quench heater studies for the LHC magnets,” *Proc. of 19th IEEE Particle Acelertor Conference, Chicago, IL, USA, 18-22 June 2001*, pp. 3451-3053 (2001).

[141] S. Izquierdo-Bermudez, G. Ambrosio, *et al.*, “Overview of the quench heater performance for MQXF, the Nb_3Sn low-β quadrupole for the high luminosity LHC,” *IEEE Trans. Appl. Supercond.*, Vol. 28 No. 4, 4008406 (6pp; 2018).

[142] E. Ravaioli, V.I. Datskov, *et al.*, "New, Coupling Loss Induced, Quench Protection System for Superconducting Accelerator Magnets," *IEEE Trans. Appl. Supercond.*, Vol. 24 No. 3, 0500905 (5pp; 2014).

[143] G.A. Kirby, B. Auchmann, *et al.*, "LHC IR upgrade Nb–Ti, 120-mm aperture model quadrupole test results at 1.8 K," *IEEE Trans. Appl. Supercond.*, Vol. 24 No. 3, 4002405 (5pp; 2014).

[144] E. Ravaioli, G. Ambrosio, *et al.*, "Quench protection performance measurements in the first MQXF magnet models," *IEEE Trans. Appl. Supercond.*, Vol. 28 No. 3, 4701606 (6pp; 2018).

[145] E. Ravaioli, G. Ambrosio, *et al.*, "Quench protection of the first 4-m-long prototype of the HL-LHC Nb_3Sn quadrupole magnet," *IEEE Trans. Appl. Supercond.*, Vol. 29 No. 5, 4701405 (5pp; 2019).

[146] D. Leroy, J. Krzywinski, *et al.*, "Quench observation in LHC superconducting one-meter-long dipole models by field perturbation measurements," *IEEE Trans. Appl. Supercond.*, Vol. 3 No. 1, pp. 781-784 (1993).

[147] T. Ogitsu, A. Devred, *et al.*, "Quench antenna for superconducting accelerator magnets," *IEEE Trans. Mag.*, Vol. 30 No. 4, pp. 2273-2276 (1994).

[148] G. Morgan, "Stationary coil for measuring the harmonics in pulsed transport magnets," *Proc. of 4th Int. Conf. on Mag. Tech., Brookhaven National Laboratory, Upton, NY, USA, 19-22 September 1972,* pp. 787-790 (1972).

[149] T. Ogitsu, A. Terashima, *et al.*, "Quench antennas for RHIC quadrupole magnets," *Proc. of the 1995 Particle Accelerator Conference, 1-5 May 1995, Dallas, TX, USA,* pp 1390-1392 (1995).

[150] F. Simon, C. Gourdin, *et al.*, "Test results of the third LHC main quadrupole magnet prototype at CEA/Saclay," *IEEE Trans. Appl. Supercond.*, Vol. 12 No. 1, pp. 266-269 (2002).

[151] J. DiMarco, G. Chlachidze, *et al*, "Application of PCB and FDM technologies to magnetic measurement probe system, development," *IEEE Trans. Appl. Supercond.*, Vol. 23 No. 3, 9000505 (5pp; 2013).

[152] J. DiMarco, G. Ambrosio, *et al*, "A full-length quench antenna array for MQXFA production series quadrupole magnet testing," *IEEE Trans. Appl. Supercond.*, Vol. 31 No. 5, 9500705 (5pp; 2021).

[153] P. Rogacki, L. Fiscarelli, *et al.*, "Measurement of fast transient in Nb_3Sn magnets by using a static harmonic coil," presented at *the Applied Superconducting Conference (ASC 2024),* Salt Lake City, UT, USA, 1-6 September 2024.

[154] D. Arbelaez, R. Teyber, *et al.*, "Training-free demonstration of a 5.4 T Nb_3Sn Canted-Cosine-Theta accelerator dipole impregnated with paraffin wax," *Supercond. Sci. Technol.*, Vol. 37, 065015 (9pp, 2024).

[155] D. Tommasini, "Dielectric insulation and high voltage issues," *Proceedings of CERN Accelerator School on Magnets, Bruges, Belgium,* D. Brandt (ed.); CERN-2010-004, pp. 335-355, Geneva, Switzerland: CERN (2010).

[156] C. Scheuerlein, J. Osuna, *et al.*, "Dielectric, thermal and mechanical properties of insulation systems for quench heaters for the protection of superconducting magnets," presented at *29th International Cryogenic Engineering Conference/International Cryogenics Material Conference, Geneva, Switzerland., 22-26 July 2024.*

[157] J. Gerhold, "Dielectric breakdown of helium at low temperatures," *Cryogenics*, pp. 370-376 (1972).

[158] E. Kuffel, W.S. Zaengl, and P. Hammond, *High Voltage Engineering: Fundamentals (Second Edition),* Oxford, England: Newnes, p. 281ff. (2000).

[159] K.T.A.L. Burn, "Calculation of the Townsend Discharge Coefficients and the Paschen Curve Coefficients," *Contrib. Plasma Phys.*, Vol. 47 No. 3, pp. 177-188 (2007).

[160] R. Massarczyk, P. Chu, *et al.*, "Paschen's law studies in cold gases," *Journal of Instrumentation,* Vol. 12, P06019 (12pp, 2017).

[161] W. Paschen, "Ueber die zum Funkenübergang in Luft, Wasserstoff und Kohlensäure beu verschiedenen Drucken erforderliche Potentialdifferenz," *Annalen der Physik,* Vol. 273, No. 5, pp 69-96 (1889).

[162] G. Wind, "Paschen curve for air," *Electra,* Vol. 32, pp. 70-74 (1974).

[163] J. Gerhold and T.W. Dawkin, "Paschen curve for Helium," *Electra,* Vol. 52, pp. 80-86 (1977).

[164] T.W. Dawkin, "Paschen curve for Nitrogen," *Electra,* Vol. 32, pp. 64-70 (1974).

[165] A.J. Dekker, "Secondary electron emission," *Solid State Physics,* Vol. 6, pp. 251– 311 (1958).

[166] H. Bajas, formerly CERN, now GSI, private communication, 2016.

[167] M.D. Grosso Xavier, J. Schundelmeier, *et al.*, "Transient heat transfer in superfluid helium cooled Nb_3Sn superconducting coil samples," *IEEE Trans Appl. Supercond.*, Vol. 29 No. 5 9500105, (5 pp, 2019).

[168] T. Catalao da Rosa and M.J. Bednarek, "Electrical design criteria for the HL-LHC 11 T dipole," HL-LHC Engineering Specification (EDMS: 1995595); Geneva, Switzerland: CERN (2020).

[169] M. Bednarek, F. Rodriguez Mateos, ""Electrical design criteria for the HL-LHC 11 T inner triplet magnets," HL-LHC Engineering Specification (EDMS: 1963398); Geneva, Switzerland: CERN (2024).

[170] ANSI/EASA Standard AR100-2020: Recommended Practice for the Repair of Rotating Electrical Apparatus, pp. 19-20, Saint Louis, MO, USA: EASA (2020).

[171] G.F. Snitchak, J.G. Cottingham and G.L. Ganetis, "Electrical Insulation requirements and test procedures for SSC dipole magnets, *Supercollider 2,* M, McAshan (ed.), pp. 397-404, New York, NY, USA: Plenum Press (1990).

[172] ITER Magnet Superconducting and Electrical Design Criteria (IDM ITER_D_22GRQH), p. 64ff., Saint Paul-lez-Durance, France: ITER (2009).

[173] F. Rodriguez Matteos, "Voltage withstand levels for electrical insulation tests on components and bus bar cross sections for the different LHC machine circuits," LHC Project Document LHC-PM-ES-0001 (EDMS 90327); Geneva, Switzerland (2004).

[174] A. Ballarino, CERN, private communication.

[175] K.-H. Mess, formerly DESY and CERN, private communication, 2004.

[176] A. Kotarba, M. Bednarek, *et al.*, "Electrical quality assurance of the superconducting circuits during LHC machine assembly," *Proc. of 11th European Particle Accelerator Conference (EPAC'08),* Genova, Italy, pp. 2440-2442 (23-27 June 2008).

[177] P. Lebrun, *et al.*, "Report of the Task Force on the incident on 19 September 2008 at the LHC," LHC Project Report 1168, Geneva, Switzerland: CERN, 31 March 2009.

[178] A. Kotarba, P. Jurkiewicz, *et al.*, "Automatic measurement system for electrical verification of the LHC superconducting circuits," *Proc. of 2011 International Particle Accelerator Conference (IPAC'11),* pp. 1756-1758, San Sebastián, Spain (4-9 September 2011).

[179] M. Bednarek and J. Ludwin, "Software tools for electrical quality assure in the LHC," *Proceedings of 13th International Conference on Accelerator and Large Experimental Physics Control Systems (ICALEPS2011),* pp. 993-995, Grenoble, France, 10-14 October 2011.

[180] J. Ludwin and P. Jurkiewicz, "Upgrade of the automatic measurement system for the electrical verification of the LHC superconducting circuits," *IEEE Trans. Appl. Supercond.*, Vol. 26 No. 3, 0600803 (5pp; 2016).

[181] J. Ludwin, M. Bednarek, and T. Catalo da Rosa, "New measurement techniques used for the electrical quality assurance of HL-LHC superconducting magnets," *IEEE Trans. Appl. Supercond.*, Vol. 34 No. 5, 9001205 (3pp; 2024).

[182] P.A. Komorowski, “Time domain reflectometry for the localization of electrical faults in the instrumentation of the LHC string magnets,” LHC Project Note 181, Geneva, Switzerland: CERN, 19 February 1999.

[183] R. Stiening, R. Flora, *et al.*, “A superconducting synchrotron power supply and quench protection scheme, *IEEE Trans. Magn.*, Vol. MAG-15 No. 1, pp. 670-672 (1979).

[184] P.S. Martin, “Design and operation of the quench protection system for the Fermilab Tevatron,” *AIP Conf. Proc.*, Vol. 184, pp. 2073-2097 (1989).

[185] K.-H. Mess, P. Schmüser and S. Wolf, *Superconducting Accelerator Magnets*, World Scientific, p. 129ff. (1996).

[186] G. Ganetis and A. Prodell, “Results using active quench protection strip heaters on a reference design D SSC dipole magnet,” *IEEE Trans. Magn.*, Vol. MAG-23 No. 2, pp. 499-502 (1987).

[187] C. Haddock, R. Jayakumar, *et al*, “SSC dipole magnet quench protection heater test results,” *Proc. of 1991 IEEE Particle Accelerator Conference (PAC 91)*, San Francisco, CA-USA, 6-9 May 1991.

[188] Z. Charifoulline, L. Bortot, *et al.*, “Overview of the performance of quench heaters for high current LHC superconducting magnets,” *IEEE Trans. Appl. Supercond.*, Vol. 27 No. 4, 4700405 (5pp; 2017).

[189] R. Rodriguez-Matteos, “Technical specification of quench heaters for the series LHC superconducting main dipole magnets,” LHC Project Document: LHC-DQH-CI-0004 (EDMS 316296), Geneva, Switzerland: CERN, June 2001.

[190] C. Scheuerlein, R. De Oliveira, *et al.*, “Quench heater technology for HL-LHC superconducting accelerator magnets,” *IEEE Trans. Appl. Supercond.*, Vol. 34 No. 5, 4701105 (5pp; 2024).

[191] GTS Flexible Materials Ltd, Unit 41, Rassau Industrial Estate, Ebbw Vale, NP23 5SD, United Kingdom

[192] S. Izquierdo-Bermudez, CERN, private communication (2019).

[193] V. Marinozzi, G. Ambrosio, *et al.*, “Study of the heater-coil electrical insulation for the HL-LHC low beta quadrupoles,” *IEEE Trans. Appl. Supercond.*, Vol. 31 No. 5, 4001705 (5pp; 2021).

[194] S. Izquierdo-Bermudez, E. Todesco and D. Tommasini, “HL-LHC decision management: modification of quench heater design layout in MQXFB,” LHC-MCBRD-ED-0002 (EDMS 2646046), 28 November 2021.

[195] D. Bozzini, “The standard instrumentation feedthrough system for the LHC cryo-magnets,” *IEEE Trans. Appl. Supercond.*, Vol. 12 No. 1, pp. 1269-1271, 8400406 (6pp; 2002).

[196] M.C. Jewell, P.J. Lee and D.C. Larbalestier, “The influence of Nb_3Sn strand geometry on filament breakage under bend strain as revealed by metallography,” *Supercond. Sci. Technol.*, Vol 16, pp. 1005-1011 (2003).

[197] C. Sanabria, P.J. Lee, *et al*, “Evidence that filament fracture occurs in an ITER toroidal field conductor after cyclic Lorentz force loading in SULTAN,” *Supercond. Sci. Technol.*, Vol 25, 075007 (11pp; 2012).

[198] M.K. Sheth, P.J. Lee, *et al*, “Study of filament cracking under uniaxial repeated loading for ITER strands,” *IEEE Trans. Appl. Supercond.*, Vol. 22 No. 3, 4802504 (4pp; 2013).

[199] C. Sanabria, P.J. Lee, *et al*, “Metallographic autopsies of full-scale ITER prototype cable-in-conduit conductors after full testing in SULTAN: 1. The mechanical role of copper strands in a CICC,” *Supercond. Sci. Technol.*, Vol 28, 085500 (13pp; 2015).

[200] C. Sanabria, P.J. Lee, *et al.*, “Metallographic autopsies of full-scale ITER prototype cable-in-conduit conductors after full cyclic testing in SULTAN: II. Significant reduction of strand movement and strand damage in short twist pitch CICCs,” *Supercond. Sci. Technol.*, Vol 28, 125003 (11pp; 2015).

[201] C. Sanabria, P.J. Lee, *et al.*, "Metallographic autopsies of full-scale ITER prototype cable-in-conduit conductors after full cyclic testing in SULTAN: III. The importance of strand surface roughness in long twist pitch conductors," *Supercond. Sci. Technol.*, Vol 29, 074002 (8pp; 2016).

[202] S. Balachandran, J. Copper, *et al.*, "Metallographic analysis of 11 T dipole coils for High Luminosity-Large Hadron Collider (HL-LHC)," *Supercond. Sci. Technol.*, Vol. 34, 025001 (9pp; 2021).

[203] I. Aviles-Santillana, S. Sgobba, *et al.*, "Advanced examination of Nb_3Sn coils and conductors for the LHC Luminosity Upgrade: a methodology based on computed tomography and materialographic Analyses," *Supercond. Sci. Technol.*, Vol. 37, 085007 (14pp, 2024).

[204] A. Moros, M.-D. Crouvizier, *et al.*, "A metallurgical inspection method to assess the damage in performance-limiting Nb_3Sn accelerator magnet coils," *IEEE Trans. Appl. Supercond.*, Vol. 33 No. 5, 4000208 (8pp; 2023).

[205] W. Sun, D.R. Symes, *et al.*, "Review of high-energy X-ray computed tomography for non-destructive dimensional metrology of large metallic advanced manufactured component," *Rep. Prog. Phys.*, Vol. 85, 016102 (39pp; (2022).

[206] Diondo GmbH, Ruhrallee 14, 45525 Hattingen Germany, info@diondo.com

[207] K. Puthran, C. Bart, *et al.*, "Onset of mechanical degradation due to transverse compressive stress in Nb_3Sn Rutherford-type cables," *IEEE Trans. Appl. Supercond.*, Vol. 33 No. 5, 8400406 (6pp; 2023).

[208] G. Lenoir, K. Puthran, *et al.*, "Effect of transverse compressive stress applied at room temperature on Nb_3Sn Rutherford cables," *Supercond. Sci. Technol.*, Vol. 37, 025013 (2024).

[209] F.J. Mangiarotti, S Izquierdo Bermudez, *et al*, Performance of a HL-LHC Nb_3Sn quadrupole magnet in the 100–200 MPa range of azimuthal prestress," *IEEE Trans. Appl. Supercond.*, Vol. 35 No. 5, 4000307 (7pp, 2025).

[210] F. Savary (ed.),"11 T Dipole Phase 1 Investigation Report," CERN-TE-MSC Internal Note 2024-19 (EDMS: 3203548), Geneva, Switzerland: CERN (2024).

[211] GE Steam Power France, 141, rue Rateau 93126 La Courneuve Cedex, France.

[212] A. Devred, T. Bush, et *al.*, "About the mechanics of SSC dipole magnet prototypes," *AIP Conference Proceedings*, No. 249(2), pp. 1309-1374 (1992).

[213] T. Ogitsu and A. Devred, "Influence of azimuthal coil size variations on magnetic field harmonics of superconducting particle accelerator magnets," *Rev. Sci. Instrum.*, Vol. 65 No. 6, pp. 1998–2005 (1994).

[214] P. Ferracin, W. Scandale, et *al.*, "Azimuthal coil size and field quality in the main CERN Large Hadron Collider dipoles," *Physical Review Special Topics – Accelerator and Beams*, Vol. 5, 062401 (8pp.; 2002).

[215] D. Pulikowski, A. Devred, *et al.*, "Analysis of geometry and of field quality along the series production of the 11 T dipole for the High Luminosity LHC," *IEEE Trans. Appl. Supercond.*, Vol. 31 No. 5, 4001006 (6pp; 2021).

[216] J. Ferradas Troitino, P. Bestmann, *et al.*, "Applied metrology in the production of superconducting model magnets for particle accelerators," *IEEE Trans. Appl. Supercond.*, Vol. 28 No. 3, 4002106 (6pp; 2018).

[217] J.-L. Rudeiros Ferńandez, D. Pulikowski, *et al.*, "The collaring of the 11 T dipole – the series production," TE-MSC Technical Note 2020-55 (EDMS: 2747007); Geneva: CERN (January 2020).

[218] L. Bottura, CERN, private communication (2018).

[219] COMSOL Multiphysics® is a general-purpose simulation software developed and commercialized by COMSOL AB, Stockholm, Sweden, www.comsol.com.

[220] C. Garion and M. Morrone, “3D Thermal Behavior of the 11 T Cold Mass During Cooldown and Mechanical Considerations,” Engineering Document TE-VSC (EDMS: 2748358); Geneva: CERN (2 October 2022).

[221] C. Garion and M. Morrone, “3D Mechanical Behavior of the 11 T Cold Mass at Cryogenic Temperature,” Engineering Document TE-VSC (EDMS 2643402 V5); Geneva: CERN (24 June 2022).

[222] C. Garion and M. Morrone, “Mitigation Solution on the 11 T Magnet,” Engineering Document TE-VSC (EDMS 2748361 V1.0); Geneva: CERN (22 June 2022).

[223] S. Sgobba, F. Savary, *et al.*, “A powder metallurgy austenitic steel for application at very low temperatures,” *Proceedings. of the 2000 Powder Metallurgy World Congress*, *Kyoto*, *Japan*, Vol. 2, pp. 1002-1005 (12-16 November 2000).

[224] C. Scheuerlein, F. Lackner, *et al*., “Thermomechanical behavior of the HL-LHC 11 Tesla Nb_3Sn magnet coil constituents during reaction heat treatment,” *IEEE Trans. Appl. Supercond.*, Vol. 28 No. 3, 4003806 (6 pp, 2018).

[225] J.P. Arnaud, “Inox 316LN – SPT1 – LX15/TX15, Thermal expansion,” Note SBT/CT14-47, Grenoble, France: CEA (2017).

[226] S.S. Lee, U.-S. Min, *et al.*, Elastic constants determination of thin cold-rolled stainless steels by dynamic elastic modulus measurements,” *J. of Materials Science*, Vol. 33, pp. 687-692 (1998) and H.M. Ledbetter, “Stainless-steel elastic constants at low temperatures,” *J. Appl. Phys.*, Vol. 52, pp. 1587-1589 (1981).

[227] R.J. Corrucini and J.J. Gniewek, “Thermal expansion of technical solids at low temperatures: a compilation from the literature,” National Bureau of Standards Monograph 29; Washington, DC: US Department of Commerce (19 May 1961).

[228] F. Bertinelli, S. Comel, *et al.*, “Production of low-carbon magnetic steel for the LHC superconducting dipole and quadrupole magnets,” *IEEE Trans. Appl. Supercond.*, Vol. 16 No. 2, pp. 1777-1781 (2006).

[229] Y. Ozaki, O. Furukimi, *et al.*, “Development of non-magnetic high manganese cryogenic steel for the construction of LHC project’s superconducting magnet,” *IEEE Trans. Appl. Supercond.*, Vol. 12 No. 1, pp. 1248-1251 (2002).

[230] F. Bertinelli, F. Fudanoki, *et al.*, “Production of austenitic steel for the LHC superconducting dipole magnets,” *IEEE Trans. Appl. Supercond.*, Vol. 16 No. 2, pp. 1773-1776 (2006).

[231] RMI Titatnium Co, 1000 Warren Avenue, Niles, OH-44446, USA and P. Bradley, R. Radebaugh and G. Hardin, “Cryogenic Technology Resources,” NIST/Material Measurement Laboratory/Applied Chemicals and Materials Division; http://cryogenics.nist.gov/.

[232] C. Scheuerlein, F. Lackner, *et al.*, “Mechanical properties of the HL-LHC 11 T Nb_3Sn magnet constituent materials,” *IEEE Trans Appl. Supercond.*, Vol. 27 No. 4, 4003007 (7pp; 2017).

[233] J.P. Arnaud, “ODS Copper Discup C3/30, Thermal expansion,” Note SBT/CT12-28, Grenoble, France: CEA (2012).

[234] F. Wolf, F. Lackner, *et al.*, “Effect of epoxy volume fraction on the stiffness of Nb_3Sn Rutherford cable stacks,” *IEEE Trans Appl. Supercond.*, Vol. 29 No. 5, 8401006 (6pp; 2019).

[235] R. Kriboo, F.M. Ten Broeke and T. Koettig, “Interferometric measurement of the low-temperature thermal expansion of impregnated Nb_3Sn 11 Tesla dipole magnet coils: dilatation of impregnated coil samples,” TE-CRG Measurement Report (EDMS 2682827), Geneva, Switzerland: CERN (November 2019).

[236] O. Sacristán de Frutos, “11 T mechanical testing: saddle G11 compression modulus test, dipole coil-head compression test,” power point presentation (EDMS: 2447618); Geneva, Switzerland: CERN (2021).

[237] M.B. Kasen, G.R. MacDonald, *et al.*, "Mechanical, electrical, and thermal characterization of G-10CR and G-11CR glass cloth/epoxy laminates between room temperature and 4 K," in *Advances in Cryogenic Engineering*, Vol. 26, pp. 235-244 (1980).

[238] L. Dufay-Chanat, "Mesure de la contraction thermique d'échantillons en G11," Cryolab Note (EDMS 2506405) ; Geneva, Switzerland: CERN (2021).

[239] A. Brem, B.J. Gold, *et al.*, "Elasticity, plasticity and fracture toughness at ambient and cryogenic temperatures of epoxy systems used for the impregnation of high-field superconducting magnets," *Cryogenics*, Vol. 115, 103260 (11 pp; 2021).

[240] M. Davidson, S. Bastian, and M. Finley, "Measurement of the elastic modulus of Kapton perpendicular to the plane of the film at room and cryogenic temperatures," *Supercollider 4*, pp. 1039-1045; New Yor, NY: Plenum Press (1992).

[241] G. Kirby, V.-I. Datskov, *et al.*, "Thermal contraction, experimental data and fits for the thermal contraction of future magnet materials at cryogenic temperature; TE-MSC Internal Note: 2016-01 (EDMS: 1576936); Geneva: CERN (1976).

[242] S. Russenschuck, ROXIE: Routine for the optimization of magnet X-sections, inverse field computation and coil end design, CERN-99-01, Geneva, Switzerland: CERN (1999); roxie.docs.cern.ch

[243] E. Farina, P. Fessia, *et al.*, "Development and manufacture of the coil end spacers of the LHC pre-series dipoles," *IEEE Trans. Appl. Supercond.*, Vol. 12 No. 1, pp. 1496-1500 4004611 (2002).

[244] M. Modena, M. Bajko, *et al* "Status of the LHC main dipole pre-series production," *Proceedings of 2003 Particle Accelerator Conference, J. Chew, P. Lucas and S. Webber (eds.),* Vol. 3, pp. 1942-1944, Piscataway, NJ, USA: IEEE (2003).

[245] B. Auchmann and D. Smekens, "11T mechanical endspacer design," private communication, 22 October 2012.

[246] A. Bertarelli, M. Guinchard, *et al.*, "A combined testing and modelling methodology for the mechanics of high-field superconducting magnets," *IEEE Trans. Appl. Supercond.*, Vol. 34 No. 5, 4004611 (11pp, 2024).

[247] D. Mergelkuhl, and K. Nikolitsas, "11 T dipole magnet coil metrology at cold and thermal contraction," Measurement Report BE-GM (EDMS 2514262); Geneva, Switzerland: CERN (11 February 2021).

[248] E. Gautheron, B. Bordini, *et al.*, "Pre-load studies on a 2-m long Nb_3Sn 11 T model magnet for the High Luminosity upgrade of the LHC," *IEEE Trans. Appl. Supercond.*, Vol. 31 No. 5, 4002606 (6pp, 2021).

[249] C.L. Goodzeit, M.D. Anerella and G.L. Ganetis, "Measurements of internal forces in superconducting accelerator magnets with strain gauge transducers," *IEEE Trans. Magn.*, Vol. 25 No. 2, pp. 1463-1468 (1989).

[250] N. Siegel, D. Tommasini and I. Vanenkov, "Design and use of capacitive force transducers for superconducting magnet models for the LHC", *Proceedings of 15th International Magnet Technology Conference, L. Liangzhen, S. Guoliao and Y. Luguang (eds)*, pp. 1458-1461, Beijing: Science Press (1998).

[251] L. Vieillard, B. Gallet, *et al.*, "Capacitive force sensors for prestress in accelerator magnet coils," *Advances in Cryogenic Engineering*, Vol. 45B, pp. 1857-1863 (2000).

[252] J. Ahlbäck, J. Ikäheimo, *et al.*, "Electromagnetic and mechanical design of a 56 mm aperture model dipole for the LHC," *IEEE Trans. Magn.*, Vol. 30 No. 4, pp. 1746–1749, 1994.

[253] J. Ahlbäck, D. Leroy, *et al.*, "Construction of a 56 mm aperture high-field two-in-one-aperture superconducting dipole magnet," *IEEE Trans. Magn.*, Vol. 32 No. 4, pp. 2097–2100, 1996.

[254] D. Leroy, L. Oberli, *et al.*, “Design features and performance of a 10 T two-in-one aperture model dipole for LHC.” In L. Lianghzhen, S. Guoliao and Y. Lugang (eds.), *Proc. of Fifteenth International Conference on Magnet Technology (MT 15)*, Beijing, People’s Republic of China: Science Press, pp. 119–122, 1998.

[255] D. Leroy, G. Spigo, *et al.*, “Design and manufacture of a large-bore 10 T superconducting dipole for the CERN cable test facility,” *IEEE Trans. Appl. Supercond.*, Vol. 10 No. 1, pp. 178–182, 2000.

[256] A. Verweij, “The 10 T Dipole Magnet of the FRESCA Facility: an overview of 6 years of operation,” AT-MAS Internal Note 2005-04 (EDMS: 677510): Geneva: CERN (November 2005).

[257] C. Abad Cabrera, D. Perini, *et al.*, “Construction and analysis of a modified Nb_3Sn, 11 Tesla, short dipole magnet,” *IEEE Trans Appl. Supercond.*, Vol. 35 No. 5, 4001407 (7pp, 2025).

[258] S. Izquierdo Bermudez, G. Ambrosio, *et al.*, “Status of the MQXFB Nb_3Sn quadrupoles for the HL-LHC,” *IEEE Trans. Appl. Supercond.*, Vol. 33 No. 5, 4001209 (9pp; 2023).

[259] M. Peyrot, J.M. Rifflet, *et al.*, “Construction of the new prototype of main quadrupole cold masses for the arc short straight section of LHC,” *IEEE Trans. Appl. Supercond.*, Vol. 10 No. 1, pp. 170-173 (2000).

[260] H. Prin, J. Axensalva, *et al.*, “First CERN cold masses for the HL-LHC Interaction Regions,” *IEEE Trans. Appl. Supercond.*, Vol. 34 No. 5, 4004805 (5pp; 2024).

[261] S. Izquierdo-Bermudez, G. Ambrosio, *et al.*, “Status and challenges in the MQXFB Nb_3Sn quadrupoles for the HL-LHC,” *IEEE Trans. Appl. Supercond.*, Vol. 35 No. 5, 4002107 (7pp; 2025).

[262] E. Takala, L. Bianchi, *et al.*, “On the mechanics of MQXFB–the low-beta quadrupole for the HL-LHC,” *Supercond. Sci. Technol.*, Vol. 34, 095002 (20pp; 2021).

[263] J. Ferradas Troitino, G. Ambrosio, *et al.*, “Optimizing the use of pressurized bladders for the assembly of HL-LHC MQXFB magnets,” *Supercond. Sci. Technol.*, Vol. 36, 065002 (17pp; 2023).

[264] N. Bourcey, CERN, private communication (2021).

[265] E. Gautheron, B. Bordini, *et al.*, “Assembly and test results of the RMM1a,b magnet, a CERN technology demonstrator towards Nb_3Sn ultimate performance,” *IEEE Trans. Appl. Supercond.*, Vol. 33 No. 5, pp. 4004108 (8pp; 2023).

[266] J.-M. Rey, M. Arnaud, *et al.*, “Cold mass integration of the ATLAS barrel toroid magnets at CERN,” *IEEE Trans. Appl. Supercond.*, Vol. 16 No. 2, pp. 553-556 (2006).

[267] S. Caspi, S. Gourlay, *et al.*, “The use of pressurized bladders for stress control of superconducting magnets,” *IEEE Trans. Appl. Supercond.*, Vol 11 No. 1, pp. 2272-2275 (2001).

[268] R.R. Hafalia, P.A. Bish, *et al.*, “A new support structure for high field magnets,” *IEEE Trans. Appl. Supercond.*, Vol. 12 No. 1, pp. 47-50 (2002).

[269] E. Todesco, private communication (2022).

[270] P. Fessia, D. Perini, *et al.*, “Comparative study of different designs of the mechanical structure for the LHC main dipoles,” LHC-Project Note 288, Geneva: CERN (2002).

[271] L. Muzzi, G. de Marzi, *et al.*, “Cable-in-Conduit conductors: lessons from the recent past for future developments with low and high temperature superconductors,” *Supercond. Sci. Technol.*, Vol. 28, 052001 (25pp; 2015).

[272] E.F. Holik, G. Ambrosio, *et al.*, “Fabrication and analysis of 150-mm-aperture Nb_3Sn MQXF coils,” *IEEE Trans. Appl. Supercond.*, Vol. 26 No. 4, 4000907 (7 pp, 2016).

[273] Composite Technology Development, Inc., 2600 Campus Drive, Suite D, Lafayette, CO 80026, USA.

[274] F. Borgnolutti, G. Ambrosio, *et al.*, “Fabrication of a second-generation of Nb_3Sn coils for the LARP HQ02 quadrupole magnet,” *IEEE Trans. Appl. Supercond.*, Vol. 24 No. 3, 4003005 (5 pp, 2014).

[275] C. Scheuerlein, CERN, private communication (2022).

[276] C. Sanabria, M. Field, *et al.*, “Controlling Cu–Sn mixing so as to enable higher critical current densities in RRP® Nb_3Sn wires,” *Supercond. Sci. Technol.*, Vol. 31, 0640011 (13 pp; 2018).

[277] M. T. Naus, P.J. Lee and D. Larbalestier, “The influence of the starting Cu–Sn phase on the superconducting properties of subsequently reacted internal-tin Nb_3Sn conductors,” *IEEE Trans. Appl. Supercond.*, Vol. 11 No. 1, pp. 3569-3572 (2001).

[278] J. Lachmann, M.J. Kriegel, *et al.*, “Thermodynamic remodeling of the Cu–Nb–Sn system: Integrating the nausite phase,” *Computer Coupling of Phase Diagrams and Thermochemistry*, Vol. 77, 102409 (pp.13; 2022).

[279] I. Pong, L.R. Oberli and L. Bottura, “Cu diffusion in Nb_3Sn internal tin superconductors during heat treatment,” *Supercond. Sci. Technol.*, Vol. 26, 105002 (10pp; 2013).

[280] C. Scheuerlein, J. Andrieux, *et al.*, “Effect of the fabrication route on the phase and volume changes during the reaction heat treatment of Nb_3Sn superconducting wires,” *Supercond. Sci. Technol.*, Vol. 33, 034004 (13pp, 2020).

[281] A.K. Ghosh, L.D. Cooley, *et al.*, Effects of reaction temperature and alloying on performance of restack-rod-process,” *IEEE Trans. Appl. Supercond.*, Vol. 17 No. 2, pp. 2623-2626 (2007).

[282] C. Tarantini, P.J. Lee, *et al.*, “Examination of the trade-off between intrinsic and extrinsic properties in the optimization of modern internal tin Nb_3Sn conductor,” *Supercond. Sci. Technol.*, Vol. 27, 065013 (20 pp; 2014).

[283] S.C. Hopkins, A. Baskys, *et al.*, “Phase evolution during heat treatment of Nb_3Sn wires under development for the FCC study,” *IEEE Trans. Appl. Supercond.*, Vol. 31 No. 5, 6000706 (6 pp, 2021).

[284] M. Michels, F. Lackner, *et al.*, “Length Changes of Unconfined Nb3Sn Rutherford Cables During Reaction Heat Treatment,” *IEEE Trans. Appl. Supercond.*, Vol. 29 No. 5, 6000605 (5 pp, 2019).

[285] D. R. Dietderich, J. R. Litty, and R. M. Scanlan, “Dimensional changes of Nb_3Sn, Nb_3Al and $Bi_2Sr_2CaCu_2O_8$ conductors during heat treatment and their implication for coil design,” *Adv. Cryogenic Eng.*, Vol. 44, pp. 1013–1020 (1998).

[286] N. Andreev, E. Barzi, *et al.*, “Volume expansion of Nb-Sn strands and cables during heat treatment,” *Advances in Cryoenic Engineering (B. Balachandran et al., eds.)*, Vol. 48, pp. 941-948 (2002).

[287] E. Rochepault, P. Ferracin, *et al.*, “Dimensional changes of Nb_3Sn Rutherford cables during heat treatment,” *IEEE Trans. Appl. Supercond.*, Vol. 26 No. 4, 4802605 (5 pp, 2016).

[288] M. Durante, L. Garcia Fajardo, *et al.*, “Geometrical behavior of Nb_3Sn cables during heat treatment,” *IEEE Trans. Appl. Supercond.*, Vol. 26 No. 4, 4802705 (5 pp, 2016).

[289] R. Bossert, S. Krave, *et al.*, “Recent progress and tests of radiation resistant impregnation materials for Nb_3Sn coils,” *AIP Conf. Proc.*, Vol. 1574, pp. 132–139 (2014).

[290] P.E. Fabian, N.A. Munsch and R.J. Denis, “highly radiation-resistant vacuum impregnation resin for fusion magnet insulation,” AIP Conf. Proc., Vol. 614, pp. 295-304 (2002).

[291] CDT-101K Epoxy Resin System Data Sheet, Lafayette, CO, USA: CTD (2014).

[292] A. Gaarud, C. Scheuerlein, *et al.*, “Fracture toughness, radiation hardness, and processibility of polymers for superconducting magnets,” *Polymers*, Vol. 16, 1287 (17pp; 2024).

[293] D. Evans, J. Knaster and H. Rajainmäki, “Vaccum pressure proceess in superconducting coils: best practice,” *IEEE Trans. Appl. Supercond.*, Vol. 22 No. 3, 4202805 (5 pp; 2012).

[294] J. Axensalva, F. Lackner and R. Gauthier, “Vacuum impregnation setup at CERN for Nb_3Sn coils,” *IEEE Trans. Appl. Supercond.*, Vol. 30 No. 4, 4003204 (4 pp; 2020).

[295] J.L. Rudeiros Fernández, formerly CERN, now LBNL, private communication (2019).

[296] J. Bertsch, C. Scheuerlein, *et al.* "Thermomechanical properties of epoxy and wax matrix composites for superconducting magnets," presented at *29th International Cryogenic Engineering Conference/International Cryogenics Material Conference, Geneva, Switzerland., 22-26 July 2024.*

[297] B. Verma, R. Piccin, et al., "Adhesion analysis of epoxy resin impregnation systems for Nb_3Sn superconducting magnets," presented at *29th International Cryogenic Engineering Conference/International Cryogenics Material Conference, Geneva, Switzerland., 22-26 July 2024.*

[298] P.B. Studer, A. Schwegler and T.A. Tervoort, "Tough epoxy resin systems for cryogenic applications," *Cryogenics*, Vol. 143, 103923 (13 pp; 2024).

[299] M. Daly, B. Auchmann, *et al.*, "Improved training in paraffin-wax impregnated Nb_3Sn Rutherford cables demonstrated in BOX samples," *Supercond. Sci. Technol.*, Vol 35, 055014 (7pp; 2022).

[300] J. Osuna, R. Piccin, "Advanced composite insulation systems for niobium-tin superconducting magnets for accelerators: electrical characterization of laminates at cryogenic temperatures," presented at *29th International Cryogenic Engineering Conference/International Cryogenics Material Conference, Geneva, Switzerland., 22-26 July 2024.*

[301] FARO Technologies, Inc., 250 Technology Park, Lake Mary, FL 32746, USA.

[302] J. Schmalzle, LBNL, private communication (2024).

[303] J. Ferradas Troitino, P. Bestmann, *et al.*, "Applied metrology in the production of superconducting model magnets for particle accelerators," *IEEE Trans. Appl. Supercond.*, Vol. 28 No. 3, 4002106 (6 pp, 2018).

[304] R.E. Sims, "Tooling and process parameters improvements leading to improved dimensional control of the cured SSC dipole coils," in *Supercollider 3* (J. Nonte ed.), New York, NY, USA: Plenum, pp. 57–74 (1991).

[305] F. Zerobin, M. Painer, *et al.*, "Size and stiffness measurements on 9.5 m long LHC dipole coils," *IEEE Trans Magn.*, Vol. 30 No. 4, pp. 2328-2331 (1994).

[306] P. Védrine, J.M Rifflet, *et al.*, "Mechanical tests on the prototype LHC lattice quadrupole," *IEEE Trans Magn.*, Vol. 30 No. 4, pp. 2475-2478 (1994).

[307] K. Couturier, P. Ferracin, *et al.*, "Thermomechanical properties of the coil of the superconducting magnets for the Large Hadron Collider," *IEEE Trans Magn.*, Vol. 12 No. 2, pp. 1804-1812 (2002).

[308] P. Védrine, B. Gallet and C. Nouvel, "Measurement of Thermo-mechanical properties of NbTi windings for accelerator magnets," *IEEE Trans Magn.*, Vol. 12 No. 2, pp. 236-239 (1999).

[309] M. Reytier, A. Devred, *et al*, "Characterization of the thermo-mechanical behavior of insulated cable stacks representative of accelerator magnet coils," *IEEE Trans. Appl. Supercond.*, Vol. 11 No. 1, pp. 3066-3069 (2001).

[310] Ó. Sacristán de Frutos, "11 T Cable Stack Compression Tests," EN-MME Measurement Report (EDMS 2208499), Geneva, Switzerland : CERN (2019).

[311] N. Lusa, A. Devred, *et al.*, "Towards MQXF series coils," *IEEE Trans. Appl. Supercond.*, Vol. 34 No. 5, 4003408 (8 pp, 2024).

[312] S. Höll, M. Guinchard, *et al.*, "Study on the thermal contraction behavior of state-of-the-art Nb_3Sn superconducting magnet coils in the longitudinal, azimuthal, and radial direction," *IEEE Trans. Appl. Supercond.*, Vol. 34 No. 5, 4003006 (6 pp; 2024).